Design of Polymeric Nanoparticles for Phenotypic Targeting

Miguel Luis Carale Sipin

A thesis presented for the degree of

Doctor of Philosophy

in Precision Nanomedicine

Department of Chemistry

University College London

Declaration

I, Miguel Luis Carale Sipin, confirm that the work presented in my thesis is my own. Where information has been derived from other sources, I confirm this has been indicated in the thesis

Abstract

A key problem in healthcare today lies in our ability to target specific cells, particularly those within the brain. The problem arises from both inadequacies to target specific cells without targeting other cells and the difficulty in crossing the blood brain barrier (BBB). For this problem, the first barrier to overcome is to specifically target the blood brain barrier to enable the crossing of the BBB. Several targeting theories have arisen from the use of multivalent interactions yet are limited as they consider targeting only one receptor type. We herein investigate a more accurate targeting mechanism, phenotypic targeting (the targeting of a cell phenotype) and the variables that influence it.

In this thesis, brain endothelial cells (bEnd3) were used as the target cell, the main cells for targeting the BBB. Nanoparticles were designed with AP2 or Glucose ligands, to target LRP-1 or Glut1 respectively, varying both the number of ligands and ligand insertion parameters (how embedded a ligand is within a polymer brush).

When performing binding assays on three different cell lines (for endothelial cells (bEnd3), astrocytes (C8-D1A) and glioblastoma (T98G), we observed that inserting a ligand within a polymer brush alters the number of ligands required for a strong bind, which we postulate is due to a novel steric repulsion between nanoparticles. We observed no specific binding towards bEnd3 when compared with the other two cell lines; however, we postulate that this is due to difference in the glycocalyx of the three cell lines and that receptor conformation could

change depending on the glycocalyx density. Crossing studies were then conducted, and we observed that embedding the ligand within a polymer brush could allow us to both ensure the endocytosis of nanoparticles into the BBB and the transcytosis across the BBB.

Impact Statement

In healthcare today, one of the biggest problems lies in the ability to target specific cells without targeting others. Looking at cancer, many chemotherapeutic medicines remain untargeted, where cancer sites are bombarded with cytotoxic material to kill the target whilst adversely delivering toxic effects to neighbouring healthy cells. One way of reducing these off-target effects is by using nanoparticles to deliver medicines directly to target sites: active targeting of cells can be achieved through multivalent interactions. In this thesis, we explore targeting to a specific cell (namely brain endothelial cells), by influencing key variables that impact the effectiveness of phenotypic targeting (targeting of a specific cell phenotype).

The results discussed within this thesis has given rise to new avenues of research for targeting. Previous studies have not investigated the impact of the insertion of a ligand within a polymer brush: herein, we showed that inserting a ligand indeed influences binding to a target cell, reducing both the binding affinity and the postulated ligand-ligand repulsion between nanoparticles. The impact of these results shows that an alternative parameter for targeting should be explored in future works. Furthermore, the inability for specific cell targeting was postulated due to the glycocalyx - this revelation impacts future studies targeting cells as previous targeting experiments did not account for the glycocalyx. The findings outlined within this thesis furthers our understanding of targeting and highlights the potential for further research into the phenotypic targeting.

More research into phenotypic targeting would impact society, as the possibilities with nanoparticles that can target cells specifically are boundless. One could create nanoparticles to target specific cancer cells for drug delivery. An alternative use for phenotypic targeting in medicine is in cancer diagnosis: a library of various fluorescent nanoparticles with multiple ligand decorations could be made to target specific receptor profiles (phenotypes), and the library could be used to “light up” areas within a person that could exhibit the beginnings of a tumour growth. Additionally, phenotypic targeting could be used to create personalised treatment: as people’s cells may differ slightly in receptor composition, drug delivery devices could be personalised to ensure the best delivery of medication to everyone.

Acknowledgements

Firstly, I would like to thank my supervisor, Prof Giuseppe Battaglia, for giving me the opportunity to undertake this fascinating project. Thank you, Beppe, for all the support you have given me, from picking me up when I would feel down due to the stresses and pressure from doing a PhD, to being my personal cheerleader when I felt optimistic about my progress and results, allowing me to keep moving forward.

I would like to thank multiple members of the Battaglia Group who tirelessly helped me throughout my PhD. I am deeply indebted to Aroa Duro Castano and Yangwei Deng for all the synthetic help they provided to me. I'm extremely grateful to Joseph Forth and Laura Rodriguez for all the help on the self-assembly of my nanoparticles and for teaching me how to be calm under pressure. I am indebted to both Diana Leite and Diana Matias for all the biological work they helped with, from teaching me how to do cell culture and western blots, and for making me laugh all the time working in the biology lab. Special thanks to Valentino Barberi, Chiara Cursi, and Barbara Ibarzo Yus who started at the same time as me and were with me every step of the way of my PhD, forming a crucial part of my friendship and support bubble.

I would like to give a huge thank you my family: thank you Dad for listening to me and helping me when times were tough, thank you Mom for supporting and encouraging me throughout my PhD process, thank you Kuya for helping me through this process and making me laugh and smile.

Finally, I would like Dave Fenning, my partner. Thank you for staying by me, through thick and thin, throughout my PhD. Thank you for helping me, from reading through my thesis with me for grammatical mistakes to picking me up nearly every day of me writing my thesis, as you know I found it difficult to write my thesis and put my thoughts into words.

Collaboration Acknowledgements

The western blot data (for fig 3.2, fig 3.3 and fig 4.13) were obtained through experiments that were done in conjunction with Diana Leite. The experiment was designed by myself, and Diana worked with me to perform the western blot assays.

The lectin assay (for fig 3.14 and fig 3.16), the ELISA assay (for fig 3.19) and one western blot (fig 3.18) was performed by both Diana Matias and I, where I grew the cells and Diana performed the lectin assay, ELISA assay and western blot. The experiments were designed by both Diana and I.

Table of Contents

Chapter 1
Introduction

1.1 Introduction

One of the key problems in medicine today is the ability to selectively target specific cells with therapeutics whilst leaving others unaffected. Many medicines, particularly in chemotherapy, opt for a more unselective targeting regime, where drugs can cause toxic effects towards both diseased and healthy cells.[1] By having a more targeted medical treatment, we could reduce side-effects to patients arising from off-target effects and toxicity towards healthy cells.[2]

Our ability to target cells with increased precision has been bolstered by the discovery of receptors and the molecules that bind to these receptors, called ligands[3–5]. A receptor is usually a protein inside a cell or on its surface[6] with binding sites for ligands (such as small molecules, peptides, antibodies).[7] The discovery of receptors and ligands has led to selective targeting, where cell receptors can be targeted on a cell.[8,9] Selective targeting is a beneficial targeting regime for when the target receptor is unique to its disease host; unfortunately, it is commonplace for target receptors to be expressed on various cells, e.g., healthy and diseased cells. Off-targeting can therefore occur when targeting a disease cell only by the presence of the target receptor. A further targeting regime should be employed that can target not only a receptor, but a receptor density.

In nature, highly specific targeting can be observed by utilising multivalency.[10,11] Multivalent interactions involve binding two or more ligands, which are part of the

same particle, to a construct displaying multiple receptors e.g., a cell. Frenkel and Martinez-Veracoechea exploited the use of multivalency to give rise to the theory of superselectivity. Superselectivity describes the exponential growth in binding probability of a ligand-decorated particle to a target as a function on the number of receptors on the target.[12] Engineering therapeutics that can exhibit superselectivity can allow cells with a high number of a specific receptors to be targeted, whilst leaving cells with a low number of the target receptor untouched. Targeting cells with a high number of receptors is particularly important in targeting cancer, as cancer cells usually have more receptors than the healthy cells, such as in the case of colon cancer or irritable bowel syndrome where the transferrin receptor is overexpressed in the intestines.[13] The proof of concept for superselectivity has been shown both computationally,[14,15] and experimentally.[16–18]

For superselectivity, a problem arises when the target cell has a lower receptor density than the surrounding cells. Some examples of this include how both myocardial beta-1 receptors and dopamine transporter receptors are downregulated (i.e., a reduction in the cell surface receptor density) in heart failure and Parkinson's disease respectively.[19,20] One way to tackle this issue is in range-selective targeting, where binding can be achieved to targets within a finite receptor density range.[21] Range-selective targeting was achieved by utilising steric repulsion between a ligand-decorated particle and the target cell. By engineering therapeutics that can adopt range-selectivity, we can achieve targeting to cells with a receptor density within a specific range, allowing for more specific targeting of cells, including those with a lower receptor density.

A drawback to the theories of both superselective and range-selective targeting is that both targeting regimes were built upon looking only at the binding of one ligand to one receptor type; however, cells display a myriad of multiple receptors. We herein introduce the possibility of “phenotypic targeting”, the selective targeting of a cell based on its phenotype. In this regard, we dub a “phenotype” in this regard as the specific composition of multiple receptors expressed by the given cell. A pictorial representation of phenotypic targeting is shown in fig 1.1.

In this thesis, we investigate the effect of phenotypic targeting and if targeting cells selectively could be achieved through phenotypic targeting. To explore factors that influence phenotypic targeting, and therefore how we can design our nanoparticles for phenotypic targeting, we must first understand its predecessors in active targeting: superselectivity and range-selectivity.

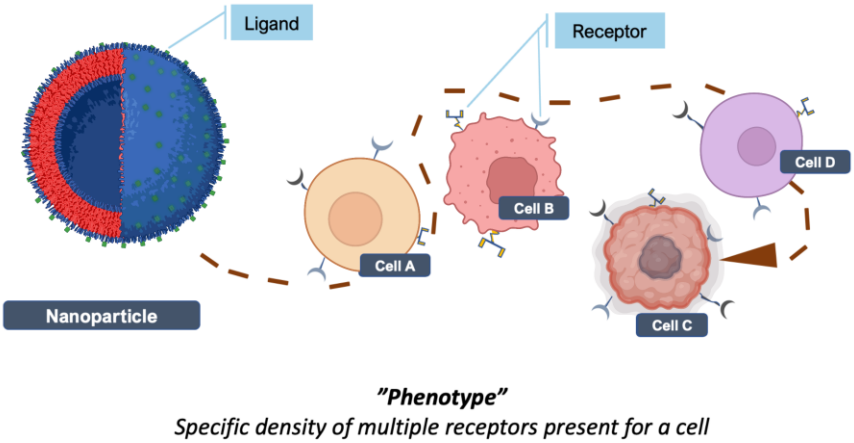

Fig 1.1 **Schematic outlining phenotypic targeting.** A nanoparticle that can achieve phenotypic targeting is shown here, where it only targets cell C amidst cells A, B and D.

1.2 Active Targeting

1.2.1 Multivalency

One common factor to both the superselectivity and range-selectivity theory lies in using multivalent interactions. Previous experiments have indicated that selective behaviour can be obtained when using multivalent interactions (i.e., the selective targeting of anti-Gal antibodies to α-Gal decorated tumour cells[22]). The total binding free energy incorporating the binding of multiple ligand-receptor bonds is considered the binding avidity.[23] Binding avidity has two major contributors: enthalpy and entropy.

The enthalpic contribution towards avidity arises from the both the binding strength of a ligand to receptor and the multiplicity of possible ligand-receptor bonds. The stronger the ligand-receptor bonds, the more negative and thus more favourable the enthalpic contribution to the binding free energy. Similarly, the more ligand-receptor bonds are formed between a ligand-decorated particle and a receptor-decorated target, the stronger the enthalpic gain to binding.

The entropic contribution for avidity is much more complex. When a ligand decorated nanoparticle binds onto a cell, there is a conformational entropic cost in the system when a ligand-decorated particle binds onto a receptor-decorated surface.[24,25] Prior to binding, ligands are free to explore the space around them and upon binding, this configurational space for exploration is lost.

Nevertheless, an entropic gain is exhibited in multivalent binding arising from avidity entropy,[23] and this comprises permutational, configurational and combinatorial entropy.[24,25] The avidity entropy arises from the different number of

permutations a ligand-decorated nanoparticle can bind onto a receptor-decorated surface. The entropic gain becomes substantial with more ligands and receptors on either the nanoparticle or target surface.[26] The permutations in which a ligand-decorated nanoparticle can bind on the receptor-decorated surface is accounted for by the function of the degeneracy of bound states, Ω. In other words, the number of possible bound states the multivalent system can form.

The degeneracy function can take on many forms and depends on the system's topology. Four topologies can be identified: the indifferent combination where only one branch of a ligand-decorated construct can interact with a binding site; the linear where binding interaction akin to a complementary nucleotide sequence or a zipper (where two species can bind only in one linear way); the circular: similar to linear (in that there is a specific orientation for binding) but circular; and finally the radial topology, where all ligands can bind onto any receptor in a binding site as described by Kitov and Bundle are depicted in fig 1.2. The equations for calculating the degeneracy function for each topology are shown in equations (1) - (4):

$$\Omega(\text{indifferent}) = N_{Ligand} \times N_{Receptor} \quad (1)$$

$$\Omega(\text{linear}) = (N_{Ligand} - i + 1) \times (N_{Receptor} - i + 1) \quad (2)$$

$$\Omega(\text{circular}) = N_{Ligand} \times N_{Receptor} \quad (3)$$

$$\Omega(\text{radial}) = \frac{N_{Ligand}!\, N_{Receptor}!}{(N_{Ligand} - i)!\,(N_{Receptor} - i)!\, i!} \quad (4)$$

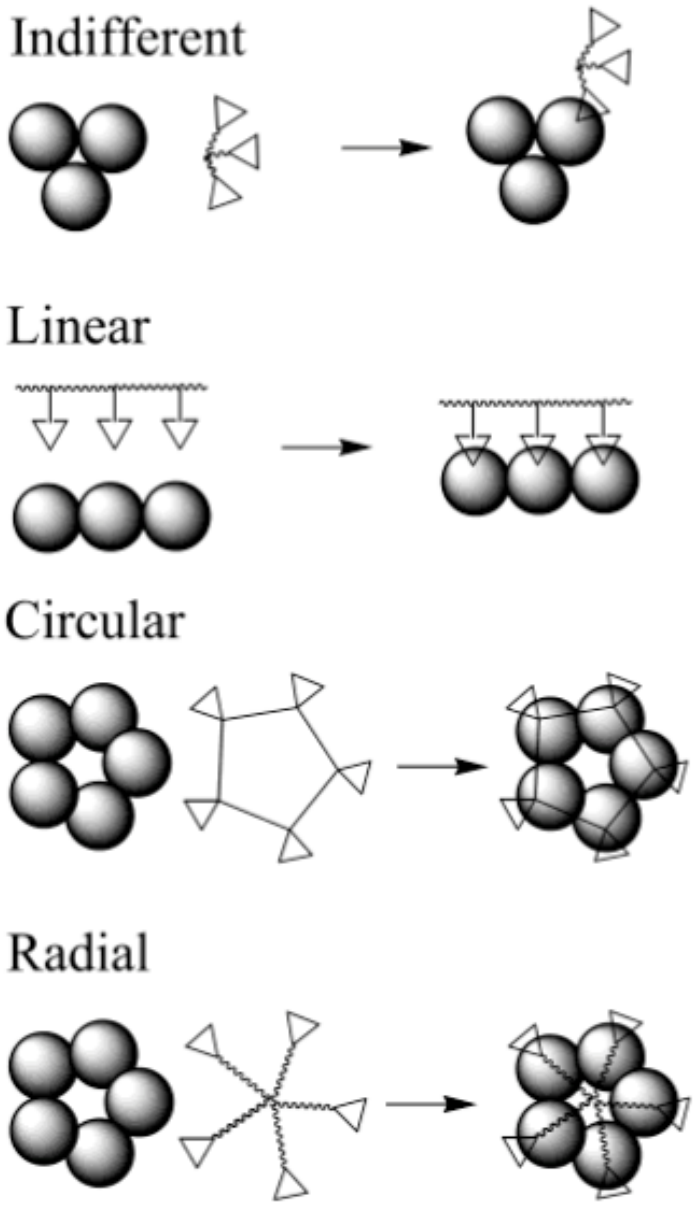

Fig 1.2 **Schematic of topologies of multivalent interactions.**[23] Reprinted from a manuscript by Bundle et al.[23]

Inspection of the equations (1) to (4) show that for all topologies, as the number of ligands (N_{Ligand}) or number of receptors ($N_{Receptor}$) increase, then the degeneracy of the system also increases. As the topology greatly influences the degeneracy of the system, topology should be carefully considered when investigating multivalent interactions.

1.2.2 Superselectivity

By utilising the principles of multivalency, Martinez-Veracoechea et al. proposed the theory of superselectivity. Superselectivity is the exponential growth in binding as a function of the number of receptors on the target or the number of ligands of the targeting moiety. The key benefit in engineering therapeutics that can exhibit superselectivity is in the ability to target cells of higher receptor densities, whilst having a reduced binding to cells with lower receptor densities. To understand superselectivity, a thorough understanding of the model used to develop the theory must be obtained. The below equations are derived from the seminal paper of Frenkel and Martinez-Veracoechea.[12] Fig 1.3 shows a diagram summarising the key points of the model, as well as giving pictorial representations of the below equations.

The model that was adopted for the theory of superselectivity assumes a flat surface, representing the cell surface membrane, divided into lattice sections, each with a set number of receptors. Each lattice can host one ligand-decorated particle, able to bind reversibly on the lattice section via ligand-receptor binding. A particle is considered bound to the surface if a ligand-receptor bond is formed between the lattice and the particle. Sectioning out the surface enables modelling of the particles binding onto the cell whilst neglecting interactions between the particles. The model assumes that the system is under thermal equilibrium, allowing for the adsorption of the particles on the cell membrane to be described in the form of a Langmuir (Hill) adsorption-isotherm:

$$\theta = \frac{zq}{1 + zq} \tag{5}$$

where Θ measures the fraction of the bound particles to the whole surface, and z is the dimensionless particle activity which practically in the case of a dilute solution of particles, is approximated to the number density of particles in solution.[12,21] q is the single-site partition function that describes the interaction between a single particle and a lattice site of the surface calculated by:

$$q = \sum_{\lambda=1}^{n_{max}} Q(\lambda) \tag{6}$$

where $n_{max} = \min(N_{Ligand}, N_{Receptor})$ is the maximum valency of the system. The valency of the system is the number of ligand-receptor bonds the system can be made up of (i.e., a valency of 2 means that 2 ligand-receptor bonds are made between a particle and the lattice site). n_{max} is equal to either N_{Ligand} or $N_{Receptor}$, whichever of the variable is the lowest. q is dependent on the $Q(\lambda)$, the probability of the particle being bound with λ bonds, where $Q(\lambda)$ is calculated by:

$$Q(\lambda) = \Omega_{\lambda}\left(N_{Ligand}, N_{Receptor}\right)e^{-\beta\lambda f_B} \tag{7}$$

where f_B is the free energy gain of binding between ligand and receptor, λ is the number of bonds, β is $\frac{1}{k_B T}$ (where k_B is the Boltzmann constant and T is temperature) and Ω_{λ} is the degeneracy of a system containing λ bonds. By combining equations (5), (6) and (7), leads to:

$$\Theta = \frac{z\sum_{\lambda=1}^{n_{max}} \Omega_{\lambda}\left(N_{Ligand}, N_{Receptor}\right)e^{-\beta f_B\lambda}}{1 + z\sum_{\lambda=1}^{n_{max}} \Omega_{\lambda}\left(N_{Ligannd}, N_{Receptor}\right)e^{-\beta f_B\lambda}} \tag{8}$$

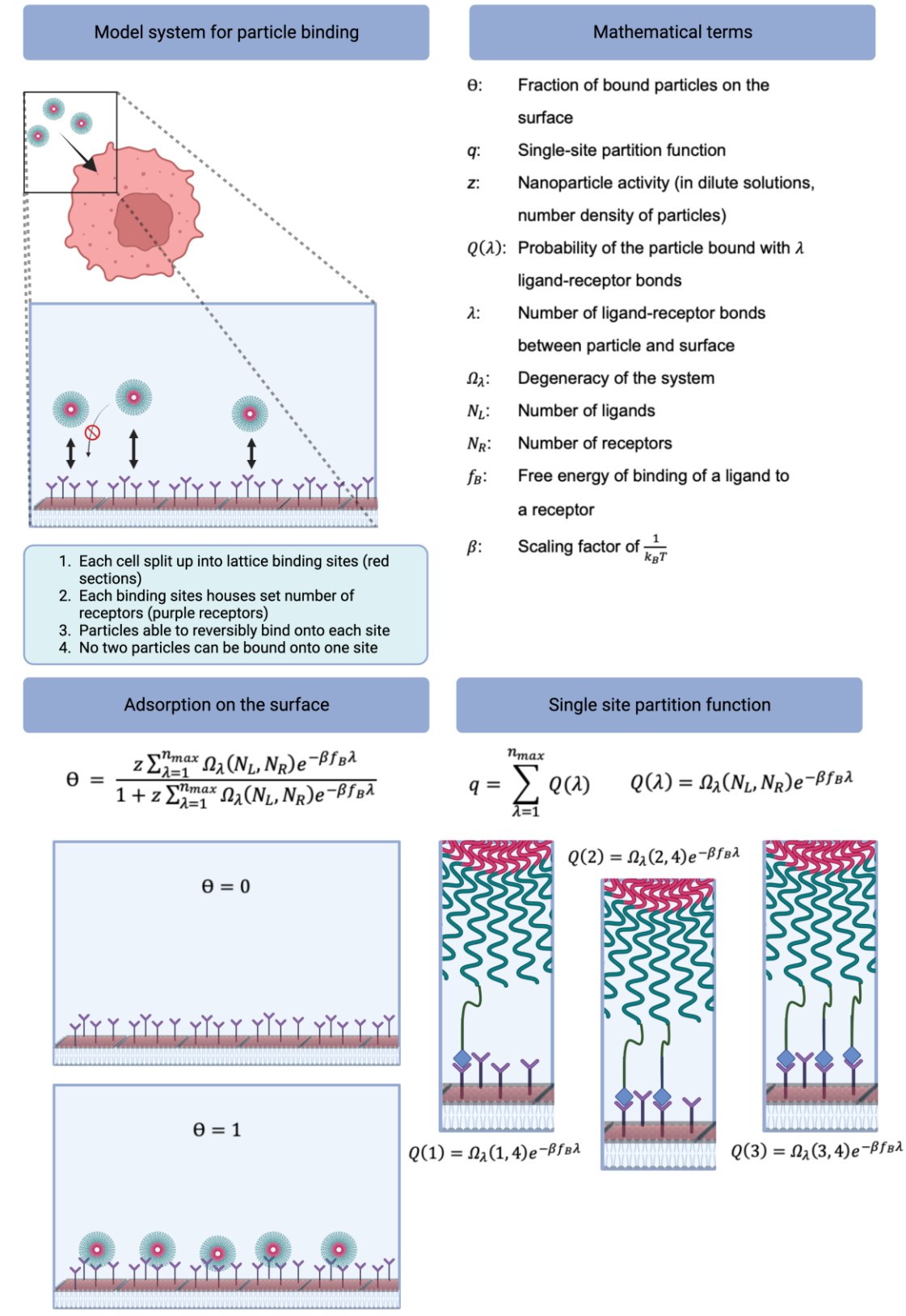

Fig 1.3 **A diagram summarising the analytical model for the discovery of the superselectivity theory.** Within the diagram, $N_L = N_{Ligand}$ and $N_R = N_{Receptor}$

Martinez-Veracoechea et al. used the model to show that when using particles that could bind onto a structure with multivalent interactions, superselectivity could be obtained. Plotting equation (8) as a function of $N_{Receptor}$ shows that a sharp transition from $\Theta = 0$ and $\Theta = 1$ couild be seen within a smaller $N_{Receptor}$ range as the valency of particle increased (fig 1.4). The sharp transition is akin to superselective targeting. Martinez-Veracocoechea et al. also showed that both a radial topology (where any ligand could bind onto any receptor on a binding site) and one in which each ligand could only bind onto one receptor, akin to a linear topology, gave rise to super selective behaviour, suggesting that superselectivity could be obtained regardless of topology.[12]

Superselectivity was only observed for multivalent particles, thus they concluded that the major contributor in achieving a super selective regime lies in the avidity entropy of the system. A superselectivity parameter, a, was introduced to quantify how superselective the particle towards a receptor decorated surface, calculated by

$$a = \frac{dln\Theta}{dlnN_{Receptor}} \tag{9}$$

The higher a, the steeper the curve and thus the more superselective the particle can be. A superselective regime was achieved when $a > 1$ at a point of $N_{Receptor}$.

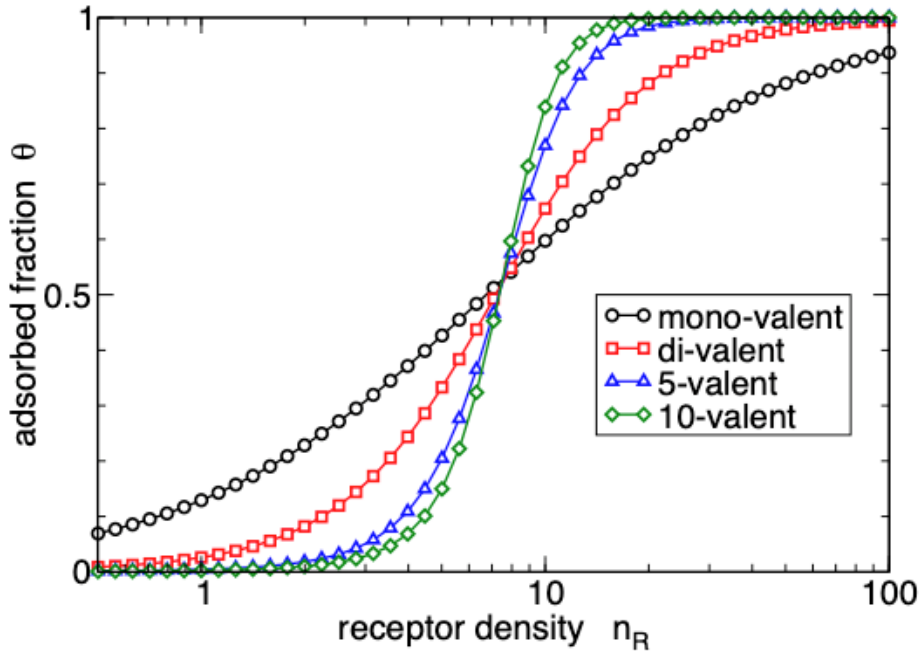

Fig 1.4 **Adsorption profile of multi-valent particles with respect to N_R, where $N_R = N_{Receptor}$.** Adsorption profiles were computed using monovalent (black) and multivalent (red, blue, green) particles. Profiles were plotted with z=0.001, and the binding affinity (f_B) was decreased as the valency increased, such that the overall avidity at $\theta = 0.5$ is kept constant for the four valences computed. A steep sigmoidal response was seen when using multivalent constructs. Reprinted from a manuscript by Curk et. al.[27]

One key factor in achieving superselectivity was shown entropically, where multivalency was essential - $N_{Receptor}$ and N_{Ligand} both influenced the degeneracy factor, Ω_λ, regardless of topology and thus θ. Nevertheless, equation (8) shows that θ also depends on two other factors: *z* and f_B, the number density of ligand-decorated particles and the binding free energy between a ligand and its target receptor respectively.

The influence of both factors (and again the valency of particles) to θ, but also to the total binding free energy between a multivalent particle and a receptor-decorated surface, with respect to $N_{Receptor}$ was computationally graphed by Albertazzi et al and shown in fig 1.5.[25] *z*, N_{Ligand} and f_B all decrease going from

red to yellow to purple in figures 1.5a, 1.5b and 1.5c respectively. Increasing the concentration of multivalent particles (and therefore *z*) on binding allows for the targeting of surfaces with lower $N_{Receptor}$, evidenced by the red curve on fig 1.5a. Increasing the number of ligands increases the selectivity of the system, evidenced by the sharper red curve on fig 1.5b, which also correlates to the same result in fig 1.4.

The effect of ligand-receptor bond strength, as seen in fig 1.5c, however, is more subtle. Indeed, as we increase the bond strength, the ability to target surfaces of lower $N_{Receptor}$ is again observed. Nevertheless, if ligands bind too strongly to their target receptor, the enthalpy of the system is the dominant factor to the multivalent binding, and a larger range of receptor densities will be targeted. In practice, using high-affinity ligands therefore reduces selectivity as all receptor densities can be targeted: indiscriminate targeting between epithelial cell adhesion molecules (EpCAM) with a high receptor density ($EpCAM^{HIGH}$) and low receptor density ($EpCAM^{LOW}$) was observed when using high-affinity constructs.[28] For designing nanoparticles for selective targeting, having multiple ligands with a lower affinity to its target is therefore more favourable to achieve more selectivity, further proven experimentally when DNA-coated nanoparticles yielded higher selectivity to their target the lower the affinity the DNA ligand was to the target receptor.[29]

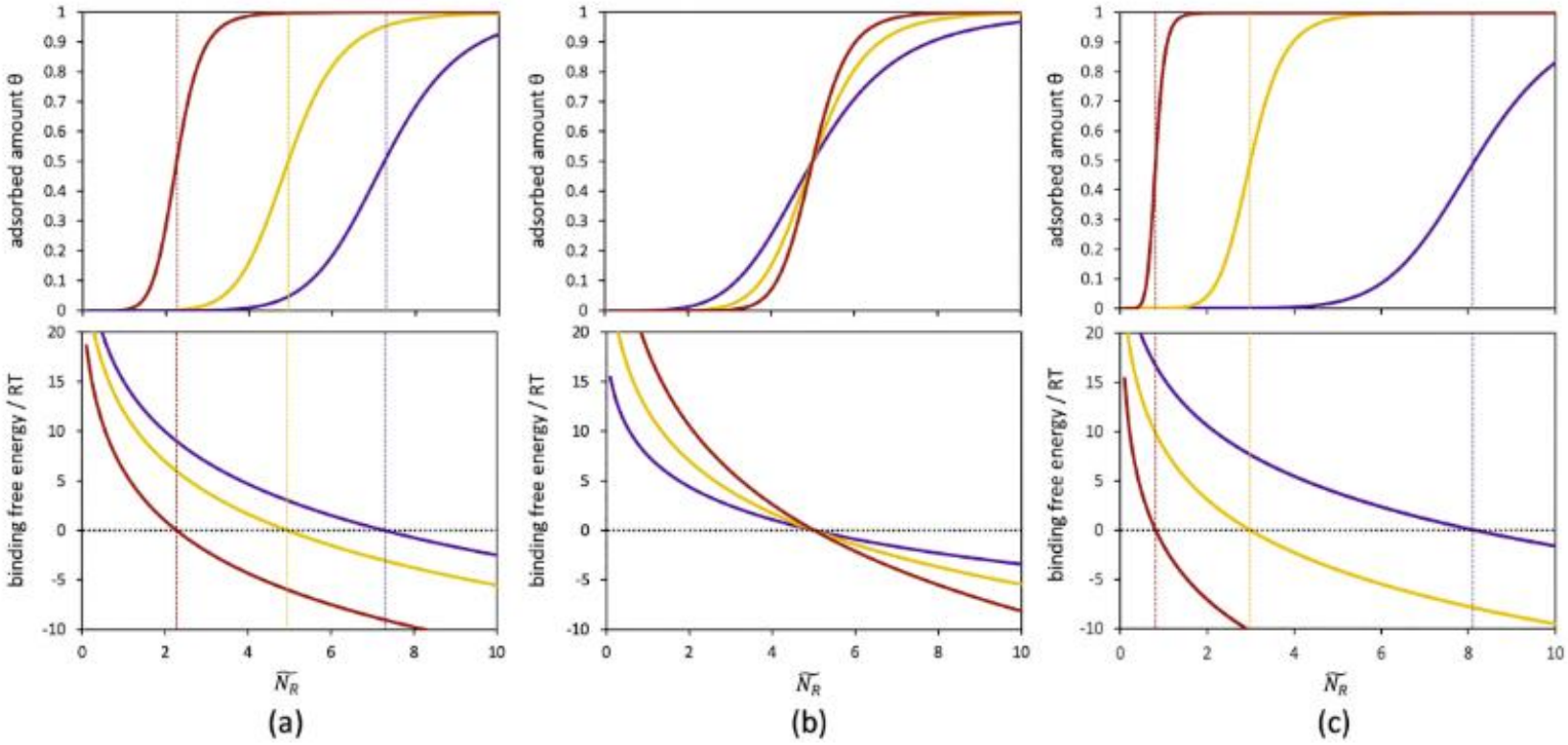

Fig 1.5 **Adsorption profiles, and total binding free energies, of multivalent particles.** The binding free energy, with respect to the number of receptors, N_R, where $N_R = N_{Receptor}$, are plotted below the adsorption profiles. In each case, one variable is altered where the other two variables are changed. (a), Concentration was altered (purple, yellow, red, from smallest to largest). (b) The number of ligands, N_L, where $N_L = N_{Ligand}$, per particle was altered for $N_L = 5{,}8{,}12$ (purple, yellow, red, smallest to largest). (c) ligand-receptor binding free energy was varied, with $f_B = -1.5, -2.5, -3.8$ (purple, yellow, red). Reprinted from a manuscript by Woythe et al. [25]

One limitation in achieving a superselective behaviour, however, lies in the binding free energy required. Martinez-Veracoechea et al. show computationally that superselectivity could be achieved when using a ligand-receptor binding free energy of βf_B = -1, 0, 2, 4 and 7;[12] however, of all of these values, the only physical value that can be obtained experimentally is βf_B = -1, as the other values indicate a positive ligand-receptor binding free energy (or 0) and binding can only occur when the free energy is negative. Furthermore, obtaining a ligand-receptor bond of βf_B = -1 is realistically difficult to achieve. Ligands usually bind onto receptors using supramolecular interactions,[30] with the lowest energy magnitude at 8 k_BT (equivalent to βf_B = -8) for a hydrogen bond[31] and the highest energy magnitude at 30 k_BT (equivalent to βf_B = -30) for the avidin/biotin complex:[32] : as observed in these values, even the lowest energy magnitude of supramolecular interaction is stronger than the binding energy required for superselectivity. Furthermore, the problem with weak multivalent nanoparticles is exacerbated as weak single-bond binding to untargeted receptors can still collectively give a high binding energy, driving non-specific adsorption of nanoparticles on cells not exhibiting the target receptors.[33]. To bring the binding free energy down to the superselective regime of ~1k_BT, a way to lower the binding free energy of the system has to be engineered, such as inducing steric hindrance between the nanoparticle and the cell.[18]

1.2.3 Range selective targeting

Nature already has its own steric hindrance mechanisms as demonstrated by the glycocalyx, a brush-like structure present on the cell membrane composed of proteoglycans and glycoproteins. The glycocalyx layer has been found to be overexpressed for example in endothelial cells[34,35] and specifically in brain

endothelial cells.[36] The glycocalyx can limit the binding of larger, high molecular weight molecules to cell surface receptors whilst allowing for the permeability of smaller molecules.[37] Indeed, cell surface receptors can sit inside the glycocalyx;[38] therefore, when ligand-decorated nanoparticle and a cell receptor is forms a ligand-receptor bond, a steric potential arises and opposes the ligand-receptor binding. When designing nanoparticles for phenotypic targeting, we therefore should consider the glycocalyx of the target cell and any steric repulsion arising due to the glycocalyx when binding onto the target cell.

Nevertheless, recent research has utilised steric hindrance to influence targeting selectivity by adjusting binding affinity. Tian et al. showed that selectivity could be tuned by the introduction of inert polymers [poly(ethylene glycol), PEG] on a nanoparticle to make a polymer brush surrounding a hydrophobic core. The inert polymers induced a steric repulsion during ligand-receptor binding. The additional steric repulsion therefore allows for binding affinity to be tuned, enabling the low affinity necessary for superselectivity.[18]

Liu et al. further expanded on the use of a polymer brush, and the presence of a glycocalyx on cells, to build the theory of range selectivity. Range selectivity describes the targeting of a specific density of receptors, where both below and above certain thresholds of receptor (or ligand) density, no binding occurred.[21] For range selective targeting, a similar model that founded superselectivity was used. The following equations were all obtained from the paper discussing range selectivity.[21] q was calculated by:[17]

$$q = v \exp(-\beta F_{tot}) \quad (10)$$

where q is again the single site partition function. v is the binding volume of the adsorption site (where $v = \pi R^2 L$, with R being the radius of the nanoparticle and L the distances to which the particle can form bonds). q was calculated in a different respect in equation (10) to equation (6), as equation (6) calculates q based on the binding energy between a ligand and receptor, and equation (10) was derived incorporating the total free energy between a nanoparticle and its' target surface. F_{tot} accounts for the total free energy of adsorption of the particle to the target site, calculated by:

$$F_{tot} = F_{att} + F_{rep} \quad (11)$$

F_{att} incorporated the attractive force for binding: it is within this term that the degeneracy function and the influence of the number of ligands and receptors are found and found logarithmic with respect to the number of ligands or receptors. F_{rep} incorporates the repulsive force for binding, and the main force that attributes towards range selectivity: the repulsive force can be split into two functions, one in which a steric hindrance can be exhibited due to the glycocalyx of a cell surrounding the receptor (F_{rep}^{gly}) and the other in which a steric hindrance can be exhibited as the receptor has to go through a polymer brush on a nanoparticle to bind onto a ligand (F_{rep}^{brush}) - (F_{rep}^{brush}) would be 0 if the ligand was on a surface of a nanoparticle, whereas it would increase the further the ligand is embedded into a nanoparticle polymer brush. The degree of how inserted a ligand is within a polymer brush, or a receptor is within the glycocalyx, was determined by δ_L or δ_R respectively.[18,21] Pictorial representations of each force are depicted in fig 1.6 and fig 1.7.

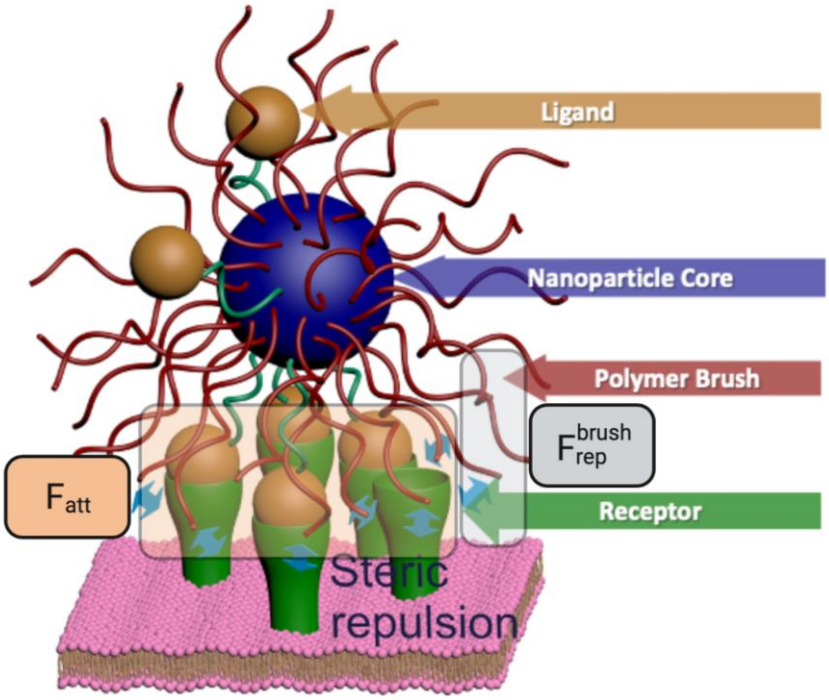

Fig 1.6 **Schematic representation of binding, emphasising the attractive and one repulsive force to binding.** A nanoparticle coated with ligands (yellow) binds onto a target surface decorated with receptors (green). The nanoparticle is decorated with a polymer brush (red tendrils). F_{att} arises from multiple ligand-receptor bonds being formed (orange highlight), and F_{rep}^{brush} arises from the repulsion exhibited when a receptor binds to a ligand embedded within the polymer brush (grey highlight). Adapted from a manuscript by Liu et al. [21]

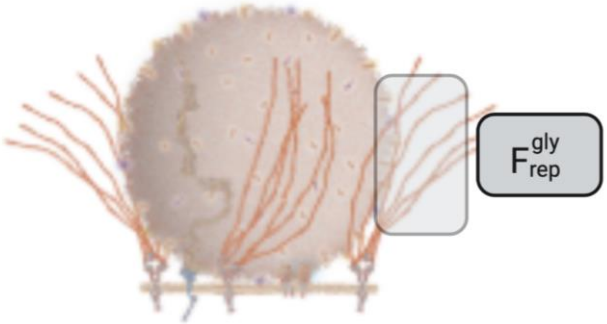

Fig 1.7 **Schematic representation of binding, emphasising one repulsive force to binding.** A ligand-decorated nanoparticle binds onto receptors deep with the glycocalyx. F_{rep}^{gly} arises from the steric potential obtained when the nanoparticle binds to a receptor amidst the glycocalyx. Adapted from a manuscript by Tian et al.[18]

Range selectivity was observed due to the balance between F_{att} and F_{rep} when using nanoparticles with ligand embedded within a polymer brush. F_{att} was logarithmic with respect to the number of ligands or receptors, and F_{rep} on the

other hand, was linear with respect to the number of ligands or receptors. When accounting for both forces in a ligand-decorated particle binding on to a receptor-decorated cell, F_{att} dominates the binding as $N_{Receptor}$ increases, leading to increased avidity and sharp increase to the number of particles binding onto the surface, but further increasing receptor density allowed the F_{rep} to dominate the binding shutting off interaction as the steric repulsion was too large to overcome, therefore range selectivity was observed where only a finite region of $N_{Receptor}$ was targeted.[21] Fig 1.8 shows a graph summarizing range selectivity, and pictorial representations of what occurs in three regions of receptor density.

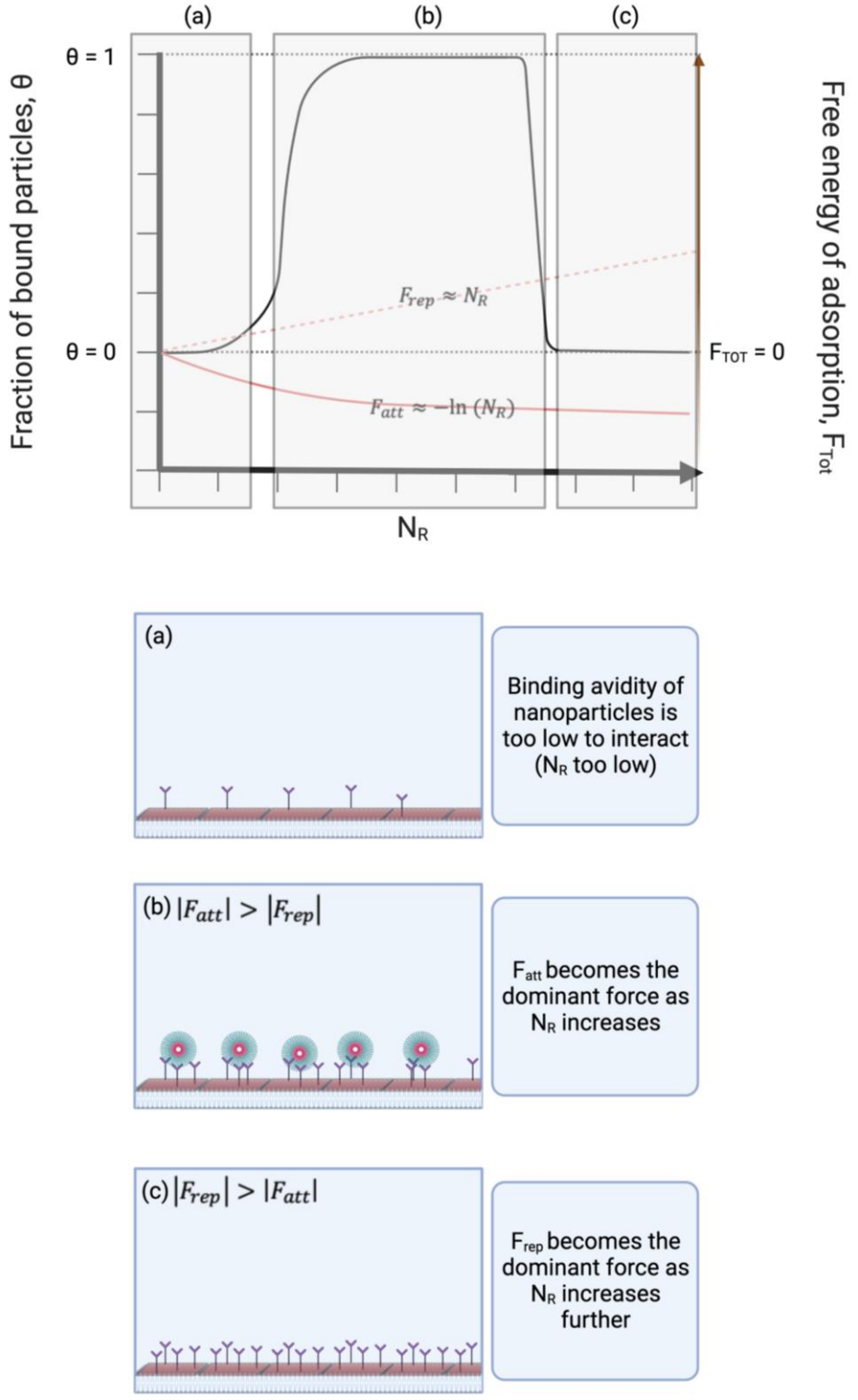

Fig. 1.8 **A diagram showing a summary of range selectivity.** The arbitrary graph shows the dependence of θ on N_R, where $N_R = N_{Receptor}$ and the attractive and repulsive forces to binding, F_{att} and F_{rep} respectively. F_{att} is logarithmic w.r.t $N_{Receptor}$ and F_{rep} is linear w.r.t N_R. Zones (a), (b) and (c) indicate binding phenomena of range selectivity, where (a) shows low avidity to binding and hence no particles on the surface, (b) shows complete adsorption of the target surface due to the dominant F_{att} and (c) shows loss of binding to the target surface attributed to the dominant F_{rep}.

1.2.4 Additional factors that influence targeting

Both multivalency, ligand affinity and steric repulsion were important in achieving super selective targeting or range selective targeting, where superselectivity was only achieved when using multivalent particles and high selectivity was obtained only when using multiple low-affinity ligands, and range selectivity emerged when introducing sterics into the system. Nevertheless, there are other variables that have been found to affect targeting, such as flexibility, non-specific interactions, and particle size.

1.2.4.1 Flexibility

Ligand flexibility has a large impact on how a ligand-decorated particle can bind onto a target cell. When ligands on a particle are longer and more flexible, the number of binding sites that a ligand can bind onto increases. The binding avidity between particle and target increases with ligand flexibility as more ligand-receptor bonds can be formed. A study utilised ligand flexibility and showed that nanoparticles with flexible Angiotensin-II ligands yielded a larger accumulation of nanoparticles on Angiotensin-II receptor positive cells when compared to nanoparticles with rigid ligands.[39]

An alternative to having ligand flexibility is to use polymers as ligands instead. Polymeric ligands are free to deform and explore different conformations. An investigation in the binding of self-assembled monolayers labelled with ferrocene (a ligand) and hyaluronic acid decorated with *β*-cyclodextrin (a receptor) was shown to achieve superselective targeting as a consequence of multivalency.[17] Further investigation on the model showed that indeed superselectivity with multivalent polymers also followed similar rules to ligand-decorated particles, as

superselectivity range shifted by either changing the linker between the polymer and ligand, the valency of the system and ligand affinity.[40] The strategy of using multivalent polymers has been further successful in the targeting of T-cells.[41]

The flexibility of both a ligand tether and the ligand itself were explored above, showing how increased flexibility can increase avidity and achieve super selective targeting. Nevertheless, a recent study has shown that, in a low-valency regime (i.e., a low number of ligands), super-selective binding can be mimicked when using rigid, planar DNA-based nanomaterials due to a more significant reduction in entropic penalty when compared to the entropic loss when using flexible ligands. The study further states that in the low valency regime, flexibility actually accounted for less selectivity.[42] Ligand rigidity should therefore also be considered when designing constructs for superselective behaviour.

1.2.4.2 Non-specific interactions

Non-specific interactions include any additional interactions that do not arise from the multivalent binding between a nanoparticle and its target. We have already discussed the use of one such non-specific interaction, such as the use of a polymer brush and introducing sterics into a system to obtain range-selectivity.[21] The binding affinity of the ligand-receptor bond was modulated by a polymer brush, and thus could allow for range-selectivity to occur.

In contrast to using non-specific interactions to adjust binding affinity, particles could be designed to induce additional non-specific interactions onto the surface only once bound to enhance selectivity. The theory of “hyper-selective” binding was shows that selectivity could be tuned when a force is applied when a particle

is bound onto a surface, where the force allows for an infinitely sharp hyper transition in binding with respect to receptor density.[43] No recent experimental work has been done to validate the theory, yet the theory promises a revolutionary design technique for influencing selectivity.

Alternatively, binding affinity could instead be tuned by including competing species. Computationally, the addition of cofactors or competitors (alternative species that compete with a ligand-decorated particle in binding to target receptors) was shown to rescale the affinity constant of ligand-receptor bonds and can in fact tune the threshold receptor density, allowing for the targeting of lower receptor densities.[44]

1.2.4.3 Particle size

In the case of targeting cells, we have previously mentioned how cells house the glycocalyx, a construct on the surface of cells that exhibits a steric potential that needs to be overcome if a particle is to bind onto the target cell. The steric potential that arises from the nanoparticle binding to a receptor within the glycocalyx was seen to depend on the radius of a particle, *R,* where smaller nanoparticles experienced a lower steric repulsion from the glycocalyx.[18] Tian et al. demonstrated how nanoparticles could experience steric repulsion from the glycocalyx also based on how large the receptor is within the glycocalyx with a pictogram demonstrating the steric repulsion in fig 1.9: if a receptor is similar in size with respect to the glycocalyx length from the base to tip, then minimal repulsion would be exhibited for a nanoparticle with ligands on the surface, and similarly, if the receptor is much smaller, then a much larger steric repulsion could be experienced.

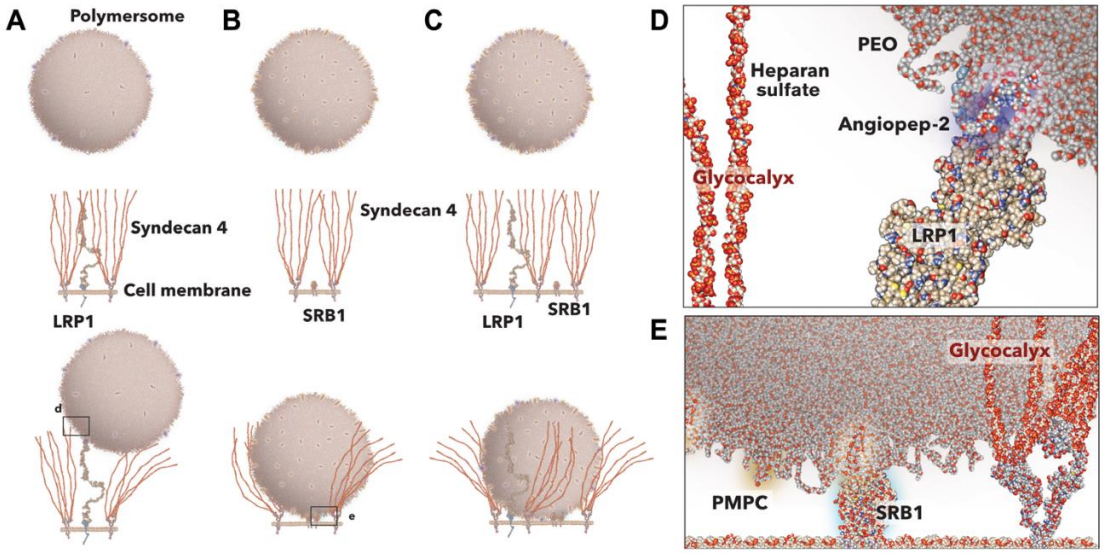

Fig. 1.9 **Repulsive steric potentials**. Schematics of a nanoparticle decorated with (A) Angiopep-2 ligands targeting the LRP-1 receptor, (B) PMPC ligands targeting the SRB1 receptor and (C) both ligands targeting both receptors. Interaction of the (D) Angiopep-2 ligand on the surface of the nanoparticle interacting with the tip of the LRP-1 receptor and (E) PMPC ligand interacting with the SRB1 are shown. Reprinted from a manuscript from Tian et al.[18]

1.2.4.4 Particle shape

In addition to particle size affecting targeting, the shape of the nanoparticle could also influence the targeting to a cell.[45] Recent studies have shown that rod-shaped particles, for example, have been thought to benefit on targeting cells due to the improved contact area with the target cell when compared to a spherical nanoparticle.[46] Da Silva-Candal et al. investigated if targeting to cells could be modulated by the shape of the nanoparticle, and that indeed rod-shaped nanoparticles coated with anti-VCAM-1 were able to target and accumulate more on hCMEC/d3 endothelial cells, both in static cell culture studies and in binding assays under flow in microfluidic devices.[47] Nevertheless, in the study, the spherical nanoparticles (200 nm in diameter) were compared to rod-shaped nanoparticles (of 400 nm in length) varying in size, making it difficult to conclude whether the increased binding was due to the shape or the size of the nanoparticle itself.

1.2.4.5 Particle charge

The charge of the nanoparticles could also heavily influence the targeting capability of nanoparticles to cells. Firstly, before the nanoparticles can bind onto cells, nanoparticles can be bound onto by serum proteins and then expelled from the body (opsonisation): this is more evident for nanoparticles with a more positive surface charge. Opsonisation can be reduced by using nanoparticles with a more neutral or negative surface charge.[48] Katoaka et al. demonstrated that micelles with neutral (1.3 mV) and anionic (-10.6 mV) surface charges had lower accumulation in the liver and hence were not taken up by serum proteins to be expelled.[49] With these facts, careful consideration should then be made to ensure that the surface charge of the nanoparticles is monitored and accounted for when designing nanoparticles for targeting specific cells

1.2.5 Targeting receptor density profiles

One limitation in the above theories for targeting is that in most cases (such as in the discovery of the superselective and range selective theories) only one ligand to one receptor type was considered. Cells have a variety of receptor types with each type having a different receptor density. Targeting cells should therefore account for targeting multiple receptors.

The superselectivity theory was expanded upon by Tian et al., giving rise to “multiplexed targeting”, where a superselective targeting could be achieved to cells in which multiple receptor types on the cell were overexpressed.[18] Super selective targeting was first achieved using nanoparticles decorated with Angiopep2 ligands or PMPC ligands, and then nanoparticles were decorated with both ligands and binding onto brain endothelial cells were done. Interestingly,

when mixing the two ligands on the nanoparticle, a synergistic effect was seen in which targeting was achieved using ligand numbers that alone would not have resulted in binding to the target cell. Computationally, they show that the selectivity could even be achieved when multiple ligand-receptor types are considered. Fig 1.10 shows the adsorption profiles of the nanoparticles tested alongside the synergistic binding effect observed.[18]

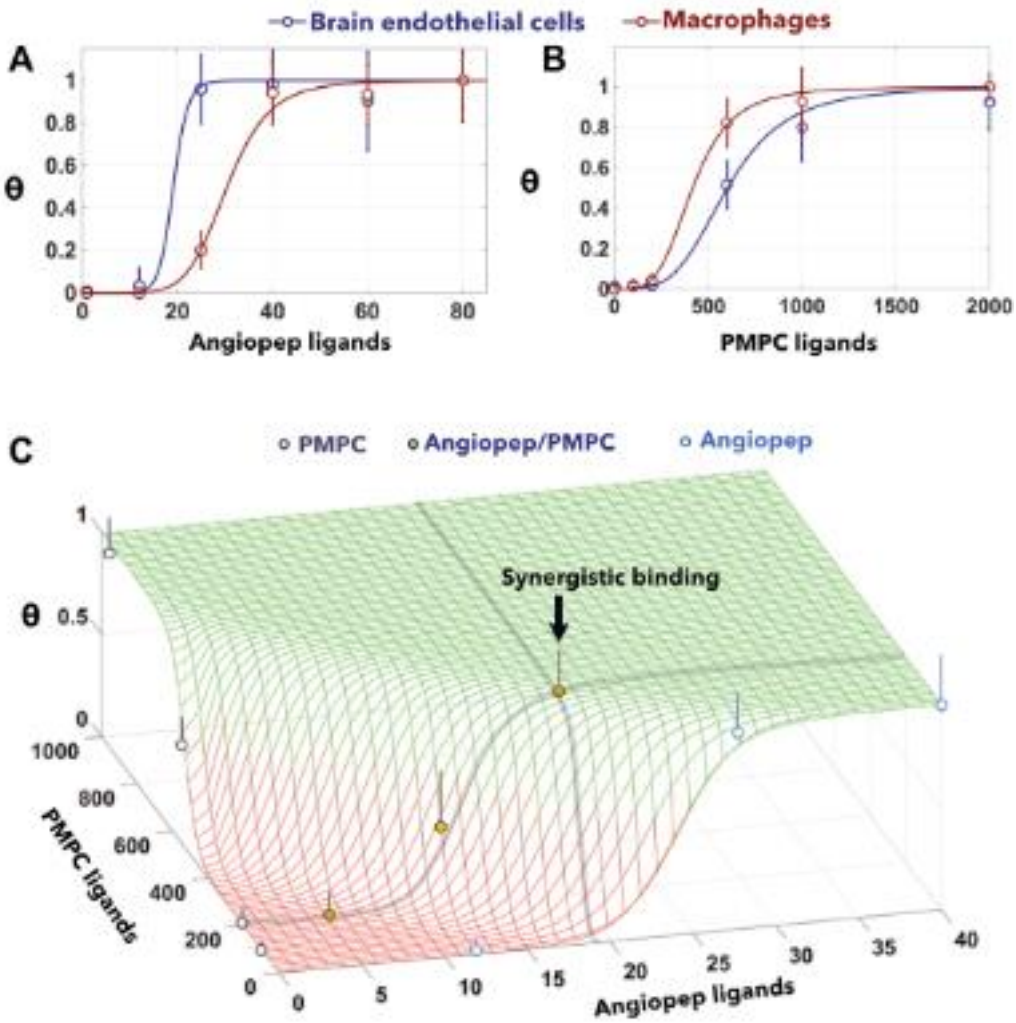

Fig. 1.10 **Superselectivity validation on brain endothelial cells**. Graphs show the surface adsorption profiles (i.e., surface coverage against the number of ligands) of nanoparticles on three cell lines, brain endothelial cells and macrophages using either only Angiopep2 (A) or PMPC (B) ligand decorated nanoparticles. (C) Binding profile to brain endothelial cells of polymersomes decorated with both sets of ligands. Reprinted from a manuscript from Tian et al.[18]

Indeed, the effect of multiplexing sounds very similar to the theory of phenotypic targeting that we intend to investigate, as multiplexing indeed looks at the targeting of multiple receptor types. However, one limitation of multiplexed targeting is that it can allow for targeting targets cells with multiple overexpressed receptors - if surrounding cells have a higher density of multiple number of expressed receptors, we again lose selectivity to a target cell, akin to a limitation in super selectivity. Curk et. al proposed a different approach of targeting, where nanoparticles could be designed to target a specific distribution of receptors, suggesting that nanoparticles have a profile with precisely the optimal number of ligands, and that the greater the number of ligands per particle, the higher the potential selectivity for targeting;[50] however, this approach of targeting was only obtained computationally, thus experimental work can be pursued to investigate if the computational findings can correlate to experimental data. We should therefore consider the variables and findings of both Battaglia and Curk when designing nanoparticles for phenotypic targeting.

1.2.6 Factors for phenotypic targeting

One main aim in this thesis is to explore whether specific cells could be targeted without targeting other cells. Overall, many variables were seen to have an influence in targeting. Specifically, the number of ligands (N_{Ligand}) and receptors ($N_{Receptor}$), the ligand-receptor bond energy (f_B) and the activity of the nanoparticles (z) were all factors that influenced superselectivity, where a high valency and a low ligand-receptor binding energy were imperative in achieving superselectivity. Further variables such as a polymer brush on the nanoparticle, the insertion of the ligand within the polymer brush (δ_L) and the insertion of a receptor within the cell glycocalyx (δ_R) all effected the attractive and repulsive

forces towards binding, giving rise to the range selectivity theory. Therefore, nanoparticles should be engineered with the variables listed accounted for, and thus we would be able to investigate if selective targeting can be achieved using the right combination of the above variables. With the design parameters for ligand-decorated nanoparticles in mind, we next decide on our target cell.

1.3 Targeting the brain

1.3.1 Blood brain barrier

One major problem in healthcare is in the treatment of brain cancers. Both global cases of brain and CNS cancers, and global deaths from the cancers, have been significantly increasing since 1990.[51] Indeed, chemotherapy, radiotherapy and surgery are all techniques that can be utilised to cure brain cancers, yet their efficacy thus far is minimal.[52]

For chemotherapy (treatment of cancers with chemicals), one major barrier for the successful treatment of brain cancers is the blood brain barrier (BBB).[53] The BBB surrounds the brain vasculature, and is an interface between the blood and the central nervous system (CNS) that strictly regulates materials (such as toxins, diseases and pathogens)[54] that travel to the central nervous system, in particular to the brain parenchyma (functional tissue of the brain, such as glial cells and neurons).[54–56] As the BBB restricts materials entering the CNS, it therefore also acts as a physical barrier for any medicine that we want to administer into the brain.[57]

The BBB is formed from a tightly regulated neurovascular unit (NVU) composed of brain endothelial cell monolayer, pericytes and astrocytes.[58,59] Structurally, in order to cross the BBB, targeting of brain endothelial cells must be done as these cells are the first line of defence to get into the brain. In the BBB, brain endothelial cells are polarised and connected by tight junctions, making it difficult for chemotherapeutics to traverse the BBB between the brain endothelial cells.[56,60] Cell polarization is when cells are all oriented in a specific direction: the apical (blood facing) and basolateral (parenchyma facing) membranes of the polarised brain endothelial cells differ in their lipid and glycoprotein composition, allowing for the brain endothelial cells to secrete and transport material in a unidirectional fashion.[61] A schematic showing the blood vasculature of the brain and components of the blood brain barrier are shown in fig 1.11.

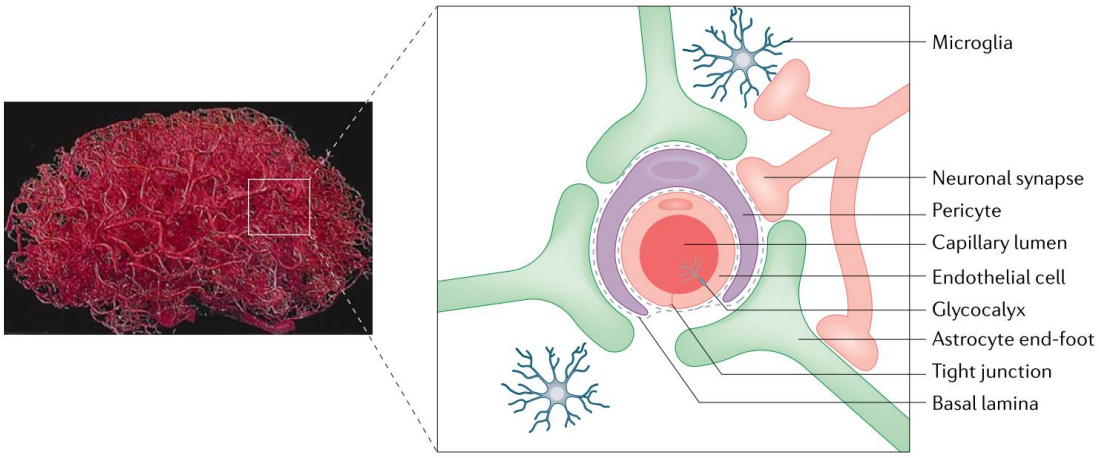

Fig. 1.11 **Brain vasculature.** A dense vascular network of the human brain (pictured on the left) branches into the microvasculature, known as the neurovascular unit (pictured on the right). The BBB comprises of the NVU between the capillary lumen and the brain parenchyma (which includes the microglia and neurons). Reprinted from a manuscript by Terstappen et al.[59]

1.3.2 Crossing the BBB

The BBB must be crossed to treat brain tumours or any other brain diseases. To this end, as brain endothelial cells both comprise most of the BBB structure and are the first lines of defence across the BBB, we decide to use brain endothelial cells as our target cell. Furthermore, by targeting the cell surface receptors of brain endothelial cells, we can induce receptor-mediated transcytosis to cross the BBB.

Receptor-mediated transcytosis occurs by binding ligands to a receptor on the apical side of the polarised brain endothelial cell layer of the BBB. Receptor-mediated transcytosis can occur using small molecules conjugated to a ligand or through ligand-decorated nanoparticles. First, receptors are bound by ligand-decorated particles, and then are endocytosed into the cell. Then, the particle can either be transported out of the cell on either the apical side, or transcytosis occurs, and the particle is delivered to the brain parenchyma. Alternatively, the particle can also be routed to a lysosome and be degraded. The steps detailed above are depicted in fig 1.12. The rate of transcytosis across the BBB is proportional to the endocytosis of the ligand-decorated particles.[62]

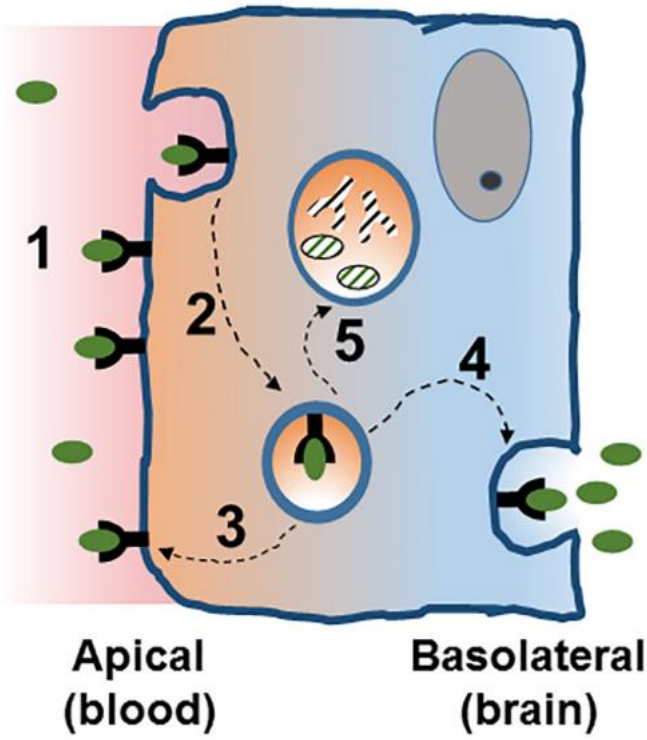

Fig. 1.12 **Receptor mediated transcytosis across brain endothelial cells.** Receptor mediated transcytosis of particles occurs via the following steps: (1) binding onto cell surface receptors (2) endocytosis of the particle into the cell and then, the particle could either (3) be recycled and transported out to the apical side of the brain endothelial cells, (4) transported across to the basolateral side of the endothelial cell or (5) routing to a lysosome for degradation. Reprinted from a manuscript by Pulgar.[63]

Multiple receptors on brain endothelial cells have been utilised for receptor-mediated transcytosis to deliver therapeutics across the BBB. Some examples of these receptors are the low-density lipoprotein receptor-related protein-1 (LRP1) and the glucose transporter protein type 1 (Glut1).

1.3.2.1 LRP-1 mediated transcytosis

LRP-1 is a receptor expressed on the surface of the BBB.[64] Recent studies have shown that Angiopep-2 (AP2), a 19 amino-acid peptide, is able the bind onto the LRP-1 receptor and can be transported across the BBB.[65] Castaigne et al. utilised this ligand and showed that when conjugating paclitaxel to Angiopep2 (to create

a conjugate labelled ANG1005), transport of the paclitaxel drug across the BBB into the brain increased both *in vitro* and *in vivo*.[66]

Recent studies further utilised the peptide and showed that nanoparticles could be conjugated with AP2 to cross the BBB for drug delivery. A recent review was conducted detailing a list of different nanoparticle systems that have been used for drug delivery to the brain with angiopep2 ligands,[67] such as using AP2-decorated poly(ethylene glycol) {PEG} - poly (ε-caprolactone) {PCL} on SU-DHL-2-LUC lymphoma xenograft mice models,[68] C6 glioma-bearing rats[69] and 3D glioma tumour spheroids intracranial glioma mouse models.[70] Other examples include the use of pH-sensitive polymeric nanoparticles (based on poly[oligo(ethylene glycol) methyl methacrylate] {POEGMA} - poly(2-(diisopropylamino)ethyl methacrylate) {PDPA}) decorated with Angiopep2 were able to cross the BBB in *in vivo* studies and deposit encapsulated IgG within astrocytes and neurons due to LRP-1-mediated transcytosis.[71] Battaglia et al. did further studies and show that the LRP-1-mediated transcytosis occurs via a tubular mechanism mediated by syndapin-2 (a protein that senses and induces curvature on membranes),[72] and that the avidity of the nanoparticle has to be tailored for transcytosis, as if the avidity is either too low or too high, transport across the BBB is reduced.[73] Furthermore, LRP-1 receptor expression can also be reduced when using particles with the highest avidity as the avidity was suggested to push the ligand-decorated nanoparticles towards degradation. The tubulation mechanism of transport across the BBB, and the degradation pathway that can be exhibited with high avidity nanoparticles, is shown in fig 1.13. Battaglia et al.'s findings indicate that having the highest avidity therefore does not necessarily translate to the best transcytosis across the BBB, mirrored in other

works looking at other receptor-mediated transcytosis, such as using the transferrin receptor[74,75] or Glut1[76].

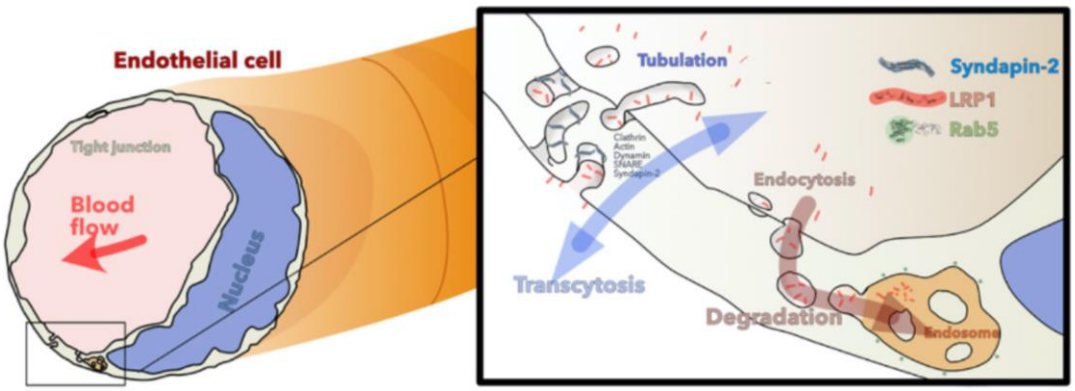

Fig. 1.13 **Diagram outlining syndapin-2-mediated LRP-1-mediated transcytosis.** Transcytosis of nanoparticles occurs via a tubulation mechanism, where syndapin-2 stabilises the tubular structures. Reprinted from a manuscript by Tian et al.[73]

1.3.2.2 Glut1 mediated transcytosis

Glut1 is a glucose transport receptor present on brain endothelial cells.[77] In the BBB, there are two families of receptors responsible for glucose transport: the glucose transporter, GLUT, family (Glut1-14)[78,79] and the sodium-glucose co transporter, SGLT, family (SGLT1-12).[80] The receptors are found throughout the BBB, with Glut1 being the highest expressed receptor at the BBB.[77] A figure detailing the glucose transport receptors in the BBB are shown in fig 1.14.

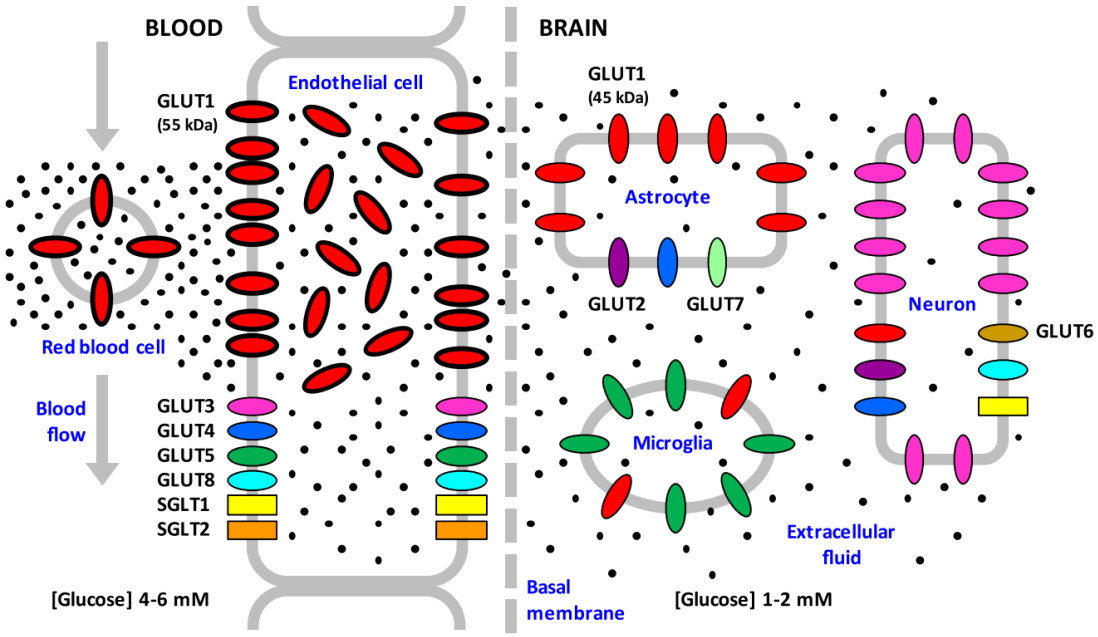

Fig. 1.14 **Transport of glucose molecules across the BBB.** Under normal physiological conditions, glucose (black dots) traverse across the BBB through the GLUT and SGLT receptor families (indicated by the coloured ovals) from areas of high concentrations (4-6 mM) to low concentrations (1-2 mM) of glucose. Glut1 (red) is the most predominant glucose transport receptor present in red blood cells and in endothelial cells and astrocytes of the BBB. Reprinted from a manuscript by Patching.[81]

Recent studies have shown that Glut1 can also be targeted by ligand-decorated nanoparticles to elicit receptor-mediated transport. Qin et al. designed liposomes (lipid-based nanoparticles) conjugated to glucose molecules and showed that liposomes were able to cross the BBB in *in vitro* studies when conjugated with

33% of glucose on the surface, however when *in vivo* studies were conducted, there was a wide accumulation of the glucose-decorated nanoparticles in throughout the body at multiple time points from 15min to 24h.[82] A similar study by Anraku et al. showed that the number glucose-decorated PEG - Poly(α,β-aspartic acid) {PAsp} nanoparticles crossing the BBB *in vivo* was boosted when mice were subjected to glycaemic control (1 day starvation, then nanoparticle injection and a further 20 wt% glucose injection 30min after nanoparticle injection), with 25% ligand decorated of the nanoparticles having the highest crossing of the formulations tested (fig 1.15).[76] Furthermore, reducing or increasing the ligand percentage (to 50% and 10% respectively) showed a reduction in the accumulation of nanoparticles in the brain, mirroring the conclusion from Battaglia et al. that a goldilocks effect can be observed where an optimum ligand percentage is required for optimum transcytosis.[73] Both studies conjugated glucose onto the nanoparticles on the 6th position of glucose mirror other studies testing transcytosis across the BBB with glucose-conjugated nanoparticles[83], indicating that the location where glucose is conjugated on a nanoparticle was important for crossing the BBB.

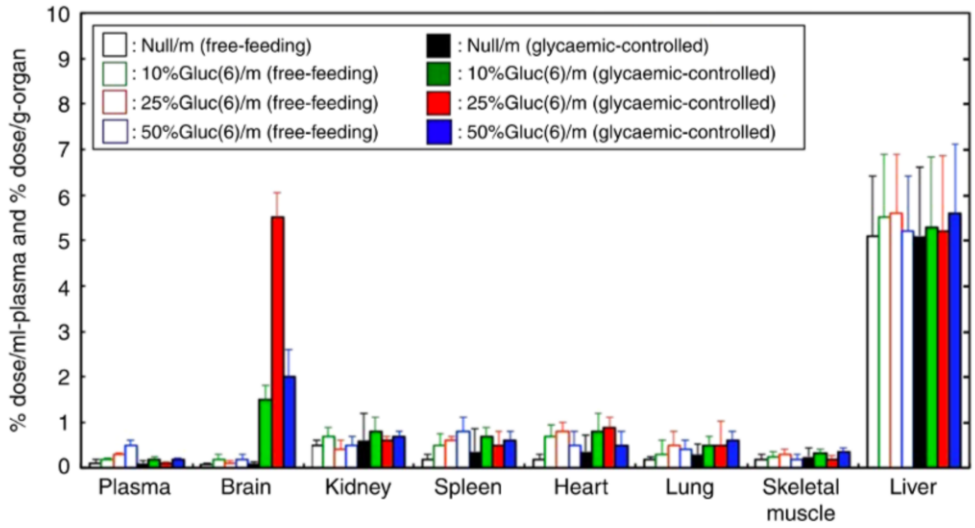

Fig. 1.15 **Biodistribution of Glucose-decorated PEG-PAsp nanoparticles in mice under different feeding conditions.** Mice were either injected with glucose-decorated nanoparticles (free-feeding), or first starved for 1 day, then injected with glucose-decorated nanoparticles and then injected with 20 wt% glucose solution 30min after the nanoparticle injection (glycaemic-controlled). Adapted from a manuscript by Anraku et al.[76]

1.3.3 *In vitro* BBB models

In vitro BBB models have been used in the literature to test transcytosis of nanoparticles prior to doing *in vivo* experiments. One of the simplest *in vitro* BBB models to be used is the transwell model.[84–86] A transwell model describes an insert placed within a well where cell lines can be co-cultured in direct contact with one another (on either side of the insert), or in indirect contact with one another (one cell line on top of the insert, and another within the well). Images of BBB transwell models are shown in fig 1.16.

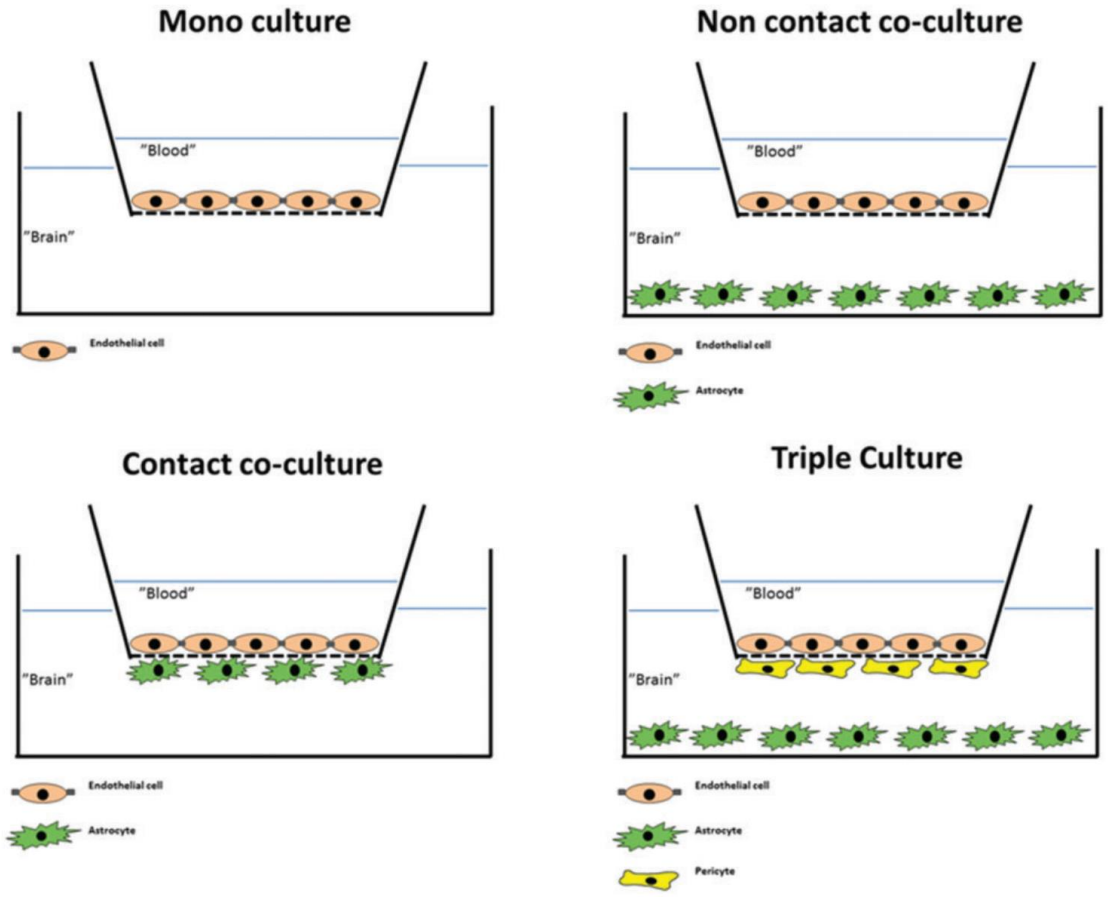

Fig. 1.16 **Common *In Vitro* BBB transwell models for transcytosis experiments.** Transwell models can be built adopting a mono culture (brain endothelial cells within the insert), non-contact co-culture (brain endothelial cells within the insert, and astrocytes within the base of the well), contact co-culture (brain endothelial cells within the insert and astrocytes grown on the opposite side of the insert) or triple culture (brain endothelial cells and pericytes either side of the insert with astrocytes grown on the base of the well). Reprinted from a manuscript by Helms et al.[87]

The simplest transwell model uses only one cell line (brain endothelial cells) within the insert whilst having media present in both the well and insert, called mono culture transwell models. Mono culture transwell models have previously been made using animal brain endothelial cells (mouse,[73,88] rat[89] or porcine[90]) or human brain endothelial cells.[91,92] For mono culture transwell models, an extracellular matrix (such as collagen) may be added to the transwell to allow for improved cell attachment onto the transwell.[93] Indeed, using a mono culture transwell model would allow for preliminary investigation of transcytosis of ligand-

decorated nanoparticles; however, the BBB is constructed with additional cell types (such as astrocytes and pericytes), thus co-culture transwell models would more closely mimic the BBB.

Non-contact and contact co-culture transwell models have been used to study transcytosis. Both models, using pericytes grown either on the base of a well (for non-contact) or in opposite side of the transwell (for contact), were used to show the pericyte's to protect the BBB, as under oxygen deprived conditions permeability across the *in vitro* BBB was reduced in the contact co-culture model, compared to the non-contact model, suggesting the pericytes role in protecting the BBB during hypoxia.[94] A contact co-culture transwell model (where mouse endothelial cells (bEnd3) were cultured on the top of the insert and mouse astrocytes (C8-D1A) were cultured on the bottom) was used by Battaglia et al. to show that AP2-decorated POEGMA - PDPA crossed the transwell system quickly with no endocytic sorting or degradation within the endothelial cells.[71] Nevertheless, even though the non-contact and contact co-culture *in vitro* models have significant benefits over the monoculture model, difficult lies in keeping both cell lines alive during the preparation of the model, as different cell lines may require different medias and conditions; this difficulty is exacerbated during a triple culture model. Additionally, although the *in vitro* models give us a way to mimic the BBB, experiments should then be done *in vivo*, as these *in vivo* models provide a more realistic scenario for crossing the BBB.

1.4 Nanoparticles for active targeting

1.4.1 Nanoparticles: lipid or polymer based?

Having achieved both an understanding of several design principles for targeting and obtained a suitable target for the study, a suitable construct can now be chosen to investigate phenotypic targeting and the possibility of targeting specific cells. As previously dictated, that in this thesis, we would use nanoparticles for the study. One major advantage of using nanoparticles for targeting specific cells is in the chemical flexibility of synthesis, as nanoparticles can be designed with multiple ligands to elicit a multivalent interaction with its target (i.e., nanoparticles were designed with multiple RGD peptide ligands to bind to endothelial cells[95]). An additional advantage is that nanoparticles can also be used as drug delivery devices: once targeting is achieved, a future aim would be to use the targeting nanoparticles to deposit therapeutic drugs into the target cells. Therefore, both targeting and drug delivery properties of nanoparticles should be examined.

The most used and clinically approved building blocks for nanoparticles for drug delivery are lipids to make lipid-based nanoparticles.[96] Lipid-based nanoparticles are easy to self-assemble with many self-assembly methods[97], biocompatible[98] and surface modification can be achieved to introduce ligands.[99] One subset of lipid-based nanoparticles are liposomes, nanoparticles produced from the self-assembly of phospholipids.[100] Liposomes are formed due to the amphiphilic nature of phospholipids (i.e., molecules consisting of a hydrophobic tail and a hydrophilic regime) with the hydrophobic effect (the attraction of the hydrophobic moieties in phospholipids) as the main driving force for their self-assembly in water. Ligand-decorated liposomes have previously been used to target specific receptors on cells, such as using octreotide as a ligand on PEG - distearoyl

phosphatidylethanolamine {DSPE} liposomes to target somatostatin receptors on various cancer cells,[101] or using mannose receptor-targeted liposomes to target dendritic cells.[102] Furthermore, liposomes are already being used clinically as drug delivery devices for the treatment of various cancers [i.e. ovarian cancer (Doxil®[103,104])], fungal diseases (i.e. Amphotec®) and for use as viral vaccines (i.e. Epaxal®),[104] indicating their success to deliver drugs to their target cells.

However, some difficulties arise when using lipid-based nanoparticles as drug carriers, such as their low colloidal stability[105] leading to leakiness[106] and therefore allows drugs to escape the confines of the delivery system before reaching the target. Low chemical versatility[107] also makes liposomes susceptible to binding of opsonin proteins on its surface (opsonisation) allowing macrophages to detect them and thus leading to their consequential early removal from the body. Opsonisation can be alleviated by attaching hydrophilic polymers (such as using PEGylated liposomes[108]) to their surface, yet the full surface of a liposome cannot usually be covered, making opsonisation still inevitable.

Polymer-based nanoparticles (produced from the self-assembly of amphiphilic block copolymers) and lipid-based nanoparticles may share similar properties, such as being able to encapsulate hydrophilic (i.e., doxorubicin HCl, a hydrophilic drug, encapsulated in both liposomes[109] and poly([N-(2-hydroxypropyl)] methacrylamide)$_{35}$-*b*-poly[2-(diisopropylamino)ethyl methacrylate]$_{75}$ [PHPMA$_{35}$-*b*-PDPA$_{75}$] pH-responsive polymersomes[110]) and hydrophobic cargo (i.e., dehydrosilymarin encapsulated within liposomes[111] and small hydrophobic agents such as curcumin encapsulated within poly(2-methyl-2-oxazoline)-*b*-poly(dimethysiloxane)-*b*-poly(2-methyl-2-oxazoline) (PMOXA-PDMS-PMOXA)

polymeric nanoparticles[112]). Both nanoparticle types can have their membrane functionalised with ligands;[99,113] nevertheless, polymer-based nanoparticles have several advantages over using lipid-based nanoparticles. Polymer-based nanoparticles can be tailored to specific needs due to polymer-based nanoparticles being more chemically versatile, such as the ability to be pH sensitive, i.e., using poly(2-(diisopropylamino)ethyl methacrylate {PDPA}[114,115] or by incorporating a benzoic imide bond into a polymer.[116] Additionally, the chemical versatility of the polymer-based nanoparticles allows for easier surface modification than liposomes.[117,118] Polymer-based nanoparticles are also more mechanically and chemically stable (polymersomes were found to be more stable than liposomes when stored at 25^{o}C over 8 weeks)[119] and will have a full surface coverage of hydrophilic polymers acting as a polymer brush to greatly reduce opsonisation. Polymer-based nanoparticles can adopt different morphologies, such as micelles, worm-like micelles and polymersomes.[120] The benefits of the polymer-based nanoparticles compared to liposomes described above are illustrated in fig. 1.17, from the review article by Messager et al.[121] The largest benefit for using polymer-based nanoparticles lies in their chemical versatility, as the nanoparticles can be designed specifically to tailored needs, thus we decided to use polymer-based nanoparticles to investigate if specific cell targeting could be achieved.

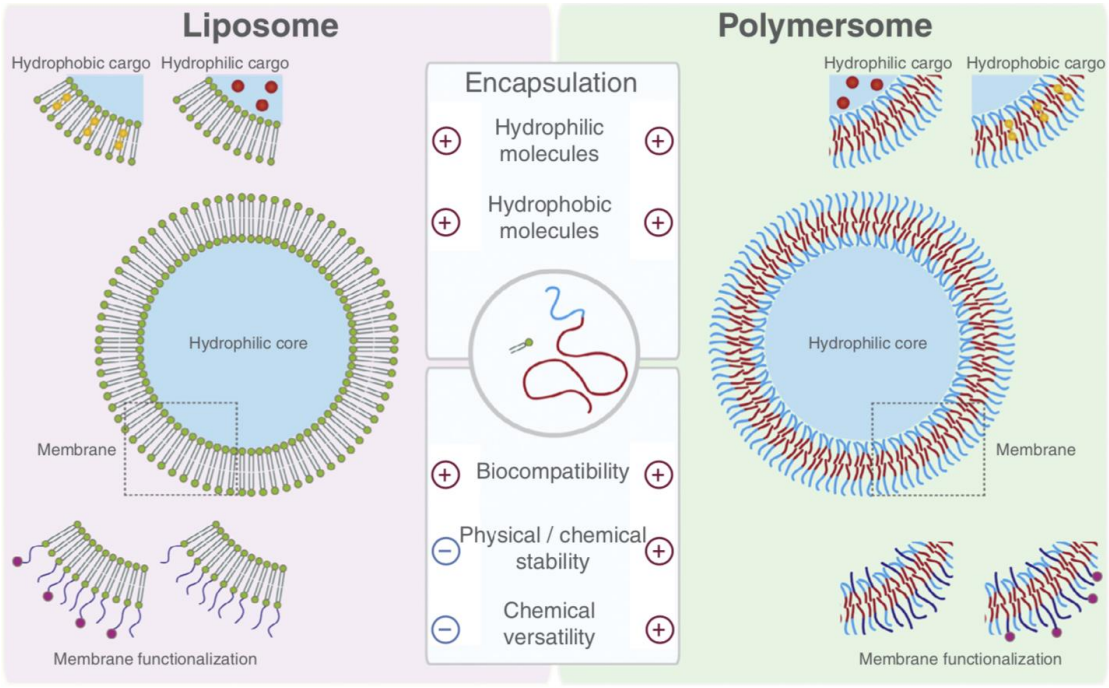

Fig. 1.17 **Liposomes and Polymersome comparison.** The properties of liposomes (left) and polymersomes (right). Reprinted from a manuscript by Messager et al.[121]

1.4.2 Polyester-based nanoparticle building blocks

The choice of polymers used when engineering polymeric nanoparticles depends on the functionality required. As an example, polymers such as poly(2-(diisopropylamino)ethyl methacrylate) {PDPA} can be used due to its pH sensitivity[122], a favourable attribute when targeting cancer cells due to their more acidic surrounding.[123] Two major aspects to consider when choosing polymers for drug delivery applications are biocompatibility and biodegradability.

One of the most widely used biocompatible hydrophilic polymers in medicine is PEG: it has been clinically approved in various forms e.g. PEGylated drugs[124] and as coating of liposomes[103]. PEG has also been found to extend the lifespan of nanoparticles in the body[125,126], due to its ability to form a highly water-bound barrier[127] making them less susceptible to opsonisation[128]. A decreased susceptibility to opsonisation is important for a drug delivery system, as it grants

the vehicle stealth capabilities from their destruction by the immune system. Other examples of polymers which decrease opsonisation are PMPC, or poly[N-(2-hydroxypropyl)metha-crylamide] {PHPMA}.[126,129]

For the hydrophobic block of an amphiphilic copolymer, polyesters are most used due to their biodegradability and biocompatibility. Poly[ε-caprolactone] {PCL} and poly[D,L-lactide] {PDLLA} are common polyesters used for biomedical applications e.g. scaffolds for tissue engineering and delivery systems.[130] PCL and PDLLA arise from the polymerisation of ε-caprolactone and D,L-lactide respectively, both monomers that are biodegradable. Poly[glycolic acid] {PGA}, arising from the polymerisation of the biodegradable glycolic acid monomer, is another polyester currently used in absorbable sutures and orthopaedic pins[131]. An emergent polyester with promising properties for biomedical applications is poly[ε-decalactone] {PεDL} due to the renewability of its monomer[132]. The conjugation of any of the above hydrophobic polyesters (PCL, PDLLA, PGA or PεDL) to the previously described biocompatible hydrophilic polymers (PEG, PMPC or PHPMA) will therefore give us an amphiphilic block copolymer that we can use as the model for phenotypic targeting.

One common amphiphilic copolymer used as a building block to produce PEG-polyester nanoparticles is PEG-PCL. PEG-PCL nanoparticles have been studied extensively for their applicability as a drug delivery device, with structures of both polymer units (PEG and PCL), and of a di-block PEG-PCL copolymer shown in fig1.18.[133] PEG-PCL copolymers have been synthesised by ring opening polymerisation (ROP) of the cyclic ε-caprolactone monomer using either a PEG polymer or a methylated PEG polymer to obtain either triblock PCL-PEG-PCL

copolymers[134,135] or diblock PEG-*b*-PCL respectively. Polymerisation of cyclic ester monomers, such as ε-caprolactone or lactides (to produce PDLLA), occurs in the presence of metallic catalysts such as $Sn(Oct)_2$[136–139]; however, metal catalysts could reduce product application for *in vivo* and future clinical studies as little is known about their long-term potential toxicity.[140] Organocatalysts for the ROP of ε-caprolactone, such as benzoic acid[141] and diphenyl phosphate (DPP),[142] have benefits over metallic catalysts as they have reduced toxicity and are cheaper. Due to the multiple synthetic methods that could be adopted to create PEG-PCL, including making different length block copolymers by adjusting the feed ratios of ε-caprolactone monomers to different length PEG initiators, PEG-PCL was chosen as the building block for our nanoparticles for targeting specific cells.

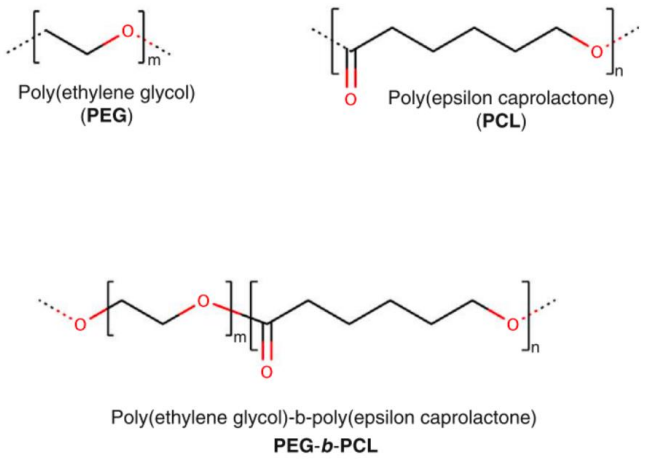

Fig. 1.18 **PEG, PCL, and PEG-*b*-PCL copolymer structures.** Adapted from a manuscript by Grossen et al.[133]

1.4.3 Block copolymer self-assembly

The driving force for an amphiphilic block-copolymer self-assembly in water is the hydrophobic effect. Through this effect, the copolymer would assemble in a way in which the hydrophobic blocks aggregate to be shielded from water. The

morphology of the structure assembled depends on a variety of factors; however, the primary reason is as a result of the inherent molecular geometry[143].

Specific aggregate morphologies can be targeted depending on the amphiphile features. Specifically, the dimensionless packing factor parameter, *p*, accounts for certain morphologies that a specific amphiphilic molecule can adopt. This parameter depends on the volume of the hydrophobic chain (*v*), the optimal area of the hydrophilic end group (a_0) and the length of the hydrophobic tail (l_c). If $p < \frac{1}{3}$, spheres are usually obtained, whereas when $\frac{1}{3} < p < \frac{1}{2}$, cylinders are obtained and when $p > \frac{1}{2}$, bilayers and vesicles can be formed. The morphologies described are depicted in fig. 1.19.[144] *p* is calculated by:

$$p = \frac{v}{a_0 l_c} \tag{12}$$

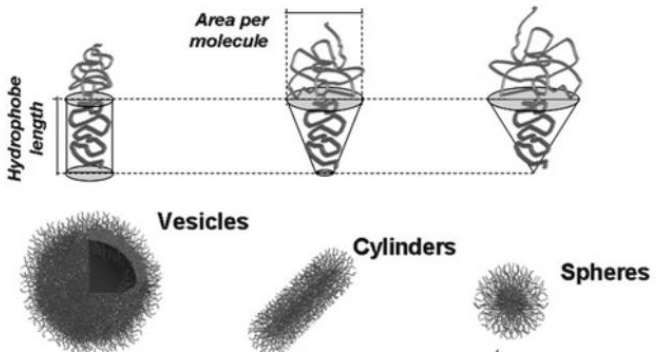

Fig. 1.19 **Amphiphilic Self-Assembled Morphologies.** Various self-assembled structures of di-block copolymers in a block-selective solvent (i.e., hydrophilic-selective solvent). Structures are formed dependent on the curvature and packing parameter. Reprinted from a manuscript by Fernyhough et al.[145]

For block copolymers, it is difficult to accurately calculate these parameters and instead it is more advantageous to look at the hydrophilic-hydrophobic molar mass ratio of the blocks ($f_{hydrophilic}$). When the ratio is high ($f_{hydrophilic} > 0.5$)

micellar/spherical structures can be formed, whereas when the ratio is smaller ($0.20 < f_{hydrophilic} < 0.40$), polymersomes can be formed.[146]

Targeting specific morphologies, however, is not as simple as just synthesising a polymer with the correct $f_{hydrophilic}$. Eisenberg et al. have shown that for a single polymer, poly(styrene) {PS} - *b* -poly(acrylic acid) {PAA}, structures from spheres to bilayers could be formed by just adjusting the polymer concentration.[147] The final morphology of the aggregate is also dependent on the temperature, concentration, and mixing rate during formation[147,148] as these affect the kinetics and thermodynamics of the system. Different methods of forming polymer aggregates have been documented using techniques like solvent switch, nanoprecipitation, film rehydration, and flash nanoprecipitation, and Mingotaud et al. have described their ability to form different morphologies.[149]

Specifically for PEG-PCL, various self-assembly methods have been utilised in the literature to create PEG-PCL nanoparticles.[133] Nanoprecipitation has been routinely used to produce PEG-PCL nanoparticles:[150–152] the method involves dissolving the polymer, or the polymer and any drug to encapsulate within a nanoparticle, in a water-soluble organic solvent (such as THF or DMF), then adding the polymer solution dropwise to a stirring solution of water, leading to the formation of small polymer droplets, then the organic solvent is removed to produce the polymeric nanoparticles. An alternative method for PEG-PCL self-assembly is in film rehydration:[134,153] the block copolymer is dissolved in a solvent with a low boiling point (such as chloroform or acetone), and the solvent is removed slowly to create a thin polymer film, which when hydrated drives the self-assembly of the copolymers due to the hydrophobic effect.[140] For PEG-PCL,

further adaptations of the film rehydration method have been employed, such as the use of heating the copolymer past the melting point of the polymer, to create monodisperse PEG-PCL micelles.[135] A benefit for using PEG-PCL as the building block for nanoparticles is the multitude of methods to produce the nanoparticles; however, the limitation is that usually the sizes and shapes of the nanoparticles differ depending on how they were formulated (i.e., PEG-PCL nanoparticles with mean diameters of 82.9nm, 87.8nm and 109.0nm were made using nanoprecipitation using acetonitrile, acetone or THF as the solvent[154]) thus a self-assembly method should be chosen and stuck with when producing nanoparticles to ensure nanoparticles are made of the same size and shape.

1.4.4 Ligand conjugation

Ligands can be conjugated onto nanoparticles either through means of post-polymerisation modification[155] (conjugation of ligands onto free block copolymers prior to self-assembly), or via direct conjugated on self-assembled structures.[156] For both methods, chemical ligand conjugation techniques well established in the literature can be employed[157], such as amide coupling using NHS coupling techniques[158], thioester coupling using free thiols to bind onto maleimide units[159] or copper click conjugation via a 1,3 Huisgen cycloaddition between an azide and alkyne.[160] Schematics of the three labelled conjugation techniques is shown in fig 1.20.

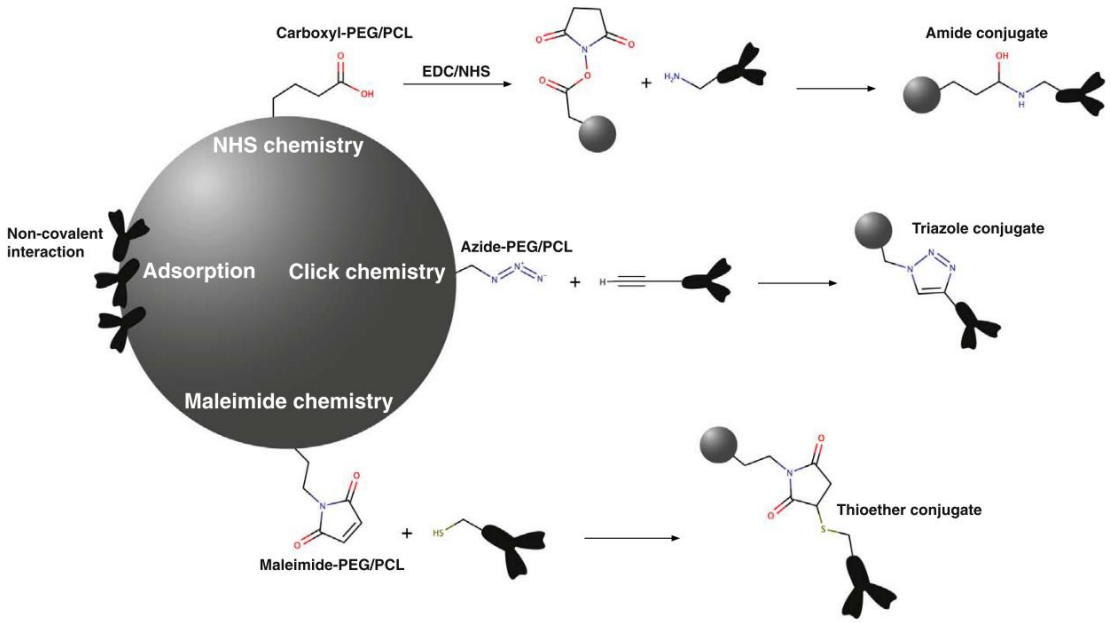

Fig. 1.20 **Conjugation of targeting ligands to PEG-PCL-based nanoparticles.** Schematic representation of 3 ligand conjugation strategies: amide coupling, 1,3-dipolar azide-alkyne conjugation and thioester conjugation. Reprinted from a manuscript by Grossen et al.[133]

EDC/NHS coupling is a very common amide coupling ligand conjugation technique used widely to link ligands to molecules.[161–163] When discussing conjugation to polymer-based nanoparticles, copolymers with an acid group on the hydrophilic end can react with EDC/NHS where the acid first reacts with the EDC chemical, then the NHS molecule reacts with the EDC-conjugated polymer to form the NHS-copolymer. A ligand with a nucleophilic amine group can then react with the NHS-conjugated copolymer to release a ligand-conjugated copolymer. Yongbin et al. utilised this ligand conjugation approach to create LS-10 conjugated PEG-PCL nanoparticles.[164]

Maleimide coupling, using thiol-containing ligands to bind onto maleimide-conjugated polymers, has also been used to link ligands to PEG-PCL nanoparticles.[165,166] Xin et al. have used this technique to conjugate Angiopep2

to PEG-PCL polymers to produce glioma targeting nanoparticles.[167] One limitation for using maleimide coupling is the requirement to use a thiol for coupling, sometime blocking the ligand from being able to target the cell (such as in peptidic ligands, where thiol-containing amino acids will no longer be available to bind onto target receptors).[168] Furthermore, when using a peptide as a ligand, the reaction is not stereospecific, as any thiol-containing amino acid could be used to bind onto maleimide-conjugated polymers.

Conjugation of ligands to polymers can also be done through “click” chemistry: click reactions give high yields, are stereospecific, produce products that are easily isolated through non-chromatographic methods and can be conducted under mild conditions (i.e. low temperature and can be conducted in water)[169]. One specific reaction in this category of reactions is the copper catalyst 1,3-dipolar cycloaddition between an azide and alkyne. A schematic of the azide-alkyne cycloaddition, hereby named click conjugation, is seen in fig. 1.21.

The flexibility of an azide-alkyne conjugation allows it to be used in a whole range of reactions, such as in polymerisation[170] and in peptide conjugation[170,171]. The copper click conjugation allows for facile removal of the catalyst through dialysis, a desirable property for a click reaction in biomedical applications. Ligands and polymers can either be made or bought with the desired groups for a click conjugation, giving us a starting point for making the ligand-conjugated copolymers.

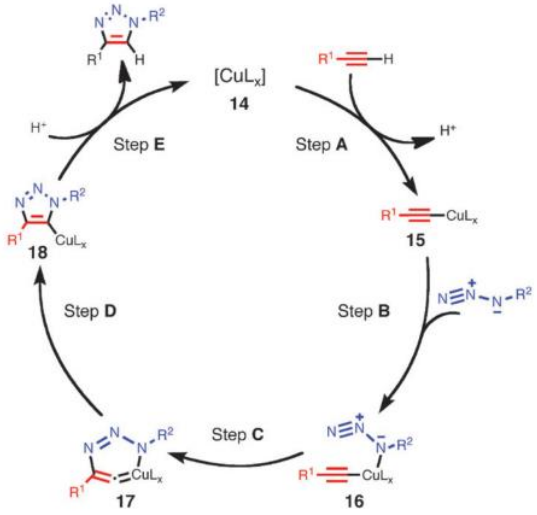

Fig. 1.21 **Copper click conjugation mechanistic cycle.** Early proposed mechanism of the copper click conjugation based on DFT calculations involving a single copper atm. Reprinted from a manuscript by Liang et al.[172]

1.5 Aims and objectives

As detailed in the introduction, our major aim in this thesis is to first explore whether we can selectively target cells. Throughout the literature review, we have discussed factors required for selective targeting, a target cell for our purposes (brain endothelial cells), and nanoparticles (PEG-PCL nanoparticles) that we could employ to investigate if we could selectively target cells. Furthermore, as we aim to target brain endothelial cells, we could extend our research and investigate why and how any of the nanoparticles made for targeting can cross an *in vitro* BBB model. In summary, the aims of this thesis are:

1. Can we selectively target brain endothelial cells?
2. Can we control the crossing of nanoparticles across the BBB?

Our objectives through this thesis are therefore:

1. To optimise multivalent targeting towards brain endothelial cells
2. Investigate targeting towards brain endothelial cells against other cell lines
3. Investigate factors that influence targeting (such as ligand insertion parameter and number of ligands) on the crossing of the BBB

Chapter 2
Nanoparticle synthesis for targeting brain endothelial cells

2.1 Introduction

Our first objective is to synthesise and characterise nanoparticles we believe that can bind onto brain endothelial cells. The creation of said nanoparticles will allow us to perform *in vitro* binding studies and crossing studies - the two studies will enable the investigation of the two research questions of the thesis.

Firstly, nanoparticles need to be biocompatible for *in vitro* studies, ensuring minimal toxicity as a drug delivery platform.[173,174] The nanoparticles also require protein anti-fouling capabilities, reducing the chances of opsonisation and consequential removal of any such nanoparticles from the body.[175] Indeed, nanoparticles will not need anti-fouling capabilities for *in vitro* studies, as opsonisation can only occur in the body; nevertheless, by synthesising nanoparticles with these capabilities, future investigation and studies can be done *in vivo* using the same nanoparticles. Secondly, the radius of the nanoparticle (*R*), number of ligands (N_{Ligand}), insertion parameter of the ligand (δ_L) and type of ligand[12,18,21] are all variables that need to be accounted for when engineering nanoparticles as the variables affect phenotypic targeting. In order to account for every variable, polymeric nanoparticles were used in this thesis, due to the chemical versatility that polymeric nanoparticles provide over using liposomes.[107]

Polymeric nanoparticles can be made from the self-assembly of amphiphilic block copolymers,[143] thus amphiphilic block copolymers needed to be synthesised.

Poly(ethylene glycol) (PEG) was used for the hydrophilic block due to its protein anti-fouling capabilities.[176] For the hydrophobic block, poly(ε-caprolactone) (PCL) was used as it is a biodegradable polyester and an approved excipient in many clinically used formulations. PCL also has a low glass transition temperature (T_g) of -60 ^oC;[177] thus, above this temperature PCL is soft, rubbery, and flexible in nature which aids in the self-assembly of the amphiphilic block copolymer. By using a PEG-PCL block copolymer as our nanoparticle building block, we can achieve two of the required parameters (protein anti-fouling and biocompatible) noted above for the nanoparticles.

Initially, the syntheses of various length PEG-PCL copolymers were conducted, as well as their subsequent self-assembly to ascertain whether the size, shape and morphology of our nanoparticles can be controlled by adjusting the length of the PCL block. The synthesis of ligand conjugated copolymers was then conducted, firstly by the synthesis of N_3PEG-PCL copolymers, then by conjugation reactions of ligands to the copolymers and lastly the quantification of the conjugation reactions. The combination of both the ligand conjugated PEG-PCL copolymers and PEG-PCL copolymers was then performed to formulate ligand-decorated micelles ready for *in-vitro* binding assays and crossing assays to assess performance in relation to the project aims.

2.2 Materials and methods

2.2.1 Materials

Table 2.1 Materials used in chapter 2

MATERIAL	ABBREVIATION	SUPPLIER
MeO-PEG(5kDa)-OH	PEG_{113}	Iris Biotech
HO-PEG(5kDa)-N3	N_3PEG_{113}	Iris Biotech
HO-PEG(3kDa)-N3	N_3PEG_{68}	Iris Biotech
HO-PEG(20)-N3	N_3PEG_{20}	Iris Biotech
HO-PEG(8)-N3	N_3PEG_8	Iris Biotech
6-O-propargyl-D-glucose [95%]	Gluc	Synthose
Propargylglycine-angiopep2	PPG-AP2	Genscript
Propargyl-Cy7 [95%]	PPG-Cy7	Lumiprobe
ε-Caprolactone [99%]	CL	Alfa Aesar
Diphenyl Phosphate [99%]	DPP	Sigma Aldrich
Copper (II) sulphate pentahydrate [98%]	$CuSO_4 \cdot 5H_2O$	Sigma Aldrich
Sodium ascorbate [98%]	NaAsc	Sigma Aldrich
Sodium phosphotungstate octadecahydrate	PT	Sigma Aldrich
Calcium hydride	CaH_2	Sigma Aldrich
Phosphate buffered saline tablets	PBS tablets	Sigma Aldrich
Chloroform-d	$CDCl_3$	Sigma Aldrich
Dimethyl sulfoxide-d_6	DMSO-d_6	Sigma Aldrich
Dimethyl sulfoxide [99%]	DMSO	Sigma Aldrich
Anhydrous toluene [99%]	-	Sigma Aldrich
Sepharose 4B	-	Sigma Aldrich
Sodium hydroxide	NaOH	Fisher Scientific
N,N-dimethyl formamide [99%]	DMF	Fisher Scientific
Methanol [99%]	MeOH	Fisher Scientific
Chloroform [99%]	$CHCl_3$	Fisher Scientific
Dichloromethane [99%]	DCM	Fisher Scientific
Tetrahydrofuran [99%]	THF	Fisher Scientific
Ethanol [99%]	EtOH	Fisher Scientific
Micro BCA™ Protein Assay Kit	-	Thermo Fisher

CL was stirred over CaH_2 for 24 hours and then distilled prior to use to ensure no water is present in the CL as future syntheses are required to be under anhydrous

conditions. Sterile PBS was produced by dissolving one PBS tablet per 200 mL of deionised water then autoclaved. Sepharose 4B was sterilised by first rinsing with 70% EtOH 3 times then with sterile PBS 4 times prior to use. All other materials were used as obtained.

2.2.2 Synthesis of PEG-PCL and N_3PEG-PCL block copolymers

PEG-PCL block copolymers were prepared by ring opening polymerisation (ROP) of CL using PEG_{113} as the initiator and DPP as the catalyst. For the synthesis of the block copolymers, the molar ratio of monomer / initiator was altered to obtain block copolymers which varied by the length of the PCL block. A typical synthesis for $PEG_{113}PCL_{50}$, altered from a previously published procedure[142] is described as follows. PEG_{113} (0.925 g, 0.185 mmol) was added to a flame dried Schlenk flask with a magnetic stirrer bar under argon and then melted at 50 ^oC under reduced pressure for 3 hours to allow for the removal of any residual water on the PEG as water can act as an alternative initiator to PEG_{113}.[178] CL (1.056 g, 9.248 mmol), the monomer, was then added to the flask. DPP (0.034 g, 0.137 mmol), dissolved in anhydrous toluene (2.5mL), was then added to the Schlenk flask to start the reaction. The reaction solution was stirred at 50 ^oC for 6 hours under inert conditions, monitoring the progress by taking small aliquots out of the reaction vessel, dissolving in $CDCl_3$, and examined using ^1H NMR. Upon the complete conversion of the monomers from CL to PCL, the solution was precipitated against cold MeOH three times. Using cold methanol allows for the polymer to precipitate out of solution, whilst keeping the DPP catalyst in the methanolic solution. The purified polymer was dried in a vacuum oven at 40 ^oC overnight to remove residual MeOH then stored at -20 ^oC until required. N_3PEG-PCL azido block copolymers were prepared following the same

protocol as the synthesis for PEG-PCL, where N_3PEG_{113}, N_3PEG_{68}, N_3PEG_{20} or N_3PEG_8 were used in place of PEG_{113}.

2.2.3 Self-Assembly of PEG-PCL nanoparticles

PEG-PCL nanoparticles were prepared by a heated film rehydration technique. A typical procedure altered from a previously published procedure[134] for the formation of a $PEG_{113}PCL_{52}$ nanoparticle solution is as follows. $PEG_{113}PCL_{52}$ (16.40 mg, 1.5 μmol) is dissolved in $CHCl_3$ (2.5 mL) in a 16 mL glass vial charged with a small stirrer bar. The solvent was slowly removed in a vacuum oven set at 40 ^oC overnight to produce a thin polymer film. Once all the solvent has been removed, the polymer film was placed in a heating block set at 65 ^oC for 30 min. Heated H_2O (3 mL, 65 ^oC) was then added and the reaction was kept at this temperature for 4 hours, stirring at 500 rpm. Subsequently the sample was cooled to room temperature and set to stir at 500 rpm for an additional 5 days. Upon completion of the self-assembly, the solution was stored at 4 ^oC until required.

2.2.4 Synthesis of ligand-conjugated PEG-PCL copolymers

Ligand-conjugated PEG-PCL block copolymers were prepared via copper(I)-catalysed alkyne azide 1,3-dipolar cycloaddition of the ligands PPG-AP2, Gluc and PPG-Cy7, to N_3PEG-PCL azido block copolymers.

A typical synthesis for AP2-PEG-PCL, using $N_3PEG_{68}PCL_{30}$, is described as follows. $N_3PEG_{68}PCL_{30}$ (22.303 mg, 3.210 μmol) was added to a flame-dried and inert reaction Schlenk flask, purged with 3 cycles of argon evacuate-refill, dissolved in degassed DMF (9 mL), and bubbled through with argon gas for 30 min at 60 ^oC. PPG-AP2 (10 mg, 4.174 μmol) was then dissolved in degassed H_2O

(500 µL) and added dropwise to the reaction Schlenk flask and bubbled through with argon gas for a further 30 min. Meanwhile, NaAsc (3.178 mg, 16.052 µmol) and $CuSO_4 \cdot 5H_2O$ (0.802 mg, 3.210 µmol) were added to separate round-bottomed flasks, dissolved in degassed H_2O (250 µL), and bubbled through with argon gas for 30 min. After bubbling, the NaAsc solution is added to the reaction Schlenk flask, followed by the $CuSO_4 \cdot 5H_2O$ solution, and the reaction vessel is bubbled through for a further 30 min. Once bubbling is completed, the reaction is allowed to proceed under inert conditions and kept at 60 ^oC for 72 hours. Upon completion of the reaction, DMF (10 mL) is added to the reaction, and the solution was dialysed, using a 3.5 kDa molecular-weight cut-off dialysis bag, for 5 days against H_2O, changing the solution 4 times per day. The aqueous solution is then lyophilised to give a light-yellow powder. The purified polymer was then stored at -20 ^oC until required. The protocol was similarly followed using N_3PEG_8PCL, $N_3PEG_{20}PCL$ and $N_3PEG_{113}PCL$, maintaining the ligand/polymer molar ratio at 1.3. The synthesis of Glucose-PEG-PCL also follows the same procedure as the synthesis of AP2-PEG-PCL, using only $N_3PEG_{113}PCL$.

Production of Cy7-conjugated copolymers followed the same protocol for AP2-PEG-PCL but with slight changes due to solubility differences between PPG-Cy7 and PPG-AP2. PPG-Cy7 (26.78 mg, 48.16 µmol) is added together with $N_3PEG_{20}PCL_{41}$ (91.73 mg, 16.05 µmol) and dissolved with degassed DMF (9 mL). An additional amount of degassed H_2O (500 µL) was also added alongside the addition of the sodium ascorbate (11.51 mg, 16.05 µmol, 250 µL) and copper (I) sulphate (4.01 mg, 16.05 µmol, 250 µL) solutions in H_2O. The dialysis step of this synthesis also differs where dialysis, using a 1 kDa molecular-weight cut-off bag, was first done for 4-6 days against DMF before following on with 3 days

against H_2O – extra dialysis in DMF was to ensure any free PPG-Cy7 would be removed during the process. The lyophilised product produced a dark green powder and stored at -20 ^oC until required.

2.2.5 Self-assembly of ligand-decorated PEG-PCL nanoparticles

Ligand-decorated nanoparticles were prepared in a similar film rehydration method to produce pure PEG-PCL nanoparticles, as described in 2.2.3, but the polymer film instead was made using pure PEG-PCL copolymers and ligand-conjugated PEG-PCL copolymers at different molar concentrations. By spiking pure PEG-PCL copolymers with ligand-conjugated PEG-PCL during the self-assembly process, nanoparticles are formed with ligands on the nanoparticles, a procedure previously performed to produce AP2-decorate PEG-b-PDPA nanoparticles.[21] Film rehydration was also done with sterile Milli-Q water under a laminar flow hood as the ligand-decorated PEG-PCL nanoparticles were to be used for future *in vitro* cell testing. The total molar concentration is maintained at 500 µM. For all ligand-decorated nanoparticles, Cy7-$PEG_{20}PCL_{60}$ (0.473 mg, 0.075 mmol) was added to allow for the nanoparticles to be fluorescently tracked during *in vitro* studies. A slight change to procedure is experienced when making AP2-decorated nanoparticles, due to the solubility of the AP2-PEG-PCL copolymers – this was not exhibited with the glucose-PEG-PCL copolymers, thus for the glucose-decorated nanoparticles, all copolymers were dissolved in $CHCl_3$, and the protocol described previously was followed. A typical procedure for the formation of $PEG_{113}PCL_{52}$ nanoparticles doped with 0.5 mol% AP2-$PEG_{113}PCL_{42}$ and labelled with 5 mol% Cy7-$PEG_{20}PCL_{60}$ is as follows. $PEG_{113}PCL_{52}$ (15.773 mg, 1.413 mmol) and Cy7-$PEG_{20}PCL_{60}$ (0.473 mg, 0.075 mmol) were dissolved in $CHCl_3$ (2425 uL). AP2-$PEG_{113}PCL_{42}$ (0.138 mg, 0.012 mmol) was dissolved in

a 1:1 solvent mix of $CHCl_3$:MeOH (75 µL) and added slowly to the $PEG_{113}PCL_{52}$ and Cy7-$PEG_{20}PCL_{60}$ solution to make a mix of the three copolymers. The solvent was then slowly removed in a vacuum oven set at 40 ^oC overnight. From here, the previous protocol of heated film rehydration from section 2.2.3 is then followed again.

2.2.6 Nanoparticle purification

Ligand-decorated nanoparticles, labelled with Cy7, were subjected to further purification by size exclusion chromatography prior to in-vitro testing. Further purification was done to change the media of the nanoparticles from water to PBS, the media required for *in vitro* cell testing. Performing a SEC column also allows for the separation of nanoparticle structures by size (i.e., separation of micelles, worm-like micelles, and vesicles), if the sample was a mixture of multiple morphologies.[179] All steps detailed below were conducted under sterile conditions (under a sterilised laminar flow hood and using only autoclaved glass vials, pipettes, and pipette tips).

A flash chromatography column (1.5 cm (diameter) x 30 cm (height)) was first rinsed with 70% EtOH 3 times to sterilise the column. The column was then filled with sterile Sepharose 4B to achieve a bed volume of 40 mL, rinsed through with sterile PBS, the mobile phase, equal to 3 times the bed volume (120 mL) and then left to pack overnight. Ligand conjugated nanoparticles (2 mL, 500 µM) were then seeded at the top of the column, left to adsorb completely onto the column, and then sterile PBS was slowly added on the top to ensure the Sepharose 4B was not disrupted, and sterile PBS was continually added whilst the column was running, and fractions were being collected. Fractions were collected in a 96 well

plate, and a fluorescence microplate reader, absorption at 750 nm and emission at 773 nm, was used to obtain the fractions containing the nanoparticles. The absorption and emission wavelengths used for the detection of Cy7. All nanoparticle fractions were combined, and the fluorescence was checked against a calibration curve of pre-purified nanoparticles to obtain the final concentration of the sample. The purified nanoparticles were stored at 4 ^{o}C until required.

2.2.7 Copolymer characterisation

^{1}H NMR spectra were recorded on a Bruker Avance Neo 500 MHz spectrometer at room temperature. Samples were made by dissolving 5 mg of polymer in $CDCl_3$ or DMSO-d_6. ^{1}H NMR was used to monitor monomer conversion over time, the degree of polymerisation (DP) of the monomer units and the calculated number average molecular weight (M_n) of the synthesised copolymers. ^{1}H NMR was also used for the quantification of the click conjugation of propargyl-glucose to $N_3PEG_{113}PCL_{41}$.

Number average molecular weight (M_n), weight average molecular weight (M_w) and the polymer polydispersity (PDI) were calculated based on the trace of refractive index (RI) of gel permeation chromatography (GPC) on an Agilent 1260 Infinity II LC system using a PLgel 5um MIXED-D 300 x 7.5 mm column. 5 mg of polymer was dissolved in 1 mL of the mobile phase, THF, and passed through a 0.45 μm PTFE filter. 100 μL of the sample is injected into the instrument at a flow rate of 1 ml/min, using THF as the mobile phase. The molecular weights were calculated from the elution volume of polystyrene standards with molecular weights between 162-45270 Da for THF.

Click conjugation efficiency between AP2 and the N_3-PEG-PCL azido block copolymers was characterised using the Pierce™ BCA Assay Kit.[180] The BCA assay uses the presence of peptide bonds for the reduction of Cu^{2+} to Cu^{1+} in the BCA stock solution, then two molecules of bicinchoninic acid chelate onto Cu^{1+} to form a light blue complex with an absorption at 562 nm:[180] the more peptide bonds, the stronger the absorption on a plate reader. A typical procedure for the click conjugation efficiency for AP2-$PEG_{68}PCL_{30}$ is described as follows. AP2-$PEG_{68}PCL_{30}$ (0.231 mg, 0.025 μmol) is dissolved in a 70:30 DMSO:Water solvent mix (1.5 mL). A serial dilution of each is done to make 7 concentrations of AP2-$PEG_{68}PCL_{30}$ and 150 μL of each dilution is added in triplicate to a 96 well plate. To each well, the BCA working reagent (150 μL) is added and the plate is shaken for 30 seconds, followed by incubation at 37 ^oC for 2 hours. The absorbance at each concentration is read at 562 nm on a plate reader and comparted to a positive control (1:1:1 molar ratio of $N_3PEG_{68}PCL_{30}$: triazole : AP2). Both readings are negative control (1:1 molar ratio of $N_3PEG_{68}PCL_{30}$: Triazole) subtracted. Conjugation efficiency (CE) of the reaction was calculated by comparison to the positive control calibration curve.

2.2.8 Nanoparticle characterisation

Nanoparticles were characterised by using dynamic light scattering (DLS) and transmission electron microscopy (TEM). It is important to note that no purification of pure PEG-PCL nanoparticles was done prior to characterisation to study the initial morphology of the system without removing any structures that could be present. Characterisation of the ligand-decorated nanoparticles was done post purification, to determine whether the morphology of the nanoparticles change after purification, and to confirm the size and shape of the nanoparticles.

DLS analysis of the polymer nanoparticle formulations was done to calculate the polydispersity and hydrodynamic diameter of the particles. DLS analyses were performed on a Malvern Zetasizer Nano ZS (Malvern Ltd. UK) using a 120-mW He-Ne laser set at 630 nm at a control temperature of 25^{o}C, and the scattered light was measured at an angle of 173^{o}. Polymer nanoparticle formulations were diluted with filtered Milli-Q water to a final concentration of 100 μM. 500 μL of the diluted sample is injected into a polystyrene microcuvette (Malvern) and analysed and then processed using Dispersion Technology Software (Malvern).

The structures of the polymer nanoparticles were determined by transmission electron microscopy (TEM). 0.5% w/v phosphotungstic acid (PTA) solution was used as a negative staining agent, as the polyester-based nanoparticles have low electron scattering powers and thus need the deposition of heavy atoms, such as tungsten, to be imaged.[181] To make the staining solution, 25 mg of PT was dissolved in 5 mL of distilled boiling water, then adjusted to pH 7 by addition of 5 M NaOH and subsequently filtered using a 0.22 μm PTFE filter.

TEM imaging was performed using a JEOL 2100 TEM imaging microscope at 200 kV, equipped with a Gatan CCD camera. Copper grids were glow-discharged for 45 seconds to create a hydrophilic surface. 5 μL of a nanoparticle sample (100 μM) was then injected on the surface of the grid and left for 1 minute to allow for the sample to dry and adsorb onto the grid. The grid was then dried with filter paper and immersed in a 20 μL drop of the PTA staining solution for 5 seconds to ensure the grid was not overstained - an overstained TEM grid would darken the grid and make it difficult to determine the sizes of the nanoparticles. The grid was dried again with filter paper, then dried under vacuum to remove excess

staining solution. The grid was prepared either on the same day, or 24 hours prior to imaging on the TEM. TEM images were then processed using the FIJI software.

2.3 Results and discussion

2.3.1 PEG-PCL synthesis

By changing the DP of PCL (N_{PCL}) whilst maintaining the DP of PEG (N_{PEG}) we can increase the hydrophobic volume of the nanoparticle to alter the shape and radius of the nanoparticles, parameters that influence targeting. Henceforth, 9 PEG-PCL block copolymers with varying N_{PCL} were synthesised via a metal-free ring opening polymerisation. Fig 2.1 shows a scheme of the polymerisation, and table 2.2 shows the structural characteristics of the synthesised copolymers, labelled from PCL10 to PCL90. Different values of N_{PCL} were obtained by altering the monomer-to-initiator ratio ($\frac{[M]}{[I]}$) feed per each polymerisation reaction, from 10 to 90. Both N_{PCL} and the number molecular weight (M_n) for each polymer was calculated by ^{1}H NMR in $CDCl_3$. An example of the molecular structure and a ^{1}H NMR spectra, i.e., for PCL50, is shown in fig 2.2, with the ^{1}H NMR spectra of the all samples in fig S.1-9. The labelled protons in fig 2.2A (labelled from 1-6) correspond to the proton signals in fig 2.2B, and the DP of CL was calculated by comparison of the integration of peaks 2, 3 and 5 to the integration of peak 1. The data in table 2.2 shows that the N_{PCL} for the copolymers matches closely to the $\frac{[M]}{[I]}$ feed, thus concluding copolymers with specific N_{PCL} could be accurately synthesised by just adjusting the $\frac{[M]}{[I]}$ feed.

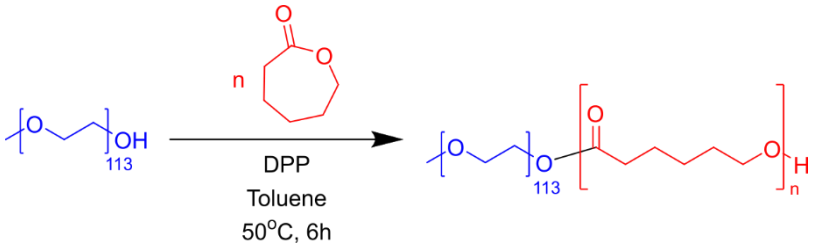

Fig 2.1 **Polymerisation scheme for the synthesis of PEG-PCL copolymers.** 'n' notes the degree of polymerisation (DP) of the PCL hydrophobic block

Table 2.2 **Summary of PEG-PCL block copolymers.**

POLYMER CODE	INITIATOR	$\frac{[M]}{[I]}$ [A]	N_{PCL} [B]	COMPOSITION	Đ [C]	$M_{N\ NMR}$ [D]
PCL10	PEG_{113}	10	10	$PEG_{113}PCL_{10}$	1.039	6141
PCL20	PEG_{113}	20	21	$PEG_{113}PCL_{20}$	1.338	7283
PCL30	PEG_{113}	30	34	$PEG_{113}PCL_{34}$	1.090	8881
PCL40	PEG_{113}	40	41	$PEG_{113}PCL_{41}$	1.205	9680
PCL50	PEG_{113}	50	52	$PEG_{113}PCL_{52}$	1.166	10935
PCL60	PEG_{113}	60	59	$PEG_{113}PCL_{59}$	1.412	11734
PCL70	PEG_{113}	70	73	$PEG_{113}PCL_{73}$	1.454	13332
PCL80	PEG_{113}	80	82	$PEG_{113}PCL_{82}$	1.384	14359
PCL90	PEG_{113}	90	90	$PEG_{113}PCL_{90}$	1.232	15273

[a] Feed molar ratio at the beginning of the reaction, where [M] and [I] are the concentrations of the monomer and initiator respectively. [b] N_{PCL}, calculated from ^1H NMR in $CDCl_3$. [c] Polydispersity of the polymer, calculated from GPC in THF. [d] Number molecular weight of the polymer calculated from ^1H NMR in $CDCl_3$ and GPC in THF.

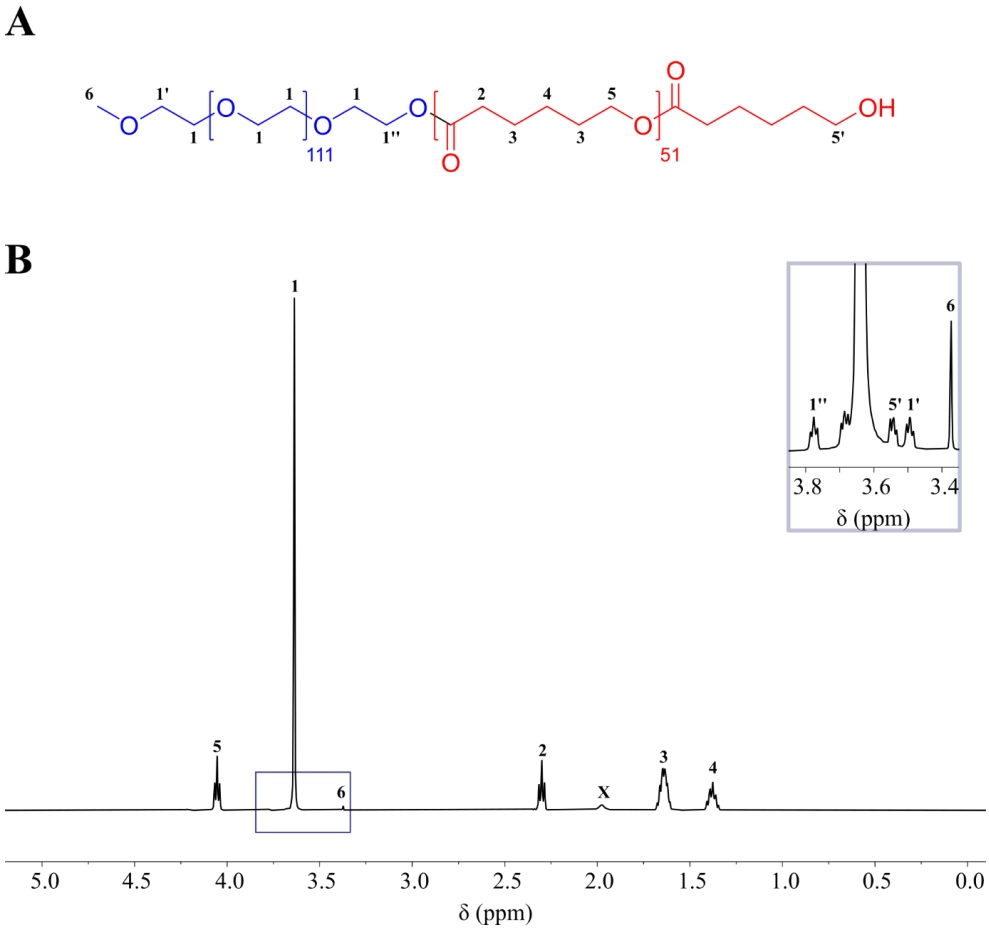

Fig 2.2 **Characterization of PCL50.** (A) Molecular structure of PCL50. The hydrophilic and hydrophobic sections of the amphiphilic polymer are coloured blue and red respectively (B) ^1H-NMR spectra of PCL50 in $CDCl_3$. The numbers on the peak correspond to the numbers depicted in A. 'X' denotes residual H_2O.

Table 2.2 also shows that the Đ of the PEG-PCL copolymers ranged from 1.039 to 1.368, indicating that some of the copolymers are not completely monodisperse. Shoulders were often recorded in the GPC traces of some of the block copolymers, such as in PCL50 and PCL90, as evidenced in fig 2.3. Shoulders in GPC traces could be explained either by residual water. Indeed, removal of residual water was attempted, but some residual water may have still been present, leading to the polymerisation of CL by water causing smaller weight polymers to have been produced. Alternatively, shoulders in the GPC traces could also be explained by transesterification:[182] during the propagation step of the polymerisation, a growing PEG-PCL polymer chain could have instead reacted with another PEG-PCL polymer chain instead of the intended CL monomer, resulting in both smaller and larger PEG-PCL polymer chains. Smaller PEG-PCL polymer chains from transesterification could be seen at earlier retention times to and larger PEG-PCL polymer chains can be seen as shoulders at later retention times, indicated on fig 2.3 by the arrows.

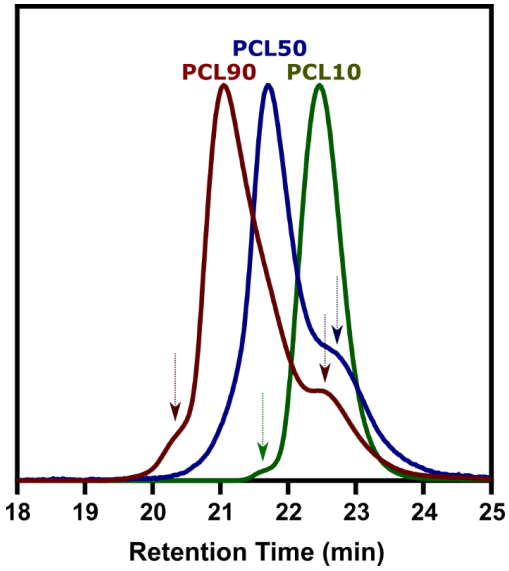

Fig 2.3 **GPC traces, using an RI detector, of PCL90, PCL50 and PCL10.** The presence of shoulders on PCL90, PCL50 and PCL10 are emphasised by the red, blue, and green arrows respectively.

In summary, 9 PEG-PCL block copolymers have been synthesised with PCL blocks of varying N_{PCL} close to the $\frac{[M]}{[I]}$ feed, whilst N_{PEG} was kept constant for all copolymers. Indeed, of the 9 copolymers, Đ > 1.2 were seen, and in the future alternative synthesis methods could be adopted to try to reduce potential water in the system (i.e, synthesise the polymers in a glovebox, or by azeotropic distillation of PEG[183]). The purpose of synthesising multiple PEG-PCL block copolymers was to ascertain whether nanoparticles could be engineered with varying radii; therefore, the self-assembly of the copolymers should be done next.

2.3.2 PEG-PCL self-assembly

Firstly, a method for the self-assembly of the 9 synthesised copolymers, PCL10-90, was investigated to determine morphologies produced from their assemblies and if the size can be controlled by changing N_{PCL}. Various methods for forming nanoparticles can be used for the self-assembly of PEG-PCL block copolymers such as nanoprecipitation, solvent switch, and film rehydration. Film rehydration was chosen as the suitable method as it includes no solvent-exchange purification via dialysis that would alter the concentration of the solution: concentration is another key variable that needs to be known for phenotypic targeting. PCL50 was used to optimise a self-assembly method that could then be applied to the other copolymers.

Initially, a suitable temperature needed to be identified for the self-assembly for PCL50. Previous studies have shown that high temperatures may be required the self-assembly of copolymers containing PCL[134,142,184], such as the self-assembly of polysarcosine (PSar)-PCL-Psar triblock copolymers at 65 ^{o}C and 90 ^{o}C to form either micelles, rods, or giant polymersomes[142] and even the self-assembly of

different concentrations of PEG_{5000}-*b*-PCL_{4100} at 65 ^{o}C to from structures based on the concentration of the sample.[184] As self-assembly was done at 65 ^{o}C for various PCL-containing copolymers, I decided to test if it would be suitable for my synthesised PEG-PCL copolymers.

To identify the optimum temperature for self-assembly, a temperature-dependent film rehydration study was done on PCL50: a PCL50 thin film was prepared as described in the materials and methods section then hydrated at 25^{o}C to a concentration of 500 μM. An aliquot of the sample was taken, diluted to 100 μM, and DLS measurements were taken at 5 ^{o}C temperature intervals. The initial sample was stirred for 4 hours, and then heated up to 65 ^{o}C, with images being taken of the nanoparticle solutions at 5 ^{o}C intervals, shown in fig 2.4A. As shown by the images in fig 2.4A, the nanoparticle solution appears very opaque at lower temperatures (25 - 45^{o}C) compared to appearing more translucent at higher temperatures (50 - 65^{o}C). The DLS correlograms taken over the range of temperatures were split and to the lower temperature (25 - 45^{o}C) correlograms in fig 2.4B and higher temperature (50 - 65^{o}C) correlograms in fig 2.4C. The correlograms in fig 2.4B show that the correlation coefficient decays (decreases quickly over time) roughly between 500 - 1000 μs, indicating the presence of larger particles due to slower diffusion of the particles. The correlation coefficient fluctuates between 10,000 - 1,000,000 μs, pointed out by the black arrows, indicates non-random motion of the particles: this motion is most likely explained by sedimentation of the solution which could explain why the solutions at low temperatures appear very opaque. In comparison, in fig 2.4C the correlogram at 50^{o}C shows that the correlation coefficient still decays between 500 - 1000 μs, but there is a reduction of fluctuation at the delay times between 10,000 -100,000

μs and no fluctuation between 100,000 – 1,000,000 μs, indicating the reduction of sedimentation. Upon increasing the temperature to 55^{o}C, the coefficient decay now starts between 1 and 10 μs, demonstrating that the particles are now smaller and diffuse faster; additionally, the region that correlation coefficient fluctuations occur has shifted to around 1,000 μs, explained by further reduction of sedimentation. Further increasing the temperature to 60^{o}C and, subsequently, 65^{o}C removes all the fluctuation of correlation coefficient after 1000 μs, signifying that the solution is colloidally stable and free of sedimentation at these higher temperatures. The results shown in fig 2.4 confirm that indeed the temperature affects the self-assembly of the copolymer, and that the optimum temperature for the self-assembly is likely between 60 and 65 ^{o}C, and thus 65 ^{o}C has been shown to be optimal for the self-assembly.

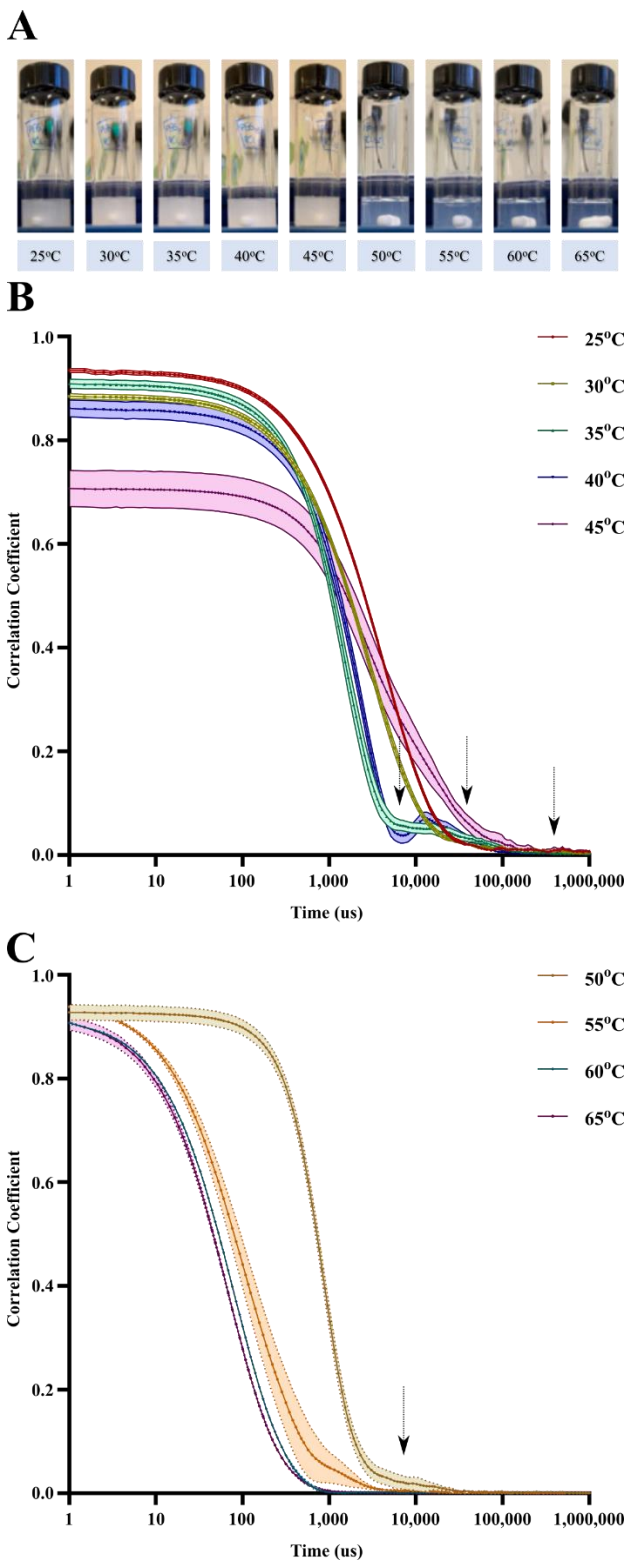

Fig 2.4 **Temperature-dependent self-assembly of PCL50.** (A) Images of nanoparticles taken at different temperatures during self-assembly. (B) DLS correlograms taken of the nanoparticle solution from 25 - 45 °C. (C) DLS correlograms taken of the nanoparticle solution from 50 - 65 °C. The shaded regions of the correlograms are ±SD (n=10) The black arrows indicate correlation coefficient fluctuations past 1000 us.

Indeed, PCL50 nanoparticles produced and analysed at 65 ^{o}C have been shown to be colloidally stable, however the sample needed to be analysed back again at room temperature to see if the sample will still be colloidally stable after production and subsequent storage at 4 ^{o}C. To investigate whether PCL50 nanoparticles can still be colloidally stable after cooling, another PCL50 nanoparticle solution was formulated: a new PCL50 thin film was prepared as described in the materials and methods section, and now hydrated at 65 ^{o}C and stirred for 4 hours, then cooled to room temperature and stirred for a further 5 days. The sample was then stored at 4 ^{o}C overnight prior to DLS analysis, to ascertain whether the sample would still be stable after storage. DLS analysis was done on this new heat-treated PCL50 solution at 25 ^{o}C and the correlograms, intensity and number graphs are shown in fig 2.5, labelled A, B and C respectively. The correlogram shows that the correlation coefficient starts to decay between 1 and 10 μs, and that there is no fluctuation in correlation coefficient after roughly 1100 μs, meaning only random motion was observed within the sample and thus the sample was colloidally stable. The intensity and number graphs show monomodal peaks, indicating that the sample is monodisperse. It is likely that upon cooling down below the melting point of PCL, the PCL hydrophobic blocks start to crystallise, thus maintaining the size and shape of the PEG-PCL nanoparticles made at high temperature. The results in fig 2.5 confirm that stable nanoparticles using PCL50 can be made by hydrating at 65 ^{o}C and remain stable upon cooling to room temperature and even after storage at 4 ^{o}C.

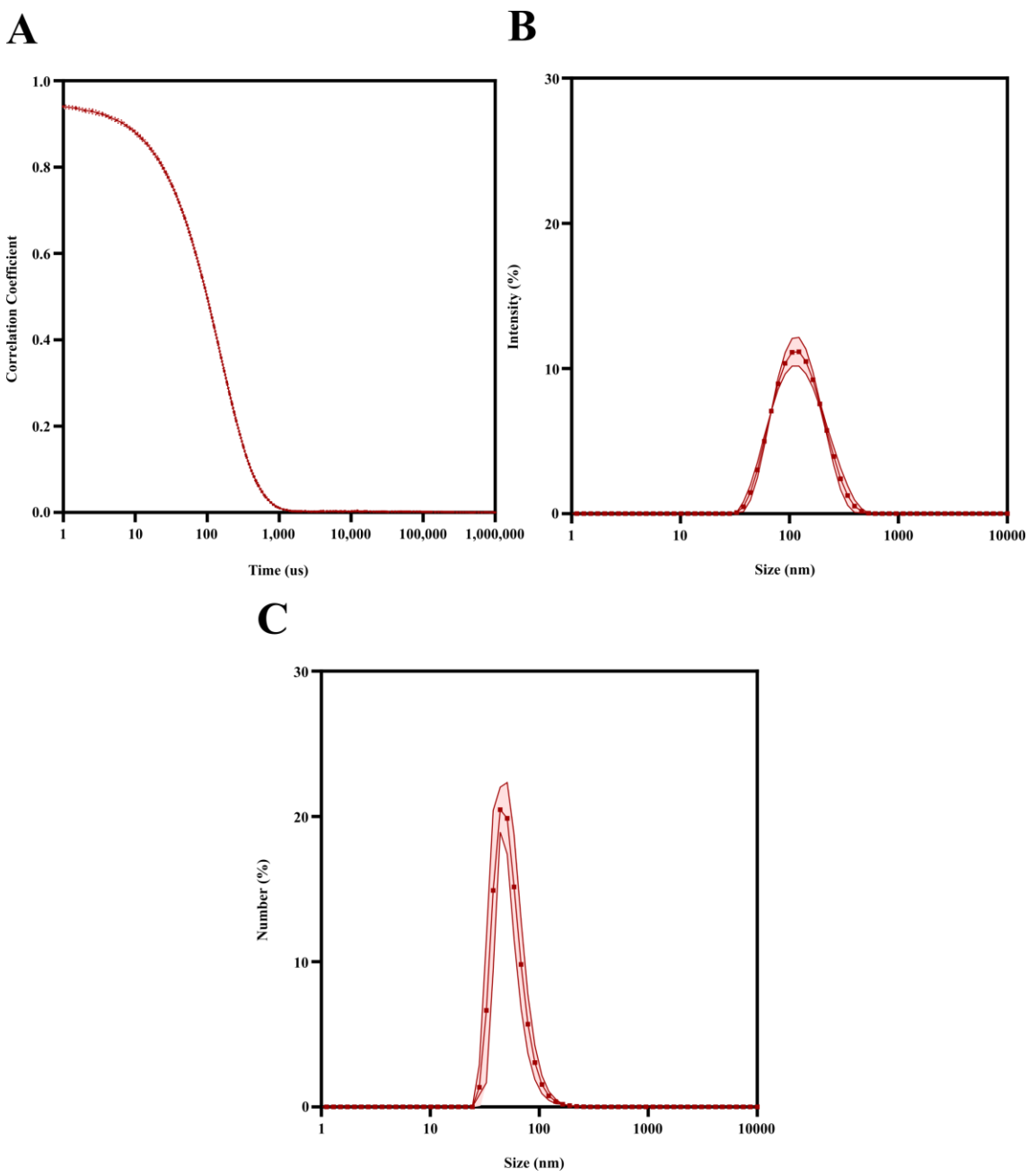

Fig 2.5 **DLS Analysis of PCL50 at 25 ºC after self-assembly at 65 ºC.** The correlogram (A), intensity (B) and size (C) graphs of PCL50

The method for self-assembly was optimised using PCL50. Prior to testing the self-assembly method on the other polymers, an investigation was then done to check the reproducibility of the self-assembly method. Three new nanoparticle samples using PCL50 were prepared by the heated film rehydration method described above, all aiming for the same final concentration, with the DLS results and a representative TEM picture of each sample shown in fig 2.6. Analysis of

the TEM images and DLS results shows that the samples were like one another in size, thus showing reproducibility of the nanoparticle preparation method designed.

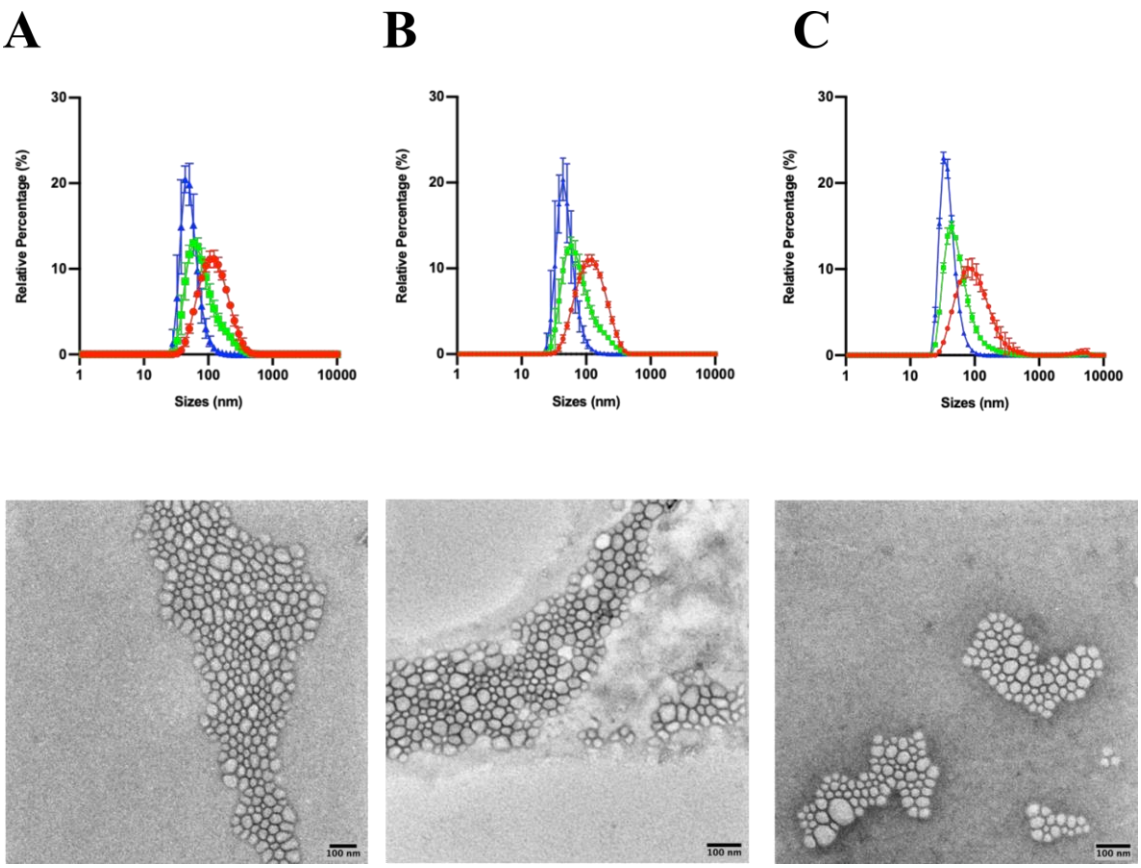

Fig 2.6 **DLS and TEM analysis of 3 independent PCL50 samples at 25 ºC after self-assembly at 65 ºC.** In the DLS analysis, the colours represent the sizes of the nanoparticles by number, volume, or intensity (blue, green, and red respectively). The scale bars of the TEM images are 100 nm.

therefore, an investigation of the self-assembly of the other copolymers was undertaken to investigate the extent to which the self-assembly method is generalisable. Additionally, the self-assembly of the other copolymers will allow us to determine if we can alter both the size and morphology of our nanoparticles by only modifying the length of the PCL block. The self-assemblies of PCL10 to PCL90 were conducted and TEM was used to ascertain the size and structures of the nanoparticles. TEM instead of DLS was used for the purpose of structure

analysis as DLS assumes a hydrodynamic diameter hence will not be reliable if the structures are not spherical.[185]

Nanoparticle formulations made using either PCL10 or PCL20 were analysed using TEM, and two images of each sample are shown in fig 2.7 and fig 2.8 respectively. For PCL10, several rigid rod-like structures, having thickness of 20 nm. We speculate that during the crystallisation of the small PCL block, long cylindrical structures can form, thus explaining why rigid rod-like structures can be seen for PCL10 nanoparticles. For PCL20, several smaller rod-like structures, having again a thickness of 20 nm, were found, however these are less rigid than the rod-like structures present in the PCL10 nanoparticle solution. Small spherical micelles, i.e., within the dotted red box, were also found throughout the TEM grid. Compared to PCL10, PCL20 copolymers have a larger hydrophobic section and the self-assembly is governed more by the hydrophobic effect, and thus spherical micelles can start to form. In this case, by increasing the block length of PCL for the copolymer, the morphology of the structures formed changes.

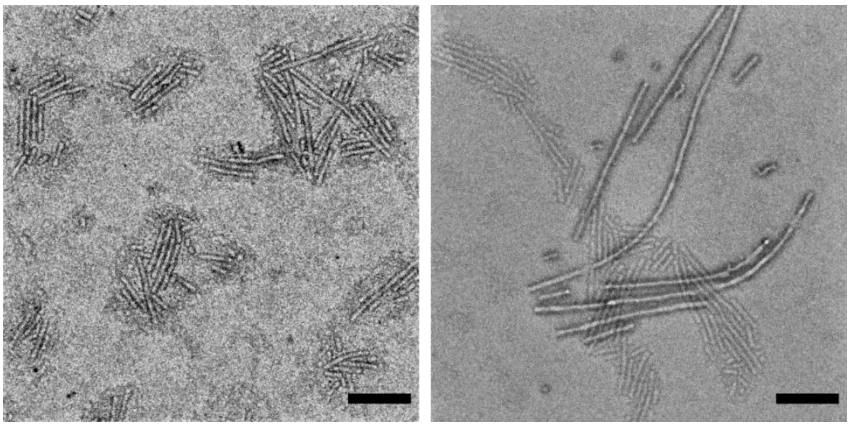

Fig 2.7 **Self-Assembled Structures of PCL10.** TEM images of PCL10 self-assembled nanoparticles. Scale bar = 200 nm

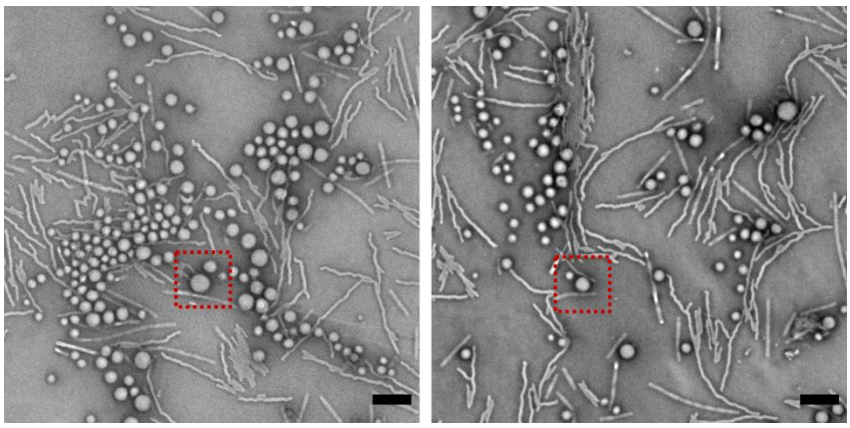

Fig 2.8 **Self-Assembled Structures of PCL20.** TEM images of PCL20 self-assembled nanoparticles. Scale bar = 200 nm

Next, nanoparticle formulations were made using PCL30, PCL40, PCL50 and PCL60 and TEM analysis was done to assess the morphology of the nanoparticles. Two TEM images for each of the PCL30, PCL40, PCL50 and PCL60 nanoparticles are shown in fig 2.9, fig 2.10, fig 2.11 and fig 2.12 respectively. The TEM images show that the nanoparticles made by the four copolymers all share the same spherical morphology, akin to micelles, adopted the some of the PCL20 nanoparticle. No more rod-like structures were found in any of the sample, indicating that the spherical structure is the most stable structure for these copolymers when self-assembled.

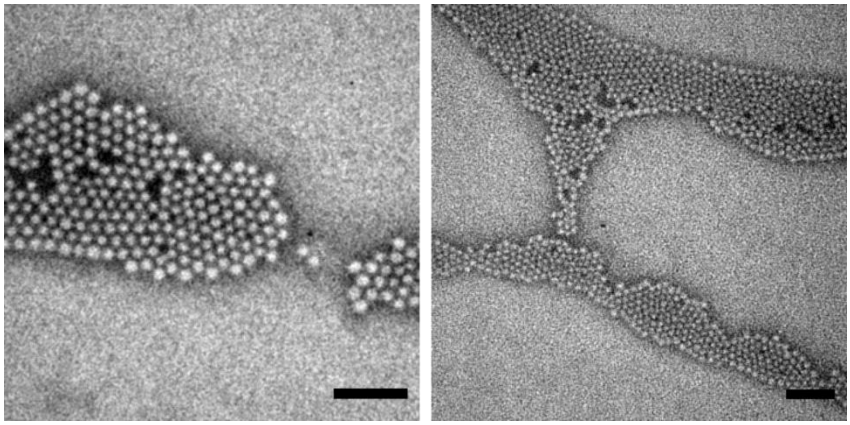

Fig 2.9 **Self-Assembled Structures of PCL30.** TEM images of PCL30 self-assembled nanoparticles. Scale bar = 200 nm

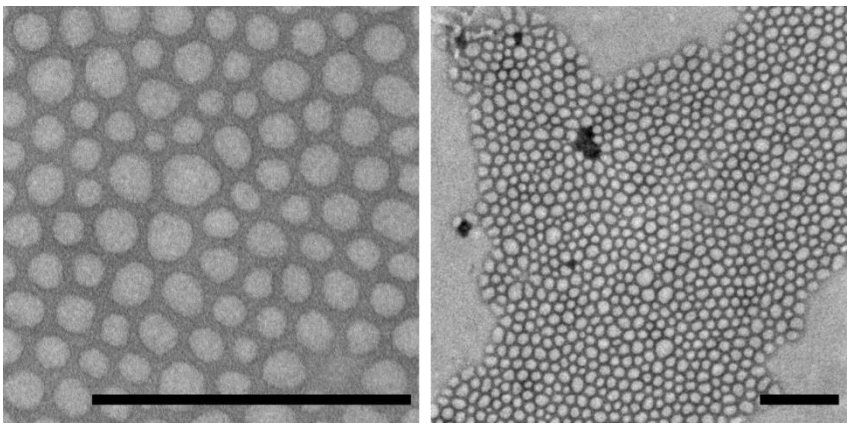

Fig 2.10 **Self-Assembled Structures of PCL40.** TEM images of PCL40 self-assembled nanoparticles. Scale bar = 200 nm

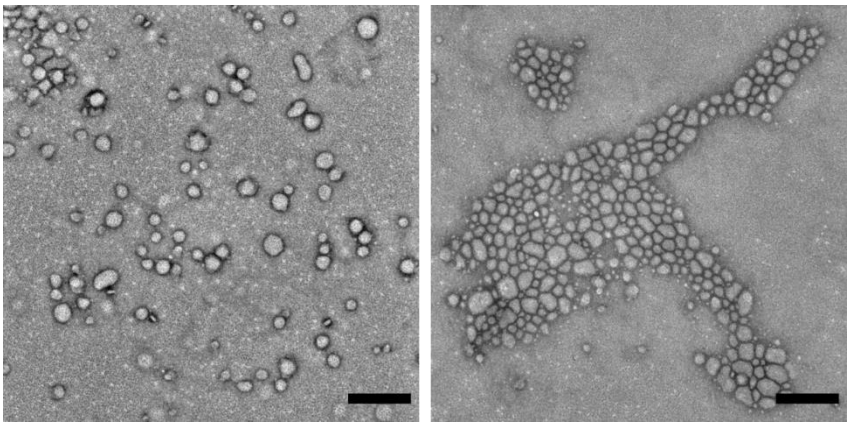

Fig 2.11 **Self-Assembled Structures of PCL50.** TEM images of PCL50 self-assembled nanoparticles. Scale bar = 200 nm

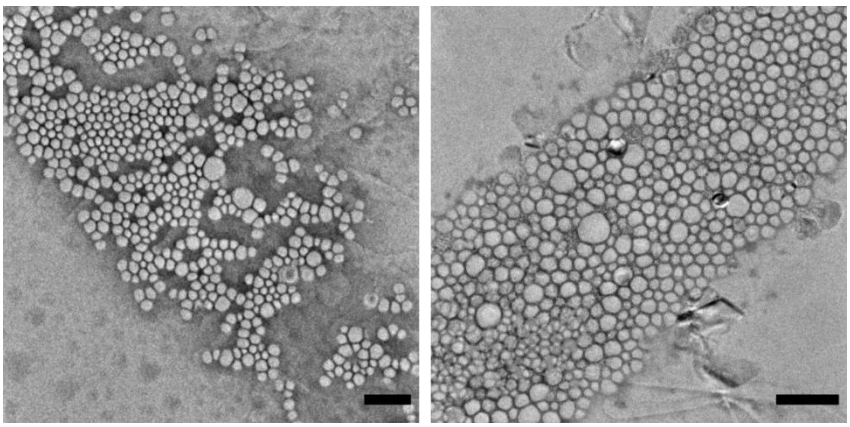

Fig 2.12 **Self-Assembled Structures of PCL60.** TEM images of PCL60 self-assembled nanoparticles. Scale bar = 200 nm

Nanoparticles were subsequently made with PCL70 and PCL80 and analysed by TEM, with images seen in fig 2.13 and fig 2.14. Spherical micelles were seen in both PCL70 and PCL80, akin to the structures seen in fig 2.9-fig 2.12. In addition

to micelles, long rod-like structures (i.e, worm-like micelles) were also observed. By increasing the PCL block length, the volume occupied by the PCL hydrophobic block in the nanoparticles increases. As discussed in the previous chapter, the increase in volume of the hydrophobic block of a copolymer changes the packing factor of the copolymer when self-assembled and therefore favouring rod-like structures over spherical structures.[143]

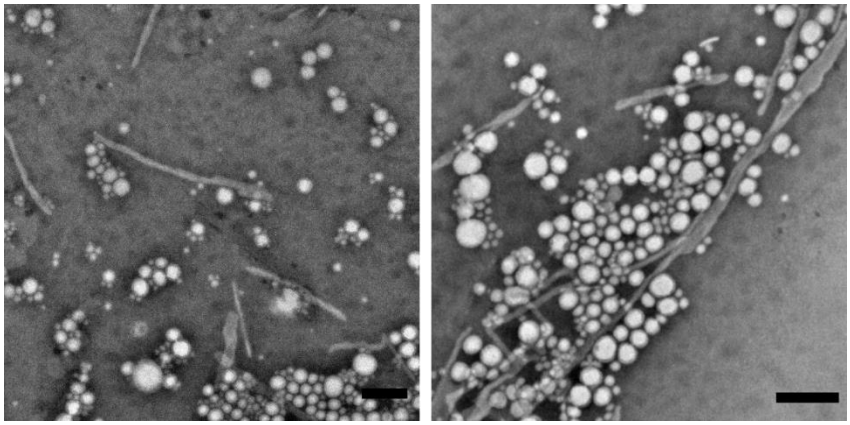

Fig 2.13 **Self-Assembled Structures of PCL70.** TEM images of PCL70 self-assembled nanoparticles. Scale bar = 200 nm

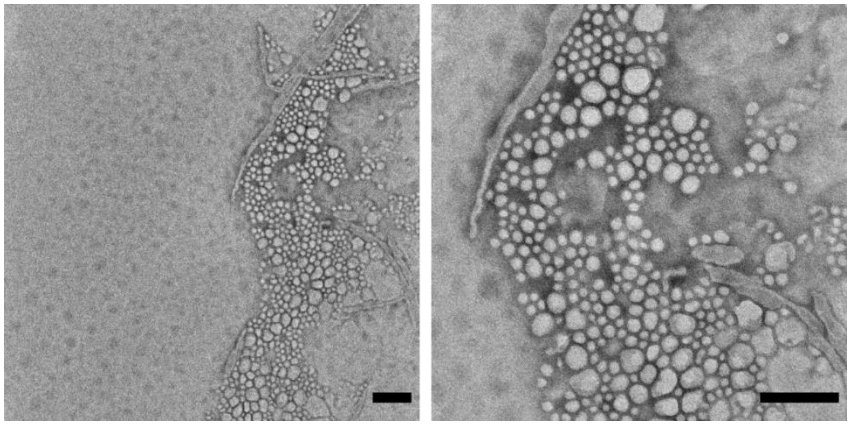

Fig 2.14 **Self-Assembled Structures of PCL80.** TEM images of PCL10 self-assembled nanoparticles. Scale bar = 200 nm

PCL90 nanoparticles were then formulated and analysed to check the morphology of the nanoparticles formed. Two TEM images are shown in fig 2.15. Only spherical structures were seen, yet the sizes of the structures are quite

varied as both larger ~200 nm diameter nanoparticles, indicating vesicular structures, and smaller ~50 nm diameter micelles were observed. N_{PCL} for PCL90 in larger than that of the other copolymers, thus the volume of the hydrophobic block in PCL90 particles is larger than the other copolymers. Upon analysis of all the nanoparticle formulations made and their TEM images shown fig 2.7 to fig 2.15, we therefore conclude that we can control the specific morphology that the PEG-PCL nanoparticles adopt by altering the PCL block length.

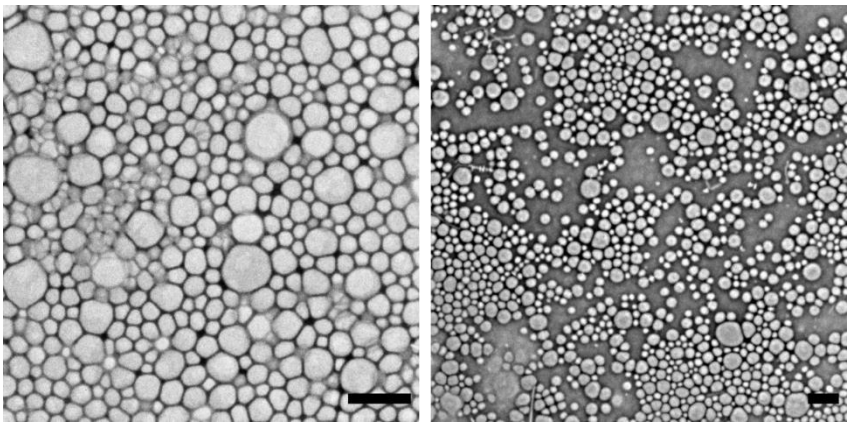

Fig 2.15 **Self-Assembled Structures of PCL90.** TEM images of PCL10 self-assembled nanoparticles. Scale bar = 200 nm

Size analysis of the PCL30-60 and PCL90 nanoparticles was completed, by manual measurement of the nanoparticles from the TEM images, to determine whether the size of the nanoparticles could be controlled by changing the PCL block length. A histogram of the manually measured diameters of nanoparticles made using PCL30-60 and PCL90 is shown in fig 2.16, with the raw data of the measured nanoparticles in table 2.3. A non-linear regression gaussian curve for each sample was overlayed on top of the histogram to guide the eye. The histogram shows that the mean diameters of the nanoparticles increase as the length of the PCL block increases (one-way ANOVA: **** $P < 0.0001$) and that

there is a significant difference in size between the samples, concluding that the size of our nanoparticles can be controlled by changing the PCL block length.

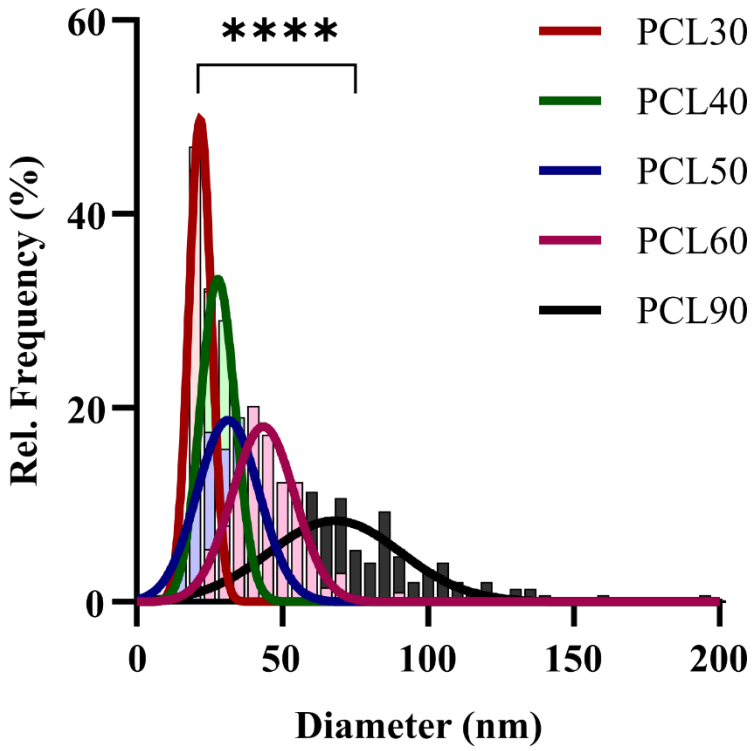

Fig 2.16 **Histogram of diameters measured for PCL30, PCL40, PCL50, PCL60 and PCL90 nanoparticles.** Non-linear regression gaussian curves were calculated and displayed to guide the eye comparison of the samples. **** $p < 0.0001$ in a one-way ANOVA test.

Table 2.3 **Summary of self-assembled sizes of PCL30-PCL60 and PCL90 nanoparticles.**

SELF-ASSEMBLED NPS OF BELOW COPOLYMER	DIAMETER (NM)	STD. DEV (NM)	N
PCL30	22.77	4.041	130
PCL40	28.47	5.915	200
PCL50	33.27	11.37	400
PCL60	45.20	12.52	203
PCL90	74.07	27.78	150

N is the number of nanoparticles manually measured using FIJI

Having confirmed that both morphology and size of the nanoparticles could be controlled by the PCL block length, we therefore need to choose which copolymer to use further for testing phenotypic targeting. PCL30-PCL60 all made nanoparticles with a spherical micellar structure, whereas PCL90 nanoparticles were vesicles, thus we can either make nanoparticles for targeting using micelles of vesicles. Vesicles have an advantage over micelles as drug delivery vehicles as they enable the encapsulation of hydrophilic drugs alongside hydrophobic drugs; however, the vesicle structure allows the hydrophilic PEG side to be inside and outside of the nanoparticle. As the ligand is going to be conjugated on the hydrophilic side to allow for the ligand to bind onto receptors, a micellar structure was chosen instead of a vesicular structure for targeting testing, as during the self-assembly of vesicles, the ligand could be placed inside the nanoparticle instead of on the surface: by using micelles only, we enforce that all the ligands will be on the outside of the nanoparticle. As PCL50 was used for the method development of the temperature-assisted self-assembly, and forms micellar structures of low polydispersity, we therefore decided to use PCL50 as the major bulk of the nanoparticles for targeting.

2.3.3 Ligand-conjugated PEG-PCL synthesis

As the radius of the nanoparticles can be controlled, ligand-conjugated PEG-PCL copolymers now need to be synthesised. Ligands are required on our nanoparticles to actively target specific receptors on the target cell. subsequent Spiking of these copolymers with the bulk PEG-PCL during self-assembly, herein decided as PCL50, will allow us to produce ligand-decorated nanoparticles for phenotypic targeting. Several parameters need to be considered when producing the ligand-conjugated PEG-PCL copolymers for the nanoparticles, namely δ_L (the

insertion parameter of the ligand within the PEG brush) and the type of ligand. δ_L can be calculated on the nanoparticle as the ratio of the PEG tether length of the ligand-conjugated PEG-PCL to the PEG length of PCL50, herein described as the PEG brush of the nanoparticle. The PEG brush was kept constant as PEG_{113} was the only initiator used to synthesise pure PEG-PCL copolymers; therefore, ligand-conjugated PEG-PCL copolymers should be created with varying N_{PEG}. Secondly, the type of ligand can be changed if we make reactive PEG-PCL copolymers of various N_{PEG}, then conjugate the ligand we want to it. In conclusion, the first step of making the ligand-conjugated PEG-PCL copolymers should be to synthesise PEG-PCL copolymers of varying N_{PEG} with a reactive group for ligand conjugation.

For the nanoparticles for phenotypic targeting, ligands would be needed on either the surface of the nanoparticle or embedded within the hydrophilic side of the nanoparticle, thus PEG-PCL copolymers should be synthesised with a reactive group on the PEG block. An azide group (N_3) was chosen to be the reactive group as it can react with alkyne groups for the bioconjugation of ligands. To this end, four N_3PEG-PCL copolymers - N3PEG8PCL, N3PEG20PCL, N3PEG68PCL and N3PEG113PCL - were synthesised following the same protocol as the synthesis for the PEG-PCL copolymers but instead using N_3PEG initiators of N_{PEG} = 8, 20, 68 and 113 respectively. A summary of the structural characteristics of the N_3PEG-PCL copolymers is seen in table 2.4. $\frac{[M]}{[I]}$ for each reaction was kept at 50 for the polymerisation reactions: it was earlier decided to initially use PCL50 as the main component of the phenotypic nanoparticles, thus the target N_{PCL} of the N_3PEG-PCL copolymers was kept the same as that of PCL50. Both the N_{PCL} and M_n for each copolymer were calculated by ^{1}H NMR in $CDCl_3$, with an example

of the molecular structure and a ^{1}H NMR spectra, i.e., for N3PEG113PCL, shown in fig 2.17. The labelled protons in fig 2.17A (labelled from 1-5) correspond to the proton signals in fig 2.17B, and the DP of CL was calculated by comparison of the integration of peaks 2, 3 and 5 to the integration of peak 1. As seen in table 2.4, the obtained N_{PCL} was relatively close to the $\frac{[M]}{[I]}$ feed for the polymerisation reactions indicating an accurate and controlled synthesis; indeed, for one of the copolymers, N3PEG68PCL, there is a noticeable difference between the N_{PCL} and the $\frac{[M]}{[I]}$ feed, 30 compared to 50, which could have occurred due to a weighing error, as the large difference was not seen in the other three N_3PEG-PCL copolymers. Additionally, table 2.4 shows that the copolymers have Đ < 1.2, indicating monodisperse copolymers were synthesised. Having completed the synthesis of the N_3PEG-PCL copolymers, ligand conjugation can now be undertaken for the future formulation of ligand-conjugated PEG-PCL nanoparticles for targeting brain endothelial cells.

Table 2.4 Summary of N_3PEG-PCL block copolymers.

POLYMER CODE	INITIATOR	$\frac{[M]}{[I]}$ [A]	N_{PCL} [B]	COMPOSITION	Đ [C]	$M_{N\ NMR}$ [D]	$M_{N\ GPC}$ [D]
N3PEG8PCL	N_3PEG_8	50	49	$N_3PEG_8PCL_{49}$	1.243	5988	5637
N3PEG20PCL	N_3PEG_{20}	50	42	$N_3PEG_{20}PCL_{42}$	1.125	7769	7014
N3PEG68PCL	N_3PEG_{68}	50	30	$N_3PEG_{68}PCL_{30}$	1.166	6424	8639
N3PEG113PCL	N_3PEG_{113}	50	41	$N_3PEG_{113}PCL_{41}$	1.140	9680	9781

[a] Feed molar ratio at the beginning of the reaction, where [M] and [I] are the concentrations of the monomer and initiator respectively. [b] N_{PCL} at the end of the reaction, calculated from ^{1}H NMR in $CDCl_3$. [c] Polydispersity of the polymer, calculated from GPC in THF. [d] Number molecular weight of the polymer, calculated from both ^{1}H NMR in $CDCl_3$ and GPC in THF.

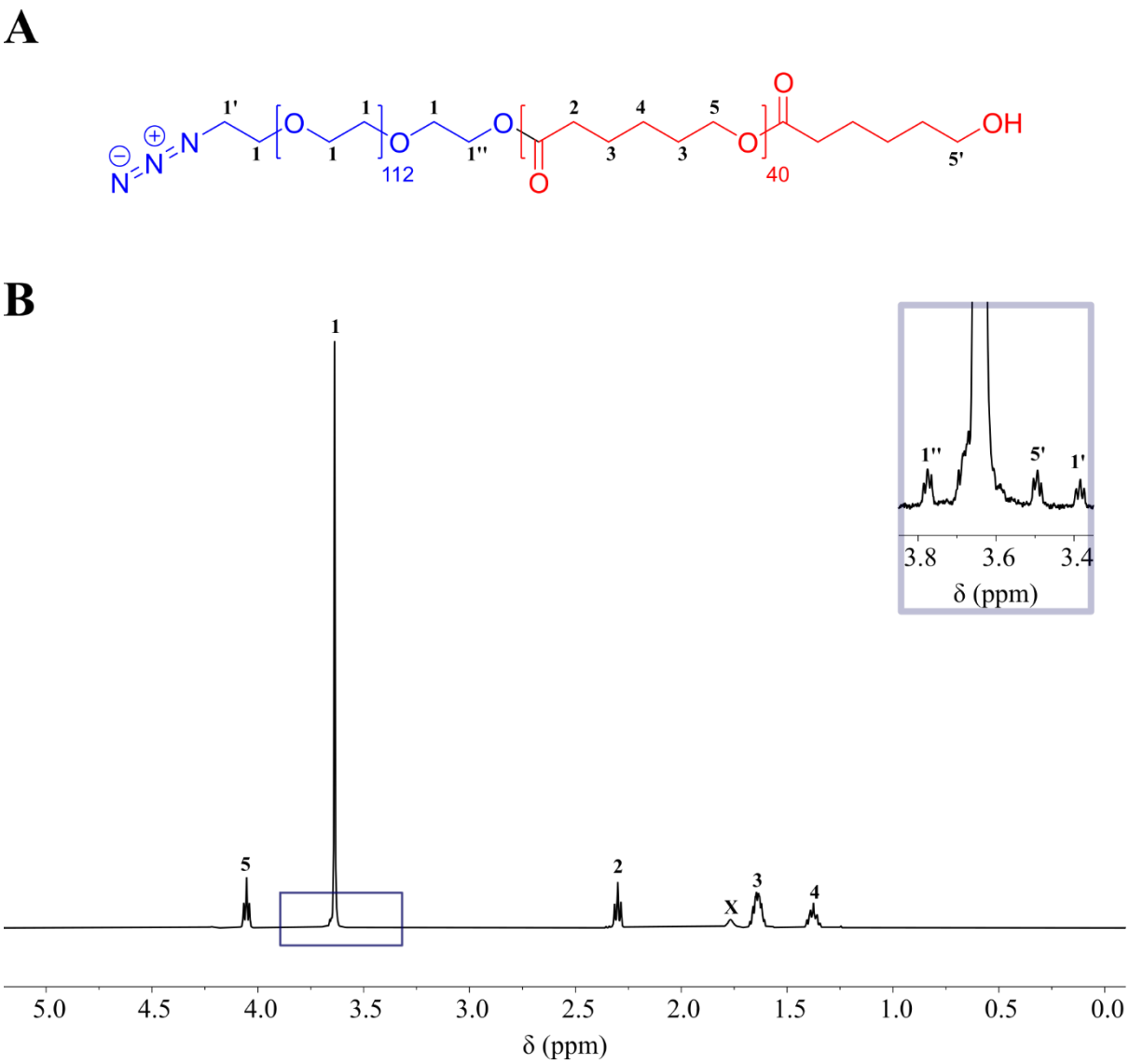

Fig 2.17 **Characterization of N3PEG68PCL.** (A) Molecular structure of N3PEG113PCL. The hydrophilic and hydrophobic sections of the amphiphilic polymer are coloured blue and red respectively (B) ^{1}H-NMR spectra of N3PEG113PCL in $CDCl_3$. The numbers on the peak correspond to the numbers depicted in A. 'X' denotes residual H_2O.

Next, ligand-conjugated PEG-PCL copolymers needed to be synthesised with the ability to target receptors on brain endothelial cells. As described in chapter 1, LRP-1 and GLUT1 are receptors present on brain endothelial cells, which can be targeted by the AP2 and Glucose ligands respectively; therefore, conjugation of these two ligands should be done on the synthesised N_3PEG-PCL copolymers. A scheme of the conjugations done is shown in fig 2.18, using copper-catalysed 1,3-dipolar cycloaddition. Fig 2.18 shows that for AP2, click conjugation was done

on three N_3PEG-PCL copolymers (namely N3PEG113PCL, N3PEG68PCL and N3PEG8PCL) to synthesise AP2-conjugated PEG-PCL copolymers (coded AP2_PEG113, AP2_PEG68 and AP2_PEG8 respectively): the three named N_3PEG-PCL copolymers were chosen for conjugation due to their differences in N_{PEG}, thus enabling the testing of different δ_L when designing the AP2-conjugated PEG-PCL nanoparticles. Similarly, fig 2.18 shows that for Gluc, conjugation was done on N3PEG113PCL: the propargyl-glucose used has the propargyl group at the C6 position of the glucose as binding to GLUT1 is believed to incorporate the OH groups on the C1, C3 and C4 positions.[76] In addition to the ligands, Cy7 was conjugated onto N3PEG20 as future in-vitro binding experiments will require the nanoparticles to be fluorescently labelled to be tracked. A summary of the structural characteristics of the 5 ligand-conjugated PEG-PCL copolymers is described in table 2.5.

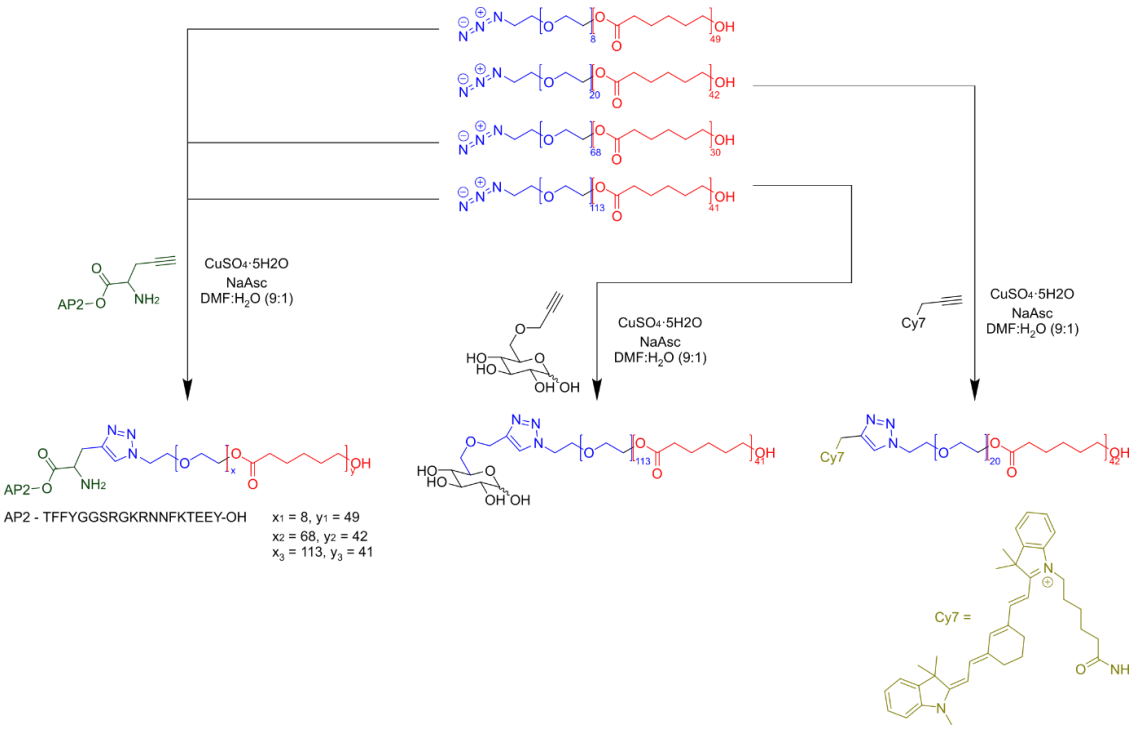

Fig 2.18 **Click reaction scheme for the synthesis of ligand-conjugated PEG-PCL copolymers.** Syntheses of 3 AP2-PEG-PCL, 1 Gluc-PEG-PCL and 1 Cy7-PEG-PCL copolymers are depicted. The AP2 amino acid sequence is also displayed with the propargylglycine connected to the N terminus.

Table 2.5 Summary of ligand-conjugated PEG-PCL copolymers.

POLYMER CODE	LIGAND (L)	INITIATOR (I)	COMPOSITION	Đ [B]	$M_{N\ GPC}$ [B]	CONJUGATION EFFICIENCY (%) [C]
AP2_PEG113	AP2	N3PEG113	AP2-$PEG_{113}PCL_{41}$	NA	NA	59.1 (± 5.7)
AP2_PEG68	AP2	N3PEG68	AP2-$PEG_{68}PCL_{30}$	NA	NA	87.0 (± 12.2)
AP2_PEG8	AP2	N3PEG8	AP2-$PEG_{8}PCL_{49}$	NA	NA	79.3 (± 12.4)
Gluc_PEG113	Gluc	N3PEG113	Gluc-$PEG_{113}PCL_{41}$	NA	NA	59.0
Cy7_PEG20	Cy7	N3PEG20	Cy7-$PEG_{20}PCL_{60}$	1.295	10776	NA

[a] Feed molar ratio at the beginning of the reaction, where [L] and [I] are the concentrations of the ligand and initiator respectively [b] Polydispersity (Đ and Number molecular weight (M_n) of the copolymers, calculated from GPC in THF. The parameters were only obtained for Cy7-PEG20 due to solubility issues of the other copolymers. [c] Conjugation efficiency calculated via BCA assay (for AP2) or ^{1}H NMR in d^6-DMSO (for Gluc). The number in the brackets corresponds is ±SD.

As seen in table 2.5, for AP2_PEG113, AP2_PEG68 and AP2_PEG8 were synthesised, and the click reaction quantified. There are, however, some discrepancies to the data shown in table 2.5. GPC analysis was not possible as the AP and Glucose conjugated polymers were unable to dissolve in THF for the GPC, and our instrument was not equipped to run DMF and LiBr as the eluent: future studies could confirm the polydispersity and M_n of the polymers by using GPC with DMF and LiBr as the eluent, as the polymers can dissolve well in DMF. Additionally, due to only a small amount of the Cy7-PEG-PCL being made (~20 mg), and with the vast amount that would be required to use for cell studies, NMR was not done to calculate for conjugation efficiency. Future studies would involve the production of a larger batch of Cy7-PEG-PCL, so that conjugation efficiency could be obtained.

Click conjugation for AP2 was quantified using a BCA assay, as AP2 is a peptide-based ligand. The BCA assay was first done on positive controls, PC113, PC68,

and PC8, solutions containing 1 : 1 : 1 molar ratios of free AP2 : N3PEG113, N3PEG68 or N3PEG8 : triazole respectively, at different concentrations and calibration curves were formed. The BCA assay was then conducted on the AP2-conjugated PEG-PCL copolymers at the same concentrations then compared to the corresponding positive control i.e., AP2_PEG113 to PC113 to calculate the conjugation efficiency. The absorbance curves and a graph showing the calculated conjugation efficiencies are shown in fig 2.19. The graph in fig 2.19B shows that the click conjugations occurred successfully, with conjugation efficiencies of 59.1 $\pm$ 5.7 for AP2_PEG113, 87.0 $\pm$ 12.2 for AP2_PEG68 and 79.3 $\pm$ 12.4 for AP2_PEG8. Lower conjugation of the AP2 occurred using N3PEG113 indicating a lower reactivity for the copolymer to AP2: the increased N_{PEG} for N3PEG113 could likely lower the reactivity of the copolymer as the N_3 reactive site could get crowding by the PEG, increasing steric hindrance around the reactive site.

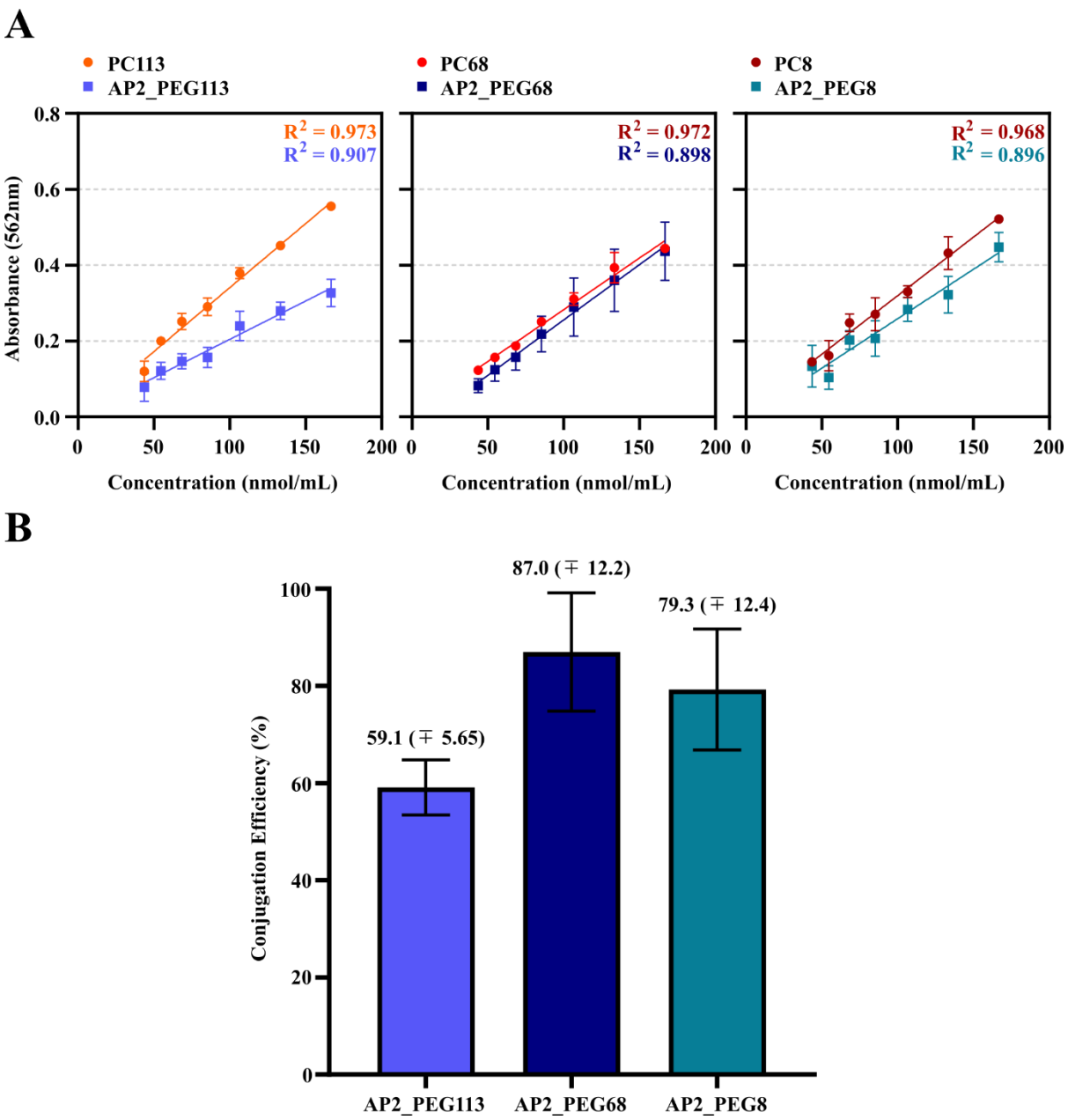

Fig. 2.19 **Conjugation Efficiency of Click Reactions for AP2-conjugated copolymers.** (A) Absorbance curves, read at 562 nm, from the BCA assay for the positive controls (PC113, PC68 and PC8) and AP2_PEG113, AP2_PEG68 and AP2_PEG8. Errors bars are ±SD, n=4 readings per concentration. (B) Graph showing the conjugation efficiencies of the click reactions for AP2_PEG113, AP2_PEG68 and AP2_PEG8, with the efficiency written above the bars. Error bars are ±SD, n=7 as conjugation efficiency was calculated at 7 concentrations.

Also shown in table 2.5 is the conjugation efficiency of Gluc_PEG113 which, unlike the AP2-conjugated PEG-PCL copolymers, has no peptide bonds thus ^{1}H NMR analysis was used to quantify the conjugation. ^{1}H NMR analysis was done on N3PEG113 and Gluc_PEG113 in d^{6}-DMSO and their ^{1}H NMR spectra are

stacked on top of one another, shown in fig 2.20. Fig 2.20 also shows the molecular structures of N3PEG113 and Gluc_PEG113 with the peaks on the spectra corresponding to the numbered protons on the structures. As evidenced by the ^{1}H NMR spectra, the peaks for the PCL block were maintained, thus when setting the integration of peak 5 for both copolymers, the quantification of the click reaction was calculated by the integration of peak 6. Peak 6 denotes the proton at the triazole ring post-cycloaddition reaction, however instead of an expected singlet peak, a doublet was found. The doublet is likely because the cycloaddition between the azide and the propargyl was done at a high temperature (60 ^{o}C) allowing a huisgen 1,3-dipolar cycloaddition to occur instead of the copper-catalysed azide-alkyne cycloaddition, thus a 1:1 mixture of stereoisomers could have been formulated, giving rise to two sharp peaks at peak 6. Nevertheless, the hydroxyl groups at C1, C3 and C4 have remained free to bind onto the GLUT1 receptor, so binding of this glucose-conjugated PEG-PCL to GLUT1 should still be maintained. Integration of the doublet peak 6 was 0.59, thereby indicating a 59.0% conjugation efficiency for the synthesis of Gluc_PEG113.

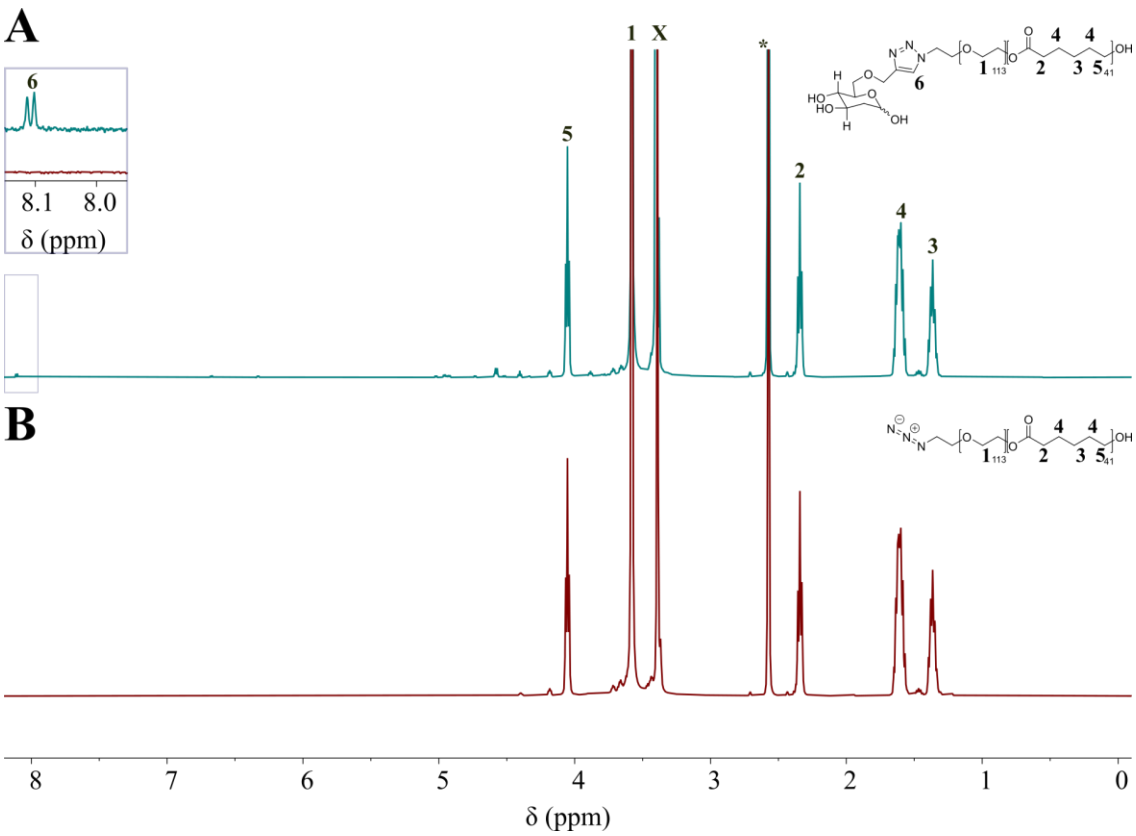

Fig. 2.20 **Conjugation Efficiency of Click Reaction for glucose-conjugated polymer.** Stacked ^{1}H NMR spectra of (A) Gluc-PEG113 and (B) N3PEG113PCL in d^{6}-DMSO. Boxed area signifies the presence and absence of a triazole proton peak for Gluc-PEG113 and N3PEG113PCL respectively. The numbers on the peaks correspond to the numbers depicted in the structures next to the spectra. 'X' denotes residual water and '*' denotes the DMSO solvent peak.

2.3.4 Angiopep2 decorated PEG-PCL micelles

As discussed earlier for the type of ligand, N_{Ligand}, and δ_L are variables to account for when engineering the ligand-decorated nanoparticles. AP2-decorated nanoparticles were first formulated: N_{Ligand} was adjusted by altering the quantity of the AP2 conjugated PEG-PCL copolymer mixed with PCL50 during the self-assembly of the nanoparticles and δ_L was accounted for by changing which AP2-conjugated PEG-PCL copolymer is used during self-assembly. For the purposes of the thesis, micelles were chosen to be the preferred structure for testing phenotypic targeting as using micelles ensures that any ligand will be present on the outside of the nanoparticle, either embedded within the PEG$_{113}$ brush ($\delta_L < 1$) or on the surface of the PEG$_{113}$ brush ($\delta_L < 1$). Micelles could also have

been made with PCL30, PCL40 or PCL60 as the major component to test the effect of *R* in phenotypic targeting, but for simplicities sake it was decided to first test the effects of n_L and δ_L for phenotypic targeting, and in the future test the effect of the radius of the nanoparticle. Cy7_PEG20 was also used in the self-assembly of AP2-decorated nanoparticles to track the nanoparticles by fluorescence in future *in vitro* studies. A diagram of an AP2-decorated PEG-PCL nanoparticle is shown in fig 2.21, summarising the above details.

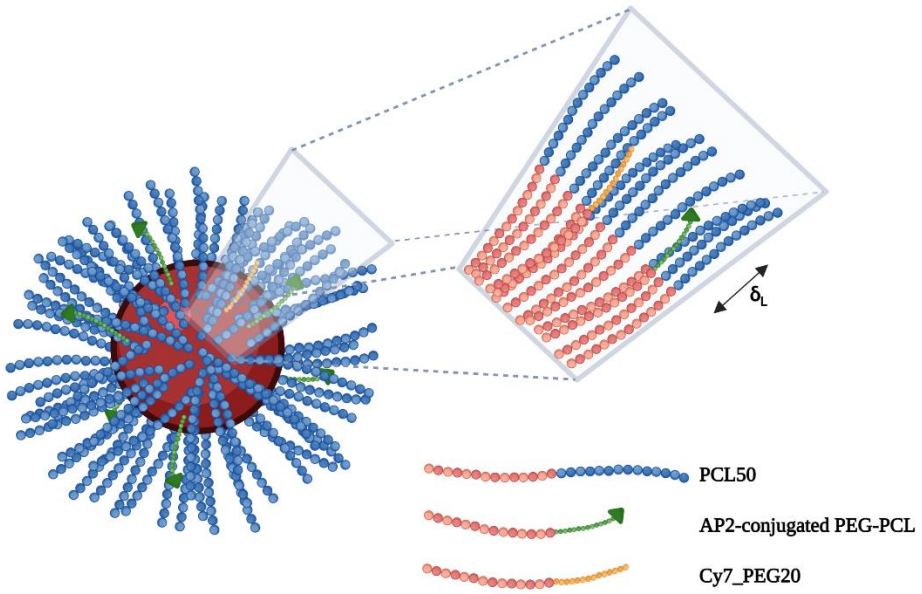

Fig 2.21 **Schematic of an AP2-decorated PEG-PCL micelles.** Micelles were engineered predominantly with PCL50 with small molar fractions of Cy7_PEG20 and AP2-conjugated PEG-PCL copolymers. $\delta_L$depicts how embedded the AP2 ligand is within the PEG_{113} brush, calculated as the ratio between the length of PEG_{113} and the tether length of the AP2-conjugated PEG-PCL copolymer.

18 AP2-decorated PEG-PCL micelle solutions were formulated using only PCL50 as the bulk component, Cy7_PEG20 to give the micelle fluorescence and either AP2_PEG113, AP2_PEG68 or AP2_PEG8 to decorate the micelle with AP2. Nanoparticle solutions of 500 uM were made and then purified using the method described in the materials and methods section. Purification was done to mainly transfer the solution media from water to PBS as the nanoparticles were to be

used for following *in vitro* cell studies. A summary of the 18 nanoparticle solutions is given in table 2.6. As noted in table 2.6, the molar fraction of Cy7_PEG20 in the nanoparticle formulations, X_{Cy7}, was maintained at 5%, to keep the Cy7 content per nanoparticle constant.

Different N_L of AP2 per nanoparticles was obtained by changing the molar percentage, X_{AP2}, of AP2-conjugated PEG-PCL (AP2_PEG113, AP2_PEG68, or AP2_PEG8) in each nanoparticle formulation. N_{Ligand} was estimated for each nanoparticle solution by using the following equation:

$$N_{Ligand} = N_{agg} \times X_{AP2} \tag{13}$$

where N_{agg} is the number of aggregation of the nanoparticle (the number of polymer strands in each nanoparticle). Furthermore, the estimation assumes that each nanoparticle has the same number of ligands. We assume that N_{agg} will be the same for all the AP2-decorated nanoparticle formulations and will be same for those nanoparticles made only using PCL50 (as PCL50 is the bulk copolymer for all AP2-decorated nanoparticle solutions)., N_{agg} was estimated at 395 using the following equation:

$$N_{agg} = \frac{V_{Core}}{V_{Polymer}} \tag{14}$$

where V_{Core} is the hydrophobic core volume of the PCL50 nanoparticle and $V_{polymer}$ is the volume of one PCL block of PCL50 in the hydrophobic core. V_{Core} was calculated by:

$$V_{Core}(nm^3) = \frac{4}{3}\pi(a_{PCL} \times N_{PCL}(PCL50)^{v_{PCL}}) \quad (15)$$

where a_{PCL} is the calculated length of a PCL monomer unit (0.875 nm), $N_{PCL}(PCL50)$ is the N_{PCL} of PCL50 (52) and v_{PCL} is the flory exponent for the PCL block of nanoparticles. 0.6 was chosen for v_{PCL} as PCL is in an unfavoured solvent when in PBS and will shrink in the bad solvent. $V_{Polymer}$ was calculated by:

$$V_{Polymer}(nm^3) = \frac{M_w^{PCL}(PCL50) \times N_{PCL}(PCL50)}{N_A \times \rho(PCL)} \quad (16)$$

where $M_w^{PCL}(PCL50)$ is the molecular weight of the PCL block of PCL50 (114 g mol^{-1}), N_A is Avogadro's constant and $\rho(PCL)$ is the density of PCL (1.13×10^{21} g nm^{-3}).

3 different δ_L were obtained by using either AP2_PEG113, AP2_PEG68 and AP2_PEG8 in the self-assembly process. The following equation, based on the calculation for a polymer chain length,[186] was used to calculate δ_L:

$$\langle \delta_L \rangle = \frac{a_{PEG} N_{PEG}(AP\_PEG)^{v_{PEG}}}{a_{PEG} N_{PEG}(PCL50)^{v_{PEG}}} = \frac{N_{PEG}(AP\_PEG)^{v_{PEG}}}{N_{PEG}(PCL50)^{v_{PEG}}} \quad (17)$$

where a_{PEG} is the length of a PEG monomer (0.320 nm), $N_{PEG}(AP\_PEG)$ and $N_{PEG}(PCL50)$ are the N_{PEG} of the AP2-conjugated PEG-PCL used and PCL50

respectively, and v is the Flory exponent for PEG of the nanoparticle in PBS. v was calculated using the following equations:

$$v_{PEG} = \frac{\ln(A_{PEG}[PCL50]) - \ln(a_{PEG})}{\ln(N_{PEG})} \quad (18)$$

$$A_{PEG}[PCL50] = \langle R_G \rangle - a_{PCL} N_{PCL} (PCL50)^{v_{PCL}} \quad (19)$$

where $A_{PEG}[PCL50]$ is the PEG length of PCL50 and $\langle R_G \rangle$ is the radius of PCL50 nanoparticles obtained by TEM, which was observed to be 16.64 nm, with the diameter of the nanoparticles shown in table 2.3.

The nanoparticles were coded based on both the n_L and δ_L of the nanoparticle solutions, i.e., AP2-1-2 were nanoparticles formulated with PCL50, Cy7_PEG20 and AP2_PEG113 – thus having a δ_L = 1 – at $n_L = 2$. The table 2.6 also separates the nanoparticles solutions into 4 sets of nanoparticles, differentiated by the AP2-conjugated PEG-PCL copolymer used in the self-assembly. Three sets hereby labelled the AP2_1, AP2_0.70 and AP2_0.16 sets differ in the δ_L of AP2 between sets and differ in the n_L of AP2 within the sets, with a control set hereby labelled Ctrl set being made with no AP2 present, were then to be analysed to determine if the nanoparticles can be used to test phenotypic targeting.

Table 2.6 Summary of AP2-conjugated PEG-PCL nanoparticles.

NANOPARTICLE CODE	AP2-CONJUGATED PEG-PCL [A]	N_{Ligand}	$X_{AP2}{}^{B}$	$X_{Cy7}{}^{C}$	$\delta_L{}^{C}$
Ctrl_1	NA	0	0	5	0
Ctrl_2	NA	0	0	5	0
Ctrl_3	NA	0	0	5	0
AP2_1_2	AP2_PEG113	2	0.5	5	1
AP2_1_4	AP2_PEG113	4	1	5	1
AP2_1_8	AP2_PEG113	8	2	5	1
AP2_1_20	AP2_PEG113	20	5	5	1
AP2_1_40	AP2_PEG113	40	10	5	1
AP2_0.70_2	AP2_PEG68	2	0.5	5	0.70
AP2_0.70_4	AP2_PEG68	4	1	5	0.70
AP2_0.70_8	AP2_PEG68	8	2	5	0.70
AP2_0.70_20	AP2_PEG68	20	5	5	0.70
AP2_0.70_40	AP2_PEG68	40	10	5	0.70
AP2_0.16_2	AP2_PEG8	2	0.5	5	0.16
AP2_0.16_4	AP2_PEG8	4	1	5	0.16
AP2_0.16_8	AP2_PEG8	8	2	5	0.16
AP2_0.16_20	AP2_PEG8	20	5	5	0.16
AP2_0.16_40	AP2_PEG8	40	10	5	0.16

[a] AP2-conjugated PEG-PCL used for the assembly of the nanoparticle. AP2-conjugated PEG-PCL polymer codes depicted here are found in Table 2.5. [b, c] Molar percentage (%) of AP2-conjugated PEG-PCL and Cy7_PEG20 respectively. [d] Ligand insertion parameter of AP2.

The Ctrl set was formulated only containing PCL50 and Cy7_PEG20 to produce fluorescently tagged nanoparticles with no AP2 ligands. The control set was made to determine whether the inclusion of 5 mol% Cy7_PEG20 alter the morphology or size of nanoparticles made with PCL50. The control set was also

formulated as in future *in vitro* studies, the control set would be used as the negative control when testing the effect δ_L and N_{Ligand} of AP2 has on phenotypic binding. DLS and TEM analysis was first done on the control nanoparticle set, Ctrl_1, Ctrl_2 and Ctrl_3, with the TEM images and DLS intensity and correlograms shown in fig 2.21. The TEM images show that spherical micelles were found in all 3 samples, akin to the morphologies and size of nanoparticles made using only PCL50 in fig 2.11. The intensity graph in fig 2.21B also shows that all three samples shared the same intensity profile, indicating that the three control samples all shared the same size. The DLS results in fig 2.21B also match the intensity and correlograms seen in fig 2.5. The results in fig 2.22 conclude that the inclusion of Cy7_PEG20 had no effect on the size and shape of PCL50 nanoparticles.

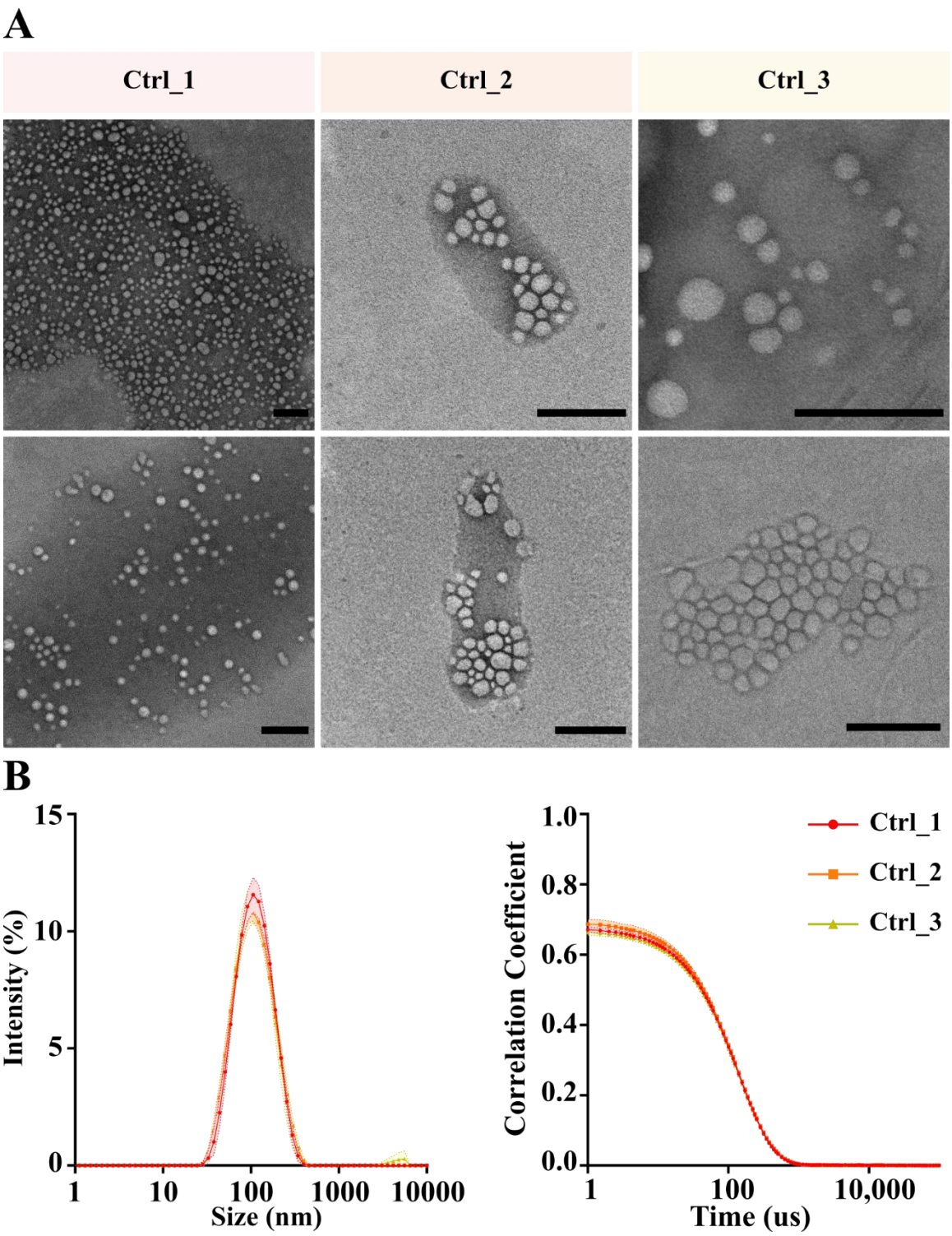

Fig 2.22 **Structure and size characterisation of nanoparticles of the Ctrl set.** (A) TEM images of control samples. Scale bar = 200nm. (B) DLS intensity and correlogram graphs of the control micelles.

Analysis of the AP2_1, AP2_0.70 and AP2_0.16 sets was then done to confirm the shape and size of these nanoparticles. TEM images of the nanoparticles of

the AP2_1, AP2_0.70 and AP2_0.16 set are shown in fig 2.23, fig 2.24 and fig 2.25 respectively. A diagram is given in each figure to help distinguish the different δ_L for AP2 between the sets. The TEM images in fig 2.23 – 2.25 show that all the nanoparticles formed were spherical and that the sizes of the nanoparticles are the same as those of the Ctrl set, therefore the introduction of AP2-conjugated PEG-PCL copolymers during the self-assembly had no effect on the size and morphology the nanoparticles could form. Changing the mol% of AP2-conjugated PEG-PCL copolymer also had no effect on the size and shape of the nanoparticles, as evidenced by comparison of the TEM images within each set.

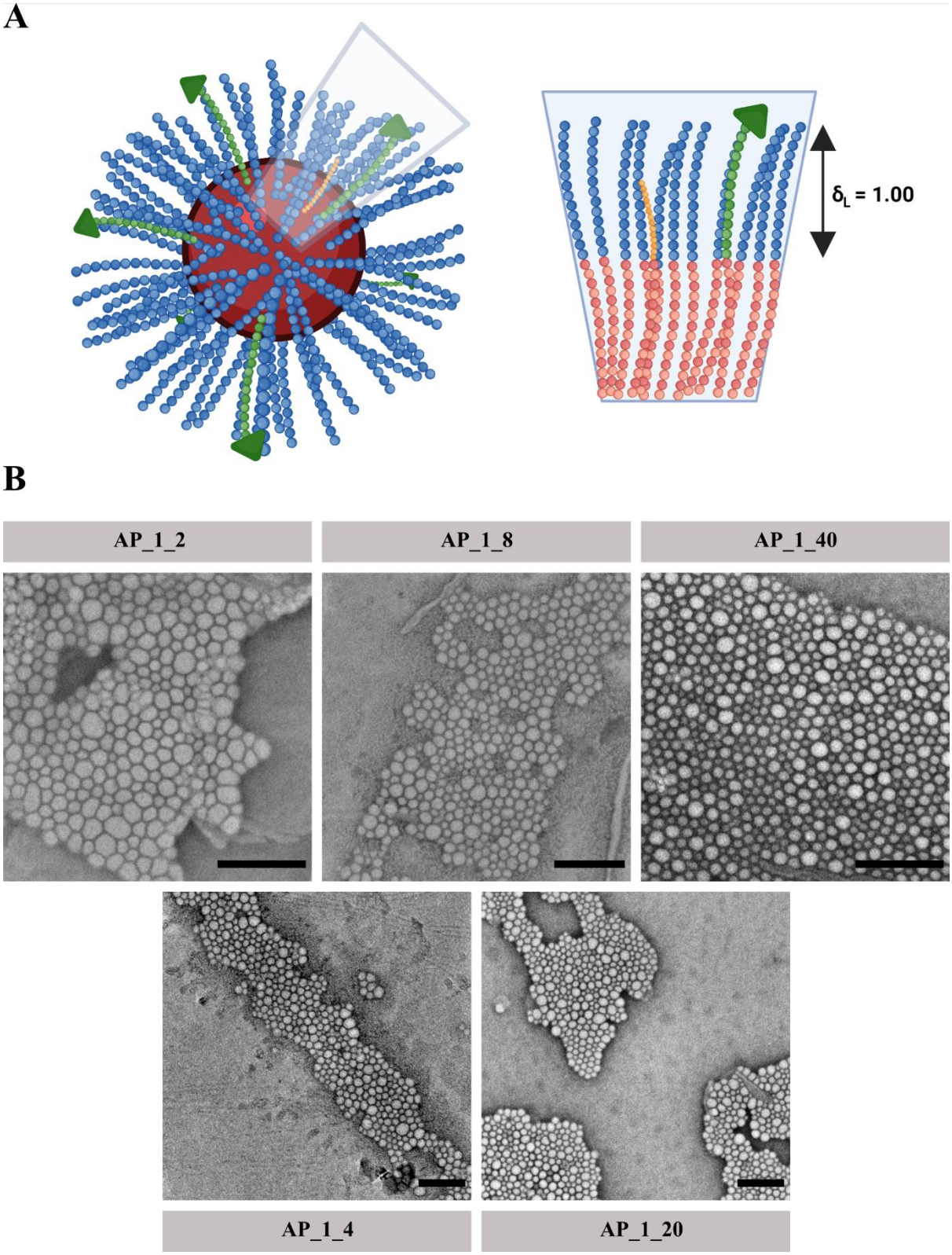

Fig 2.23 **Structure characterisation of nanoparticles of the AP2_1 set.** (A) Schematic of the designed nanoparticles for set AP2_1 (B) TEM images of AP2_1 set of micelles. Scale bar = 200nm.

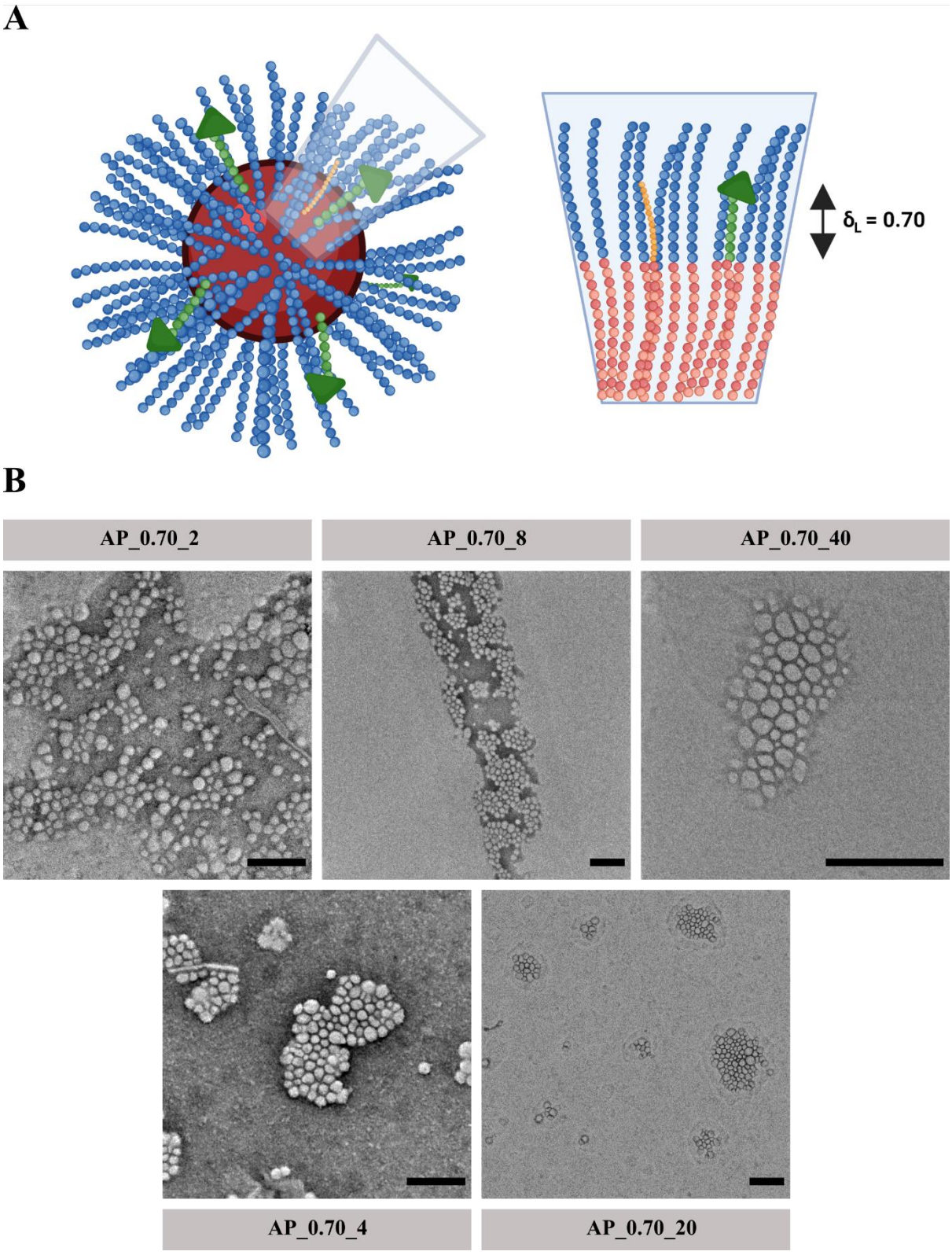

Fig 2.24 **Structure characterisation of nanoparticles of the AP2_0.70 set.** (A) Schematic of the designed nanoparticles for set AP2_1 (B) TEM images of AP2_0.70 set of micelles. Scale bar = 200nm.

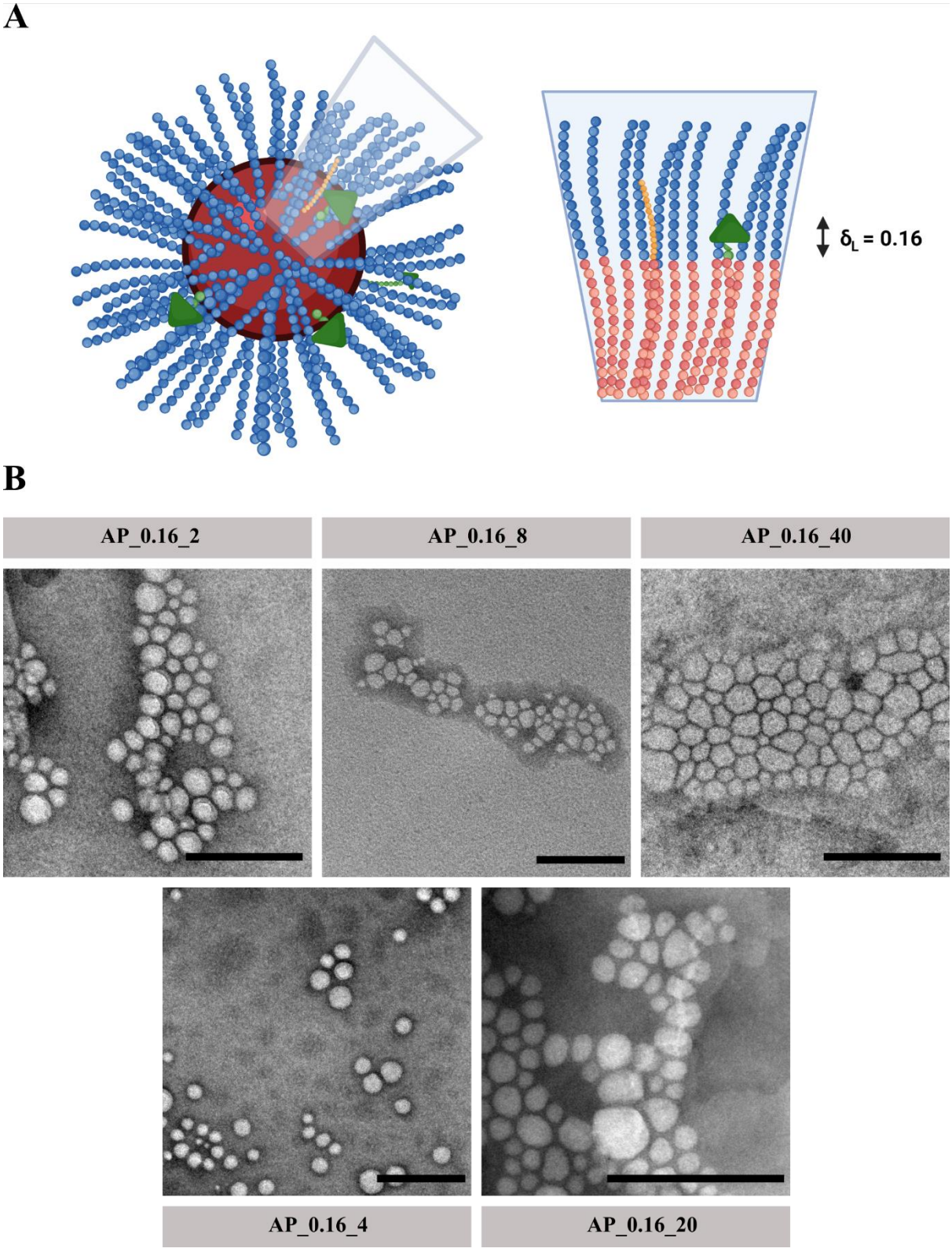

Fig 2.25 **Structure characterisation of nanoparticles of the AP2_0.16 set.** (A) Schematic of the designed nanoparticles for set AP2_1 (B) TEM images of AP2_0.11 nanoparticles. Scale bar = 200nm.

2.3.5 Glucose decorated PEG-PCL micelles

The type of ligand used is another factor for phenotypic targeting, therefore Gluc-decorated nanoparticles were synthesised. In comparison to the AP2-decorated nanoparticles, the gluc-decorated nanoparticles will test $N_{Ligand}$for phenotypic targeting: the ligand-receptor binding energy between glucose and GLUT1 is low (where $K_M = 6.5mM$[187]). As glucose to GLUT1 binding energy is low, an assumption is that embedding it within the nanoparticle hydrophilic PEG chains would increase the steric hindrance to the point where binding could no longer occur. Previous studies, such as targeting and uptake studies of glucose-conjugated nanoparticles on the RG-2 glioma cell line[188] and the transport of glucose-decorated micelles across the BBB[76] have also used glucose on the surface of the nanoparticles; therefore, it was decided to first test glucose only using N_{Ligand} as the variable. Like the AP2-decorated nanoparticles, PCL50 will be used as the major component and 5 mol% Cy7_PEG20 will be used during the self-assembly. A diagram of a gluc-decorated nanoparticle to be engineered is shown in fig 2.26.

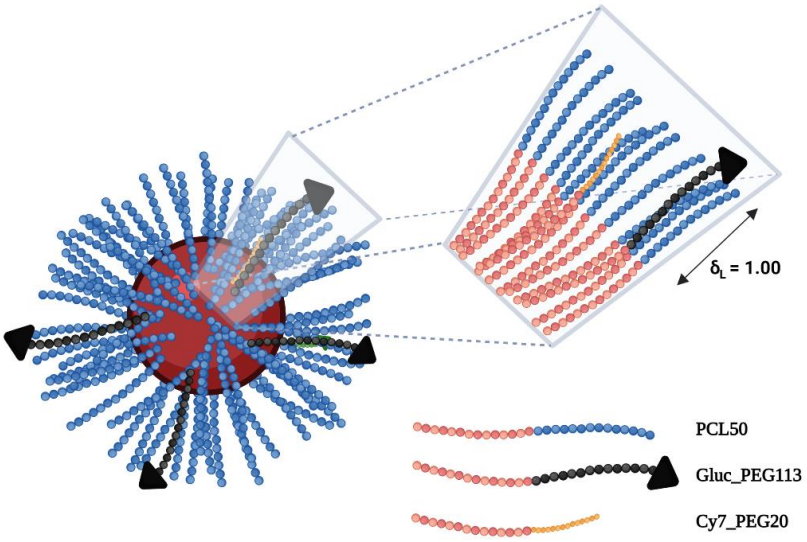

Fig 2.26 **Schematic of an AP2-decorated PEG-PCL micelles.** Nanoparticles are engineered predominantly with PCL50 with small molar fractions of Cy7_PEG20 and Gluc_PEG113. $\delta_L$depicts how embedded the Gluc ligand is within the PEG_{113} brush, calculated as the ratio between the length of PEG_{113} and the tether length of Gluc_PEG113.

6 Gluc-conjugated nanoparticle formulations were made varying in N_{Ligand} of glucose, and a summary of the nanoparticles and the variables being tested is shown in table 2.7. Nanoparticles with different N_{Ligand} of glucose was obtained by changing the X_{Gluc} during self-assembly. N_{Ligand} was again calculated using the equations in 2.3.4. Compared to X_{AP2}, nanoparticles with a higher X_{Gluc} formed, from 5-50%, to mimic the X_{Gluc} of glucose-decorated nanoparticles used by the Katoaka group and their BBB crossing studies.[76] δ_L for the gluc ligand on each nanoparticle sample is equal to 1 as the gluc-conjugated PEG-PCL used has N_{PEG} = 113, akin to that of PCL50. TEM images of each sample were taken and are shown in fig 2.26. As seen in the images, spherical structures were seen for each sample. Non-spherical structures were also seen in some of the samples, such as in Gluc_1_15 and Gluc_1_50, however these structures were only found in a few sections of the grid and the predominant structure was still of a spherical micelle. The structures seen in fig 2.27 are the same as those found

in fig 2.11 and 2.22-2.25, therefore the introduction of gluc-conjugated PEG-PCL did not alter the sizes and shapes of the nanoparticles formed.

Table 2.7 Summary of Glucose-conjugated PEG-PCL nanoparticles.

NANOPARTICLE CODE	GLUC-CONJUGATED PEG-PCL [A]	N_{Ligand}	X_{Gluc} (%) [B]	X_{Cy7} (%) [C]	δ_L [D]
Gluc_1_20	Gluc_PEG113	20	5	5	1
Gluc_1_39	Gluc_PEG113	39	10	5	1
Gluc_1_59	Gluc_PEG113	59	15	5	1
Gluc_1_79	Gluc_PEG113	79	20	5	1
Gluc_1_99	Gluc_PEG113	99	25	5	1
Gluc_1_197	Gluc_PEG113	197	50	5	1

[a] Gluc-conjugated PEG-PCL used for the assembly of the nanoparticle. Gluc-conjugated PEG-PCL polymer codes depicted here are found in Table 2.5. [b,c] Molar fractions (%) of Gluc_PEG113 and Cy7_PEG20 respectively. [d] Ligand insertion parameter of Gluc.

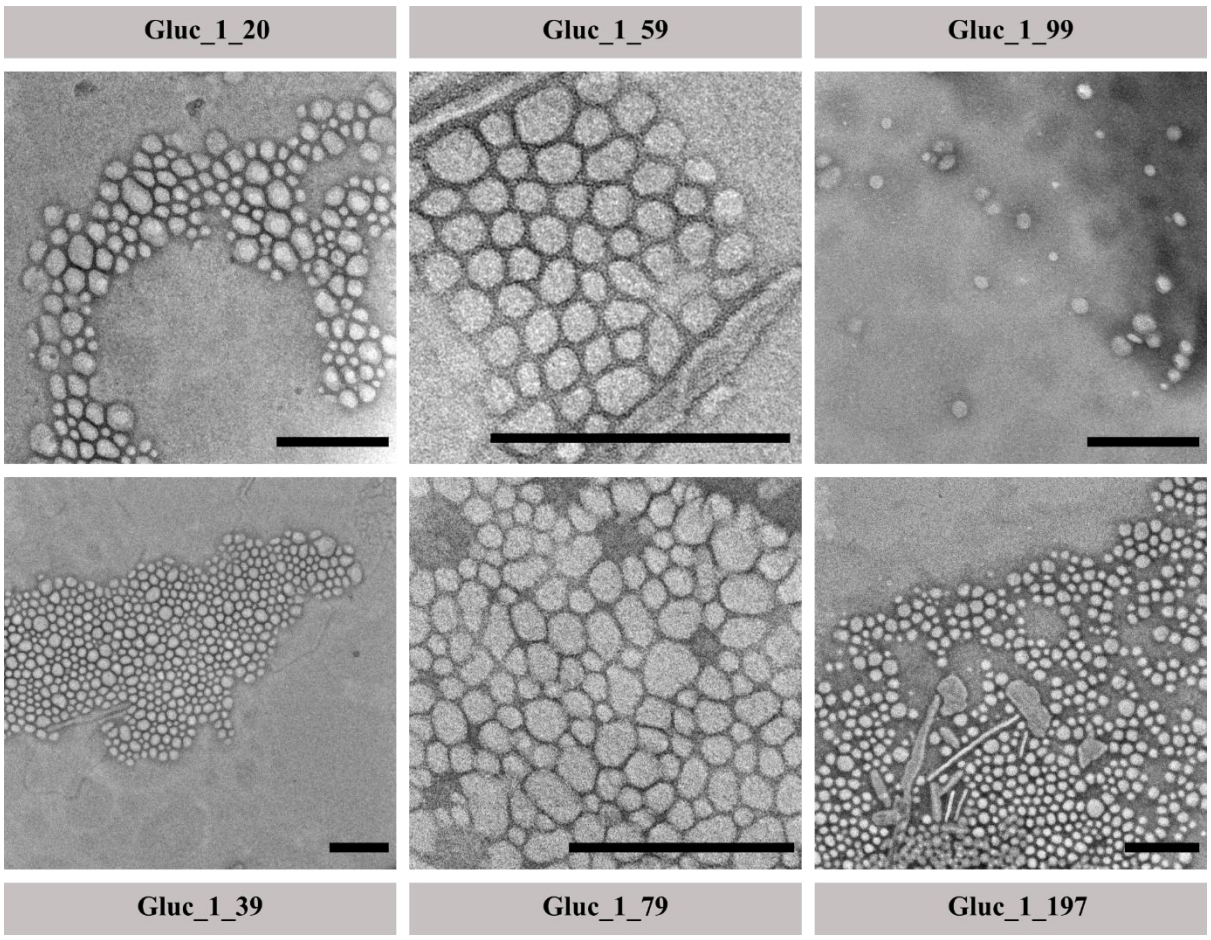

Fig 2.27 **Structure characterisation of nanoparticles of the Gluc set.** (A) Schematic of the designed nanoparticles for set Gluc (B) TEM images of AP2_0.11 nanoparticles. Scale bar = 200nm.

2.4 Conclusions

The first step in answering our research questions was to synthesise and develop nanoparticles with the ability to target receptors on the brain endothelial cells. In this chapter, we have described the formulation of ligand-decorated nanoparticles that differ in three variables that influence targeting: N_{Ligand} (number of ligands), δ_L (ligand insertion parameter - for AP2) and type of ligand (AP2 or Glucose). We can therefore first optimise targeting to brain endothelial cells using these variables, and then further investigate if selective targeting of brain endothelial cells can be achieved to answer our first research question. We can next use these nanoparticles in *in vitro* crossing assays to assess the influence of δ_L in transcytosis to answer our second research question.

Several shortcomings arose from the results. Firstly, the synthesised PEG-PCL copolymers have a varying range of polydispersities, Đ: in the future, several alterations in the synthesis procedure (such as azeotropic distillation of the PEG initiator) may prove to optimise the purity of the synthesised products and make the polydispersities of the copolymers narrower. Furthermore, the results also assume that during the production of the ligand-decorated nanoparticles, the distribution of the ligands is consistently uniform, with each nanoparticle having an equal number of ligands - further work examining the distribution of the ligands on the nanoparticle may prove beneficial, particularly in linking experimental data and any future computational study.

Chapter 3
Targeting brain endothelial cells

3.1 Introduction

In this chapter, we focus on the first research question of the thesis: can we selectively target brain endothelial cells? To answer the research question, we must first optimise multivalent targeting towards brain endothelial cells. We can then investigate binding to brain endothelial cells against other brain-derived cells to see if we can phenotypically target the specific brain endothelial cell phenotype (density of multiple receptors).

For phenotypic targeting (which builds on the principles of superselectivity and range-selectivity) the fraction of bound nanoparticles on a receptor-decorated surface (θ) relies heavily on the single site partition function describing a bound nanoparticle (q). q was calculated in equation (10), where $q = v \exp(-\beta F_{tot})$.[17,21] v is the binding volume of the nanoparticle at the adsorption site, β is $\frac{1}{k_B T}$ (k_B is the Boltzmann constant and T is temperature) and F_{tot} is the total free energy of binding between the nanoparticle and the target cell. F_{tot} is the combination of both attractive and repulsive forces to binding, relying on the number of ligands on a nanoparticle (N_{Ligand}), the insertion parameter of the ligand (δ_L), the free energy of binding between a ligand and receptor (f_B) and the number of receptors on the surface (N_R)

In chapter 2, ligand-decorated nanoparticles were formulated, varying N_{Ligand}, δ_L and the type of ligand (using either AP2 or Gluc to bind onto LRP-1 or Glut1 receptors on brain endothelial cells respectively). With the synthesised ligand-decorated nanoparticles, investigation on the effects of N_{Ligand}, δ_L and the type of ligand on targeting can be undertaken. An investigation of the effects of the variables will allow us to optimise our targeting brain endothelial cells prior to testing if we can selectively target brain endothelial cells.

In this study, we use mouse brain endothelial cells (bEnd3) as our brain endothelial cell line for testing: bEnd3 has been used in the literature in both targeting experiments[18,21] and crossing experiments[71,189]. By using bEnd3 cells for targeting, we can therefore relate the results to future crossing assays using bEnd3 to create our *in vitro* BBB model. The other two cell lines chosen for the investigation include mouse astrocytes (C8-D1A) and human glioblastoma (T98G). Both cell lines were chosen for comparison with bEnd3 as they are both also brain-isolated cell lines, with C8-D1A as astrocytes being cells as part of the BBB, and T98G glioblastoma as an aggressive brain cancer cell type.

In this chapter, a cytotoxicity assay was first performed to investigate whether the synthesised ligand-decorated PEG-PCL nanoparticles were toxic to bEnd3, C8-D1A and T98G. Receptor expressions of LRP-1 and GLU1 for each line were analysed by Western blot to ascertain whether the three cell lines differ in receptor densities. Binding assays were then done on bEnd3 to investigate the effect of N_L and δ_L on binding. Further binding studies were performed on C8-D1A and T98G to investigate the effect of $N_{Receptor}$ and to verify if any nanoparticle formulation bound strongly to bEnd3 and not to the other cells.

Finally, the glycocalyx of each cell line was investigated to examine the effect of δ_R on binding, and subsequent binding assays on glycocalyx-shed bEnd3 was undertaken to see if the effect of glycocalyx shedding on the binding to bEnd3.

3.2 Materials and Methods

3.2.1 Materials

Table 3.1 Materials used in chapter 3

MATERIAL	ABBREVIATION	SUPPLIER
bEnd3 (mouse endothelial cells)	bEnd3	ATCC
C8-D1A (mouse astrocytes)	C8-D1A	ATCC
T98G (human glioma cells)	T98G	ATCC
Dulbecco's modified eagle's medium	DMEM	ATCC
Eagle's minimum essential medium	EMEM	ATCC
Fetal bovine serum	FBS	Sigma Aldrich
Penicillin/streptomycin	PS	Sigma Aldrich
Dulbecco's phosphate buffered saline	dPBS	Sigma Aldrich
Trypsin-EDTA (0.25%), phenol red	Tryp	Thermo Fisher
Trypan blue	TryB	Sigma Aldrich
RIPA buffer	RIPA	Sigma Aldrich
Protease inhibitor cocktail	PI	Sigma Aldrich
Bio-Rad protein assay kit	-	Bio-rad
Bovine serum albumin	BSA	Bio-rad
Laemmli 4x concentrate	-	Bio-rad
2-Mercaptoethanol	-	Sigma Aldrich
Acrylamide/Bis-acrylamide 30%	Acrylamide/bis	Sigma Aldrich
Tris Base	Tris	Sigma Aldrich
Hydrochloric acid	HCl	Sigma Aldrich
Sodium dodecyl sulfate	SDS	Sigma Aldrich
Distilled water	dH_2O	Sigma Aldrich
Ammonium persulphate	APS	Sigma Aldrich
Tetramethylethylenediamine	TEMED	Thermo Fisher
Glycine	-	Sigma Aldrich

Methanol	MeOH	Fisher Scientific
Tris-buffered saline	TBS 10x	Sigma Aldrich
Tween® 20 detergent	Tween	Sigma Aldrich
Milk	-	Sigma Aldrich
Recombinant Anti-LRP1 antibody	1º LRP-1	Abcam
Glut1 Antibody	1º GLUT1	Novus biologicals
GADPH Mouse McAb	1º GADPH	Protein Tech
Goat anti-Rabbit IgG (H+L) Secondary Antibody, DyLight™ 800 4x PEG	Anti-Rabbit	Invitrogen
Goat anti-Mouse IgG (H+L) Secondary Antibody, DyLight™ 800 4x PEG	Anti-Mouse	Invitrogen
3-(4,5-Dimethylthiazol-2-yl)-2,5-Diphenyltetrazolium Bromide	MTT	Thermo Fisher
Dimethyl sulfoxide	DMSO	Fisher Scientific
Hoechst 34580	Hoechst	Fisher Scientific
Fluorescein isothiocyanate labelled lectin from *Lycopersicon esculentum*	FTIC-lectin	Sigma Aldrich
Paraformaldehyde	PFA	Sigma Aldrich
Recombinant heparinase I	Hep-I	R&D Systems
Recombinant heparinase II	Hep-II	R&D Systems
Recombinant heparinase III	Hep-III	R&D Systems
ELISA KIT for Low Density Lipoprotein Receptor Related Protein 1 (LRP-1)	-	Cloud-Clone Corp.

The following solutions were made in house.

1.5M Tris-HCl-8.8 (150 mL) - Tris (27.23 g) was dissolved in dH_2O (80 mL). The pH was adjusted to 8.8 with 6M HCl, then dH_2O was added to reach the final volume (150 mL).

0.5M Tris-HCl-6.8 (100 mL) - Tris (6.00 g) was dissolved in dH_2O (60 mL). The pH was adjusted to 6.87 with 6M HCl, then dH_2O was added to reach the final volume (100 mL).

TBST (1000 mL) - TBS 10x (100 mL) and Tween (1 mL) was added to dH_2O (900 mL) and stirred for 30 min.

Ligand-decorated nanoparticles used in this chapter were described tables 2.6 and 2.7 and discussed as sets of nanoparticles for ease. In brief, the Ctrl set includes the nanoparticle formulations where $N_{Ligand} = 0$ (AP2 or Gluc), the AP2_1, AP2_0.70 and AP2_0.16 sets house AP2-decorated nanoparticle formulations (where $\delta_L = 1$, 0.70 and 0.16 respectively), and Gluc_1 set described the Gluc-decorated nanoparticle formulations (where $\delta_L = 1$).

3.2.2 Cell Culture

bEnd3, C8-D1A and T98G cells were stored in 90:10 FBS:DMSO in a liquid nitrogen vapour container until required. Cells were thawed by removing them from the liquid nitrogen vapour storage and gently agitated in a 37 ^oC water bath for 1-2 min. Cells were then transferred to a T75 flask with media (10 mL), pre-warmed in a 37 ^oC water bath, and incubated at 37 ^oC for 24 hours. Media chosen for defrosting, and for all subsequent experiments, was as follows:

Table 3.2 Media used for cell culture and subsequent experiments on each cell line

CELL LINE	MEDIA	SUPPLIMENT
bEnd3	DMEM	10% (v/v) FBS 1% (v/v) PS
C8-D1A	DMEM	10% (v/v) FBS 1% (v/v) PS
T98G	EMEM	10% (v/v) FBS 1% (v/v) PS

After 24 hours, cells were treated by media removal, dPBS (5 mL) wash, and new media (10 mL) addition. Cells were then maintained and kept incubated at 37 ^{o}C. Every 2-3 days, the cells were fed by old media removal, dPBS (5 mL) wash, and new media (10 mL) addition.

Cell subculture was routinely performed when cell confluency (percentage of adhered cells on the surface of the T75 flask) reached >80%. Confluency was monitored daily using an optical microscope. All reagents required for subculture were first warmed using a water bath set at 37 ^{o}C for 30 min. Upon reaching optimum cell confluency, the culture media was removed, the cells were washed with dPBS (5 mL) and then the cells were incubated with TRYP (3 mL) at 37 ^{o}C for 3 min. Trypsin is a proteolytic enzyme that breaks down the proteins that enable cells to adhere to the flask surface.[190] The flask was then inspected under an optical microscope to see if full detachment of all cells was obtained, and then fresh media (7 mL) was then added to deactivate trypsin. Trypsin deactivation was required after cell detachment as ongoing proteolysis could lead to cell damage. The cell suspension was transferred to a 15 mL falcon tube and centrifuged at 1200 RPM for 5 min, then the supernatant was discarded to obtain a cell pellet. The cell pellet was then resuspended in 2 mL of media, and 10 µL

of this suspension was added to 10 µL of Trypan blue for cell counting using a Bio-Rad Automated Cell Counter.

Depending on which assay followed, different cellular concentrations were plated:
[1] Cells (1×10^6 cells, 1 mL media) were subcultured in T75 flasks with fresh media (14 mL) for further experiments. The passages number were registered indicating the number of times the cells have been subcultured.
[2] Cells (1×10^6 cells, 1 mL media) were transferred into 1 mL Eppendorf tubes, centrifuged at 1200 RPM for 5 min, and supernatant was discarded. The pellet was washed via resuspension in dPBS (1 mL), centrifugation at 1200 RPM for 5 min and subsequent supernatant removal. The washed pellet, containing 1×10^6 cells, was stored in a Mr. Frosty™ freezing container at -80C.
[3] Cells were seeded into either clear or black 96 well plates (1×10^4cells, 100 µL media per well), clear 12 well plates (5×10^4 cells, 1 mL media per well) or clear 6 well plates (1×10^6 cells, 2 mL media) for future experiments. For all future experiments, bEnd3, C8-D1A and T98G cells were used from passage 26-30, passage 2-7 and passage 3-11 respectively. A narrow passage range for each cell line was chosen as a cell line's characteristics is affected over time.[191]

3.2.3 Cell viability assay after nanoparticle incubation

Cell metabolic activity (for bEnd3, C8-D1A and T98G) was determined after nanoparticle incubation using the MTT assay to investigate the cytotoxicity of the nanoparticles. For drug delivery, the nanoparticles should not be cytotoxic to the target cells. The assay is based on metabolic activity of the cells by the reduction of MTT to formazan by the NADPH-dependent oxidoreductase enzymes present in viable cells. The formazan crystals can then be dissolved adding 100uL of

DMSO and the absorption of the resulting solution is measured at 570 nm using a plate reader. A MTT assay looking at the cytotoxicity of a nanoparticle formulation is described as follows. Cells (1×10^4cells in 100 µL media) were seeded on a clear 96 well plate, as described in 3.2.2, and incubated at 37 ^{o}C for 24 hours. Media was aspirated out of the cells and a nanoparticle formulation (20 µM in 100 µL media) was added to the cells and incubated at 37 ^{o}C for 1 hour, the timeframe used in previous binding studies.[21] After 1 hour, nanoparticles were removed from the cells, an MTT solution (0.5 mg mL^{-1} MTT in 100 µL in media) was added to each well and the cells were further incubated for a further 2 hours. The MTT solutions were then carefully removed from the cells and DMSO (100 µL) was added to each well to dissolve the formed formazan crystals. The absorbance of the wells was then read at 570 nm. Cell viability was then calculated using the following:

$$Cell\ viability\ (\%) = \frac{A_n}{A_m} \times 100 \tag{20}$$

where A_n and A_m were the absorbances from nanoparticle treated wells and negative control (media only) treated wells respectively. The MTT assay was done in duplicate and 3 individual times (n=3) per cell line, with each individual time using a different passage number for the cell line.

3.2.4 Protein extraction and lysate preparation

Protein extraction from bEnd3, C8-D1A and T98G cells was done by cell lysis (the breaking down of the cell membrane) to produce lysates (fluids containing the contents from cell lysis). An example of the production of a bEnd3 lysate is described as follows. RIPA (98 µL) and PI (2 µL) were added to bEnd3 cell pellets

– obtained from 3.2.2 – and incubated in ice for 30 min. RIPA induces efficient cell lysis and the solubilisation of the proteins of the cells. PI was used to prevent proteolysis of the proteins. After incubation, the sample was slowly passed through a small needle 5 times via a 1 mL syringe to aid cell lysis. The sample was then centrifuged at 13300 RPM for 20 min at 4 ^{o}C, and the supernatant, hence the bEnd3 lysate, was retained. C8-D1A and T98G lysates were obtained following the exact method described above using C8-D1A and T98G cell pellets.

Protein quantification of each lysate was obtained using the Coomassie® Brilliant Blue G-250 dye included in the Bio-Rad protein assay kit. Coomassie® Brilliant Blue G-250 binds onto basic amino acids in proteins which produces a protein-dye complex with a maximum absorbance at 595 nm. An example of the quantification of a bEnd3 lysate is described as follows. bEnd3 lysate (2 µL) was added to water (48 µL), and 10 µL of the solution was added to a 96 well plate. The Bradford assay reagent (200 µL), formulated as per the manufacturer's instructions, was added to each well and left for 5 min. The absorbance of the well was then read at 595 nm. Total protein content of the lysate was calculated using a BSA calibration curve (from 0.250-0.004 mg mL^{-1}). Quantification of protein content per lysate was done in triplicate.

3.2.5 Protein expression

Protein expression of LRP-1 and GLUT1 for bEnd3, C8-D1A and T98G was assessed by the western blot assay to compare the LRP-1 and GLUT1 receptor densities of each cell line. For the western blot assay, the following steps were done in sequence:

3.2.5.1 Lysate preparation

Lysates were prepared by adding 25 µL of a laemmli solution (9:1 Laemmli 4x Concentrate: 2-mercaptoethanol) to 100 µL of each lysate and heated for 5 min at 95 ^{o}C. The laemmli 4x concentrate solution contains glycerol, LDS, and bromophenol blue. The laemmli solution was added to denature and unfold the proteins – LDS disturbed the hydrogen bonds, hydrophobic interaction, and ionic interactions within the proteins, whereas 2-mercaptoethanol cleaved the disulphide bonds – and the sample was heated to allow LDS to bind onto the protein giving the protein a net negative charge, allowing their separation by molecular weight when performing sodium dodecyl sulphate–polyacrylamide gel electrophoresis (SDS-PAGE).

3.2.5.2 SDS-PAGE polyacrylamide gel casting

The polyacrylamide gel required for SDS-PAGE was cast in-house 24 hours prior to SDS-PAGE. The gel was made following a previously published protocol.[192] The gel for SDS-PAGE consisted of two sections, the stacking gel (where the sample will be loaded) and the resolving gel (where proteins will be separated based on molecular weight). The stacking gel was made by mixing 30% Acrylamide/bis (1.98 mL), 0.5M Tris-HCl-6.8 (3.78 mL, pH 6.8), 10% SDS (150 µL), dH_2O (9 mL) and 10% APS (75 µL), whereas the resolving gel was made by mixing 30% Acrylamide/bis (6 mL), 1.5M Tris-HCl-8.8 (3.75 mL, pH 8.8), 10% SDS (150 µL), dH_2O (5.03 mL), and 10% APS (75 µL). To cast the gel for SDS-PAGE, TEMED (7.5 µL) was added to the resolving gel and the resulting resolving gel mixture was poured into the cast and left for 60 minutes. TEMED and APS were used as free radical catalysts for the free radical polymerisation between acrylamide and bis-acrylamide: APS was used as the free radical initiator and

TEMED accelerated the rate of free radical formation from APS. Bis-acrylamide was used during the polymerisation as a cross-linker of the polymer chains. After the resolving gel had set, a comb was placed on top of the gel, TEMED (15 µL) was added to the stacking gel and the resulting stacking gel poured onto the comb and left for 60 minutes again for the polymerisation of acrylamide and bis-acrylamide in the stacking gel to occur. Once the gel had set, the comb was removed creating wells in the gel for samples to be loaded for SDS-PAGE. The gel was stored at 4 ^{o}C until required.

3.2.5.3 SDS-PAGE

An electrophoresis setup was then established using the in-house cast polyacrylamide gels with the running buffer - 25 mM Tris base, 190 mM glycine, 0.1% SDS, pH-adjusted to 8.3 using HCl. Lysates (20 µg total protein) of each cell line (bEnd3, C8-D1A and T98G) were loaded into the stacking gel wells. A precision plus protein dual colour standard (2 µL) was also added into a stacking gel well as a ladder to give a scale for the molecular weight of proteins. The glycerol present in the prepared lysates increased the density of the samples so that the sample fell to the bottom of the wells, and the bromophenol blue helped visualise the samples within the wells.

Electrophoresis was performed to separate proteins based on molecular weight. After loading the samples into the gel, electrophoresis was performed at 80 V for 30 min, then 120 V for an additional 90 min. During electrophoresis, an electric field is produced, and the negatively charged denatured proteins move down the gel towards the positive electrode. During the initial 30 min at 80 V, the samples move down the stacking gel, which was at a pH of 6.8: at this pH, glycine from

the running buffer held a neutral charge and moved down the gel slowly, whereas chloride ions moved quickly down the gel, consequently trapping all the proteins between the two and concentrating the proteins into a narrow band on the gel. During the 90 min at 120 V, samples moved down the resolving gel, which was at a pH of 8.8: at this pH, glycine from the running buffer now held a negative charge and migrate faster than the proteins, hence separating the proteins, with smaller proteins running down the gel faster than larger proteins due to being able to pass through the pores within the polyacrylamide gel more easily. The bromophenol blue ran the fastest due to its small size, thus the electrophoresis could be monitored and stopped before the bromophenol blue reached the bottom of the gel.

3.2.5.4 Protein transfer

Once the proteins from each cell lysate were separated based on molecular weight, electrophoretic transfer was conducted to move the proteins from the gel to an Immun-Blot® polyvinylidene fluoride (PVDF) membrane. Protein transfer was necessary to make proteins accessible to antibody detection on a membrane. The protein-containing gel was stacked on top of the membrane and placed in an electrophoretic chamber with the membrane towards the positive electrode side and the chamber was filled with the transfer buffer - 25 mM Tris base, 190 mM glycine, 20% methanol and pH-adjusted to 8.3 using HCl. Electrophoretic transfer was then conducted at 50 V for 30 min, then 100 V for 2 hours to allow the proteins to move from the gel to the membrane, following the same principle that the negatively charged proteins move towards the positive electrode. To confirm that the proteins have been transferred successfully, the membranes were stained with Ponceau S for 1 min. Ponceau S rapidly and

reversibly binds to both the positively charged and non-polar regions of proteins, evidenced by red bands on the membrane. The membranes were further washed with dH2O to remove the excess of ponceau.

3.2.5.5 Blocking

After protein transfer onto the membrane, the membrane was incubated and slowly agitating in 5% milk in TBST for 1 hour. Incubation in milk was the process of blocking: proteins in the milk bind onto the membrane where the target proteins from the protein transfer have not attached, reducing the chances for antibodies to bind onto the membrane non-specifically during the next step during antibody incubation.

3.2.5.6 Antibody incubation

Once the membrane containing the transferred proteins from the lysates of bEnd3, C8-D1A and T98G from SDS-PAGE has been blocked, the membrane could then be incubated with antibodies to first quantify the expression of either LRP-1 or GLUT1, then GADPH. GADPH expression was quantified as the GADPH protein is expressed highly in almost all tissues and was used for protein normalisation (i.e., to obtain LRP-1/GADPH or GLUT1/GADPH for each cell line).[193] Antibody incubation for quantifying LRP-1 followed by GADPH expression is described as follows. After blocking, the membrane was incubated with the LRP-1 primary (1^{o}) antibody, 1^{o}-LRP-1 (2 µL), in 1% milk in TBST (10 mL) and gently agitated for 12 hours at 4 ^{o}C. A rabbit monoclonal antibody for LRP-1 was chosen as it binds to both mouse LRP-1 (in bEnd3 and C8-D1A) and human LRP-1 (in T98G) on the membrane. After 1^{o}-LRP-1 incubation, the membrane was washed with TBST buffer 3 times and incubated with a secondary

(2º) antibody, goat anti-Rabbit (1 µL) in 1% milk in TBST (10 mL) and incubated for 2 hours at room temperature. anti-Rabbit was used to bind onto the bound 1º-LRP-1 on the membrane, as the host species used to produce 1º-LRP-1 was a rabbit. The membrane was then washed again 3 times and then imaged using an Odyssey CLx imager. The imager scans at an excitation wavelength of 783 nm and emission wavelength of 797 nm, corresponding to the DyLight™ 800 conjugated onto the anti-Rabbit antibody. The bands corresponding to the LRP-1 protein was then found on the image, and the intensity of the band was obtained using FiJi, with the intensity of the band corresponding to its expression. After LRP-1 expression, the membrane was washed with TBST buffer 3 times and then incubated with the GADPH 1º antibody, 1º-GADPH (2 µL) in 1% milk in TBST (10 mL) and gently agitated for 2 hours at room temperature. 1º-GADPH was used as it binds to both mouse and human GADPH. After incubation, the membrane was washed again with TBST buffer 3 times and incubated with the 2º antibody, anti-Mouse (1 µL) in 1% milk in TBST (10 mL), incubated for 2 hours, washed again and then imaged. anti-Mouse was used as host species of 1º GADPH was a mouse, and was conjugated to DyLight™ 800, akin to that of anti-Rabbit thus could be seen using the same Odyssey CLx imager.

Antibody incubation to quantify GLUT1 followed by GADPH expression follows the same procedure as above, but using the GLUT1 1º antibody, 1º-GLUT1 (which can bind to both mouse and human GLUT1) and anti-Rabbit (as the host species of 1º-GLUT1 is a rabbit)

3.2.6 Binding assays

Binding assays were performed on bEnd3, C8-D1A and T98G cells using previously synthesised PEG-PCL nanoparticles from chapter 2. A binding assay looking at the how many nanoparticles of different formulations bound on cells is described as follows. Cells (bEnd3, C8-D1A or T98G) were seeded on a black 96 well plate (1×10^4cells with 100 µL media per well) and incubated at humified chamber at 37 ^{o}C for 12 hours. Media was then removed and nanoparticle formulations (20 µM, 100 µL in media) were added to the cells and incubated at 37 ^{o}C for 1 hour. After incubation, the nanoparticle formulations were carefully aspirated out and transferred to a separate black 96 well plate. The concentration of the nanoparticle formulations after cell incubation was calculated via fluorescence measurements. The fluorescence was read using a TECAN Spark® microplate reader, using an excitation wavelength of 750 nm and emission wavelength of 779 nm corresponding to the excitation and emission wavelengths for the Cy7 fluorophore that was tagged on all synthesised PEG-PCL nanoparticles described in 2.3.4 and 2.3.5. Percentage of nanoparticles bound (NB%) onto the bEnd3 cells was then calculated using:

$$NB\% = 100 - \left(\frac{[NP]_R}{[NP]_0} \times 100\right) \quad (21)$$

where $[NP]_0$ and $[NP]_R$ were the concentrations of the nanoparticle solution initially added to the cells (20 uM) and the concentration of the nanoparticle solution aspirated out of the wells after 1 hour incubation in cells. The nanoparticle concentration to add to cells was chosen to match the same concentration that had previously been used for PMPC-PDPA nanoparticles in cell binding studies within the Battaglia group.[21] Only one concentration was

chosen for this preliminary study; however, as superselectivity also depends on the concentration of nanoparticles administered to the cells (see equation (5) from the theory of superselectivity), future studies could be done using concentration as a variable. $[NP]_R$ was calculated using a calibration curve of the nanoparticle formulation (varying between 0.31 - 40.00 uM in 100 uL media). The gain – the amplification of the fluorescence readings – for the analysis was set at a constant 108 for all binding assays, obtained when creating a calibration curve of the nanoparticle solutions. NB (%) was then converted to the number of nanoparticles bound per cell by:

$$\frac{NPs}{cell} = \frac{NB\% \times n(NPs) \times \frac{N_A}{N_{agg}}}{\#(cells)} \tag{22}$$

where $n(NPs)$ is the number of mols of the nanoparticle solution incubated on the cells, N_A is Avogadro's number, N_{agg} is the number of aggregation for the nanoparticles and $\#(cells)$ is the number of cells initially seeded for the binding study. For all calculations, $n(NPs) = 2 \times 10^{-9}$, $N_{agg} = 395$ (estimated in chapter 2) and $\#(cells) = 10{,}000$.

The currently described method was established from previous experiments, where calculation of the nanoparticles bound was calculated instead by measuring the fluorescence of the wells with the nanoparticle-treated cells within (hence measuring the concentration of nanoparticles left in the well after aspiration of the nanoparticle solutions), herein described as the initial method. The results from the initial method showed very few nanoparticles and when compared with the newer method described above (herein dubbed revised

binding method, where the concentration of nanoparticles bound was calculated from the aspirated nanoparticle solution), there was a significant difference in the number of nanoparticles bound for both binding methods. The difference in the methods can be seen in fig A.27. Therefore the revised binding method was then used.

3.2.7 Lectin assay

A lectin assay was performed on bEnd3, C8-D1A and T98G cells to determine the glycocalyx concentration of each cell line. Cells (bEnd3, C8-D1A or T98G) were seeded on a 12 well plate (5×10^4 cells in 1 mL media per well) as described in 3.2.2 and incubated at 37 ^{o}C in humified chamber overnight. Media was then removed, and FTIC-lectin diluted in dPBS (1 mL) was added to the cells at different concentrations (0 – 10 ug/mL) and incubated at 37 ^{o}C for 30 min. Lectin binds onto N-acetyglucosamine (GlcNAc) present on the glycocalyx of cells, and the FTIC was used as a fluorescent tag to monitor how much lectin was bound on the cells. After 30 minutes, cells were washed with dPBS twice and left in dPBS (1 mL). A cell scrapper was used to remove the cells from surface of the wells. The cells were then centrifuged at 1200 RPM and the cell pellet was resuspended in 2% PFA in dPBS. PFA was used to fix the cells and preserve the cell structure. The bind specificity of the FTIC-labelled lectin in the cells was assessed by Flow Cytometry.

3.2.8 Glycocalyx shedding

The glycocalyx of bEnd3 cells was shed by incubation with a heparinase cocktail, consisting of heparinase I, II and III. Heparinases are enzymes that cleave heparin sulfate chains in the glycocalyx, thus decreasing the glycocalyx content.

A major component of the glycocalyx is heparan sulphate, and its more sulphated form heparin. Heparinase I recognises more sulphated regions of the glycocalyx and has a greater activity to heparin, heparinase II digests both heparin and heparan sulphate, and heparinase III is more active on heparan sulphate.

3.2.8.1 Glycocalyx-shed binding assay and lectin assay

A binding assay and lectin assay were done on glycocalyx-shed bEnd3 cells. The protocols for the binding assay and lectin assay follow the same protocols found in 3.2.5 and 3.2.6 with a prior additional step. bEnd3 cells were first subjected to the heparinase cocktail (0.03 ug/mL for each of Hep I, Hep II and Hep III in dPBS, 100 µL) and incubated at 37 ^{o}C for 2 hours. After incubation, the supernatant was retained and stored at -80 ^{o}C for future ELISA experiments, and the cells were washed twice with dPBS. The binding protocol (described in 3.2.5) and lectin assay (described in 3.2.6) were then conducted on the hep-treated cells.

3.2.8.2 Glycocalyx-shed western blot

A western blot of glycocalyx-shed bEnd3 cells was done to investigate LRP-1 expression after glycocalyx shedding. bEnd3 cells were first seeded in a clear 6 well plate (1×10^6 cells, 1 mL media per well) and incubated at 37 ^{o}C overnight. Media was then replaced with the heparinase cocktail (0.03 ug/mL for each of Hep I, Hep II and Hep III in dPBS, 1 mL) and incubated at 37 ^{o}C for 2 hours. The heparinase cocktail was removed, the cells were washed twice with dPBS, and then RIPA (90 µL) and PI (10 µL) were added to the cells and scratched with a cell scrapper. The resulting solution was then passed through a small needle 5 times via a 1 mL syringe to aid cell lysis, centrifuged at 13300 RPM for 20 min at 4 ^{o}C, and then the supernatant, hence the hep-treated bEnd3 lysate, was retained

and the protein content quantified (as described in 3.2.4). The western blot protocol was then followed as described in 3.2.5.

3.2.8.3 LRP-1 ELISA post- glycocalyx-shedding

The supernatant from 3.2.7.1 was analysed by ELISA to determine if there was any LRP-1 protein floating in the supernatant post- glycocalyx shedding. The supernatant retained after glycocalyx-shedding was first diluted in a dilution of 1:5 to create samples for the ELISA kit for Low Density Lipoprotein Receptor Related Protein 1 (LRP-1) from Cloud-Clone Corp. The ELISA kit from Cloud-Clone Corp incorporates the use of a sandwich enzyme immunoassay: the plate provided is coated with a capture antibody for free LRP-1. Upon complexation with free LRP-1, an additional labelled-antibody is added to bind onto a different location on the LRP-1. A substrate is then added to react with the labelled antibody, and then a further chemical reaction is done to create a reaction product that can be quantified by a microplate reader.

A brief description of the ELISA protocol is as follows. Supernatants (2 μL) following the glycocalyx-shedding of bEnd3 cells from 3.2.7.1 was first diluted with dPBS (98 μL). The diluted supernatants were then added to the pre-coated 96-well strip plate, alongside diluted standards, and blanks from the kit, and incubated for 2 hours at 37 ^{o}C. The solutions were then removed from each well, and 100 uL of the provided detection reagent A working solution was added to each well, and the plate was incubated a further 1 hour at 37 ^{o}C. The solutions were aspirated from each well and washed with 350 uL of the provided wash solution, followed by an addition of 100 uL of detection reagent B and subsequent incubation for 30 min at 37 ^{o}C. The plate was aspirated and then washed a further

5 times. The substrate solution (90 uL) was then added to each well, incubated for 10-20 min at 37 ^{o}C protected from light. The stop solution (50 uL) was then added to each well, and then immediate run at the microplate reader set at 450 nm. The absorbance given from the sample wells was then cross-referenced with a standard calibration curve and the concentration of free LRP-1 in the supernatants was calculated.

3.2.9 Statistical analysis

The results are shown either as the mean ± standard deviation (SD) or as the mean ± standard error of the mean (SEM). Statistical analyses were obtained using unpaired t-tests, one-way ANOVA tests (with a post hoc Tukey's multiple comparison test) or two-way ANOVA tests (with either a post hoc Tukey's multiple comparison test for comparison between data sets or a post hoc Dunnett's multiple comparison test for comparison of data sets to a control). In all subsequent figures, n refers to the number of independent experiments performed (i.e., n = 3 denotes 3 independent experiments were conducted)

3.3 Results and Discussion

3.3.1 Evaluation of cell toxicity of nanoparticles on bEnd3, C8-D1A and T98G

Prior to any *in vitro* binding studies being done, the cell toxicity of the synthesised ligand-decorated PEG-PCL nanoparticles to be used was investigated by an MTT assay. Formulations should not induce side effects of cytotoxic effects to the target cells which could alter the physical characterisations of the cells (i.e., their receptor density) as these characterisations should be maintained constant during cell studies. Previous reports have already assessed that PEG-PCL nanoparticles have had non-toxic effects have towards several cell lines, e.g., brain capillary endothelial cells (BCEC) and glioblastoma (U87 MG);[167] however, it is important to still determine whether the synthesised PEG-PCL nanoparticles will also exhibit non-toxic effects to the chosen cell lines for this project.

bEnd3, C8-D1A and T98G were incubated for 1 hour with different AP2- and gluc-decorated PEG-PCL nanoparticle formulations (Ctrl_3, AP2_1_40, AP2_0.70_40, AP2_0.16_40, Gluc_1_197) to test if there was any cytotoxic material leftover from the synthesis of PCL50 or Cy7_PEG20 (i.e., $CuSO_4 \cdot 5H_2O$, which has been shown to have a cytotoxic effect on multiple cell lines, such as the human adrenocortical carcinoma cell line[194]) and from the self-assembly process (i.e., $CHCl_3$, which has been shown to be cytotoxic to multiple cell lines, such as A-549[195]). Gluc_1_50, AP2_1_10, AP2_0.70_10 and AP2_0.16_10 samples were chosen to test the cytotoxicity of the synthesised ligand-conjugated copolymers as they had the largest mol concentration of Gluc_PEG113, AP2_PEG113, AP2_PEG68 and AP2_PEG8 respectively: if there is no significant difference between these nanoparticle samples to the media negative

control, it will be assumed that there will be no significant difference of nanoparticles with lower molar concentrations of the ligand-conjugated copolymers.

The cell viabilities of bEnd3, C8-D1A and T98G after incubation with the above chosen nanoparticle formulations are presented in figure in Fig 3.1. We observed no significant difference in the cytotoxicity of the nanoparticle formulations when compared to the untreated cells (two-way ANOVA (Cell Line): ns $P > 0.05$, two-way ANOVA (Formulation): ns $P > 0.05$) on all three cell lines, indicating that the addition of ligand-decorated polymers to the nanoparticle had no effect on the cytotoxicity. A sample is deemed toxic for *in vitro* studies if cell viability is reduced to <70%:[196] the mean viability of the cells after nanoparticle incubation was >80%, indicating no cytotoxic effects to the cells *in vitro* were found and that *in vitro* assays can performed using the nanoparticles without worry of cell death.

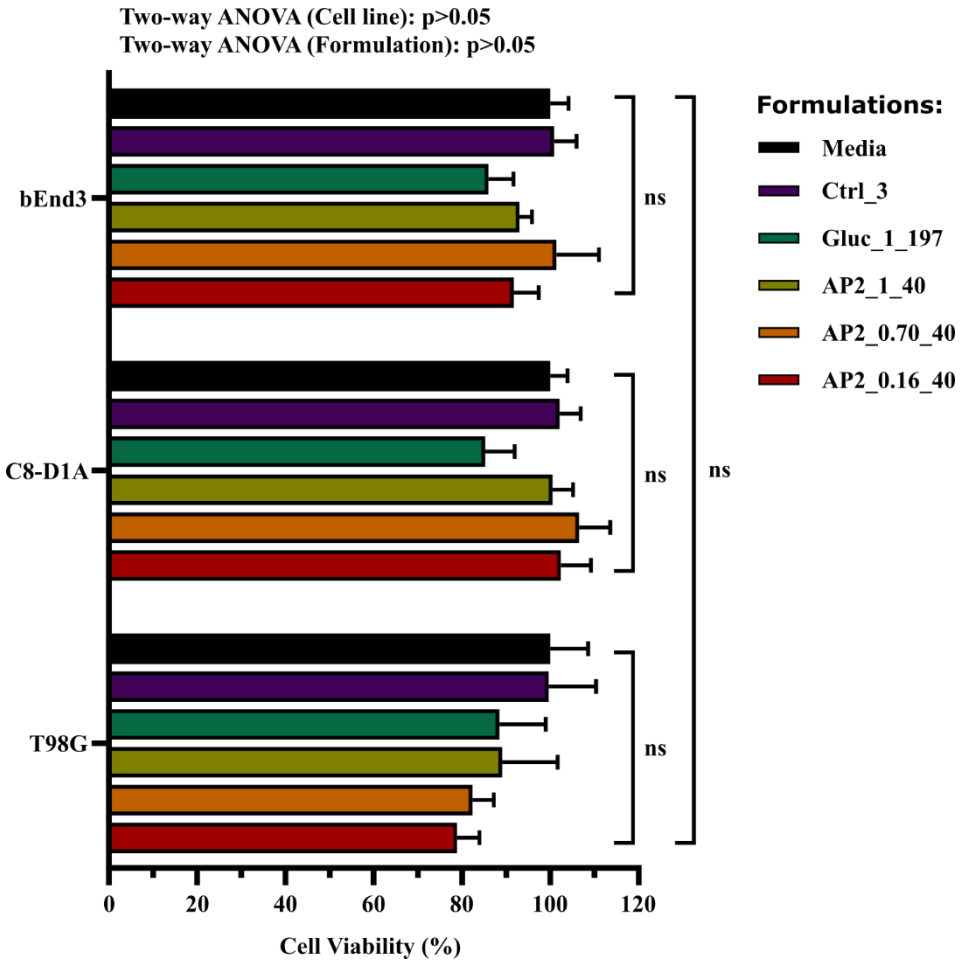

Fig 3.1 **Cell viability assessed by MTT Assay in bEnd3, C8-D1A and T98G treated with PEG-PCL nanoparticles.** Cells were incubated with 5 nanoparticle formulations (Ctrl_3, Gluc_1_197, AP2_1_40, AP2_0.70_40, AP2_0.16_40) at 20 μM concentration for 1 hour and the cell viability was obtained by the MTT assay. Two-way ANOVA was used for the statistical analysis (ns: $P > 0.05$ between the cell lines, ns: $P > 0.05$ between the formulation,) alongside a post hoc Dunnett's multiple comparison test (ns: $P > 0.05$ for all formulations when compared to Ctrl_3). Each bar represents the mean ± SEM (n=3).

3.3.2 LRP-1 and Glut1 expression of bEnd3, C8-D1A and T98G

Having established beyond a reasonable doubt that the ligand-decorated PEG-PCL nanoparticles do not present cytotoxic effects to the bEnd3, C8-D1A and T98G, the receptor expression for each cell was investigated by western blot. The number of receptors ($N_{Recepetor}$) was described an important factor for targeting;[12,21,27] therefore, investigating the LRP-1 and GLUT1 receptor expression for each cell line will give us an estimate to the difference in $N_{receptor}$ between the three cell lines.

Firstly, we characterize the relative expression of LRP-1 for each of cell line, bEnd3, C8-D1A or T98G. The western blot to test for LRP-1 expression was done with lysates of each cell line on the same blot to compare the differences in relative LRP-1 expression, hence receptor density, between each cell line. A graph plotting the intensity of the LRP-1 band normalised with the intensity of the corresponding GADPH band (i.e., LRP-1/GADPH intensity), and the corresponding blot for LRP-1 protein band (at 85 kDa) and GADPH (at 37 kDa) are shown in fig 3.2A and fig 3.2B respectively. LRP-1 expression was found to be the higher in C8-D1A compared to bEnd3 and T98G whilst there was no difference between bEnd3 and T98G (post-hoc Tukey's multiple comparison: **** $P \leq 0.0001$, ns $P > 0.05$). The results therefore indicate that when looking at receptor density between the three cell lines, relatively C8-D1A has a higher LRP-1 receptor density than both bEnd3 and T98G.

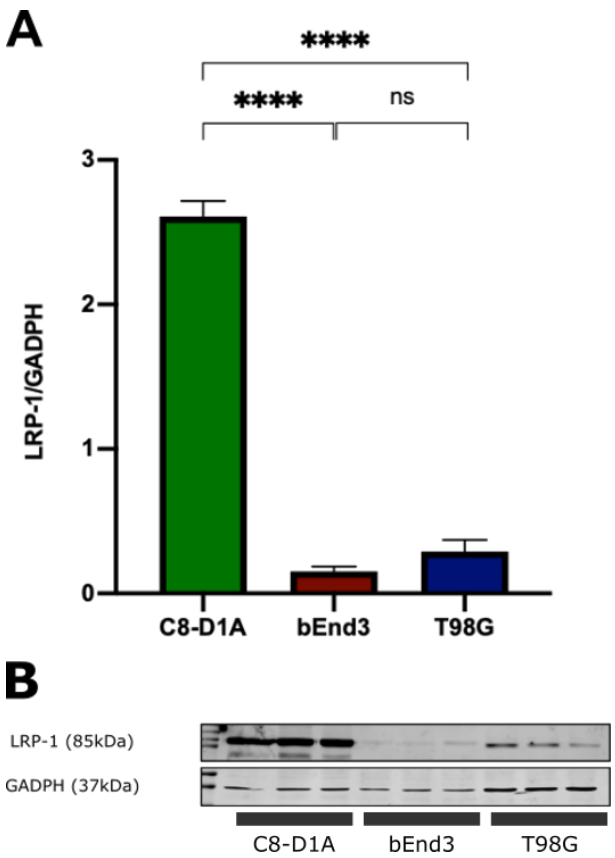

Fig 3.2 **LRP-1 expression in C8-D1A, bEnd3 and T98G by western blot.** (A) Relative expression of LRP-1 in all three cell lines determined by densitometry analysis relative to GAPDH. One-way ANOVA was used for the statistical analysis alongside a post hoc Tukey's multiple comparison test (**** $P \leq 0.0001$; ns $P > 0.05$). Each bar represents the mean ± SD (n=3). (B) Immunoblotting for the expression of LRP-1 and GAPDH (loading control) in the three cell lines. Intensity of the bands are calculated using imaging software (Fiji) and the intensity for LRP-1 was normalised to the intensity of GADPH to get the relative LRP-1 expression for the cell lines.

A second western blot analysed GLUT1 and GADPH expression on the three cell lines. As shown in Fig. 3.3a, GLUT1 receptor expression is distinctly expressed between the three cell lines (post-hoc Tukey's multiple comparison: **** $P \leq 0.0001$, ** $P \leq 0.001$, * $P \leq 0.05$). Notably, T98G cell line presents a lower relative expression of GLUT1 as compared to C8-D1A and bEnd3 as shown in Fig. 3.3b, while bEnd3 expressed higher expression compared to C8-D1A. The implication of these results is that all three cell lines have significantly different GLUT1 receptor densities, thus we hypothesise that selective targeting can be achieved between the cell lines.

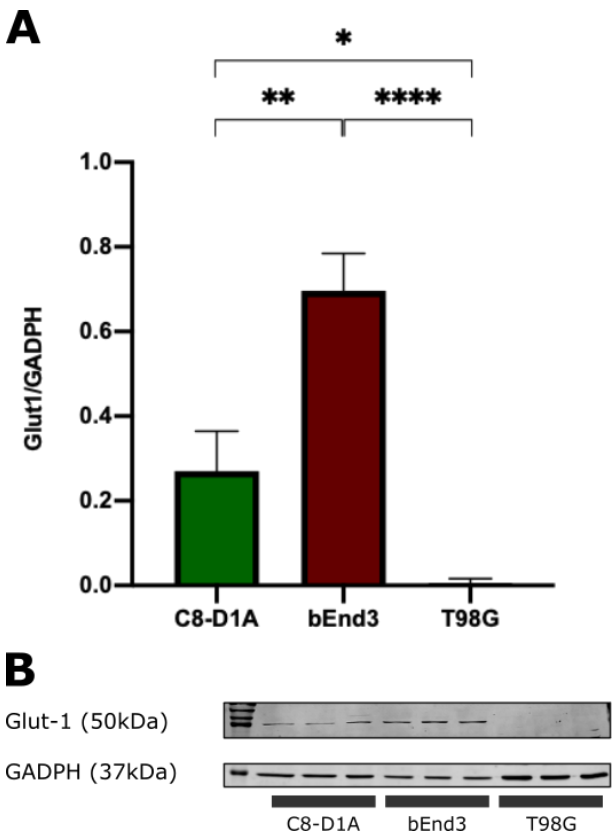

Fig 3.3 **GLUT1 expression in C8-D1A, bEnd3 and T98G by western blot.** (A) Relative expression of GLUT1 in all three cell lines determined by densitometry analysis relative to GAPDH. One-way ANOVA was used for the statistical analysis alongside a post hoc Tukey's multiple comparison test (**** $P \leq 0.0001$; ** $P \leq 0.001$; * $P \leq 0.05$). Each bar represents the mean ± SD (n=3). (B) Immunoblotting for the expression of GLUT1 and GAPDH (loading control) in the three cell lines. Intensity of the bands are calculated using imaging software (Fiji) and the intensity for GLUT1 was normalised to the intensity of GADPH to get the relative GLUT1 expression for the cell lines

The combination of the results of fig 3.2 and fig 3.3 indicate that the cells differ in receptor density profile. Indeed, bEnd3 and T98G are shown to have relatively similar LRP-1 receptor profile; nevertheless, they both express a significantly different receptor density for Glut1. Using the findings of the above results, a schematic was drawn up of the three cell lines in fig 3.4, showing the cell phenotype incorporating only 2 receptor types LRP-1 and Glut1. Indeed, we have previously said that phenotype incorporates the receptor density of multiple receptor types - in fact, bEnd3, C8-D1A and T98G do not only express LRP-1 and Glut1, but express multiple other receptors; however, as we are only testing binding to LRP-1 and Glut1 receptors, using AP2 or Glucose respectively, we first

looked at binding to the cell phenotypes based only on two receptors. Future work should therefore look at alternative ligand-receptor binding pairs and incorporate the pairs in future phenotypic targeting studies.

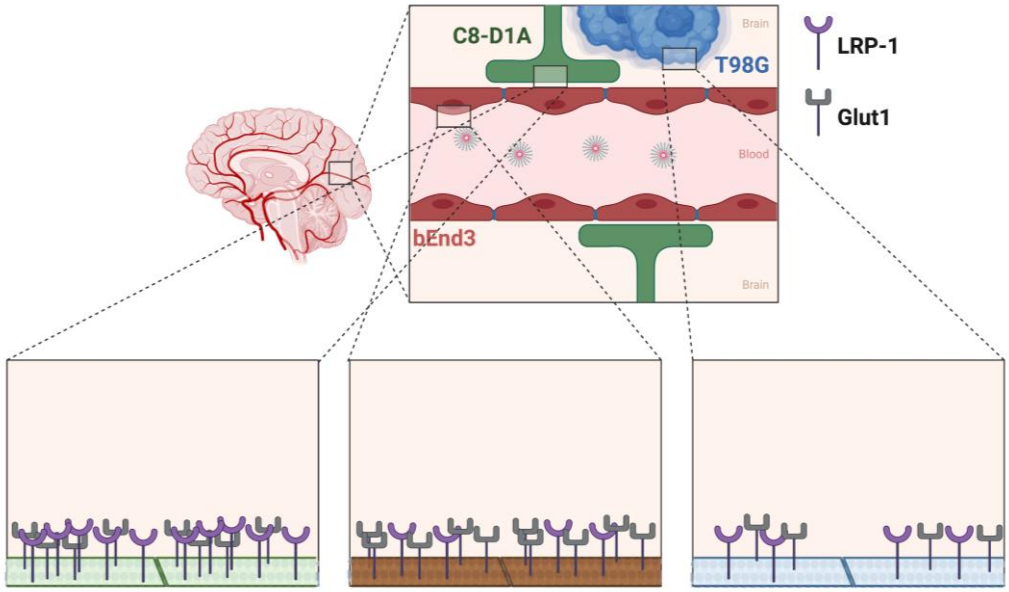

Fig 3.4 **Schematic of the three cell line phenotypes.** The three cell lines, C8-D1A (in green), bEnd3 (in red) and T98G (in blue), and their phenotypes (based only on LRP-1 and Glut1) are depicted here. LRP-1 (purple circle receptors) receptor density was highest for C8-D1A and the same for bEnd3 and T98G. Glut1 (Green square receptors) receptor density was highest for bEnd3 and lowest for T98G, with C8-D1A having a density between the two cell lines.

3.3.3 Optimising binding towards bEnd3

Binding studies were next performed using the synthesised ligand-conjugated nanoparticles in chapter 2 to first investigate the influence of N_{Ligand}, δ_L and type of ligand on binding. An investigation of the influence of the three variables will allow us to optimise binding to bEnd3 prior to ascertaining if we can selectively target bEnd3 without targeting C8-D1A and T98G. To assess the influence of the variables, binding profiles were obtained between nanoparticles and target cells. Herein, we describe a "binding profile" as a profile investigating the effect that the number of ligands (N_{Ligand}) that ligand-decorated nanoparticles have to the

binding of the nanoparticles to specific receptors expressed in target cells, keeping δ_L and the type of ligand constant.

Initially, binding profiles using the AP2_1 and Ctrl sets of nanoparticles (where $\delta_L = 1, N_{Ligand} = 2 - 40,$ and $N_{Ligand} = 0$ respectively) to target bEnd3 were performed to investigate the effect of N_{Ligand} on binding to bEnd3. Previous studies have shown that binding towards bEnd3 using AP2-decorated polymersomes increases sharply at a certain N_{Ligand} and then a plateau is reached (where we hypothesise that all binding sites on bEnd3 are fully occupied) akin to superselective behaviour;[12] therefore, we hypothesise a similar binding profile to superselective behaviour when testing the AP2_1 set. A schematic of the initial hypothesis of how the binding of the nanoparticles to the bEnd3 cells is shown in fig 3.5. The schematic was drawn up from data of the computation work by Tian et al., showing the LRP-1 receptor stretched out within the glycocalyx, and the scales made computationally.[18] The schematic shows that we hypothesise that the AP2 ligand on the surface of the nanoparticle can interact with the LRP-1 receptor that is stretched. Additionally, we also hypothesise that the size of the nanoparticle will allow for multiple receptors to be bound onto by one nanoparticle, allowing for a superselective regime to be exhibited. Additionally, a schematic of what we expected to see from this experiment is shown in fig 3.6. We expected to see this type of result as we hypothesised that the AP2_1 set of nanoparticles would exhibit a superselective behaviour.

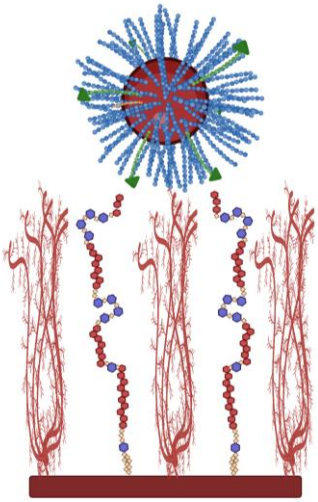

Fig 3.5 **Hypothesised binding schematic of AP2-decorated nanoparticle on the surface of the bEnd3 cell.** Based on computational experiments by Tian et al.,[18] the receptor would be stretched out and the tip of the receptor could interact with the AP2 ligand. Additionally, we hypothesise that the size of the nanoparticle is large enough to bind on to multiple receptors.

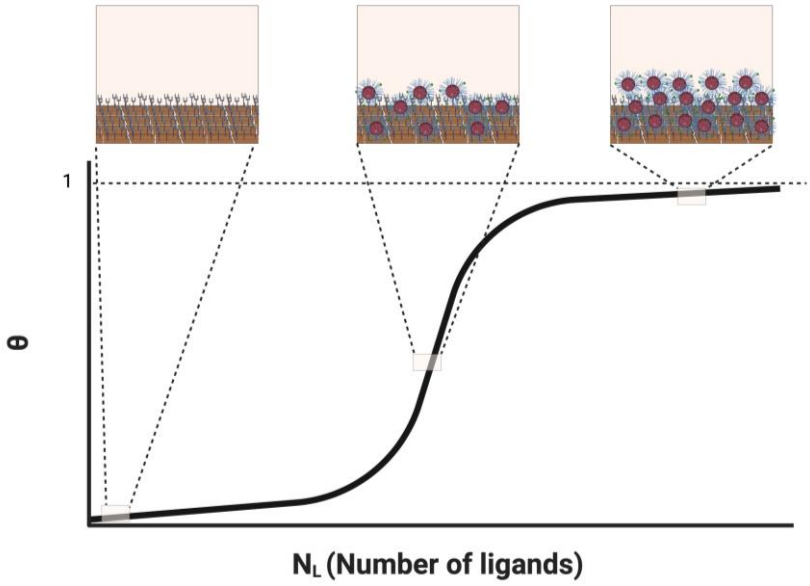

Fig 3.6 **Expected binding profile of AP2_1 set of nanoparticles targeting bEnd3.** Expected binding profile is that of a superselective regime.

Figure 3.7 shows the binding assay results, where $\frac{NPs}{cell_L}$ denotes the control-subtracted $\frac{NPs}{cell}$ (with the control being the $\frac{NPs}{cell}$ obtained when $N_{Ligand} = 0$, i.e., the Ctrl set): subtraction of the control removes any binding to the cells caused by passive targeting. The binding profile shows that as N_L increases, more ligand-

decorated nanoparticles bind onto the bEnd3 cells, as evidenced by the sharp increase in $\frac{NPs}{cell_L}$ when $N_{Ligand} = 4$ and $N_{Ligand} = 8$ (post-hoc Dunnett's multiple comparison: **** P ≤ 0.0001). However, by further increasing N_{Ligand}, we noticed a reduction in the number of nanoparticles binding onto the bEnd3 cells, evidenced by the drop in $\frac{NPs}{cell_L}$ when $N_{Ligand} = 20 - 40$. These results indicate that a superselective behaviour was not obtained, contradicting the hypothesis and the expected outcome of the binding profile shown in fig 3.6 of these nanoparticles towards bEnd3.

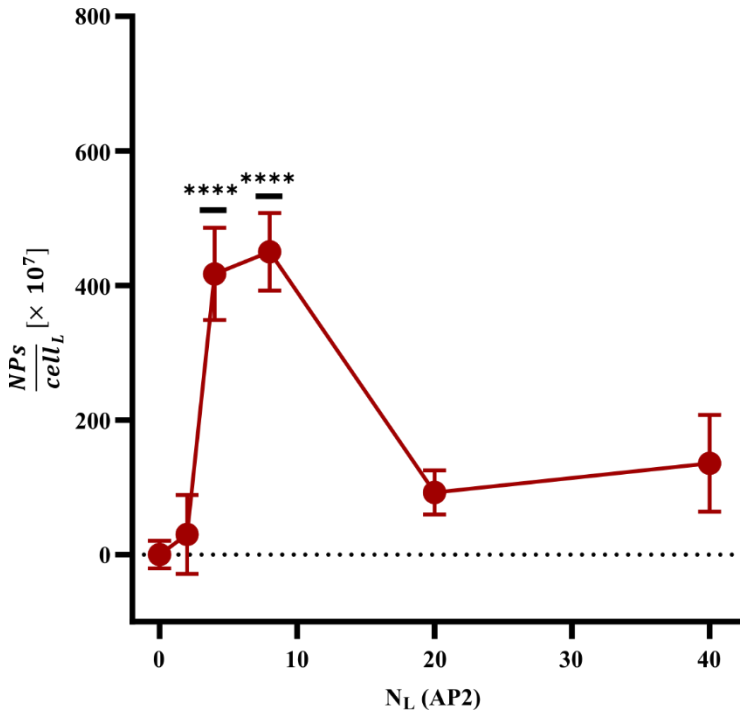

Fig 3.7 **Binding profile of AP2_1 set of nanoparticles targeting bEnd3.** bEnd3 cells were incubated for 1h with nanoparticles (20 μM) from the AP2_1 set ($\delta_L = 1, N_{Ligand} = 2 - 40$) and the Ctrl set ($N_{Ligand} = 0$) as a control. Plotted is the calculated control-subtracted NPs/cell. Each point represents the mean ± SEM (n=3). In the diagram, $N_L = N_{Ligand}$. A one-way ANOVA was used for the statistical analysis alongside a post-hoc Dunnett's multiple comparison test (**** P ≤ 0.0001).

Contrary to expectations, these findings demonstrate behaviour expected in range selectivity, not superselectivity, as evidenced by the drop in $\frac{NPs}{cell_L}$ as N_{Ligand}

increases. Range selectivity dictates that a strong binding could occur within a finite range of N_{Ligand} (or $N_{Receptor}$),[21] an observation seen in fig 3.7. We theorise that another previously unaccounted steric repulsive force is present, giving rise to the range selective behaviour. One possible cause of the steric repulsive force is ligand-ligand repulsion between the nanoparticles, herein labelled as F_{rep}^{lig}.

We consider that F_{rep}^{lig} occurs between nanoparticles prior to binding to the target receptor. F_{rep}^{lig} would also depend on N_{Ligand}: as N_{Ligand} increases, more ligand-ligand repulsion between the nanoparticles occurs, explaining why $\frac{NPs}{cell_L}$ drops in fig 3.7 between $N_{Ligand} = 8$ and $N_{Ligand} = 40$. With this hypothesised repulsive force, we can therefore alter the equation for total free energy of binding (F_{tot}) between nanoparticles to target cells to:

$$F_{tot} = F_{att} + F_{rep}^{brush} + F_{rep}^{gly} + F_{rep}^{lig} \quad (23)$$

where F_{att} is the attractive free energy of binding (from multivalent ligand-receptor interactions between a nanoparticle and the cell), F_{rep}^{brush} is the steric repulsive interaction exhibited when the receptor has to embed itself in a polymer brush to bind onto a ligand and F_{rep}^{gly} is the steric repulsive interaction when the nanoparticle inserts itself to the cell past the glycocalyx. For binding to occur, the magnitude of F_{att} must exceed the magnitude of $F_{rep}^{brush} + F_{rep}^{gly} + F_{rep}^{lig}$. A schematic of the proposed theory and the energies related to the binding are shown in fig 3.8.

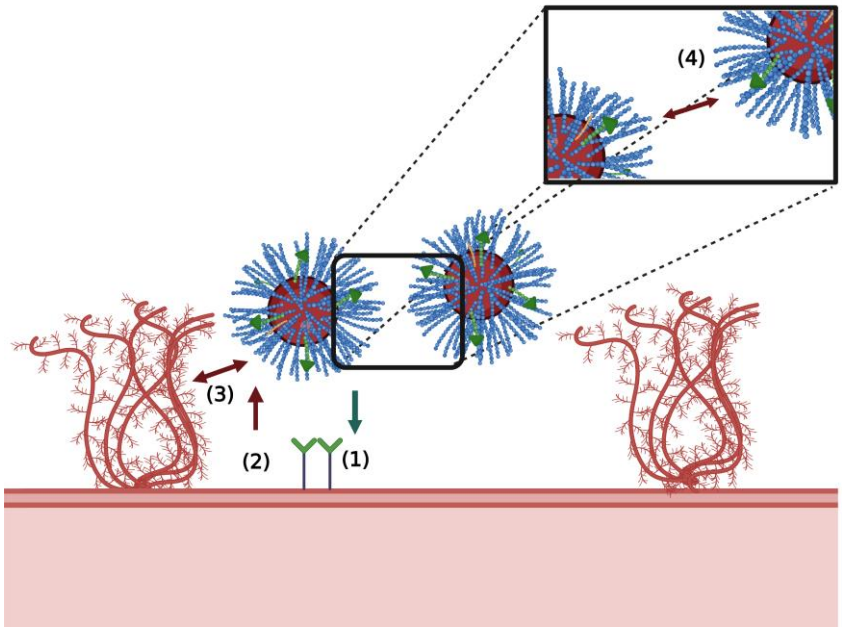

Fig 3.8 **Schematic of the binding of AP2-decorated nanoparticles to bEnd3 cells.** The schematic details the binding of spherical AP2-decorated nanoparticles (red, blue, and green for the hydrophobic core, hydrophilic polymer brush, and AP2 ligand respectively) to the LRP-1 receptor (green) on the glycocalyx-decorated (red tendrils) surface of the bEnd3 cell. The free energy terms, and how they relate to the binding, are depicted in the schematic evidenced by the numbered labels, where (1) F_{att} is the attractive free energy of binding, (2) F_{rep}^{brush} is the steric repulsive interaction induced when the receptor embeds itself within the nanoparticle polymer brush, (3) F_{rep}^{gly} is the steric repulsive interaction arising between the nanoparticle and the glycocalyx and (4) F_{rep}^{lig} is the theorised ligand-ligand repulsion between nanoparticles.

The theory presented for F_{rep}^{lig} was founded when using AP2-decorated nanoparticles with $\delta_L = 1$ and was shown to depend on N_{Ligand}; therefore, to assess whether F_{rep}^{lig} also depended on δ_L, binding assays using AP2_0.70 and AP2_0.16 sets of nanoparticles ($\delta_L = 0.70, N_{Ligand} = 2 - 40$ and $\delta_L = 0.16,\ N_{Ligand} = 2 - 40$ respectively) were undertaken. We hypothesised that F_{rep}^{lig} should decrease as δ_L decreases: if the ligand is hidden within a polymer brush (i.e., $\delta_L < 1$), the polymer brush could reduce the ligand-ligand interaction. The results of the binding assays using the AP2_0.70, AP2_0.16 and Ctrl sets of nanoparticles are shown in fig 3.9 and fig 3.10 respectively, normalised to $\frac{NPs}{cell}$ of the Ctrl set.

The binding profile in fig 3.9 shows that, when $\delta_L = 0.70$, there was only an increase in $\frac{NPs}{cell_L}$ when $N_L = 40$ (post-hoc Dunnett's multiple comparison: ** P ≤ 0.001) in bEnd3 cells, while at lower N_{Ligand} there were no significant differences observed to the control ($N_{Ligand} = 0$). Regarding these results, we postulate that indeed F_{rep}^{lig} decreases as δ_L decreases from 1 to 0.70, yet still large enough to exhibit a strong steric repulsion towards binding. As the ligand is within the polymer brush, $F_{rep}^{brush} \neq 0$. Thus, F_{tot} for $\delta_L = 0.70$ will now have contributions from both F_{rep}^{lig} and F_{rep}^{brush}, explaining why a much higher N_{Ligand} was needed for F_{att} to overcome the strong repulsion factors exhibited.

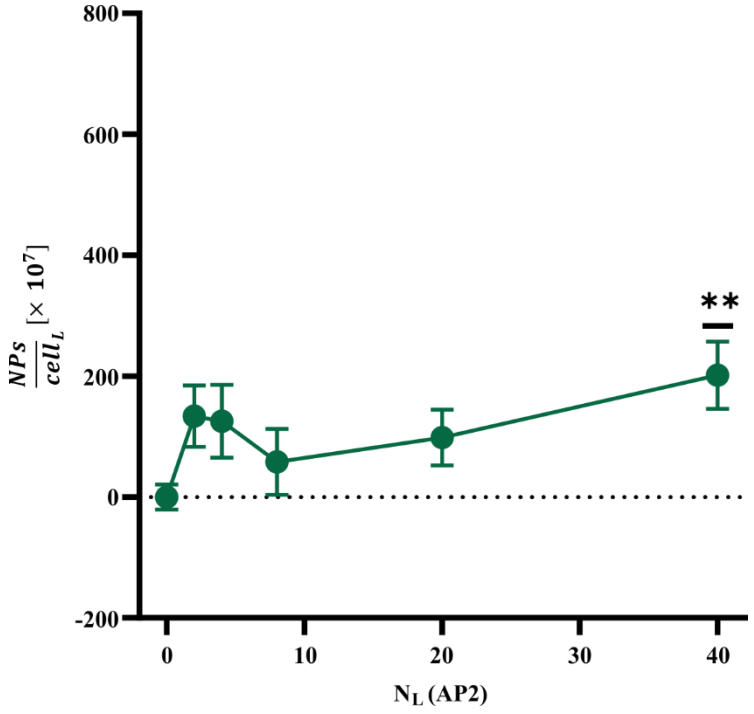

Fig 3.9 **Binding profile of AP2_0.70 set of nanoparticles targeting bEnd3.** bEnd3 cells were incubated for 1h with nanoparticles (20 µM) from the AP2_1 set ($\delta_L = 0.70, N_{Ligand} = 2 - 40$) and the Ctrl set ($N_{Ligand} = 0$) as a control. Plotted is the calculated control-subtracted NPs/cell. Each point represents the mean ± SEM (n=3). In the diagram, $N_L = N_{Ligand}$. A one-way ANOVA was used for the statistical analysis alongside a post-hoc Dunnett's multiple comparison test (** P ≤ 0.001).

Embedding AP2 deeper within the polymer brush, i.e., $\delta_L = 0.16$ shows a further change in the binding profile of AP2-decorated nanoparticles to bEnd3. The binding profile in fig 3.10 shows more nanoparticles bound onto bEnd3 as N_{Ligand} increased, evidenced by the increase in $\frac{NPs}{cell_L}$ when $N_{Ligand} = 4$, and a further increase when $N_{Ligand} = 20$ (post-hoc Dunnett's multiple comparison: **** P ≤ 0.0001, * P ≤ 0.05). We assume that at some point after $N_{Ligand} > 40$, $\frac{NPs}{cell_L}$ will drop again as F_{rep}^{brush} increases as N_{Ligand} increases. A plausible explanation to the differences observed in binding profiles between $\delta_L = 0.70$ (fig 3.9) and $\delta_L = 0.16$ (fig 3.10) is due to the changes in both F_{rep}^{lig} and F_{rep}^{brush}. By embedding the ligand further in a polymer brush, F_{rep}^{brush} increases as the receptor must push through further into a polymer brush to bind to the ligand. We also assume that embedding the ligand into the brush (to $\delta_L = 0.16$) drastically lowers F_{rep}^{lig}, as the PEG molecules of the polymer can act as a barrier by hiding the AP2 molecules. Therefore, for $\delta_L = 0.16$, F_{tot} will have an increased contribution from F_{rep}^{brush}, but a much lower contribution from F_{rep}^{lig}, explaining why a lower N_{Ligand} was needed for F_{att} to overcome the steric repulsive forces, causing a surge in the number of nanoparticles binding to bEnd3.

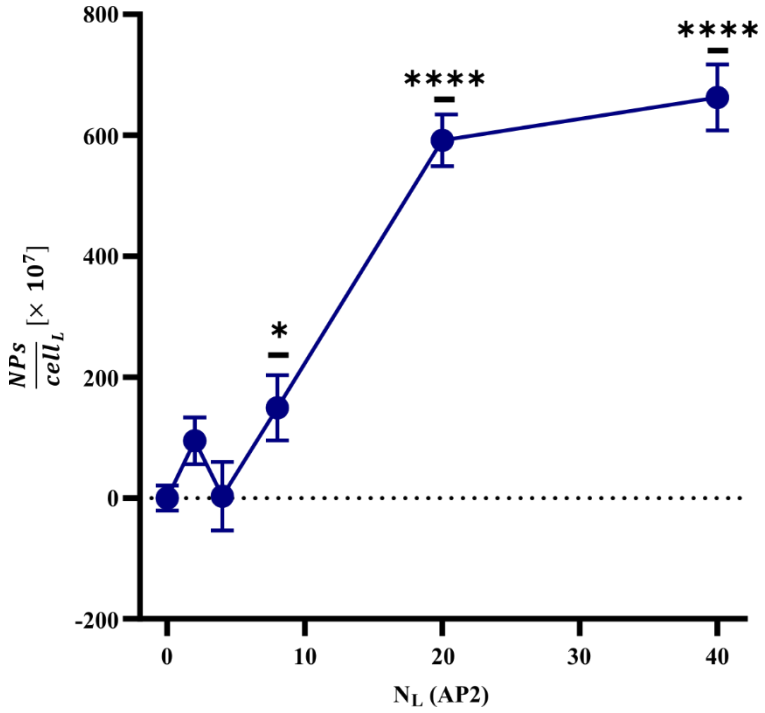

Fig 3.10 **Binding profile of AP2_0.16 set of nanoparticles targeting bEnd3.** bEnd3 cells were incubated for 1h with nanoparticles (20 μM) from the AP2_1 set ($\delta_L = 0.17, N_{Ligand} = 2 - 40$) and the Ctrl set ($N_{Ligand} = 0$) as a control. Plotted is the calculated control-subtracted NPs/cell. In the diagram, $N_L = N_{Ligand}$.Each point represents the mean ± SEM (n=3). A one-way ANOVA was used for the statistical analysis alongside a post-hoc Dunnett's multiple comparison test (* P ≤ 0.05, **** P ≤ 0.0001).

We also examined whether targeting a different receptor with another ligand influenced the binding profile to bEnd3. A binding assay using the Gluc_1 ($\delta_L = 1, N_{Ligand} = 20 - 197$), and Ctrl ($N_{Ligand} = 0$) sets of nanoparticles was performed on bEnd3 cells. As $\delta_L = 1$ for the Gluc_1 set, we should expect to observe a binding profile targeting bEnd3 akin to that using AP2_1 in fig 3.7 if F_{rep}^{lig} was not specific only to AP2. The binding profile in fig 3.11 shows that by using a small amount of Gluc ligands ($N_{Ligand} = 20$), nanoparticles bind strongly to the GLUT1 receptors expressed on bEnd3 cells, evidence by the sharp increase of $\frac{NPs}{cell_L}$ (post-hoc Dunnett's multiple comparison: **** (P ≤ 0.001)). We also observed no change in the number of nanoparticles binding to bEnd3 when further increasing N_{Ligand} (post-hoc Tukey's multiple comparison: ns (P > 0.05)).

Therefore, we found that all available sites for binding onto the cells were filled and that the cells were fully saturated with nanoparticles (indicative of superselective binding), evidenced by the plateau of $\frac{NPs}{cell_L}$ in relation to N_{Ligand}. The results in fig 3.11 suggest that a shorter range of ligands ($0 < N_{Ligand} \leq 20$) should be investigated to better understand at what N_L the steep change increase of $\frac{NPs}{cell_L}$ towards bEnd3 cells occurred. As superselectivity was observed, matching the initial hypothesise posed when testing AP2_1, and that $F_{rep}^{brush} \approx 0$ (as $\delta_L = 1$), we hypothesise that no additional steric effect (like F_{rep}^{lig} when using AP2 as a ligand) was placed on the binding system, hence why we achieved superselectivity.

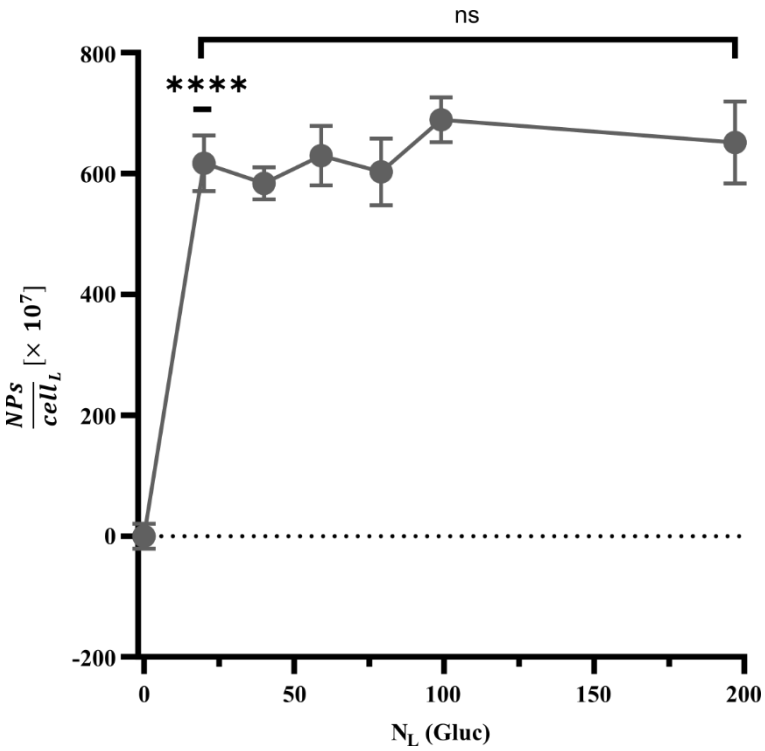

Fig 3.11 **Binding profile of Gluc_1 set of nanoparticles targeting bEnd3.** bEnd3 cells were incubated for 1h with nanoparticles (20 μM) from the Gluc_1 set ($\delta_L = 0.17, N_{Ligand} = 20 - 197$) and the Ctrl set ($N_{Ligand} = 0$) as a control. Plotted is the calculated control-subtracted NPs/cell. Each point represents the mean ± SEM (n=3). In the diagram, $N_L = N_{Ligand}$. A one-way ANOVA was used for the statistical analysis alongside a post-hoc Dunnett's multiple comparison test (** P $\leq$ 0.001) and a post-hoc Tukey's multiple comparison test (ns P $>$ 0.05).

No additional steric effect was observed when using the Gluc-decorated nanoparticles. One possibility for the observation could be due to the change of ligand: glucose is a small molecule, compared to the AP2, a long peptide which has charged parts across the ligand. AP2 has many charged amino acids (threonine (T), tyrosine (Y), glycine (G) and asparagine (N)), and the peptide has previously been shown to have a net charge of +2,[197] thus as the ligands have a net charge, electrostatic repulsion could occur between Angiopep2-decorated nanoparticles. Glucose, on the other hand, is uncharged, hence when using the Gluc set of nanoparticles, F_{rep}^{lig} was negligible. Alternatively, another possibility is that glucose is a small ligand, whereas AP2 is a large ligand - as the size of the glucose ligand is small, ligand repulsion may be minimal when compared to AP2.

Overall, the investigation was performed to optimise multivalent targeting towards brain endothelial cells. To this end, we have shown that binding indeed is influenced by N_L, δ_L and the type of ligand and have postulated the existence of a new steric force, F_{rep}^{lig}, we had previously not accounted for. For all values of δ_L, we found nanoparticles that were able to bind strongly to the target cell (evidenced by a large $\frac{NPs}{cell_L}$) and thus have shown that we can achieve strong binding to brain endothelial cells with any of the three δ_L by changing the number of ligands.

3.3.4 Indiscriminate targeting between bEnd3, C8-D1A and T98G

We next performed binding studies on all three cells lines using the AP2 and Gluc decorated nanoparticles. Fig 3.4 showed a schematic of the cell phenotypes and indicated that they were different to one another: we hypothesise that we can target bEnd3 without C8-D1A or T98G as the cells have different receptor densities.

Figure 3.12 shows the binding profiles obtained using (A) AP2_1, (B) AP2_0.70, (C) AP2_0.16 and (D) Gluc_1 sets of nanoparticles on C8-D1A, T98G and bEnd3. We assumed that the binding profiles in bEnd3 and T98G could be the same due to LRP-1 expression seen in fig 3.3. C8-D1A had the highest relative LRP-1 receptor density compared to both bEnd3 and T98G, thus we expected that the binding profiles using the AP2_1, AP2_0.70 and AP2_0.16 would be different for C8-D1A compared to bEnd3, with more nanoparticles binding onto C8-D1A when using a lower N_{Ligand} of AP2. Our results showed an equivalent binding profile on C8-D1A compared to T98G and bEnd3 (Two-Way ANOVA (Cell Line): ns (P >

0.05)). The binding profiles therefore suggest that $N_{Receptor}$ had no influence on the number of nanoparticles binding onto the cells when using AP2 as the ligand.

On the other hand, the GLUT1 expression is distinct in all three cell lines, with bEnd3 presenting the highest expression, followed by C8-D1A and then T98G. Therefore, we hypothesise that nanoparticles will need a higher N_{Ligand} of Gluc to fully saturate the receptors in C8-D1A, and an even higher N_{Ligand} of Gluc to T98G. Binding assays on C8-D1A and T98G using the Glu-decorated nanoparticles will allow us to test this hypothesis, and the influence of $N_{Receptor}$ on binding. Furthermore, no differences were observed in the binding profile between the three cell lines (Two-Way ANOVA (Cell Line): ns (P > 0.05)) when using Glu-decorated nanoparticles (Figure 3.12D). We therefore did not observe any difference between the three cell lines, contracting our hypothesis when using this set of nanoparticles. However, as previously mentioned, we do not know when the “sweet spot” in binding towards bEnd3 occurred (i.e., at what N_L did binding start to sharply increase for bEnd3), so further investigation should be done using Glu-decorated nanoparticles with $0 < N_{Ligand} \leq 20$ to conclude the effect $N_{Receptor}$ for Glut1 has on binding.

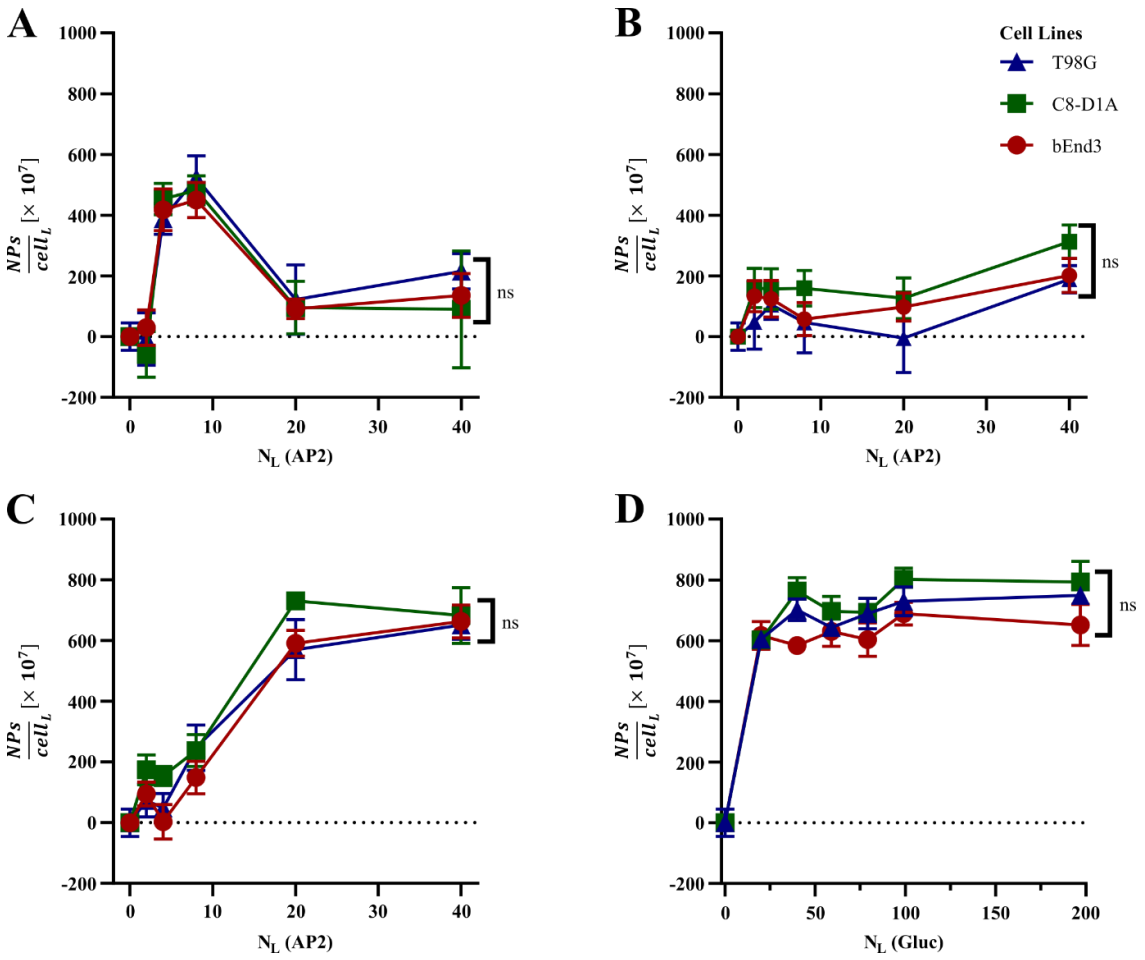

Fig 3.12 **Binding profiles of AP2- and Gluc- decorated nanoparticles targeting bEnd3, C8-D1A and T98G.** Cells were incubated for 1h with either nanoparticles (20 μM) from the (A) AP2_1 ($\delta_L = 1, N_{Ligand} = 2-40$), (B) AP2_0.70 ($\delta_L = 0.70, N_{Ligand} = 2-40$), (C) AP2_0.16 ($\delta_L = 1, N_{Ligand} = 2-40$) or (D) Gluc_1 ($\delta_L = 1, N_{Ligand} = 20-197$) sets of nanoparticles and the Ctrl set ($N_{Ligand} = 0$) as a control. Plotted is the calculated control-subtracted NPs/cell. Each point represents the mean ± SEM (n=3). In the diagram, $N_L = N_{Ligand}$. A two-way ANOVA was used for the statistical analysis alongside a post-hoc Tukey's multiple comparison test (ns $P > 0.05$).

We postulate that $N_{Receptor}$ had no influence on nanoparticle binding when using AP2 could be due to the LRP-1 receptor itself and the glycocalyx of the target cell. Firstly, throughout the above experiments, we have had an assumption that each receptor is one binding site (which can be evidenced by the schematic shown in fig 3.5, where one AP2 ligand could bind only to the tip of an LRP-1 receptor, thus making LRP-1 only have one binding site): in fact, if receptors have multiple binding sites instead, multiple nanoparticles would be able to bind onto a single receptor, instead of multiple receptors being bound onto by a single

ligand-decorated nanoparticle via the multivalent effect. LRP-1 itself is a large receptor of 515 kDa, containing four clusters of compliment-type repeat units (CR), often referred to as ligand-binding repeats.[198,199] A recent molecular docking-based strategy was undertaken, which shows that angiopep2 can bind onto CR56 in cluster II and CR17 in cluster III of the LRP-1 receptor,[200] proving that multiple binding sites for Angiopep-2 decorated nanoparticles are present on a single LRP-1 receptor. We herein postulate that multiple of the synthesised nanoparticles can bind onto one single LRP-1 receptor, as the synthesised nanoparticles are very small compared to the size of the receptor. An altered schematic of the LRP-1 receptor,[198] with the four clusters of binding repeats and multiple nanoparticles binding onto a single LRP-1 receptor are shown in fig 3.13. Within the figure, we also note the new scale factor of the diagram. We previously postulated that the nanoparticles could bind onto multiple receptors; however, looking at the literature size of the LRP-1 versus the size of our tested nanoparticles, it is more likely that the receptor could vastly outsize our nanoparticles. We also hypothesise that the grafting of the glycocalyx on the surface of the target cell is low enough that nanoparticles can bind onto the LRP-1 receptor at multiple locations even within the glycocalyx as our nanoparticles are small.

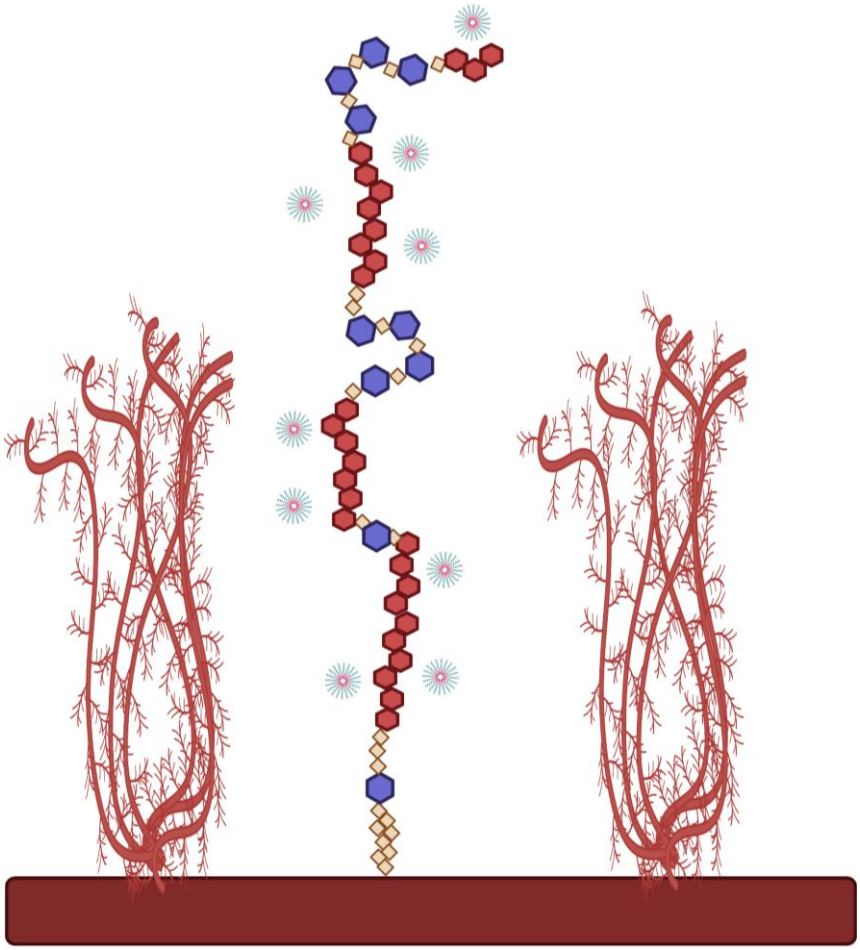

Fig 3.13 **Schematic of the proposed binding phenomenon on a fully stretched LRP-1 receptor, with nanoparticles binding on various binding sites.** The receptor houses four clusters of complement-type repeats (CRs), depicted by the regions of red hexagons. Nanoparticles are shown that could bind onto the clustered regions.

Regardless on the number of binding sites on LRP-1, we should still see a difference in binding profiles between each cell line, as the number of receptors (and therefore the number of binding sites) is different. As C8-D1A still has the largest number of receptors, we should expect it to have the highest number of binding sites possible, thus the binding profile towards C8-D1A would still be different to bEnd3 and T98G. We therefore hypothesise that the three cell lines did have a different number of receptors but held the same number of binding sites. One possible explanation for why the number of binding sites is the same between each cell line would be the glycocalyx: if the glycocalyx is very dense,

receptors may be more sterically hindered thus reducing the number of binding sites per receptor. We should therefore investigate the glycocalyx density of each cell line to investigate our hypothesis that the number of binding sites between the cell lines were the same and due to the glycocalyx.

3.3.5 Effect of the glycocalyx on binding

The glycocalyx of bEnd3, C8-D1A and T98G were investigated using a lectin assay. As shown in fig 3.14, our results showed that there was indeed a significant difference in ρ_R between each cell line (Two-Way ANOVA (Cell Line): **** $P \leq 0.0001$). A non-linear regression, based on a Hill slope, was plotted and the dissociation constant (K_D) was calculated for each cell line to lectin: K_D (bEnd3) = 0.2733, K_D (T98G) = 0.6102, and K_D (C8-D1A) = 2.150. A low K_D implies a high association constant (K_A), equating to a high sugar content as less lectins were required for binding. These results suggest that bEnd3 possess higher sugar content (i.e. [GlcNAc] 1,3-N-acetylglucosamine), and in turn likely the highest ρ_G, followed by T98G and C8-D1A.

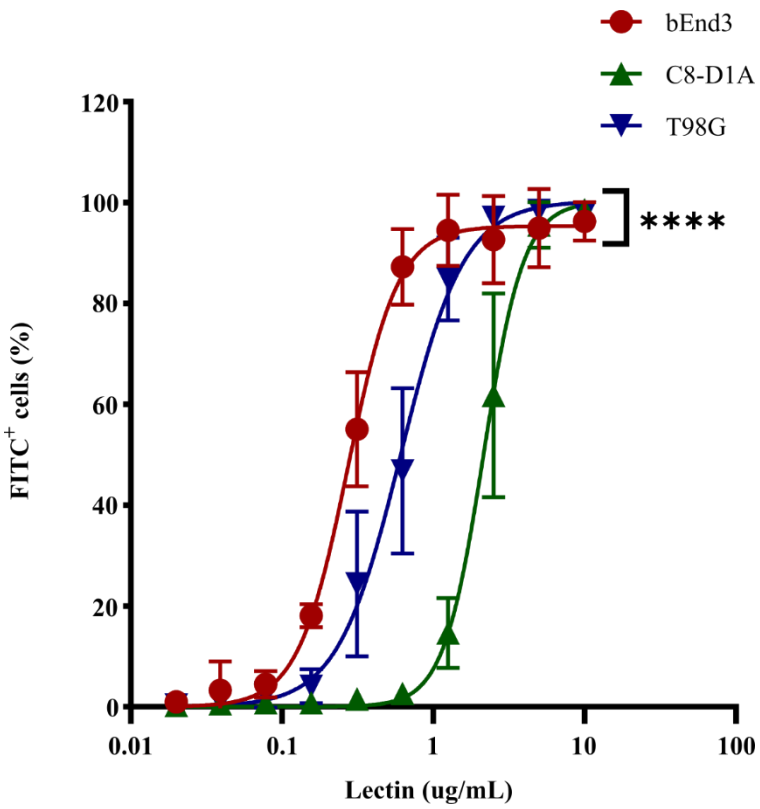

Fig 3.14 **Lectin Assay on bEnd3, C8-D1A and T98G cells.** Each point represents the mean ± SEM (n=3 for bEnd3, n=4 for C8-D1A and T98G). Two-way ANOVA was used for the statistical analysis (****: $P \leq 0.0001$).

We hypothesised that the three cell lines held the same number of binding sites. Focusing on binding towards LRP-1, the results in fig 3.3 suggests that C8-D1A has the highest density of LRP-1 receptors, with bEnd3 having the lowest, whereas fig 3.14 suggests that C8-D1A has the lowest glycocalyx concentration, with bEnd3 having the highest. From the results of fig 3.3 and fig 3.14, we speculate that having a highly dense glycocalyx may increase the number of binding sites on the receptor, whereas a low density glycocalyx reduces then number of binding sites. Having a high density glycocalyx, and hence having glycocalyx strands possibly grafted much closer to each other, could allow the LRP-1 to fully stretch, allowing many binding sites to be exposed to very small nanoparticles, whereas a low density glycocalyx could allow the LRP-1 to collapse (akin to a polymer grafted on a surface), reducing the number of binding sites. A schematic illustrating the conformation change of the receptor based on

the glycocalyx density is outlined in fig 3.15. Our speculation would therefore explain why we had no difference in binding profile between the three cell lines, even if the number of receptors between the three were different.

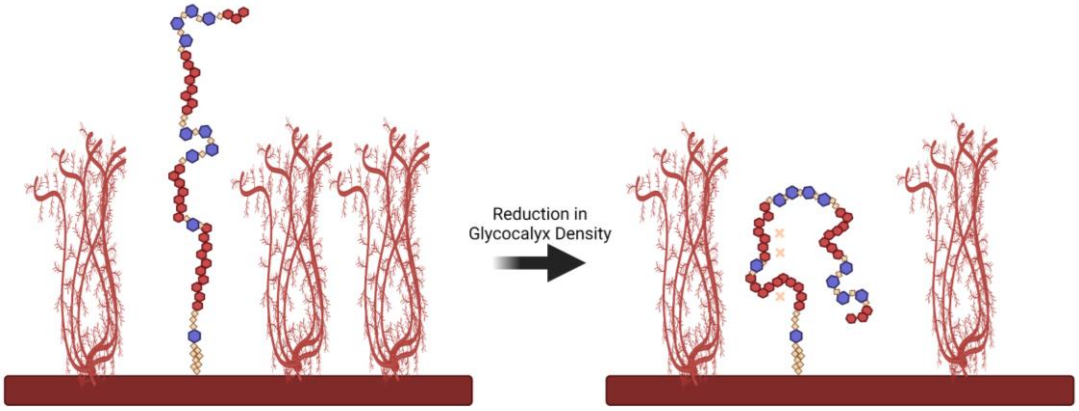

Fig 3.15 **Schematic of LRP-1 conformation based on glycocalyx density.** Having a denser glycocalyx can stretch the LRP-1 receptor, exposing more binding sites for small nanoparticles, whereas a less dense glycocalyx could cause the receptor to change conformation and could block certain binding sites, indicated by the X marks on the LRP-1 receptor

One problem with our justification on the grafting of the glycocalyx, and thus our proposed LRP-1 conformation based on the glycocalyx density, is that we have not accounted for the shape of the cells. Indeed, in fig 3.14, we calculated density of the glycocalyx based on the number of cells; however, astrocytes, glioma and endothelial cells do not share the same size and shape. As the cell types are different sizes, the glycocalyx sugar content should be looked at and compared to the sizes of the cells in future studies: if the sugar contents divided by the cell surfaces of each cell type is equivalent, we could deduce that the grafting of the glycocalyx and conformation of the receptors on the different cell types could be the same, and that another factor may be responsible for why the binding profiles were the same for the three cell lines, despite their differences in number of LRP-1 receptors.

Additionally, it is difficult to judge the conformation of the receptor based on the glycocalyx density without further tests. Cellular imaging could be done to actually examine the grafting of the glycocalyx on the cells and the distances between the base of the glycocalyx strands: additionally, cellular imaging of the cells in question would allow us to gain a more thorough scale between the receptor size and the glycocalyx size (from the tip of the glycocalyx to the base of the cell membrane).

Nevertheless, to investigate our hypothesis that the glycocalyx could affect the number of binding sites on the LRP-1 receptor, we mimic the shedding of the glycocalyx on the cells by treated the cells with heparinases, and then perform a binding assay on the hep-treated cells. By reducing the glycocalyx density, we hypothesise that binding sites on the LRP-1 decreases.

Prior to doing any binding assays, a lectin assay was done comparing hep-treated bEnd3 cells and untreated bEnd3 cells to investigate whether heparinase-treatment reduced ρ_R, as showed in fig 3.16. Our results show that there is a significant difference between untreated and hep-treated bEnd3 cells (paired t-test: * $P < 0.05$), indicating that ρ_R is different after the shedding of glycocalyx with heparinase cocktail in bEnd3. A non-linear regression, based on a Hill slope, was plotted and K_D (Hep Treated) was calculated. K_D (Hep-Treated bEnd3) = 0.6537, higher than K_D (bEnd3) = 0.2733, indicating that the glycocalyx density was indeed reduced with hep treatment due to the newly absent [GlcNAc] 1,3-N-acetylglucosamine in the surface of hep-treated bEnd3.

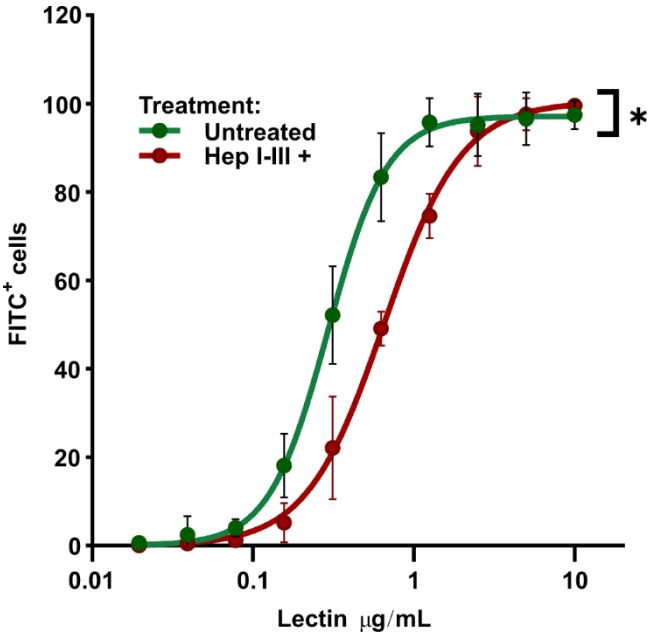

Fig 3.16 **Lectin Assay on untreated and Hep-treated bEnd3 cells.** Each point represents the mean ± SEM (n=5). Non-linear regression curves were plotted for the two treatments (R^2 > 0.95 for untreated and hep-treated bEnd3 cells)

Binding assays of the AP2_1, AP2_0.70 and AP2_0.16 (where $\delta_L = 1, 0.70, 0.16$ respectively) sets of nanoparticles on glycocalyx-shed bEnd3 cells were next conducted, with the results shown in fig 3.17A-C respectively. The binding profiles obtained using the same nanoparticle sets on the untreated bEnd3 cells (fig 3.7 and fig 3.9-10) were replotted in fig 3.17 and compared to hep-treated bEnd3 cells to investigate how different the binding profiles were between untreated and hep-treated bEnd3 cells. We hypothesise that the binding profiles for binding towards hep-treated bEnd3 cells would show that nanoparticles would require a higher N_{Ligand} to have a peak in $\frac{NPs}{cell_L}$, as we speculated that a reduced glycocalyx density would mean that fewer binding sites would be available for binding (due to the receptor conformation change).

The results show that when using AP2-decorated nanoparticles with $\delta_L = 1$, the only significant difference in $\frac{NPs}{cell_L}$ towards hep-treated and untreated bEnd3 cells

occurred when $N_L = 40$, where a larger $\frac{NPs}{cell_L}$ was observed when binding towards hep-treated bEnd3 cells. The above result contradicts our hypothesis as there was no significant difference in $\frac{NPs}{cell_L}$ when $N_{Ligand} = 4$ and $N_{Ligand} = 8$, where the peak in $\frac{NPs}{cell_L}$ occurred in untreated bEnd3 cells, indicating that we observe a similar trend in binding between hep-treated and untreated bEnd3 cells. A similar observation was found when using AP2-decorated nanoparticles with $\delta_L = 0.70$, where there were no significant differences observed in $\frac{NPs}{cell_L}$ within the tested range of $0 < N_{Ligand} < 40$. When using AP2-decorated nanoparticles with $\delta_L = 0.16$, we observed a significant difference in $\frac{NPs}{cell_L}$ when $N_{Ligand} = 20$ and $N_{Ligand} = 40$, the N_{Ligand} range where the peak in $\frac{NPs}{cell_L}$ occurred for untreated bEnd3 cells, but $\frac{NPs}{cell_L}$ was lower on hep-treated bEnd3 cells: to investigate our hypotheses with these results, however, we would have needed to test nanoparticles with a higher N_{Ligand} to investigate if a binding peak occurred at higher N_{Ligand}

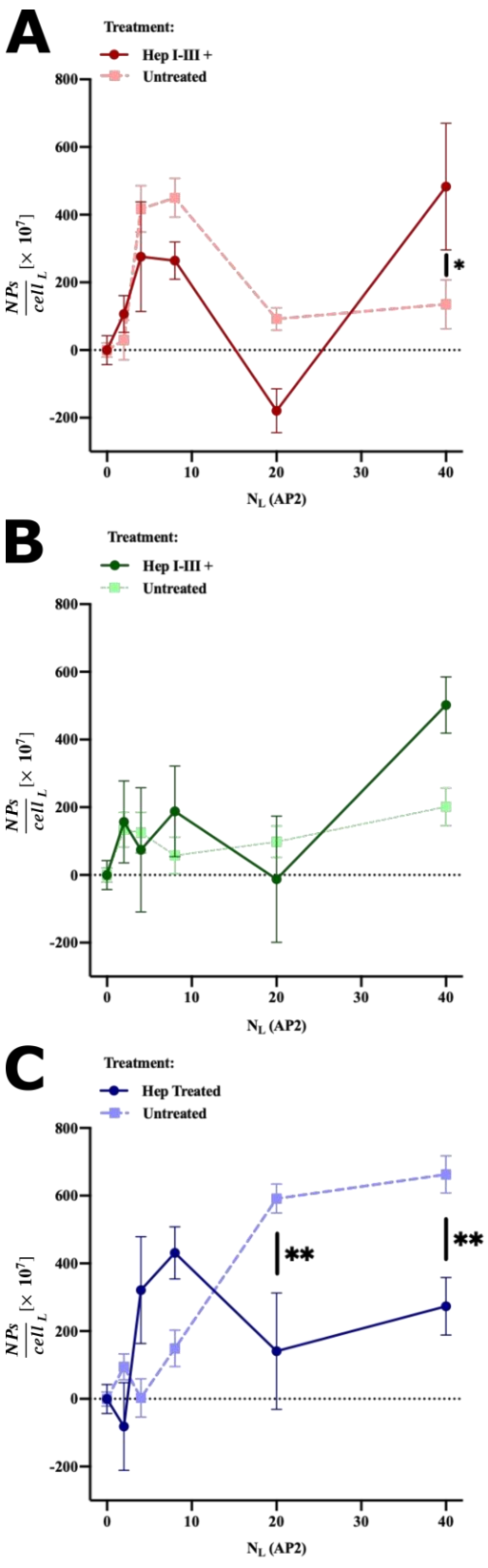

Fig 3.17 **Binding profiles of AP2-decorated nanoparticles to either glycocalyx-shed or untreated bEnd3 cells.** Binding profiles using (A) AP2_1 (B) AP2_0.70 and (C) AP2_0.16 sets of nanoparticles**.** Each point represents the mean ± SEM (n=3). One-way ANOVA was used for the statistical analysis alongside a post-hoc Bonferroni's multiple comparison test (**: P<0.005, ***: P<0.001 for binding towards Hep I-III+ treated cells). In the diagram, $N_L = N_{Ligand}$.The Ctrl set was used for the N_L = 0 control.

One limitation of the experiment conducted on the hep-treated bEnd3 cells is that the error bars obtained were very large: the standard error of the mean (SEM) of each data point was much larger in the hep-treated bEnd3 cells compared to the untreated bEnd3 cells (i.e., when testing nanoparticles where $\delta_L = 1$, $N_{Ligand} = 40$, the SEM of $\frac{NPs}{cell_L}$ (x10^7) was 72.1 for untreated bEnd3 and 187.058 for hep-treated bEnd3 cells). We therefore obtained much more varied data for binding to the hep-treated bEnd3 cells compared to the untreated bEnd3 cells.

To investigate why we obtained more varied data when binding to hep-treated bEnd3, an investigation was undertaken to assess whether the glycocalyx shedding interfered with the LRP-1 receptors. In fig 3.16 and fig 3.17, we assumed that the number of receptors on the hep-treated cells were the same and thus could try to compare binding between untreated and hep-treated cells. A western blot was done to compare LRP-1 expression between untreated and hep-treated bEnd3 cells, with the results shown in fig 3.18. As seen in the figure, by treating the bEnd3 cells with heparinase I-III, there was a downregulation (reduction in the expression of the protein) of LRP-1 of the bEnd3 cells, meaning we have fewer receptors for binding. As the receptor density changes during heparinase treatment, we should therefore look at the results in fig 3.17 with a bit of scepticism, as the experiment assumed that the receptor density remained equal.

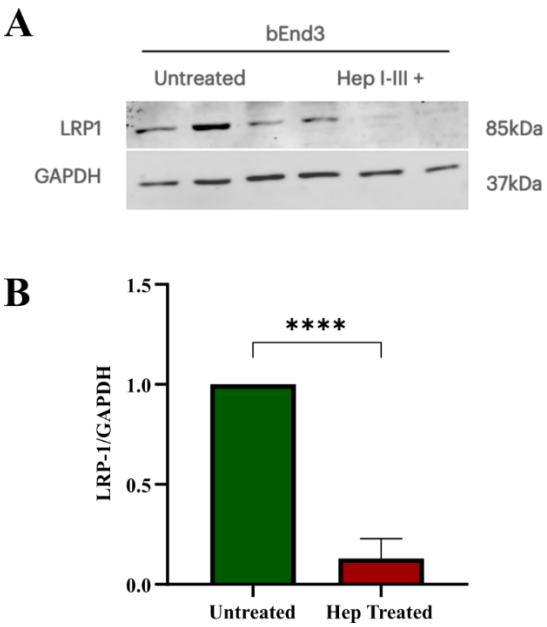

Fig 3.18 **Effect of heparinases treatment on LRP-1 expression in bEnd3 cells** (A) Immunoblotting for LRP-1 expression and GAPDH (loading control) in bEnd3 treated with heparinases cocktail after 2hours. (B) Densitometry analysis of LRP-1 relative to GAPDH in untreated and hep-treated bEnd3. An unpaired t-test was used for the statistical analysis ($P \leq 0.0001$). Each bar represents the mean ± SD (n=3).

An ELISA on the serum leftover after heparinase treatment on the bEnd3 cells was also done to investigate what the heparinase treatment did to the LRP-1 receptors. Fig 3.19 shows the results of the ELISA, showing a marked increase in free LRP-1 within the serum after heparinase treatment. By having free LRP-1 in the serum, it shows that the heparinase treatment may have also shed some LRP-1 receptors, and not just downregulated the receptors. Furthermore, as shown in fig 3.19, there was a large variance in the LRP-1 soluble concentration in the serum after heparinase treatment, showing there was little control on how many LRP-1 receptors were shed during the heparinase treatment. We therefore conclude that a newer experimental method for glycocalyx shedding should be obtained before continuing further investigation on the effect of the glycocalyx on binding.

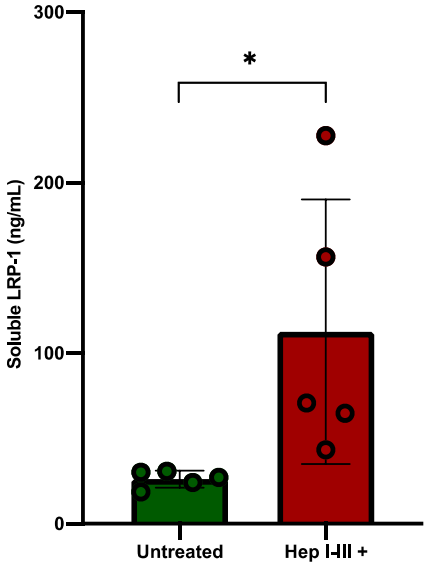

Fig 3.19 **LRP-1 soluble levels in untreated and Hep I/II/III treated bEnd3 cells by ELISA.** The bEnd3 were treated with heparinases cocktail and LRP-1 soluble levels were detected in supernatant after 2h of the treatment. An unpaired t-test was used for the statistical analysis (* $P \leq 0.05$). Each bar represents the mean ± SD (n=5)

3.4 Conclusions

In this chapter, we explored whether we could selectively target endothelial cells. We first optimised multivalent targeting towards bEnd3, showing that we could modulate binding towards bEnd3 by embedding the ligand deeper into a polymer brush (reducing δ_L), and we also postulated the presence of new steric potential term that can be explored. However, when testing the nanoparticles on binding towards bEnd3, C8-D1A and T98G, we were unable to achieve selective targeting towards the endothelial cells using the parameters tested.

Nevertheless, through this thesis, we have investigated why we were unable to selectively target endothelial cells. We first postulated that the number of receptors did not affect binding due to the size of the LRP-1 receptor and it having multiple binding sites: we further hypothesise that the glycocalyx could deform the LRP-1 receptor, where a dense glycocalyx could allow the receptor to fully expand and have the binding sites available for binding by small nanoparticles, whereas the less dense glycocalyx could allow the receptor to collapse and reduce the number of binding sites. We further tested a method of glycocalyx shedding and binding to glycocalyx-shed bEnd3; however, the large variance in the data obtained, both from binding and from the free soluble LRP-1, suggests that the method needs to be further optimised. These investigations give way for new avenues of research, where computational work could be done to investigate LRP-1 morphology based on the glycocalyx and a new methodology for glycocalyx shedding can be created and optimised.

There were several shortcomings witnessed throughout this investigation. One of the shortcomings was in the design of the glucose-decorated nanoparticles. We

were not able to see a difference in binding when comparing nanoparticles with varying N_{Ligand}, leading us to hypothesise that nanoparticle with much fewer ligands could be tested as a complete coverage of all the binding sites on the cells could have been achieved already with just the small number of ligands tested. Furthermore, in order to answer the research question, we only tested nanoparticles with 1 type of ligand towards binding to the target cell phenotypes, when we have previously suggested that nanoparticles with multiple ligands targeting multiple receptors would be advantageous in phenotypic targeting: future work should therefore include the combination of both glucose and AP2 as ligands on a nanoparticle, and further still the addition of more ligands that can target receptors on brain endothelial cells.

Chapter 4
In vitro BBB crossing of AP2-decorated nanoparticles

4.1 Introduction

In this chapter, we focus on the second research question of the thesis: can we control the crossing of nanoparticles across the BBB using sterics? To answer the research question, we must there use previously synthesised AP2-decorated nanoparticles for crossing studies. Answering this question would further our understanding of crossing the BBB, allowing us to learn more about how deliver medicines to the brain.

The BBB is a highly impermeable wall, built mainly by brain endothelial cells housing stable tight junctions (protein architectures connecting the endothelial cells). Previous research has shown that crossing of the BBB can occur via receptor-mediated transcytosis, both using LRP-1 and Glut1 as the receptors. One way to test for transport of nanoparticles past the BBB is by using an *in vitro* BBB model. *In vitro* BBB models have previously been with a monolayer of endothelial cells grown in a transwell®, whilst media is present both below and above the cell layer to mimic the BBB. Further studies have also explored a more complex *in vitro* BBB model, where both brain endothelial cells and pericytes were cocultured together, more closely mimicking the BBB. For this project, we opted for a simpler *in vitro* BBB model, with bEnd3 grown on a transwell® and no coculturing of additional cells, for a preliminary study of transcytosis. Future work should include using a more complex *in vitro* BBB model, and furthermore can

include *in vivo* experiments to see if the nanoparticles can cross an animal BBB and accumulate within the brain.

In chapter 3, we were able to optimise targeting towards bEnd3, showing that embedding the ligand into a polymer brush influenced the binding of nanoparticles onto the target cell, and concluded that nanoparticles with specific variables of N_L or δ_L could yield a high targeting to bEnd3 (namely, when $\delta_L = 1, N_{Ligand} = 4-8,\ \delta_L = 0.7, N_{Ligand} = 40$ and $\delta_L = 0.16, N_{Ligand} = 20-40$). We herein investigate the crossing of all the synthesised nanoparticles across an *in vitro* BBB model, comparing the crossing results to the binding results found previously to investigate the link between binding to the target cells and crossing of the BBB. Previous results have shown that N_{Ligand}, and thus the avidity of the nanoparticle, plays a major role in the transcytosis of nanoparticles across the BBB.[201] We therefore hypothesise that δ_L should also affect the transcytosis of nanoparticles across the BBB, as δ_L affects the avidity of the nanoparticle to bind onto the target receptors.

In this chapter, a cytotoxicity assay was again performed to investigate whether the synthesised ligand-decorated PEG-PCL nanoparticles were toxic to bEnd3. Receptor expressions of LRP-1 on both unpolarised bEnd3 and polarised bEnd3 was analysed by Western blot to ascertain if LRP--1 expression changed. Previously synthesised AP2-decorated nanoparticles were next tested on *in vitro* BBB models to test the effect of (N_{Ligand} or δ_L) on the permeability of the nanoparticles.

4.2 Materials and methods

4.2.1 Materials

Many of the materials used in chapter 3 are also used in this chapter, in addition to collagen type 1 solution from rat tail (Sigma Aldrich). Ligand-decorated nanoparticles used in this chapter were described table 2.5 and discussed as sets of nanoparticles for ease. In brief, the Ctrl set includes the nanoparticle formulations with no ligands, the AP2_1, AP2_0.70 and AP2_0.16 sets house AP2-decorated nanoparticle formulations where $\delta_L = 1$, 0.70 and 0.16 respectively.

4.2.2 Cell culture

bEnd3 cells were defrosted as described in 3.2.2. Media for bEnd3 was again DMEM supplemented with 10% (v/v) FBS and 1% (v/v) PS.

Cell subculture followed the same procedure described in 3.2.2 with one addition. Briefly, cell subculture was routinely performed every 2-3 days by washing the cells with dPBS (5 mL), incubation of the bEnd3 cells with TRYP (3 mL) at 37 ^{o}C for 3 min, then addition of fresh media (7 mL) followed by centrifuging the cell suspension at 1200 RPM for 5 min, supernatant removal, resuspension of the pellet and then cell counting. Different cellular concentrations were then plated:

[1] Cells (1×10^6 cells, 1 mL media) were seeded in T75 flasks with fresh media (14 mL) for cell subculture. The passages number were registered indicating the number of times the cells have been sub cultured (as described in 3.2.2).

[2] Cells (2.5×10^4 cells, 500 µL media) were seeded on collagen-treated 12 mm Transwell® inserts (1.12 cm^2 cell growth area, 0.4 µm pore size) placed within a clear 12 well plate containing media (1 mL) per well and incubated at 37 ^{o}C for

crossing experiments. Transwell® inserts were collagen-treated first by incubation of a 1:10 diluted Collagen type I solution from rat tail in dH_2O (300 µL) at 4 ^oC overnight and secondly by carefully washing the inserts with dH_2O two times.

4.2.3 Cell viability assay of bEnd3 after nanoparticle incubation

Cell metabolic activity was again determined via the MTT assay to investigate the cytotoxicity of the nanoparticles. The MTT assay was performed again for bEnd3, following the same protocol outlined in section 3.2.3 but altering the nanoparticle incubation time to 4 hours, the timeframe used in previous *in vitro* BBB crossing assays.[73]

4.2.4 *In vitro* BBB model

An *in vitro* BBB model, comprising a polarised confluent bEnd3 monolayer, was obtained for protein expression analysis of polarised bEnd3 and for permeability assays. A previously published protocol was followed to obtain a polarised bEnd3 monolayer.[73] Briefly, cells (2.5×10^4 cells, 500 µL media) were seeded on collagen-treated 12 mm Transwell® inserts within a clear 12 well plate containing media (1 mL) per well as a reservoir and incubated at 37 ^oC, as described in 4.2.2. Seeding the bEnd3 cells on collagen-treated inserts allows for polarization of bEnd3 cells enabling the reorganisation of the cells to adhere to one-another via tight junctions,[202] thereby mimicking the structure endothelial cells adopt at the BBB. After three days, the media within the inserts was replaced with fresh media, and the reservoir media was replaced with an altered media containing only DMEM supplemented with 1% (v/v) PS (i.e., serum-free media) and further incubated at 37 ^oC for another three days. Growth of the bEnd3 cells with serum-

free media in the basolateral side of the bEnd3 monolayer has been shown to produce a suitable model for the BBB, closely mimicking primary cultures of BBB endothelial cells. At day 6 optical microscopy was done to confirm confluency of the polarised bEnd3 cells. After day 6, protein analysis and permeability assays were conducted as depicted below.

4.2.4.1 Protein expression of polarised bEnd3

LRP-1 expression of polarised bEnd3 was obtained to ascertain whether polarisation of bEnd3 altered LRP-1 content. LRP-1 expression of polarised bEnd3 cells were obtained by western blot. Briefly, polarised bEnd3 cells were washed twice with PBS, and RIPA (98 µL) and PI (2 µL) were added directly onto the polarised bEnd3 cells grown on the transwell inserts and left on ice for 1 hour. Cells were then collected, centrifuged and the protein content of the polarised bEnd3 lysate was quantified, following the protocol outlined in 3.2.4. A western blot was then performed using both the polarised and unpolarised bEnd3 lysates, following the protocol outlined in 3.2.5.

4.2.4.2 Permeability assay of AP2-decorated nanoparticles

To investigate the rate of transport of ligand-decorated nanoparticles across the polarised bEnd3 monolayer, a permeability assay was performed on the *in vitro* BBB model, following a previously published protocol.[73] Media on top of the polarised bEnd3 monolayer was replaced with AP2-decorated nanoparticles (20 µM, 400 µL in media), the altered media in the reservoir of the transwell membrane was replaced with fresh media (600 µL) and the nanoparticle-treated polarised bEnd3 cells were then incubated at 37 ^{o}C for 4 hours, with aliquots (200 µL) collected from the reservoir every 30 mins, and fresh media (200 µL) to

replace the volume. The concentration of nanoparticles in each aliquot obtained were then calculated via fluorescence measurements, following the same method used in 3.2.5. Briefly, fluorescence was read using a TECAN Spark® microplate reader, using an excitation wavelength of 750 nm and emission wavelength of 779 nm (for the Cy7 label on the nanoparticles) and the concentration of the sample was calculated using a calibration curve of the nanoparticle formulations (varying between 0.31 - 40.00 uM in 100 uL media). The gain was set again at 130 for all crossing experiments. The following equation was then used to calculate the apparent permeability coefficient, P_{app}, for each tested nanoparticle formulation:

$$P_{app} = \frac{1}{C_0 A}\frac{dQ}{dT} \quad (24)$$

where C_0 is the initial cargo concentration of nanoparticles on top of the polarised bEnd3 monolayer ($3.05 \times 10^{10}\ NPs\ uL^{-1}$), A is the total surface area of the transwell membrane (1.12 cm^2) and $\frac{dQ}{dT}$ is the transport rate of nanoparticles across the membrane (in number of nanoparticles crossed per second).[203] $\frac{dQ}{dT}$ was calculated using the aliquots obtained at 30 min intervals, assuming nanoparticles that crossed were equally dispersed within the reservoir media in the basal side of the bEnd3 cells.

To investigate the influence of only the number of ligands (N_L) and the insertion parameter of the ligand in a polymer brush (δ_L), P_{app}^0 (the P_{app} obtained for the Ctrl set, where $N_L = 0$) was subtracted from all calculated P_{app} for the other nanoparticle formulations to obtain P_{app}^*, subtracting any effect of passive

transport across the *in vitro* BBB model. A schematic detailing the *in vitro* BBB model, alongside nanoparticles present in the media during the transcytosis experiment, is shown in fig 4.1.

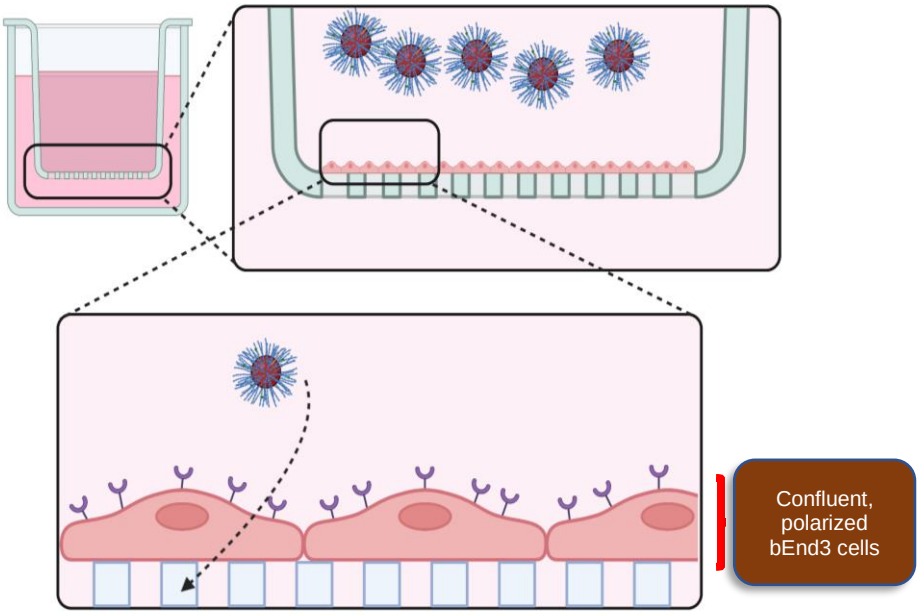

Fig 4.1 ***In vitro* BBB schematic for permeability assays.** A confluent polarised bEnd3 cell monolayer was made at the bottom of a transwell to mimic the BBB. Nanoparticles are shown in the schematic to show how we postulate the nanoparticles would cross the BBB.

4.2.5 Statistical Analysis

The results are shown either as the mean ± standard deviation (SED) or as the mean ± standard error of the mean (SEM). Statistical analyses were obtained using unpaired t-tests and one-way ANOVA tests (with a post hoc Dunnett's multiple comparison test to compare data sets to a control). In all subsequent figures, n refers to the number of independent experiments performed (i.e., n = 3 denotes 3 independent experiments were conducted)

4.3 Results and discussion

4.3.1 Evaluation of cell toxicity of AP2-decorated nanoparticles on bEnd3

Prior to any crossing studies of AP2-decorated nanoparticles across the *in vitro* BBB model for the last objective of this thesis, the cell toxicity of the nanoparticles to bEnd3 was investigated via an MTT assay. Indeed, in 3.3.1, we showed that our synthesised ligand-decorated nanoparticles had no cytotoxic effect on bEnd3; however, the incubation time tested previously was set only for binding incubation, and for the crossing assay, nanoparticles were to be incubated for 4 hours. An MTT assay, increasing incubation time of AP-decorated nanoparticles to bEnd3 to 4 hours, was therefore performed to investigate whether the increased incubation time could cause any harm to the bEnd3 cells.

The same nanoparticle formulations used previously (Ctrl_3, AP2_1_40, AP2_0.70_40, and AP2_0.16_40) were investigated again for the MTT assay. Ctrl_3 was used to test nanoparticles with no ligands ($N_{Ligand} = 0$). AP2_1_40, AP2_0.70_40 and AP2_0.17_40 samples were used to test nanoparticles housing the highest number of AP2 ligands ($N_{Ligand} = 40$) and to examine the different synthesised ligand-conjugated copolymers AP2_PEG113, AP2_PEG68 and AP2_PEG8 respectively. The cell viabilities of bEnd3 after a 4-hour incubation with the chosen nanoparticle formulations are presented in fig 4.2. We observed no significant difference in cytotoxicity of the nanoparticle formulations towards bEnd3 (post-hoc Dunnett's multiple comparison: ns P> 0.05). As described previously, a sample is deemed toxic for *in vitro* studies if cell viability is reduced to <70%:[196] the mean viability of the cells after nanoparticle incubation was again >80%, indicating no cytotoxic effects to the cells *in vitro* were found at

the new incubation time and that the *in vitro* crossing assay can performed using the nanoparticles at the 4-hour incubation.

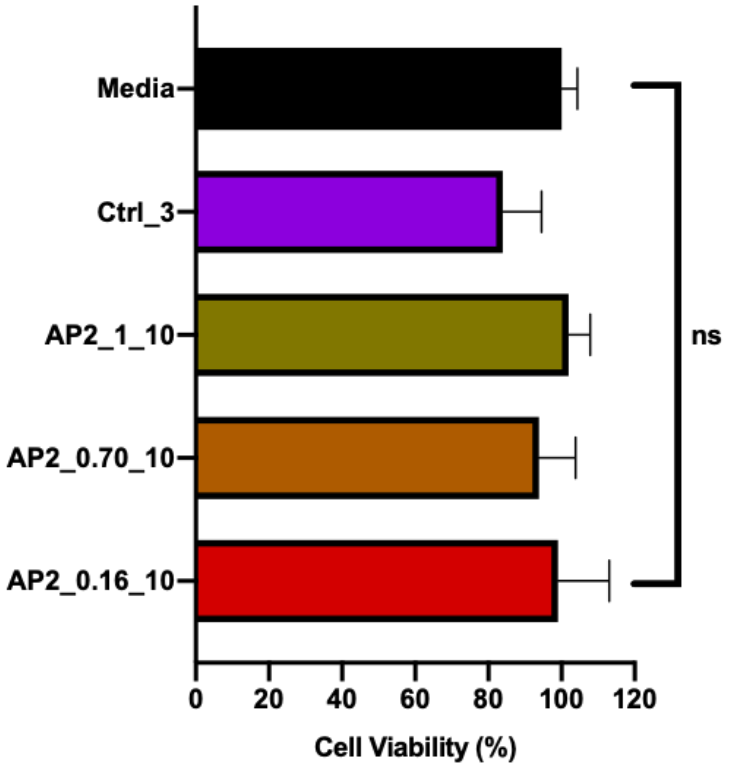

Fig 4.2 **Cell viability assessed by MTT Assay in bEnd3 with AP-decorated PEG-PCL nanoparticles.** Cells were incubated with 4 nanoparticle formulations (Ctrl_3, AP2_1_40, AP2_0.70_40, AP2_0.16_40) at 20 μM concentration for 4 hours and the cell viability was obtained by the MTT assay. One-way ANOVA was used for the statistical analysis alongside a post hoc Dunnett's multiple comparison test (ns: $P > 0.05$ for all formulations when compared to media). Each bar represents the mean ± SEM (n=3).

4.3.2 LRP-1 expression between polarised and unpolarised bEnd3

LRP-1 expression was then obtained for polarised bEnd3 cells. Previous studies have shown that the polarization of cells could change the protein expression, hence receptor expression, of cells;[204] therefore, it was decided to investigate whether LRP-1 expression is different for polarised and unpolarised cells. If LRP-1 expression is the same after polarization, the binding results for AP2 conjugated nanoparticles could be used and compared to any crossing studies. A western

blot was therefore done, with lysates of unpolarised and polarised cells placed side by side, with the results shown in fig 4.3. The graph shows that there was no significant difference in LRP-1 /GADPH expression between the polarised and unpolarised bEnd3 cells, hence we can therefore assume we can compare the binding results seen in chapter 3 to future crossing studies.

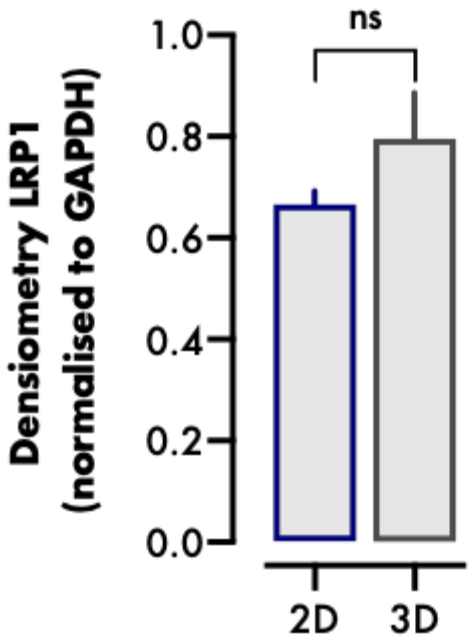

Fig 4.3 **LRP-1 expression in bEnd3 and polarised bEnd3 by western blot.** Relative expression of LRP-1 between unpolarised (2D) and polarised (3D) bEnd3 cells was determined by densitometry analysis relative to GADPH. One-way ANOVA was used for the statistical analysis alongside a post hoc Tukey's multiple comparison test (ns: $P > 0.05$).

4.3.3 Steric modulated transcytosis and endocytosis of AP2-decorated nanoparticles

Having concluded that the AP2-decorated nanoparticles were not toxic to bEnd3 after a 4-hour incubation, and that the LRP-1 expression stayed constant after the polarization of bEnd3 cells, the permeability of the nanoparticles on an *in vitro* BBB model were then investigated. AP2-decorated nanoparticles have been shown to permeate across the BBB via receptor-mediated transcytosis.

Transcytosis involves binding of nanoparticles to the BBB, endocytosis of nanoparticles into the bEnd3 cells, trafficking of nanoparticles across BBB, exocytosis to the opposite side of the cells then unbinding from the receptors to deposit nanoparticles inside the brain. Previous studies have shown that there is a specific sweet spot of N_{Ligand} for transcytosis, where having too few ligands will not allow for the formation of ligand/receptor bonds that last long enough for nanoparticles to be trafficked across the BBB, whilst having too many ligands lowers the ability of the nanoparticles to be detached once across the BBB indicating the effect avidity plays on transcytosis.[73,201] We therefore hypothesise that, in addition to N_{Ligand}, δ_L should also affect transcytosis across the BBB, as in chapter 3 we see that embedding the AP2 ligand within a polymer brush alters the binding of the nanoparticle to the target cell.

A crossing assay was performed using the AP2_1 set of nanoparticles ($\delta_L = 1$, $N_{Ligand} = 2 - 40$) to first investigate the effect N_{Ligand} had on permeability across the *in vitro* BBB model, whilst keeping $\delta_L = 1$ (i.e., ligand on the surface of the nanoparticle), with the results shown in fig 4.4. The results show that we do not observe a sweet spot for permeability as we see no peak in apparent permeability at $N_{Ligand} = 4$ and $N_{Ligand} = 8$, where a peak in the number of nanoparticles being bound was previous found for this set of particles in fig 3.5. The result coincides greatly with research by Wiley et al., where they observed that particles with a high avidity towards their target receptor (in this case the Transferrin receptor) indeed bound onto the BBB but demonstrated reduced accumulation in the brain parenchyma relative to nanoparticles with reduced avidity.[201] Interestingly, we show that apparent permeability of the nanoparticles, compared to the control where $N_{Ligand} = 0$, is negative when $N_{Ligand} = 40$ (post-hoc

Dunnett's multiple comparison: **** P ≤ 0.0001). We hypothesise that at $N_{Ligand} = 40$, the rate of unbinding from the receptors is low when nanoparticles have a high number of ligands, leading to their accumulation within the brain endothelial cell layer of the BBB, and thus the negative apparent permeability. A schematic of the proposed process when $N_{Ligand} = 40$ is seen in fig 4.5, with a zoomed in image of the proposed process in fig 4.6. The results of the experiment therefore show that we have found a nanoparticle formulation with specific parameters to stay embedded within the BBB giving us a method for transporting any medicines into the BBB if required.

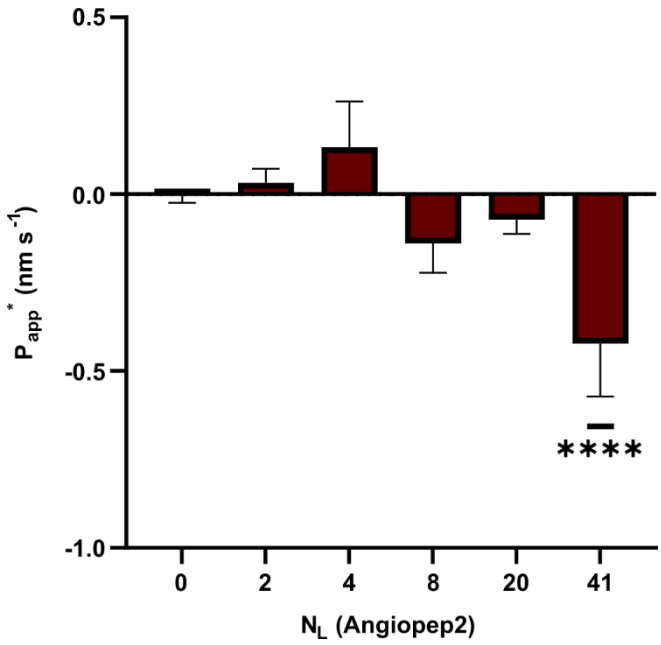

Fig 4.4 **Control-subtracted permeability of the AP2_1 set of nanoparticles across an *in vitro* BBB model.** Polarised bEnd3 cells were incubated for 4h with nanoparticles (20 μM) from the AP2_1 set ($\delta_L = 1, N_{Ligand} = 2 - 40$) and the Ctrl set ($N_{Ligand} = 0$) as a control. Each bar represents the mean ± SEM (n=3). In the diagram, $N_L = N_{Ligand}$. A one-way ANOVA was used for the statistical analysis alongside a post-hoc Dunnett's multiple comparison test (**** P ≤ 0.0001).

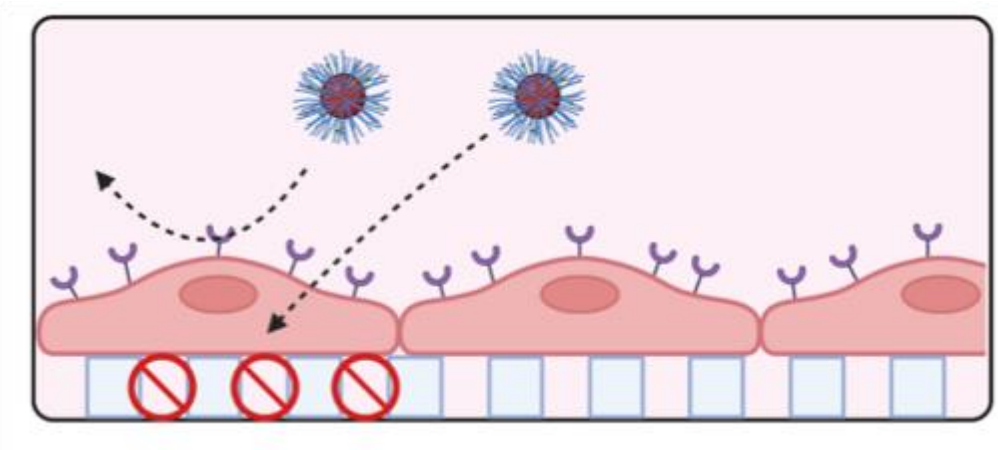

Fig 4.5 **Schematics of endocytosis of AP2-decorated nanoparticles ($\delta_L = 1$, $N_L = 40$) in an *in vitro* BBB model.** The schematic shows that nanoparticles could either not bind onto LRP-1 receptors for receptor-mediated transcytosis or did bind but may have stayed within the BBB. As the rate of unbinding of the nanoparticles did not allow the nanoparticles to get through the BBB, and thus have nanoparticles stay within the brain endothelial cell layer

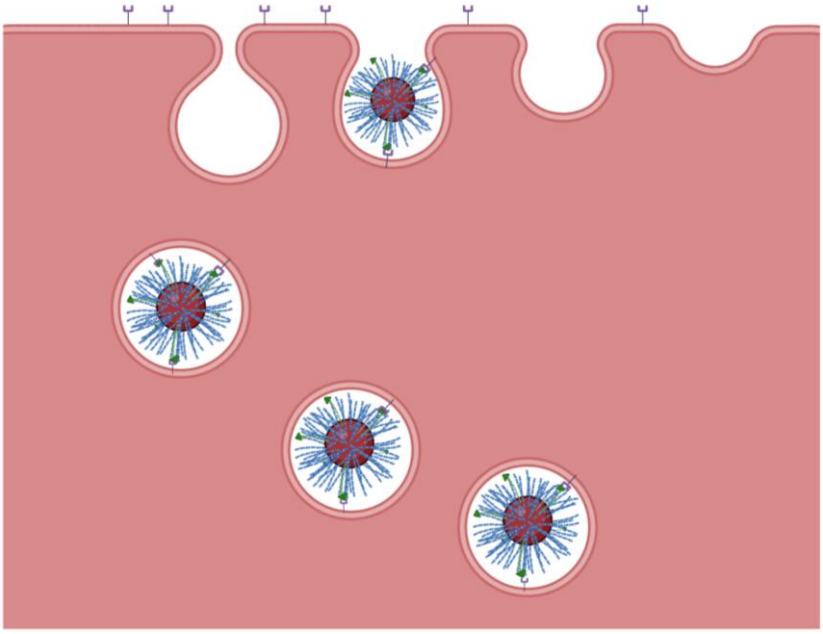

Fig 4.6 **Zoomed in schematic of the transcytosis of the AP2-decorated nanoparticles ($\delta_L = 1$, $N_L = 40$) in an *in vitro* BBB model.** Nanoparticles bound onto the receptors and nanoparticles can be endocytosed into the cell; however, the nanoparticles are unable to be exocytosed within the schematic.

A crossing assay was then performed using the AP2_0.70 set of nanoparticles ($\delta_L = 0.70$, $N_{Ligand} = 2 - 40$) to see the effect of embedding the ligand into the nanoparticle PEG polymer brush has on permeability across the BBB model. The results are shown in fig 4.7. The graph in fig 4.7 shows that there was a

statistically significant positive apparent permeability when $N_{Ligand} = 8$ for $\delta_L = 0.70$: this result again does not match the binding results found in fig 3.7 (which showed the more nanoparticles were bound on bEnd3 when $N_{Ligand} = 40$ for $\delta_L = 0.70$). The result again matches the results from Wiley et al., as by embedding the ligand within the brush, we reduced the binding avidity of the nanoparticle, and thus transcytosis could be seen.[201] The results therefore show that embedding the ligand within a polymer brush has an effect in the permeability across the BBB, as the avidity of the nanoparticle decreases with the insertion of the ligand within a polymer brush.

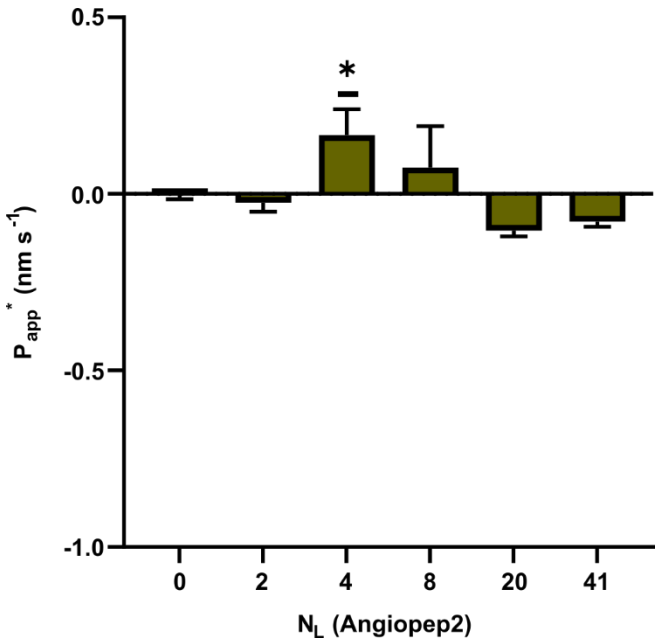

Fig 4.7 **Control-subtracted permeability of the AP2_0.70 set of nanoparticles across an *in vitro* BBB model.** Polarised bEnd3 cells were incubated for 4h with nanoparticles (20 μM) from the AP2_0.70 set ($\delta_L = 0.70, N_{Ligand} = 2 - 40$) and the Ctrl set ($N_{Ligand} = 0$) as a control. Each bar represents the mean ± SEM (n=3). In the diagram, $N_L = N_{Ligand}$. A one-way ANOVA was used for the statistical analysis alongside a post-hoc Dunnett's multiple comparison test (* P ≤ 0.05).

A study was conducted to see the effect of further embedding the ligand into the polymer brush on apparent permeability of the nanoparticles. The results of the permeability assay using the AP2_0.16 set of nanoparticles ($\delta_L = 0.16$, $N_{Ligand} = 2 - 40$) in shown in fig 4.8. When comparing the crossing results in fig

4.6 to the binding results in fig 3.8, we again see no correlation between the two as more nanoparticles of $N_{Ligand} = 20 - 40$, $\delta_L = 0.16$ bound to bEnd3 (fig 3.8) whilst there was no difference in apparent permeability across the N_{Ligand} range (fig 4.7). We assume that, when the ligand is embedded in the nanoparticle brush, we shut off the interaction with the *in vitro* BBB model.

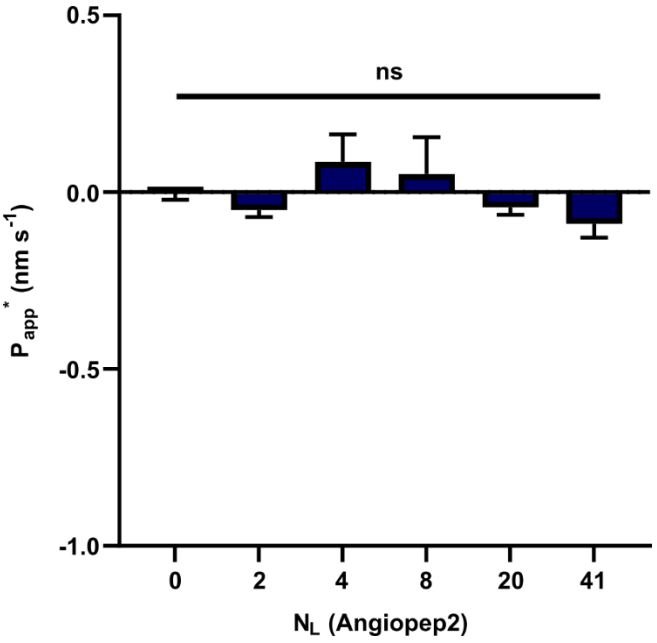

Fig 4.8 **Control-subtracted permeability of the AP2_0.16 set of nanoparticles across an *in vitro* BBB model.** Polarised bEnd3 cells were incubated for 4h with nanoparticles (20 μM) from the AP2_0.70 set ($\delta_L = 0.16, N_{Ligand} = 2 - 40$) and the Ctrl set ($N_{Ligand} = 0$) as a control. Each bar represents the mean ± SEM (n=3). In the diagram, $N_L = N_{Ligand}$. A one-way ANOVA was used for the statistical analysis alongside a post-hoc Dunnett's multiple comparison test (ns $P > 0.05$).

We have shown through the results that permeability can be adjusted by adjusting the sterics of the nanoparticle. However, the permeability of the nanoparticles is very low when compared to previously investigated AP2-decorated nanoparticles in literature. The maximum P_{app}^{*} we were able to obtain with a formulation was ~0.2 nm s^{-1}, whereas other AP2-decorate nanoparticles obtained P_{app}^{*} up to 6 nm s^{-1},[73] showing that even if the data obtained was significant, the permeability was still very low compared to previous AP2-decorated nanoparticles. We herein

hypothesise that the size of the nanoparticles may affect the crossing of the nanoparticles. The nanoparticles used to obtain a P^*_{app} of up to 6 nm s^{-1} were ~100 nm in diameter, much larger than the nanoparticles tested in this thesis (~33.27nm): in the literature, small transferrin-decorated nanoparticles of 20 nm were unable to breach into the brain parenchyma, whereas larger transferrin-decorated nanoparticles (45 and 80 nm) were able to cross the BBB and accumulate in the brain.[201] Further investigation should be conducted, altering the size of the nanoparticles, to see whether the size of nanoparticles can influence the crossing of AP2-decorated nanoparticles.

4.4 Conclusions

The second research question was explored in this chapter, where we investigate whether the crossing of nanoparticles across an *in vitro* BBB model could be controlled using sterics. We show that by embedding the ligand into a polymer brush, increasing the sterics induced with a ligand binds onto a receptor, we can control the crossing of the nanoparticles: we see that when the ligand is on the surface of the nanoparticle ($\delta_L = 1$), we were able to obtain a formulation that stayed endocytosed within the BBB model, and that when we embedded the ligand, ($\delta_L = 0.70$), we obtained a formulation able to travel across the BBB model. We further show that we could shut off interaction for crossing the BBB by embedding the ligand too far into a polymer brush. Indeed, we tested only a finite number of ligand insertion and ligand number; however, the results displayed herein gives us a starting point for further investigation on the influence of sterics on the crossing of nanoparticles across the BBB, when using LRP-1 as a ligand.

One limitation of the study was the assumption that we could compare the binding results previously to the crossing data. We assumed that as the receptor expression is the same for polarised and unpolarised bEnd3 cells, we could compare the data. Further research should be conducted, where certain binding studies should also be done on polarised bEnd3 cells, to keep the bEnd3 cell conformation constant. Furthermore, the P^*_{app} data obtained for the nanoparticles was markedly lower than previous AP2-decorated nanoparticles used in literature, which we suggest could be caused by the size of the nanoparticles. Further investigation could be performed to assess the influence of the size of the nanoparticles on the crossing of the BBB.

Chapter 5
Conclusion and Further Work

The first aim of this thesis was to investigate whether selective targeting of brain endothelial cells could be achieved. Nanoparticles were formulated with ligands for brain endothelial cell receptors LRP-1 and Glut (AP2 and Glucose). Multivalent binding was optimised towards bEnd3, a murine brain endothelial cell line we used as our model target. When using AP2-decorated nanoparticles, we observed nanoparticle formulations at all ligand insertion parameters that could bind strongly toward bEnd3: inserting the ligand deeper in a polymer brush changes the number of ligands required for a stronger bind to the target cell. This observation is novel, as to the best of my knowledge, this is the first instance in the literature investigating the effect of ligand insertion parameters on binding. We postulated the existence of an additional steric repulsion term between nanoparticles that could be reduced by embedding the ligand deeper within a polymer brush. When using glucose-decorated nanoparticles, we observed that all formulations tested held the same number per cell. A limitation when using glucose-decorated nanoparticles was that we reached a plateau in binding. Increasing the number of glucose ligands did not affect the number of nanoparticles binding to the brain endothelial cells. Future work should be done testing nanoparticles with fewer glucose ligands. When testing binding towards bEnd3 and two other cell lines (murine astrocytes, C8-D1A, and human glioblastoma, T98G), no selectivity between the three brain-isolated cell lines was observed as the binding profiles to each cell line for all three ligand insertion parameters tested were equivalent. We also observed no selectivity between the

three cell lines when using glucose as the ligand. We conclude that we could not achieve selective targeting of brain endothelial cells when comparing targeting to astrocytes and glioblastoma cell lines using either AP2 or Glucose decorated nanoparticles.

Nevertheless, we postulate that we could not achieve selective targeting due to the glycocalyx of each cell line. We herein propose that the density of the glycocalyx could correlate to the receptor conformation: a dense glycocalyx could stretch the large LRP-1 receptor, exposing binding sites on the receptor for small nanoparticles to bind to. Additionally, a novel binding experiment on glycocalyx shed brain endothelial cells was also performed to investigate what effect reducing the glycocalyx density had on binding towards the cell; however, a large limitation of the experiment was the downregulation of LRP-1 receptors and the presence of free LRP-1 in the media present after glycocalyx shedding, making it difficult to compare the data between binding to bEnd3 cells and glycocalyx shed bEnd3.

The second aim of this thesis was to deduce if we could control the crossing of nanoparticles across the BBB. Indeed, previous studies have already shown that receptor-mediated transcytosis could facilitate transport across the BBB. Still, the novelty of this thesis was to investigate the effect of inserting the ligand within a polymer brush on crossing the BBB. We observed that when the ligand was on the nanoparticle's surface (where it was not embedded within a polymer brush), the nanoparticles stayed endocytosed within the BBB at a high number of ligands. By embedding the ligand into the polymer brush, we observed a formulation (where N_{Ligand} = 4) that could cross the blood-brain barrier—further embedding

the ligand shut off any endocytosis or transcytosis, making these ligand-decorated nanoparticles akin to nanoparticles with no ligands. By embedding the ligand into a polymer brush, we could control the transcytosis across the BBB and devise a way to deliver the drug directly into the BBB. A limitation of the crossing study conducted was that the BBB *in vitro* model used was the simplest model, using only a brain endothelial cell monolayer rather than including astrocytes in the BBB model.

Multiple studies expanding from work in this thesis can be conducted. We first showed that nanoparticles could be made with specific sizes; therefore, future work can test the effect of size in addition to ligand insertion parameters and the number of ligands. The first postulation about ligand-ligand nanoparticle repulsion can be further expanded using nanoparticles with different ligands. As we observed this phenomenon using peptide ligands (such as AP2), other peptide ligands should be investigated. We observed no specific binding towards the three cell lines (when using AP2 decorated nanoparticles), which we hypothesise was due to the differences in glycocalyx density of the three cell lines: computational work should be done to investigate the influence of the glycocalyx on the LRP-1 receptor conformation. A glycocalyx shed binding assay was developed in the thesis yet had several shortcomings, such as the downregulation of LRP-1 on the glycocalyx-shed bEnd3 - future studies can be done to expand on this novel binding study, investigating for an alternative way to reduce glycocalyx density without altering the LRP-1 expression. Finally, the crossing study performed herein utilised the simplest *in vitro* BBB model, using only a monoculture of brain endothelial cells: further work can expand on this,

using either a more complex *in vitro* BBB model (one that uses both endothelial cells and astrocytes), or test the nanoparticles *in vivo*.

One of the key problems in medicine today is the ability to selectively target specific cells with therapeutics whilst leaving others unaffected. From the results in this thesis, we have furthered our knowledge on how to selectively target cells by raising awareness of both the impact of ligands being embedded within a polymer brush and the likelihood of the glycocalyx influencing receptor conformation. By building on the knowledge obtained in this thesis, we take one step closer to the elusive “magic bullet” posed by Paul Ehrlich: the concept that medicines go straight to their intended cell-structural targets.[4,205]

Chapter 6
References

1. Bracci, L., Schiavoni, G., Sistigu, A. & Belardelli, F. Immune-based mechanisms of cytotoxic chemotherapy: Implications for the design of novel and rationale-based combined treatments against cancer. *Cell Death Differ.* **21**, 15–25 (2014).
2. Srinivasarao, M. & Low, P. S. Ligand-Targeted Drug Delivery. *Chem. Rev.* **117**, 12133–12164 (2017).
3. Baker, M. Homing in on delivery. *Nature* **464**, 1225–1230 (2010).
4. Ehrlich, P. Croonian Lecture: On Immunity with Special Reference to Cell Life. *Proc. R. Soc. London. 66* **66**, 424–428 (1900).
5. Rolland, O., Turrin, C. O., Caminade, A. M. & Majoral, J. P. Dendrimers and nanomedicine: Multivalency in action. *New J. Chem.* **33**, 1809–1824 (2009).
6. Uings, I. J. & Farrow, S. N. Cell receptors and cell signalling. *Mol. Pathol.* **53**, 295–299 (2000).
7. Dai, Q. *et al.* Particle Targeting in Complex Biological Media. *Adv. Healthc. Mater.* **7**, 1–32 (2018).
8. Byrne, J. D., Betancourt, T. & Brannon-Peppas, L. Active targeting schemes for nanoparticle systems in cancer therapeutics. *Adv. Drug Deliv. Rev.* **60**, 1615–1626 (2008).
9. Attia, M. F., Anton, N., Wallyn, J., Omran, Z. & Vandamme, T. F. An overview of active and passive targeting strategies to improve the nanocarriers efficiency to tumour sites. *J. Pharm. Pharmacol.* **71**, 1185–1198 (2019).

10. Haag, R. Multivalency as a chemical organization and action principle. *Beilstein Journal of Organic Chemistry* vol. 11 848–849 (2015).
11. Mammen, M., Choi, S.-K. & Whitesides, G. M. Polyvalent Interactions in Biological Systems: Implications for Design and Use of Multivalent Ligands and Inhibitors. *Angew. Chemie* **37**, 2754–2794 (1998).
12. Martinez-Veracoechea, F. J. & Frenkel, D. Designing super selectivity in multivalent nano-particle binding. *Proc. Natl. Acad. Sci.* **108**, 10963–10968 (2011).
13. Yong, J. M., Mantaj, J., Cheng, Y. & Vllasaliu, D. Delivery of nanoparticles across the intestinal epithelium via the transferrin transport pathway. *Pharmaceutics* **11**, 298 (2019).
14. Wang, S. & Dormidontova, E. E. Nanoparticle design optimization for enhanced targeting: Monte carlo simulations. *Biomacromolecules* **11**, 1785–1795 (2010).
15. Wang, S. & Dormidontova, E. E. Nanoparticle targeting using multivalent ligands: Computer modeling. *Soft Matter* **7**, 4435–4445 (2011).
16. Albertazzi, L. *et al.* Spatiotemporal control and superselectivity in supramolecular polymers using multivalency. *Proc. Natl. Acad. Sci.* **110**, 12203–12208 (2013).
17. Dubacheva, G. V. *et al.* Superselective targeting using multivalent polymers. *J. Am. Chem. Soc.* **136**, 1722–1725 (2014).
18. Tian, X., Angioletti-Uberti, S. & Battaglia, G. On the design of precision nanomedicines. *Sci. Adv.* **6**, 1–12 (2020).
19. Ahmed, A. Myocardial beta-1 adrenoceptor down-regulation in aging and heart failure: Implications for beta-blocker use in older adults with heart failure. *Eur. J. Heart Fail.* **5**, 709–715 (2003).

20. Seeman, P. & Niznik, H. B. Dopamine receptors and transporters in Parkinson's disease and schizophrenia. *FASEB J.* **4**, 2737–2744 (1990).
21. Liu, M. *et al.* Combinatorial entropy behaviour leads to range selective binding in ligand-receptor interactions. *Nat. Commun.* **11**, (2020).
22. Carlson, C. B., Mowery, P., Owen, R. M., Dykhuizen, E. C. & Kiessling, L. L. Selective Tumor Cell Targeting Using Low-Affinity, Multivalent Interactions. *ACS Chem. Biol.* **2**, 119–127 (2007).
23. Kitov, P. I. & Bundle, D. R. On the Nature of the Multivalency Effect: A Thermodynamic Model. *J. Am. Chem. Soc.* **125**, 16271–16284 (2003).
24. Martinez-Veracoechea, F. J. & Leunissen, M. E. The entropic impact of tethering, multivalency and dynamic recruitment in systems with specific binding groups. *Soft Matter* **9**, 3213–3219 (2013).
25. Woythe, L., Tito, N. B. & Albertazzi, L. A quantitative view on multivalent nanomedicine targeting. *Adv. Drug Deliv. Rev.* **169**, 1–21 (2021).
26. Flock, T., Weatheritt, R. J., Latysheva, N. S. & Babu, M. M. Controlling entropy to tune the functions of intrinsically disordered regions. *Curr. Opin. Struct. Biol.* **26**, 62–72 (2014).
27. Curk, T., Dobnikar, J. & Frenkel, D. Design principles for super selectivity using multivalent interactions. 1–30 (2016).
28. Csizmar, C. M. *et al.* Multivalent Ligand Binding to Cell Membrane Antigens: Defining the Interplay of Affinity, Valency, and Expression Density. *J. Am. Chem. Soc.* **141**, 251–261 (2019).
29. Scheepers, M. R. W., IJzendoorn, L. J. va. & Prins, M. W. J. Multivalent weak interactions enhance selectivity of interparticle binding. *Proc. Natl. Acad. Sci. U. S. A.* **117**, 22690–22697 (2020).
30. Williams, D. H., Stephens, E., O'Brien, D. P. & Zhou, M. Understanding

noncovalent interactions: Ligand binding energy and catalytic efficiency from ligand-induced reductions in motion within receptors and enzymes. *Angew. Chemie - Int. Ed.* **43**, 6596–6616 (2004).

31. Israelachvili, J. Differences between non-specific and bio-specific, and between equilibrium and non-equilibrium, interactions in biological systems. *Q. Rev. Biophys.* **38**, 331–337 (2005).
32. Evans, E., Merkel, R., Nassoy, P., Leung, A. & Ritchie, K. Energy landscapes of receptor-ligand bonds explored with dynamic force spectroscopy. *Nature* **397**, 50–53 (1999).
33. Angioletti-Uberti, S. Exploiting Receptor Competition to Enhance Nanoparticle Binding Selectivity. *Phys. Rev. Lett.* **118**, 1–5 (2017).
34. Weinbaum, S., Tarbell, J. M. & Damiano, E. R. The Structure and Function of the Endothelial Glycocalyx Layer. *Annu. Rev. Biomed. Eng.* **9**, 121–167 (2007).
35. Reitsma, S., Slaaf, D. W., Vink, H., Van Zandvoort, M. A. M. J. & Oude Egbrink, M. G. A. The endothelial glycocalyx: Composition, functions, and visualization. *Pflugers Arch. Eur. J. Physiol.* **454**, 345–359 (2007).
36. Kutuzov, N., Flyvbjerg, H. & Lauritzen, M. Contributions of the glycocalyx, endothelium, and extravascular compartment to the blood–brain barrier. *Proc. Natl. Acad. Sci.* **115**, E9429–E9438 (2018).
37. Van Haaren, P. M. A., VanBavel, E., Vink, H. & Spaan, J. A. E. Localization of the permeability barrier to solutes in isolated arteries by confocal microscopy. *Am. J. Physiol. Circ. Physiol.* **285**, H2848–H2856 (2003).
38. Kuo, J. C. H., Gandhi, J. G., Zia, R. N. & Paszek, M. J. Physical biology of the cancer cell glycocalyx. *Nat. Phys.* **14**, 658–669 (2018).

39. Maslanka Figueroa, S., Fleischmann, D., Beck, S. & Goepferich, A. The Effect of Ligand Mobility on the Cellular Interaction of Multivalent Nanoparticles. *Macromol. Biosci.* **1900427**, (2020).

40. Dubacheva, G. V., Curk, T., Auzély-Velty, R., Frenkel, D. & Richter, R. P. Designing multivalent probes for tunable superselective targeting. *Proc. Natl. Acad. Sci.* **112**, 5579–5584 (2015).

41. Hammink, R. *et al.* Controlling T-Cell Activation with Synthetic Dendritic Cells Using the Multivalency Effect. *ACS Omega* **2**, 937–945 (2017).

42. Bila, H., Paloja, K., Caroprese, V., Kononenko, A. & Bastings, M. M. C. Multivalent Pattern Recognition through Control of Nano-Spacing in Low-Valency Super-Selective Materials. *J. Am. Chem. Soc.* (2022)

43. Curk, T. & Tito, N. B. First-order 'hyper-selective' binding transition of multivalent particles under force. *J. Phys. Condens. Matter* **32**, 1–22 (2020).

44. Curk, T., Dubacheva, G. V., Brisson, A. R. & Richter, R. P. Controlling Superselectivity of Multivalent Interactions with Cofactors and Competitors. *J. Am. Chem. Soc.* **144**, 17346–17350 (2022).

45. Muro, S. *et al.* Control of endothelial targeting and intracellular delivery of therapeutic enzymes by modulating the size and shape of ICAM-1-targeted carriers. *Mol. Ther.* **16**, 1450–1458 (2008).

46. Liu, X. *et al.* Size Dependent Cellular Uptake of Rod-like Bionanoparticles with Different Aspect Ratios. *Sci. Rep.* **6**, 2–11 (2016).

47. Da Silva-Candal, A. *et al.* Shape effect in active targeting of nanoparticles to inflamed cerebral endothelium under static and flow conditions. *J. Control. Release* **309**, 94–105 (2019).

48. Blanco, E., Shen, H. & Ferrari, M. Principles of nanoparticle design for

overcoming biological barriers to drug delivery. *Nat. Biotechnol.* **33**, 941–951 (2015).

49. Yamamoto, Y., Nagasaki, Y., Kato, Y., Sugiyama, Y. & Kataoka, K. Long-circulating poly(ethylene glycol)-poly(D,L-lactide) block copolymer micelles with modulated surface charge. *J. Control. release Off. J. Control. Release Soc.* **77**, 27–38 (2001).

50. Curk, T., Dobnikar, J. & Frenkel, D. Optimal multivalent targeting of membranes with many distinct receptors. *Proc. Natl. Acad. Sci.* **114**, 7210–7215 (2017).

51. Fan, Y. *et al.* Burden and trends of brain and central nervous system cancer from 1990 to 2019 at the global, regional, and country levels. *Arch. Public Heal.* **80**, 1–14 (2022).

52. Koo, Y. E. L. *et al.* Brain cancer diagnosis and therapy with nanoplatforms. *Adv. Drug Deliv. Rev.* **58**, 1556–1577 (2006).

53. Wang, G. Y., Rayner, S. L., Chung, R., Shi, B. Y. & Liang, X. J. Advances in nanotechnology-based strategies for the treatments of amyotrophic lateral sclerosis. *Mater. Today Bio* **6**, 100055 (2020).

54. Daneman, R. & Prat, A. The Blood-Brain Barrier. *Cold Spring Harbot Perspect. Biol.* **7**, 1–23 (2015).

55. Arvanitis, C. D., Ferraro, G. B. & Jain, R. K. The blood–brain barrier and blood–tumour barrier in brain tumours and metastases. *Nat. Rev. Cancer* **20**, 26–41 (2020).

56. Kadry, H., Noorani, B. & Cucullo, L. A blood–brain barrier overview on structure, function, impairment, and biomarkers of integrity. *Fluids Barriers CNS* **17**, 1–24 (2020).

57. Banks, W. A. From blood-brain barrier to blood-brain interface: New

opportunities for CNS drug delivery. *Nat. Rev. Drug Discov.* **15**, 275–292 (2016).

58. Gastfriend, B. D., Palecek, S. P. & Shusta, E. V. Modeling the blood–brain barrier: Beyond the endothelial cells. *Curr. Opin. Biomed. Eng.* **5**, 6–12 (2018).
59. Terstappen, G. C., Meyer, A. H., Bell, R. D. & Zhang, W. Strategies for delivering therapeutics across the blood–brain barrier. *Nat. Rev. Drug Discov.* **20**, 362–383 (2021).
60. Xiao, G. & Gan, L.-S. Receptor-Mediated Endocytosis and Brain Delivery of Therapeutic Biologics. *Int. J. Cell Biol.* **2013**, 1–14 (2013).
61. Worzfeld, T. & Schwaninger, M. Apicobasal polarity of brain endothelial cells. *J. Cereb. Blood Flow Metab.* **36**, 340–362 (2016).
62. Haqqani, A. S. *et al.* Endosomal trafficking regulates receptor-mediated transcytosis of antibodies across the blood brain barrier. *J. Cereb. Blood Flow Metab.* **38**, 727–740 (2018).
63. Pulgar, V. M. Transcytosis to cross the blood brain barrier, new advancements and challenges. *Front. Neurosci.* **13**, 1–9 (2019).
64. Demeule, M. *et al.* Identification and Design of Peptides as a New Drug Delivery System for the Brain. *J. Pharmacol. Exp. Ther.* **324**, 1064 LP – 1072 (2008).
65. Demeule, M. *et al.* Involvement of the low-density lipoprotein receptor-related protein in the transcytosis of the brain delivery vector Angiopep-2. *J. Neurochem.* **106**, 1534–1544 (2008).
66. Régina, A. *et al.* Antitumour activity of ANG1005, a conjugate between paclitaxel and the new brain delivery vector Angiopep-2. *Br. J. Pharmacol.* **155**, 185–197 (2008).

67. Habib, S. & Singh, M. Angiopep-2-Modified Nanoparticles for Brain-Directed Delivery of Therapeutics: A Review. *Polymers* vol. 14 (2022).

68. Shi, X. X. *et al.* Angiopep-2 conjugated nanoparticles loaded with doxorubicin for the treatment of primary central nervous system lymphoma. *Biomater. Sci.* **8**, 1290–1297 (2020).

69. Lu, F. *et al.* Angiopep-2-conjugated poly(ethylene glycol)-co- poly(ε-caprolactone) polymersomes for dual-targeting drug delivery to glioma in rats. *Int. J. Nanomedicine* **12**, 2117–2127 (2017).

70. Tao, J. *et al.* Angiopep-2-Conjugated "Core–Shell" Hybrid Nanovehicles for Targeted and pH-Triggered Delivery of Arsenic Trioxide into Glioma. *Mol. Pharm.* **16**, 786–797 (2019).

71. Tian, X. *et al.* LRP-1-mediated intracellular antibody delivery to the Central Nervous System. *Sci. Rep.* **5**, 1–14 (2015).

72. Wang, Q. *et al.* Molecular mechanism of membrane constriction and tubulation mediated by the F-BAR protein Pacsin/Syndapin. *Proc. Natl. Acad. Sci.* **106**, 12700–12705 (2009).

73. Tian, X. *et al.* On the shuttling across the blood-brain barrier via tubule formation: Mechanism and cargo avidity bias. *Sci. Adv.* **6**, 1–16 (2020).

74. Yu, Y. J. *et al.* Boosting brain uptake of a therapeutic antibody by reducing its affinity for a transcytosis target. *Sci. Transl. Med.* **3**, 84ra44 (2011).

75. Niewoehner, J. *et al.* Increased Brain Penetration and Potency of a Therapeutic Antibody Using a Monovalent Molecular Shuttle. *Neuron* **81**, 49–60 (2014).

76. Anraku, Y. *et al.* Glycaemic Control Boosts Glucosylated Nanocarrier Crossing the BBB into the Brain. *Nat. Commun.* **8**, 1–9 (2017).

77. Uchida, Y. *et al.* Quantitative targeted absolute proteomics of human blood-brain barrier transporters and receptors. *J. Neurochem.* **117**, 333–345 (2011).

78. Joost, H. G. & Thorens, B. The extended GLUT-family of sugar/polyol transport facilitators: nomenclature, sequence characteristics, and potential function of its novel members (review). *Mol. Membr. Biol.* **18**, 247–256 (2001).

79. Mueckler, M. & Thorens, B. The SLC2 (GLUT) family of membrane transporters. *Mol. Aspects Med.* **34**, 121–138 (2013).

80. Vemula, S. *et al.* A functional role for sodium-dependent glucose transport across the blood-brain barrier during oxygen glucose deprivation. *J. Pharmacol. Exp. Ther.* **328**, 487–495 (2009).

81. Patching, S. G. Glucose Transporters at the Blood-Brain Barrier: Function, Regulation and Gateways for Drug Delivery. *Mol. Neurobiol.* **54**, 1046–1077 (2017).

82. Qin, Y. *et al.* In vitro and in vivo investigation of glucose-mediated brain-targeting liposomes. *Journal of Drug Targeting* vol. 18 536–549 (2010).

83. Xie, F. *et al.* Investigation of glucose-modified liposomes using polyethylene glycols with different chain lengths as the linkers for brain targeting. *Int. J. Nanomedicine* **7**, 163–175 (2012).

84. Cucullo, L., Aumayr, B., Rapp, E. & Janigro, D. Drug delivery and in vitro models of the blood-brain barrier. *Curr. Opin. Drug Discov. Dev.* **8**, 89–99 (2005).

85. Ramos-Zaldívar, H. M. *et al.* Extracellular vesicles through the blood–brain barrier: a review. *Fluids Barriers CNS* **19**, 1–15 (2022).

86. Hajal, C., Le Roi, B., Kamm, R. D. & Maoz, B. M. Biology and Models of

the Blood-Brain Barrier. *Annu. Rev. Biomed. Eng.* **23**, 359–384 (2021).

87. Helms, H. C. *et al.* In vitro models of the blood-brain barrier: An overview of commonly used brain endothelial cell culture models and guidelines for their use. *J. Cereb. Blood Flow Metab.* **36**, 862–890 (2015).

88. Qosa, H. *et al.* High-Throughput Screening for Identification of Blood-Brain Barrier Integrity Enhancers: A Drug Repurposing Opportunity to Rectify Vascular Amyloid Toxicity. *J. Alzheimers. Dis.* **53**, 1499–1516 (2016).

89. Garcia-Garcia, E. *et al.* A relevant in vitro rat model for the evaluation of blood-brain barrier translocation of nanoparticles. *Cell. Mol. Life Sci.* **62**, 1400–1408 (2005).

90. Patabendige, A., Skinner, R. A., Morgan, L. & Joan Abbott, N. A detailed method for preparation of a functional and flexible blood-brain barrier model using porcine brain endothelial cells. *Brain Res.* **1521**, 16–30 (2013).

91. Eigenmann, D. E. *et al.* Comparative study of four immortalized human brain capillary endothelial cell lines, hCMEC/D3, hBMEC, TY10, and BB19, and optimization of culture conditions, for an in vitro blood-brain barrier model for drug permeability studies. *Fluids Barriers CNS* **10**, (2013).

92. Chen, C. C. *et al.* Elucidation of Exosome Migration across the Blood-Brain Barrier Model In Vitro. *Cell. Mol. Bioeng.* **9**, 509–529 (2016).

93. Gaillard, P. J. *et al.* Establishment and functional characterization of an in vitro model of the blood-brain barrier, comprising a co-culture of brain capillary endothelial cells and astrocytes. *Eur. J. Pharm. Sci.* **12**, 215–222 (2001).

94. Hayashi, K. *et al.* Effects of hypoxia on endothelial/pericytic co-culture model of the blood-brain barrier. *Regul. Pept.* **123**, 77–83 (2004).

95. Montet, X., Funovics, M., Montet-Abou, K., Weissleder, R. & Josephson, L. Multivalent Effects of RGD Peptides Obtained by Nanoparticle Display. *J. Med. Chem.* **49**, 6087–6093 (2006).

96. Anselmo, A. C. & Mitragotri, S. Nanoparticles in the clinic: an update. Bioeng Transl Med 4: e10143. (2019).

97. Letao Xu, Xing Wang, Yun Liu, Guangze Yang, Robert J. Falconer, and C.-X. Z. Lipid Nanoparticles for Drug Delivery. *Adv. NanoBiomed Res.* **2**, 2100109 (2022).

98. Viegas, C., Seck, F. & Fonte, P. An insight on lipid nanoparticles for therapeutic proteins delivery. *J. Drug Deliv. Sci. Technol.* **77**, (2022).

99. Ahmad, E. *et al.* Ligand decorated biodegradable nanomedicine in the treatment of cancer. *Pharmacol. Res.* **167**, 105544 (2021).

100. Bangham, A. D., Standish, M. M. & Watkins, J. C. Diffusion of univalent ions across the lamellae of swollen phospholipids. *J. Mol. Biol.* **13**, 238–252 (1965).

101. Song, X.-L. *et al.* Application of multifunctional targeting epirubicin liposomes in the treatment of non-small-cell lung cancer. *Int. J. Nanomedicine* **12**, 7433–7451 (2017).

102. Markov, O. V. *et al.* Multicomponent mannose-containing liposomes efficiently deliver RNA in murine immature dendritic cells and provide productive anti-tumour response in murine melanoma model. *J. Control. Release* **213**, 45–56 (2015).

103. Barenholz, Y. Doxil® - The first FDA-approved nano-drug: Lessons learned. *J. Control. Release* **160**, 117–134 (2012).

104. Bulbake, U., Doppalapudi, S., Kommineni, N. & Khan, W. Liposomal formulations in clinical use: An updated review. *Pharmaceutics* **9**, 1–33 (2017).

105. Vemuri, S. & Rhodes, C. T. Preparation and characterization of liposomes as therapeutic delivery systems: a review. *Pharm. Acta Helv.* **70**, 95–111 (1995).

106. De Gier, J., Mandersloot, J. G. & Van Deenen, L. L. M. Lipid composition and permeability of liposomes. *BBA - Biomembr.* **150**, 666–675 (1968).

107. Rideau, E., Dimova, R., Schwille, P., Wurm, F. R. & Landfester, K. Liposomes and polymersomes: a comparative review towards cell mimicking. *Chem. Soc. Rev.* **47**, 8572–8610 (2018).

108. Mohamed, M. *et al.* PEGylated liposomes: immunological responses. *Sci. Technol. Adv. Mater.* **20**, 710–724 (2019).

109. Green, A. E. & Rose, P. G. Pegylated liposomal doxorubicin in ovarian cancer. *Int. J. Nanomedicine* **1**, 229–239 (2006).

110. Albuquerque, L. J. C. *et al.* pH-responsive polymersome-mediated delivery of doxorubicin into tumor sites enhances the therapeutic efficacy and reduces cardiotoxic effects. *J. Control. Release* **332**, 529–538 (2021).

111. Chu, C. *et al.* Proliposomes for oral delivery of dehydrosilymarin: preparation and evaluation in vitro and in vivo. *Acta Pharmacol. Sin.* **32**, 973–980 (2011).

112. Moquin, A., Ji, J., Neibert, K., Winnik, F. M. & Maysinger, D. Encapsulation and Delivery of Neutrophic Proteins and Hydrophobic Agents Using PMOXA-PDMS-PMOXA Triblock Polymersomes. *ACS Omega* **3**, 13882–13893 (2018).

113. Noble, G. T., Stefanick, J. F., Ashley, J. D., Kiziltepe, T. & Bilgicer, B.

Ligand-targeted liposome design: challenges and fundamental considerations. *Trends Biotechnol.* **32**, 32–45 (2014).

114. Wang, W. liang, Ma, X. jing & Yu, X. fei. pH-responsive polymersome based on PMCP-b-PDPA as a drug delivery system to enhance cellular internalization and intracellular drug release. *Chinese J. Polym. Sci. (English Ed.* **35**, 1352–1362 (2017).
115. Pearson, R. T., Warren, N. J., Lewis, A. L., Armes, S. P. & Battaglia, G. Effect of pH and Temperature on PMPC − PDPA Copolymer Self-Assembly. (2013).
116. Puglisi, A., Bayir, E., Timur, S. & Yagci, Y. pH-Responsive Polymersome Microparticles as Smart Cyclodextrin-Releasing Agents. *Biomacromolecules* **20**, 4001–4007 (2019).
117. Patel, T., Zhou, J., Piepmeier, J. M. & Saltzman, W. M. Polymeric nanoparticles for drug delivery to the central nervous system. *Adv. Drug Deliv. Rev.* **64**, 701–705 (2012).
118. Lu, H., Zhang, S., Wang, J. & Chen, Q. A Review on Polymer and Lipid-Based Nanocarriers and Its Application to Nano-Pharmaceutical and Food-Based Systems. *Front. Nutr.* **8**, 1–13 (2021).
119. Aibani, N., Khan, T. N. & Callan, B. Liposome mimicking polymersomes; A comparative study of the merits of polymersomes in terms of formulation and stability. *International Journal of Pharmaceutics: X* vol. 2 (2020).
120. Smart, T. *et al.* Block copolymer nanostructures. *Nano Today* **3**, 38–46 (2008).
121. Messager, L., Gaitzsch, J., Chierico, L. & Battaglia, G. Novel aspects of encapsulation and delivery using polymersomes. *Curr. Opin. Pharmacol.*

18, 104–111 (2014).

122. Lomas, H. *et al.* Efficient encapsulation of plasmid DNA in pH-sensitive PMPC-PDPA polymersomes: Study of the effect of PDPA block length on copolymer-DNA binding affinity. *Macromol. Biosci.* **10**, 513–530 (2010).
123. Kato, Y. *et al.* Acidic extracellular microenvironment and cancer. *Cancer Cell Int.* **13**, 1–8 (2013).
124. Kang, J. S., DeLuca, P. P. & Lee, K. C. Emerging PEGylated drugs. *Expert Opin. Emerg. Drugs* **14**, 363–380 (2009).
125. Gref, R. *et al.* Biodegradable Long-Circulating Polymeric Nanospheres. **263**, 1600–1603 (1994).
126. Knop, K., Hoogenboom, R., Fischer, D. & Schubert, U. S. Poly(ethylene glycol) in drug delivery: Pros and cons as well as potential alternatives. *Angew. Chemie - Int. Ed.* **49**, 6288–6308 (2010).
127. Wei, Q. *et al.* Protein interactions with polymer coatings and biomaterials. *Angew. Chemie - Int. Ed.* **53**, 8004–8031 (2014).
128. Alcantar, N. A., Aydil, E. S. & Israelachvili, J. N. Polyethylene glycol-coated biocompatible surfaces. *J. Biomed. Mater. Res.* **51**, 343–351 (2000).
129. Duncan, R. Polymer conjugates as anticancer nanomedicines. *Nat. Rev. Cancer* **6**, 688–701 (2006).
130. Glavas, L., Olsén, P., Odelius, K. & Albertsson, A. C. Achieving micelle control through core crystallinity. *Biomacromolecules* **14**, 4150–4156 (2013).
131. Ceonzo, K. *et al.* Polyglycolic Acid-Induced Inflammation: Role of Hydrolysis and Resulting Complement Activation. *Tissue Eng.* **12**, 301–308 (2006).

132. Olsén, P., Borke, T., Odelius, K. & Albertsson, A. C. ε-Decalactone: A thermoresilient and toughening comonomer to poly(l -lactide). *Biomacromolecules* **14**, 2883–2890 (2013).

133. Grossen, P., Witzigmann, D., Sieber, S. & Huwyler, J. PEG-PCL-based nanomedicines: A biodegradable drug delivery system and its application. *J. Control. Release* **260**, 46–60 (2017).

134. Zhang, L. *et al.* Preparation and evaluation of PCL-PEG-PCL polymeric nanoparticles for doxorubicin delivery against breast cancer. *RSC Adv.* **6**, 54727–54737 (2016).

135. Alami-Milani, M., Zakeri-Milani, P., Valizadeh, H., Salehi, R. & Jelvehgari, M. Preparation and evaluation of PCL-PEG-PCL micelles as potential nanocarriers for ocular delivery of dexamethasone. *Iran. J. Basic Med. Sci.* **21**, 153–164 (2018).

136. Stjerndahl, A., Finne-Wistrand, A., Albertsson, A. C., Bäckesjö, C. M. & Lindgren, U. Minimization of residual tin in the controlled Sn(II)octoate-catalyzed polymerization of ε-caprolactone. *J. Biomed. Mater. Res. - Part A* **87**, 1086–1091 (2008).

137. Xiao, R. Z. *et al.* Recent advances in PEG-PLA block copolymer nanoparticles. *Int. J. Nanomedicine* **5**, 1057–1065 (2010).

138. Jalali, N. *et al.* Surface modification of poly(lactide-co-glycolide) nanoparticles by d-α-tocopheryl polyethylene glycol 1000 succinate as potential carrier for the delivery of drugs to the brain. *Colloids Surfaces A Physicochem. Eng. Asp.* **392**, 335–342 (2011).

139. Jikei, M., Suga, T., Yamadoi, Y. & Matsumoto, K. Synthesis and properties of poly(L-lactide-co-glycolide) -b-Poly(ε-caprolactone) multiblock copolymers formed by self-polycondensation of diblock

macromonomers. *Polym. J.* **49**, 369–375 (2017).

140. Rodríguez-Arco, L. *et al.* Molecular bionics – engineering biomaterials at the molecular level using biological principles. *Biomaterials* **192**, 26–50 (2019).
141. Mezzasalma, L., De Winter, J., Taton, D. & Coulembier, O. Benzoic acid-organocatalyzed ring-opening (co)polymerization (ORO(c)P) of l-lactide and ε-caprolactone under solvent-free conditions: From simplicity to recyclability. *Green Chem.* **20**, 5385–5396 (2018).
142. Deng, Y. *et al.* Poly(ε-caprolactone)-block-polysarcosine by Ring-Opening Polymerization of Sarcosine N-Thiocarboxyanhydride: Synthesis and Thermoresponsive Self-Assembly. *Biomacromolecules* **16**, 3265–3274 (2015).
143. Blanazs, A., Armes, S. P. & Ryan, A. J. Self-assembled block copolymer aggregates: From micelles to vesicles and their biological applications. *Macromol. Rapid Commun.* **30**, 267–277 (2009).
144. Israelachvili, J. N. *Intermolecular and Surface Forces*. (2011).
145. Fernyhough, C., Ryan, A. J. & Battaglia, G. PH controlled assembly of a polybutadiene-poly(methacrylic acid) copolymer in water: Packing considerations and kinetic limitations. *Soft Matter* **5**, 1674–1682 (2009).
146. Discher, D. E. & Ahmed, F. Polymersomes. *Annu. Rev. Biomed. Eng.* **8**, 323–341 (2006).
147. Zhang, L. & Eisenberg, A. Thermodynamic vs kinetic aspects in the formation and morphological transitions of crew-cut aggregates produced by self-assembly of polystyrene-b-poly(acrylic acid) block copolymers in dilute solution. *Macromolecules* **32**, 2239–2249 (1999).
148. Contini, C. *et al.* Bottom-Up Evolution of Vesicles from Disks to High-

Genus Polymersomes. *iScience* vol. 7 132–144 (2018).

149. Dionzou, M. *et al.* Comparison of methods for the fabrication and the characterization of polymer self-assemblies: what are the important parameters? *Soft Matter* **12**, 2166—2176 (2016).
150. Shuai, X., Ai, H., Nasongkla, N., Kim, S. & Gao, J. Micellar carriers based on block copolymers of poly(ε-caprolactone) and poly(ethylene glycol) for doxorubicin delivery. *J. Control. Release* **98**, 415–426 (2004).
151. Aliabadi, H. M., Mahmud, A., Sharifabadi, A. D. & Lavasanifar, A. Micelles of methoxy poly(ethylene oxide)-b-poly(ε-caprolactone) as vehicles for the solubilization and controlled delivery of cyclosporine A. *J. Control. Release* **104**, 301–311 (2005).
152. Hu, Y., Xie, J., Tong, Y. W. & Wang, C. H. Effect of PEG conformation and particle size on the cellular uptake efficiency of nanoparticles with the HepG2 cells. *J. Control. Release* **118**, 7–17 (2007).
153. Song, Z., Zhu, W., Liu, N., Yang, F. & Feng, R. Linolenic acid-modified PEG-PCL micelles for curcumin delivery. *Int. J. Pharm.* **471**, 312–321 (2014).
154. Aliabadi, H. M. *et al.* Encapsulation of hydrophobic drugs in polymeric micelles through co-solvent evaporation: The effect of solvent composition on micellar properties and drug loading. *Int. J. Pharm.* **329**, 158–165 (2007).
155. Gauthier, M. A., Gibson, M. I. & Klok, H. A. Synthesis of functional polymers by post-polymerization modification. *Angew. Chemie - Int. Ed.* **48**, 48–58 (2009).
156. Miura, Y. *et al.* Cyclic RGD-Linked Polymeric Micelles for Targeted Delivery of Platinum Anticancer Drugs to Glioblastoma through the

Blood–Brain Tumor Barrier. *ACS Nano* **7**, 8583–8592 (2013).

157. Nobs, L., Buchegger, F., Gurny, R. & Allémann, E. Current methods for attaching targeting ligands to liposomes and nanoparticles. *J. Pharm. Sci.* **93**, 1980–1992 (2004).
158. Chattopadhyay, N. *et al.* Design and characterization of HER-2-targeted gold nanoparticles for enhanced X-radiation treatment of locally advanced breast cancer. *Mol. Pharm.* **7**, 2194–2206 (2010).
159. Petrelli, A., Borsali, R., Fort, S. & Halila, S. Oligosaccharide-based block copolymers: Metal-free thiol-maleimide click conjugation and self-assembly into nanoparticles. *Carbohydr. Polym.* **124**, 109–116 (2015).
160. Lallana, E., Riguera, R. & Fernandez-Megia, E. Reliable and efficient procedures for the conjugation of biomolecules through huisgen azide-alkyne cycloadditions. *Angew. Chemie - Int. Ed.* **50**, 8794–8804 (2011).
161. Fievez, V. *et al.* Targeting nanoparticles to M cells with non-peptidic ligands for oral vaccination. *Eur. J. Pharm. Biopharm.* **73**, 16–24 (2009).
162. Zhong, Y. *et al.* CRGD-directed, NIR-responsive and robust AuNR/PEG-PCL hybrid nanoparticles for targeted chemotherapy of glioblastoma in vivo. *J. Control. Release* **195**, 63–71 (2014).
163. Zhu, Y. *et al.* CRGD-functionalized reduction-sensitive shell-sheddable biodegradable micelles mediate enhanced doxorubicin delivery to human glioma xenografts in vivo. *J. Control. Release* **233**, 29–38 (2016).
164. Chi, Y. *et al.* Glioma homing peptide-modified PEG-PCL nanoparticles for enhanced anti-glioma therapy. *J. Drug Target.* **24**, 224–232 (2016).
165. Pang, Z. *et al.* Preparation and brain delivery property of biodegradable polymersomes conjugated with OX26. *J. Control. Release* **128**, 120–127 (2008).

166. Hu, Q. *et al.* CGKRK-modified nanoparticles for dual-targeting drug delivery to tumor cells and angiogenic blood vessels. *Biomaterials* **34**, 9496–9508 (2013).

167. Xin, H. *et al.* Anti-glioblastoma efficacy and safety of paclitaxel-loading Angiopep-conjugated dual targeting PEG-PCL nanoparticles. *Biomaterials* **33**, 8167–8176 (2012).

168. Lahnsteiner, M. *et al.* Improving the Stability of Maleimide-Thiol Conjugation for Drug Targeting. *Chemistry* **26**, 15867–15870 (2020).

169. Kolb, H. C., Finn, M. G. & Sharpless, K. B. Click Chemistry: Diverse Chemical Function from a Few Good Reactions. *Angew. Chemie - Int. Ed.* **40**, 2004–2021 (2001).

170. Parrish, B., Breitenkamp, R. B. & Emrick, T. PEG- and Peptide-Grafted Aliphatic Polyesters by Click Chemistry. 7404–7410 (2005)

171. Li, H., Aneja, R. & Chaiken, I. Click Chemistry in Peptide-Based Drug Design. 9797–9817 (2013)

172. Liang, L. & Astruc, D. The copper (I) -catalyzed alkyne-azide cycloaddition (CuAAC) “ click ” reaction and its applications . An overview. *Coord. Chem. Rev.* **255**, 2933–2945 (2011).

173. Kohane, D. S. & Langer, R. Biocompatibility and drug delivery systems. *Chem. Sci.* **1**, 441–446 (2010).

174. Williams, D. F. On the mechanisms of biocompatibility. *Biomaterials* **29**, 2941–2953 (2008).

175. Gulati, N. M., Stewart, P. L. & Steinmetz, N. F. Bioinspired Shielding Strategies for Nanoparticle Drug Delivery Applications. *Mol. Pharm.* **15**, 2900–2909 (2018).

176. Yu, Q., Zhang, Y., Wang, H., Brash, J. & Chen, H. Anti-fouling bioactive

surfaces. *Acta Biomater.* **7**, 1550–1557 (2011).

177. Labet, M. & Thielemans, W. Synthesis of polycaprolactone: A review. *Chem. Soc. Rev.* **38**, 3484–3504 (2009).
178. Macdonald, R. T. *et al.* Enzyme-Catalyzed e-Caprolactone Ring-Opening Polymerization. 73–78 (1995).
179. Robertson, J. D. *et al.* Purification of Nanoparticles by Size and Shape. *Sci. Rep.* **6**, 1–9 (2016).
180. Smith, P. K. *et al.* Measurement of protein using bicinchoninic acid. *Anal. Biochem.* **150**, 76–85 (1985).
181. Brenner, S. & Horne, R. W. A negative staining method for high resolution electron microscopy of viruses. *BBA - Biochim. Biophys. Acta* **34**, 103–110 (1959).
182. Kovuttikulrangsie, S. & Sakdapipanich, J. T. The molecular weight (MW) and molecular weight distribution (MWD) of NR from different age and clone Hevea trees. *Songklanakarin J. Sci. Technol.* **27**, 338–342 (2005).
183. Kinard, L., Kasper, K. & Mikos, A. Drying poly (ethylene glycol). *Protoc. Exch.* 1–4 (2015).
184. Fairley, N., Hoang, B. & Allen, C. J. Morphological control of poly(ethylene glycol)-block-poly(ε-caprolactone) copolymer aggregates in aqueous solution. *Biomacromolecules* **9**, 2283–2291 (2008).
185. Bhattacharjee, S. DLS and zeta potential - What they are and what they are not? *J. Control. Release* **235**, 337–351 (2016).
186. Teraoka, I. *Polymer Solutions: An Introduction to Physical Properties*. vol. 1 (2002).
187. Manolescu, A. R., Witkowska, K., Kinnaird, A., Cessford, T. & Cheeseman, C. Facilitated hexose transporters: New perspectives on

form and function. *Physiology* **22**, 234–240 (2007).

188. Jiang, X. *et al.* Nanoparticles of 2-deoxy-d-glucose functionalized poly(ethylene glycol)-co-poly(trimethylene carbonate) for dual-targeted drug delivery in glioma treatment. *Biomaterials* **35**, 518–529 (2014).
189. Joseph, A. *et al.* Chemotactic synthetic vesicles: Design and applications in blood-brain barrier crossing. *Sci. Adv.* **3**, (2017).
190. Marin, V., Kaplanski, G., Grès, S., Farnarier, C. & Bongrand, P. Endothelial cell culture: Protocol to obtain and cultivate human umbilical endothelial cells. *J. Immunol. Methods* **254**, 183–190 (2001).
191. Chennazhy, K. P. & Krishnan, L. K. Effect of passage number and matrix characteristics on differentiation of endothelial cells cultured for tissue engineering. *Biomaterials* **26**, 5658–5667 (2005).
192. BioRad. Handcasting Polyacrylamide Gels. 3–6 (2014).
193. Gorr, T. A. & Vogel, J. Western blotting revisited: Critical perusal of underappreciated technical issues. *Proteomics - Clin. Appl.* **9**, 396–405 (2015).
194. Bilcikova, J. *et al.* Copper affects steroidogenesis and viability of human adrenocortical carcinoma (NCI-H295R) cell line in vitro. *J. Environ. Sci. Heal. - Part A Toxic/Hazardous Subst. Environ. Eng.* **55**, 1070–1077 (2020).
195. Wang, X. yang *et al.* Cytotoxic activities of some selected medicinal plants of the genus euphorbia. *J. Med. Plant Res.* **5**, 6766–6769 (2011).
196. ISO 10993-5 Biological evaluation of medical devices - Part 5: Tests for in vitro cytotoxicity. *Int. Stand.* 1–34 (2009).
197. Bertrand, Y. *et al.* Transport characteristics of a novel peptide platform for CNS therapeutics. *J. Cell. Mol. Med.* **14**, 2827–2839 (2010).

198. Lillis, A. P., Duyn, L. B. Van, Murphy-ullrich, J. E. & Dudley, K. The low density lipoprotein receptor-related protein 1: Unique tissue-specific functions revealed by selective gene knockout studies. *Physiol. Rev.* **88**, 887–918 (2009).

199. Bres, E. E. & Faissner, A. Low density receptor-related protein 1 interactions with the extracellular matrix: More than meets the eye. *Front. Cell Dev. Biol.* **7**, 1–32 (2019).

200. di Polidoro, A. C. *et al.* Revealing Angiopep-2/LRP1 Molecular Interaction for Optimal Delivery to Glioblastoma (GBM). *Molecules* **27**, (2022).

201. Wiley, D. T., Webster, P., Gale, A. & Davis, M. E. Transcytosis and brain uptake of transferrin-containing nanoparticles by tuning avidity to transferrin receptor. *Proc. Natl. Acad. Sci. U. S. A.* **110**, 8662–8667 (2013).

202. Qosa, H. M. High-throughput screening for identification of blood-brain barrier integrity enhancers: a drug repurposing opportunity to rectify vascular amyloid toxicity Hisham. *Physiol. Behav.* **176**, 139–148 (2019).

203. Hubatsch, I., Ragnarsson, E. G. E. & Artursson, P. Determination of drug permeability and prediction of drug absorption in Caco-2 monolayers. *Nat. Protoc.* **2**, 2111–2119 (2007).

204. Rappel, W. J. & Edelstein-Keshet, L. Mechanisms of cell polarization. *Curr. Opin. Syst. Biol.* **3**, 43–53 (2017).

205. Ullrich Axel & Strebhardt Klaus. Ehrlich magic bullet concept 100 years of progress Ullrich 2008. *Nat. Rev. Cancer* **8**, 473–480 (2008).

Chapter 7
Appendix

7.1 Polymer Characterisation

The NMR and GPC data obtained for the polymers detailed in tables 2.2 and 2.4 are shown in the figures (A.1 - A.26) below. Polymers were analysed using the methods described in chapter 2 for copolymer characterisation. In all ^{1}H NMR spectra, the peak at δ7.26 correlates to $CDCl_3$. Each peak integral outlined corresponds to peaks on the polymers described in figure 2.2A and 2.17A for PEG-PCL and N_3PEG-PCL respectively.

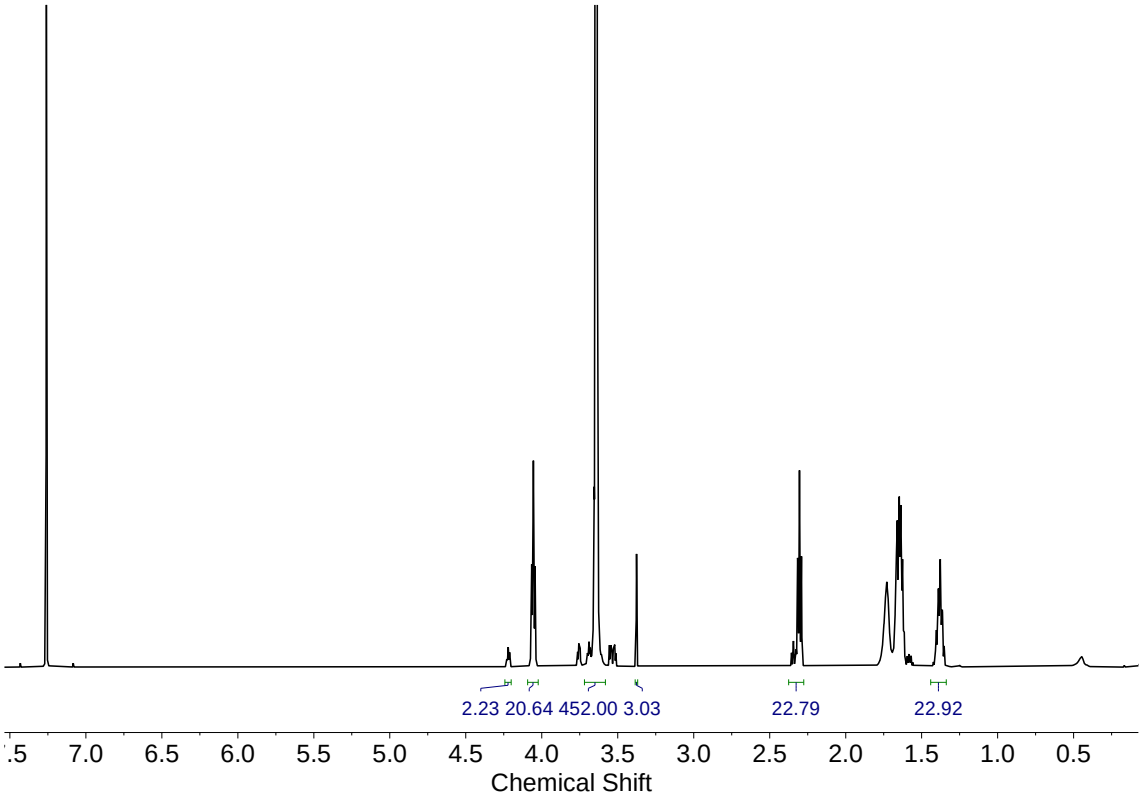

Fig A.1 NMR Spectra of PCL10

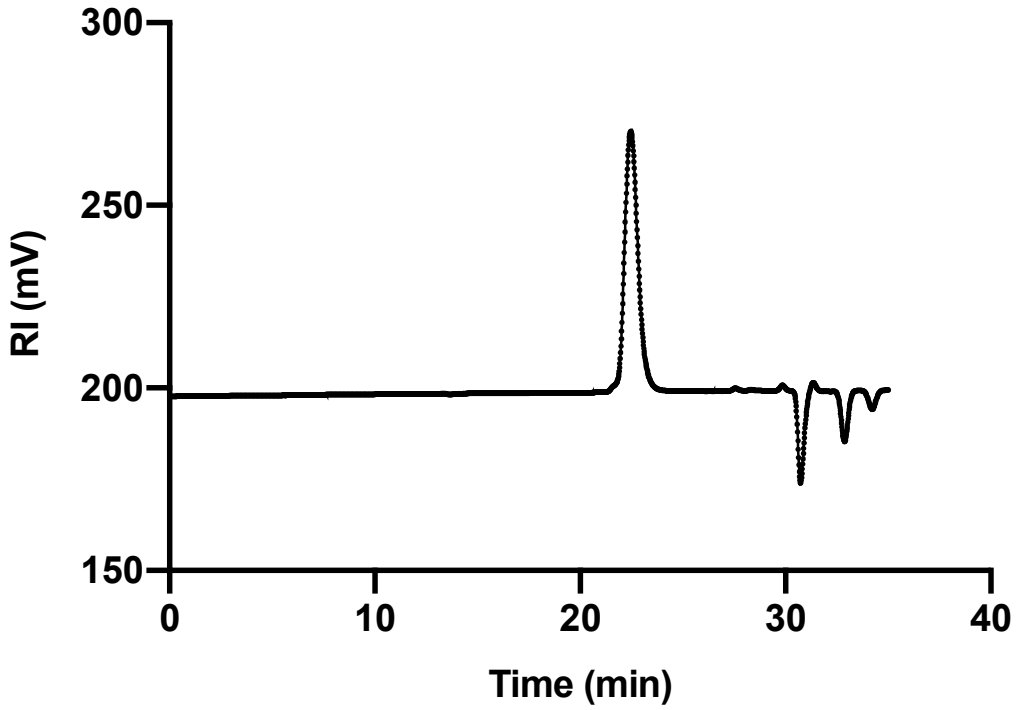

Fig A.2 GPC Trace of PCL10.

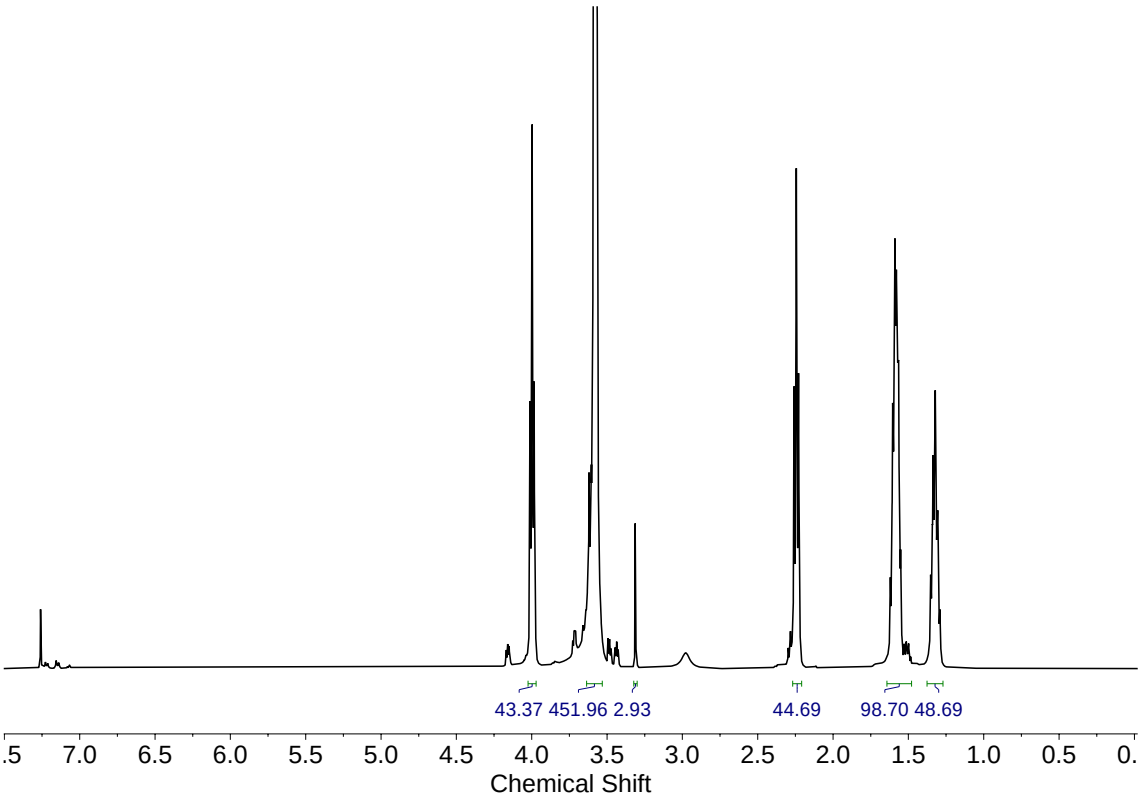

Fig A.3 NMR Spectra of PCL20

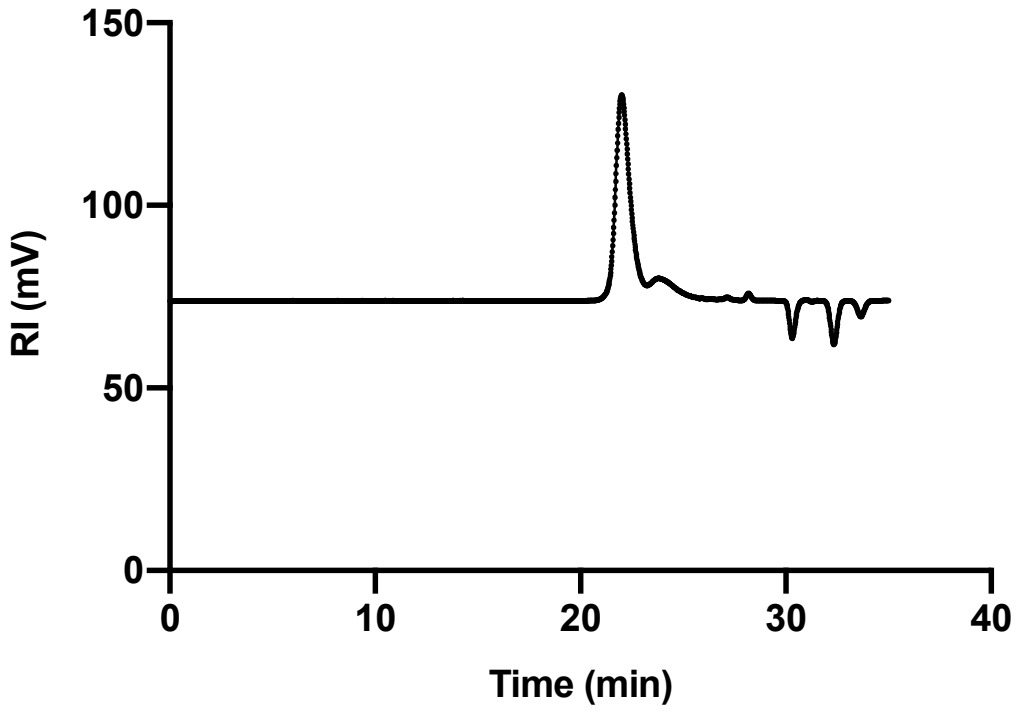

Fig A.4 GPC Trace of PCL20.

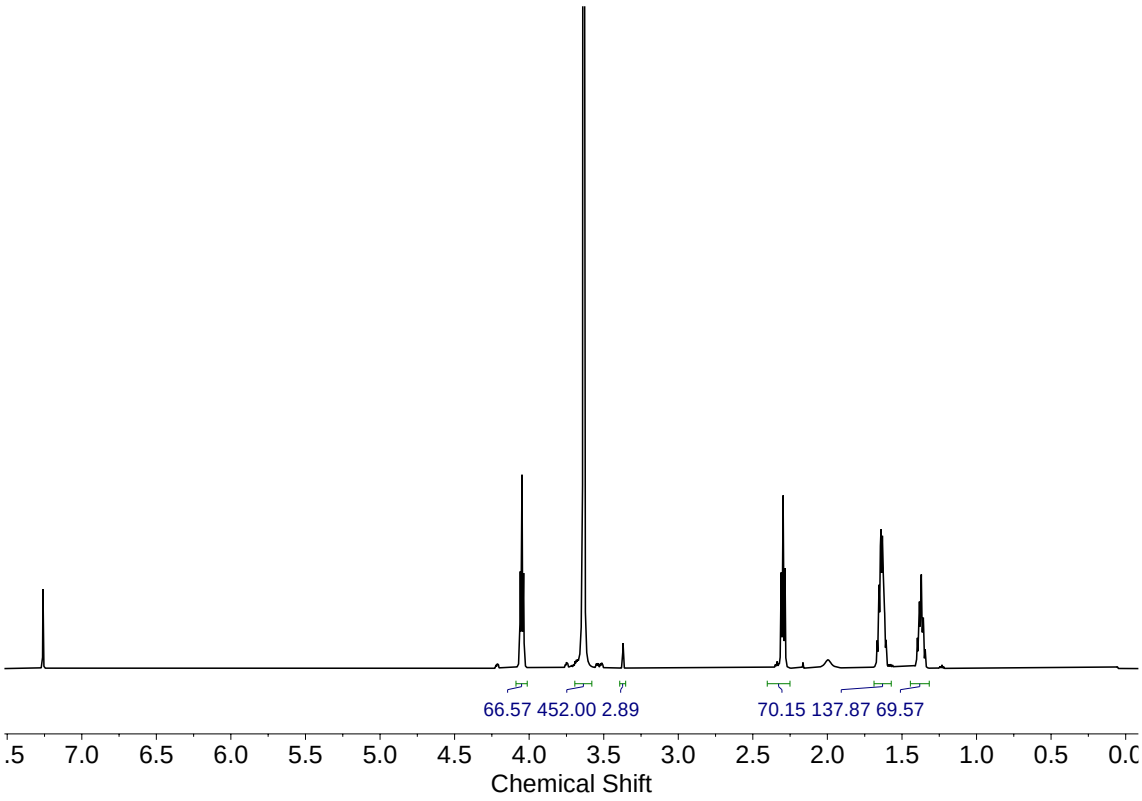

Fig A.5 NMR Spectra of PCL30

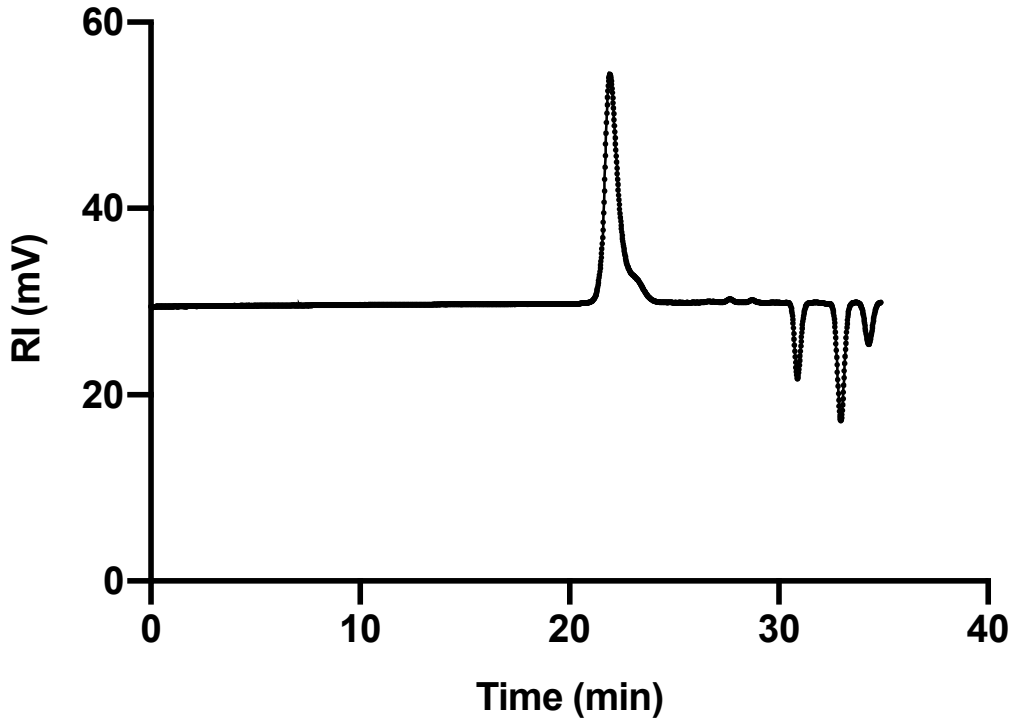

Fig A.6 GPC Trace of PCL30.

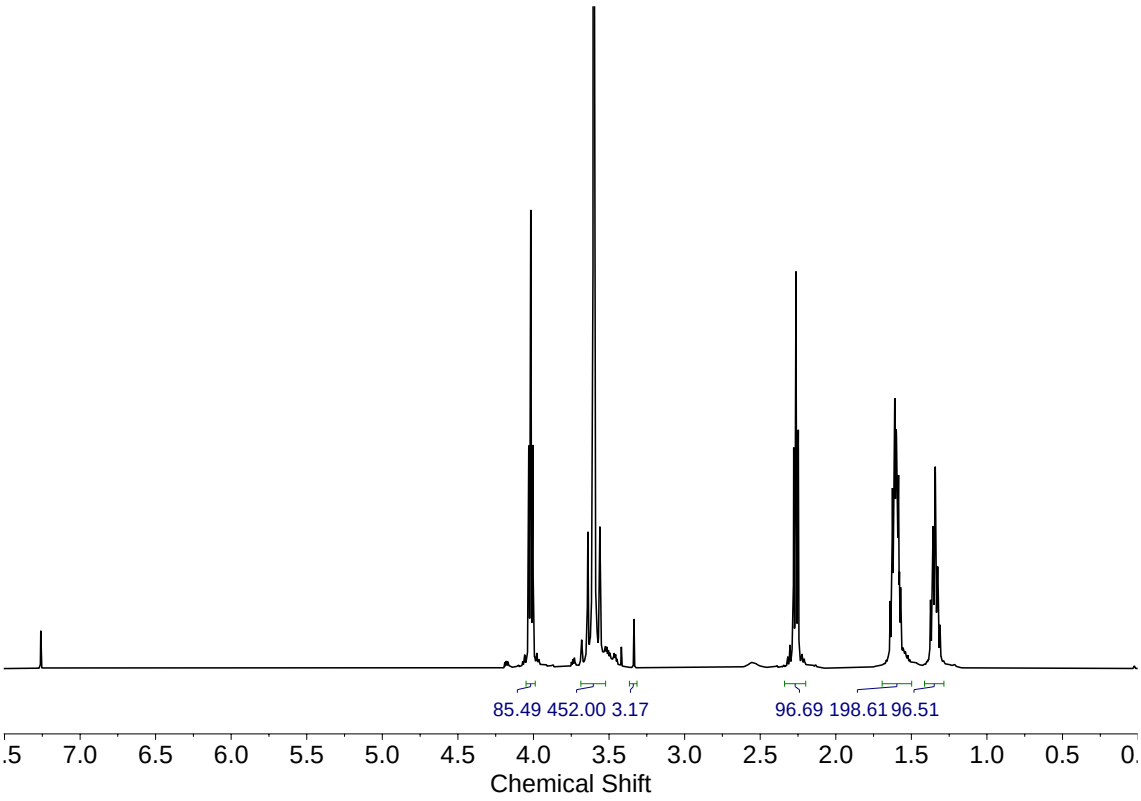

Fig A.7 NMR Spectra of PCL40

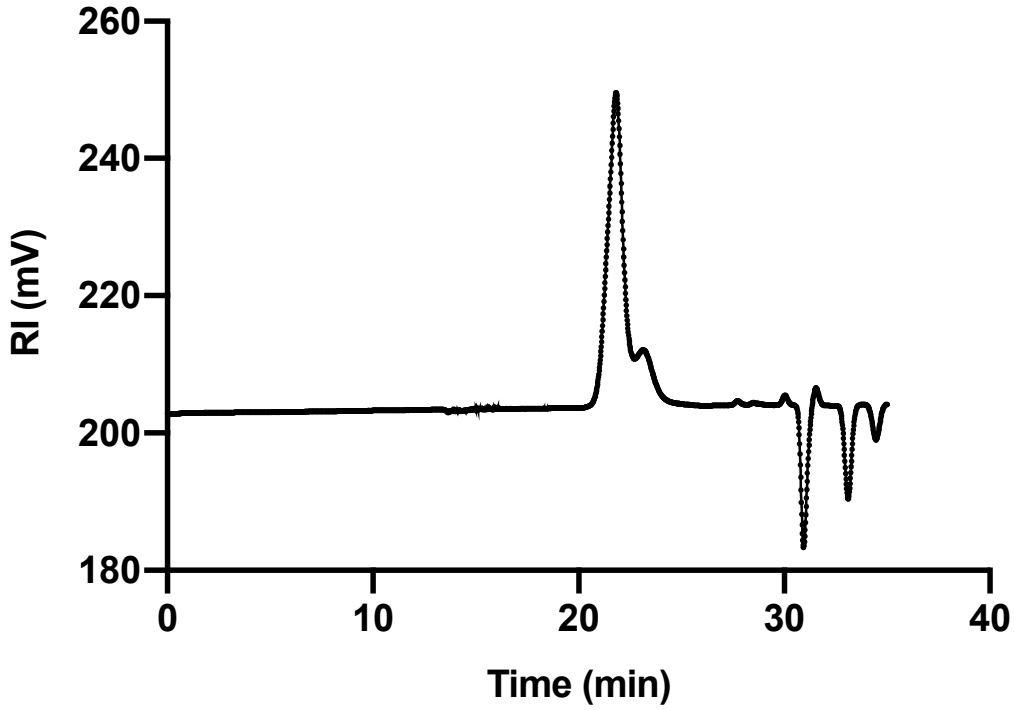

Fig A.8 GPC Trace of PCL40.

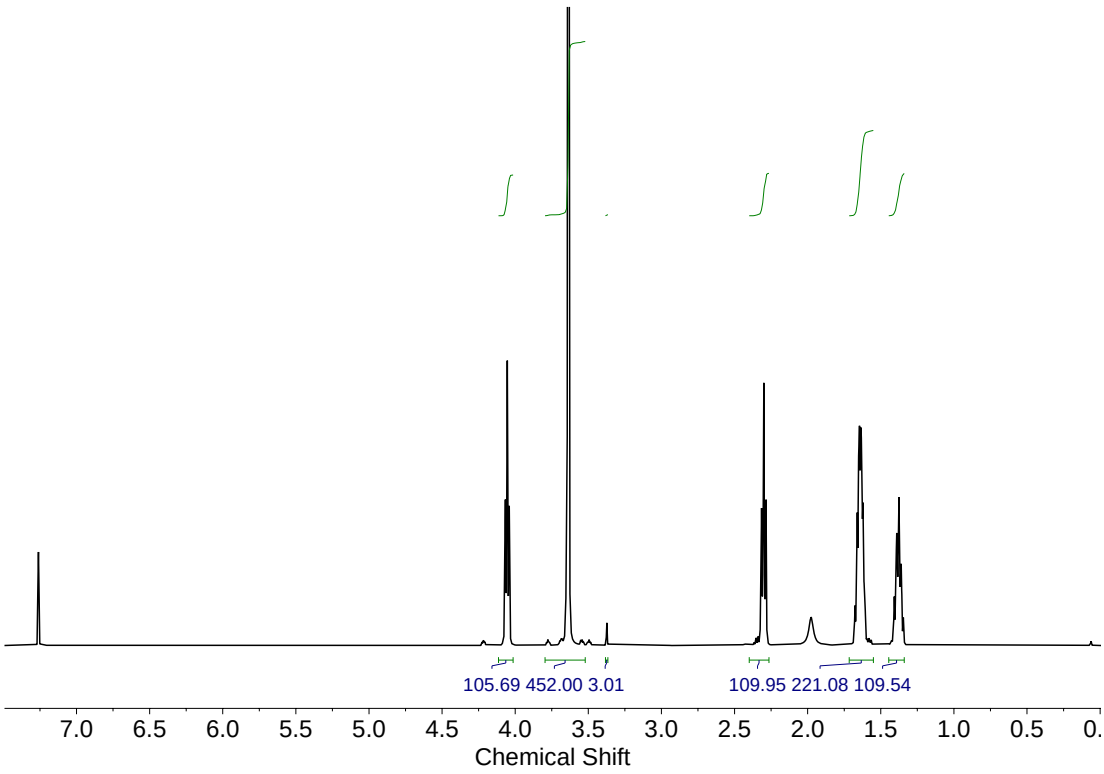

Fig A.9 NMR Spectra of PCL50

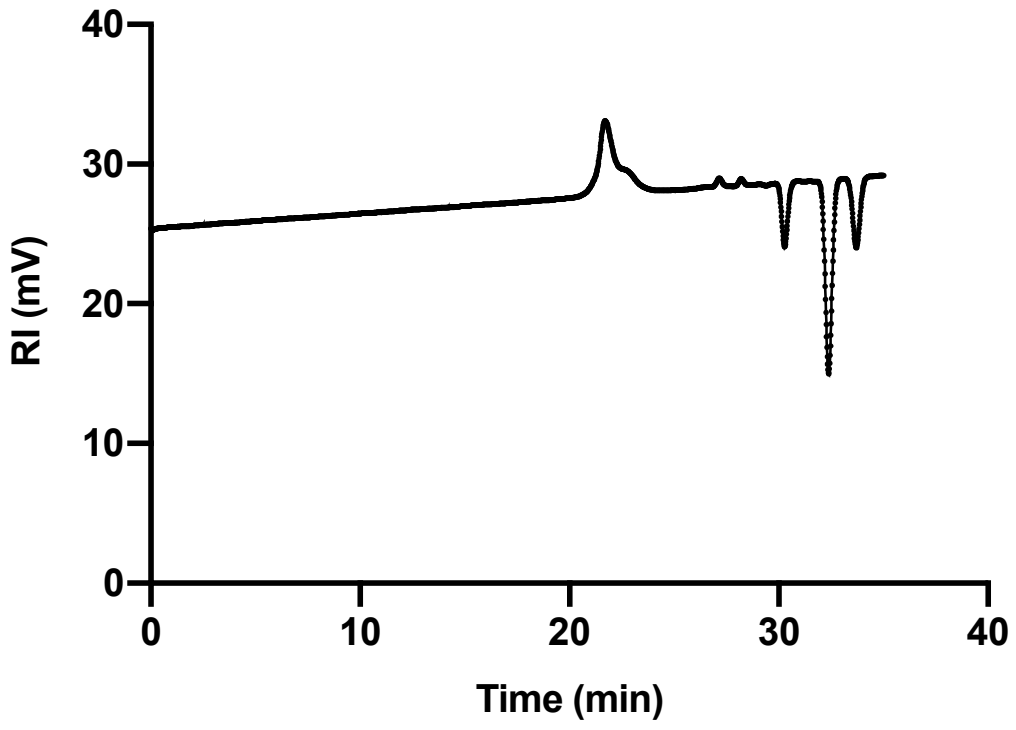

Fig A.10 GPC Trace of PCL50.

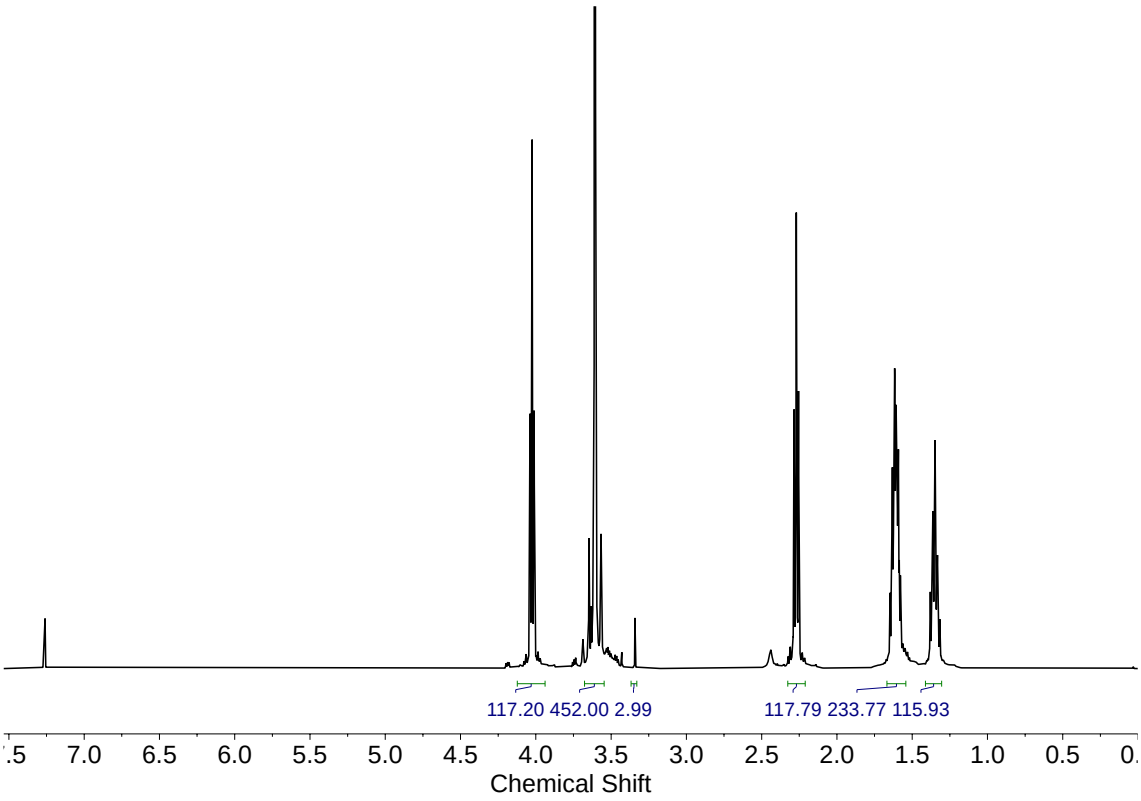

Fig A.11 NMR Spectra of PCL60

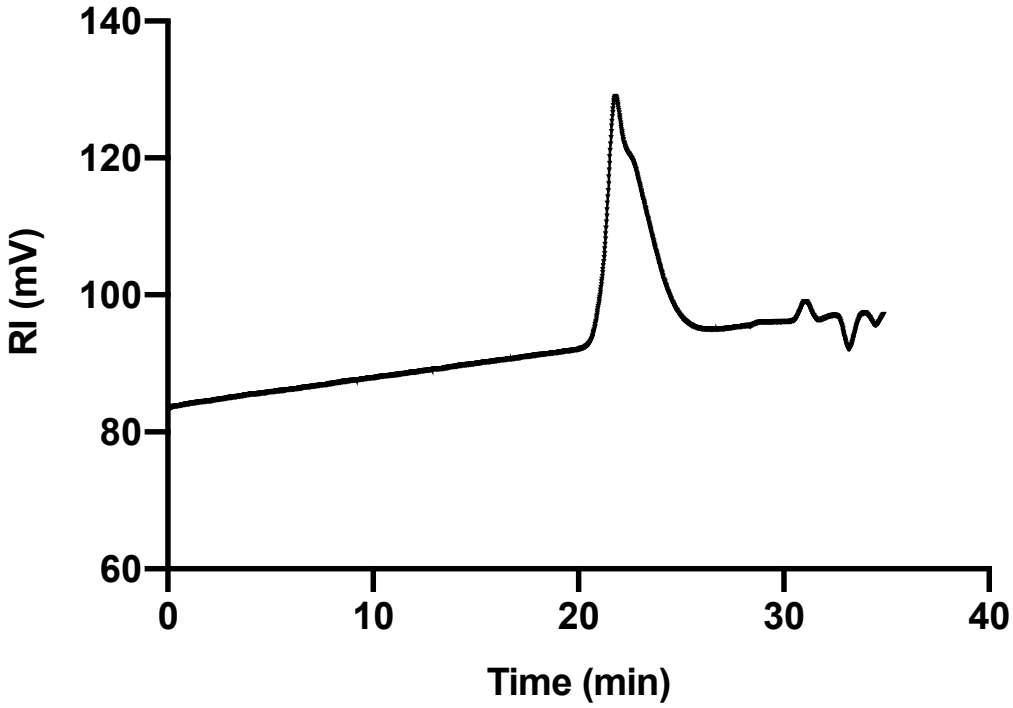

Fig A.12 GPC Trace of PCL60

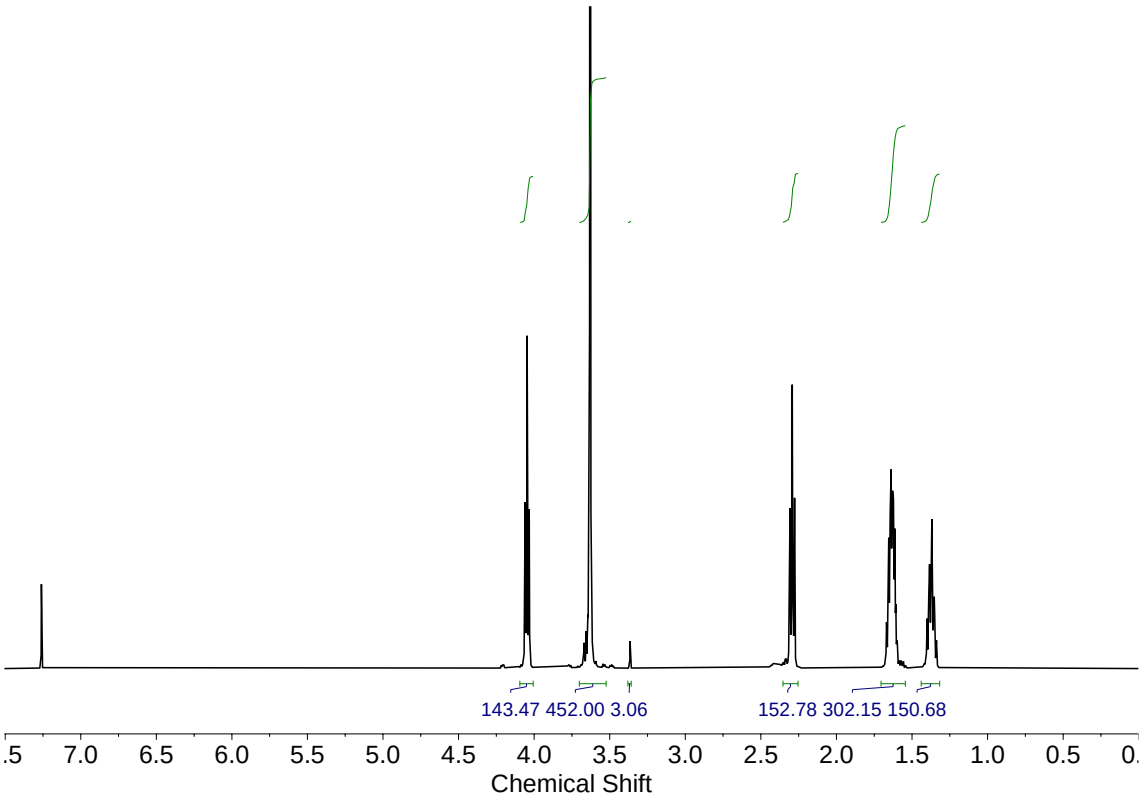

Fig A.13 NMR Spectra of PCL70

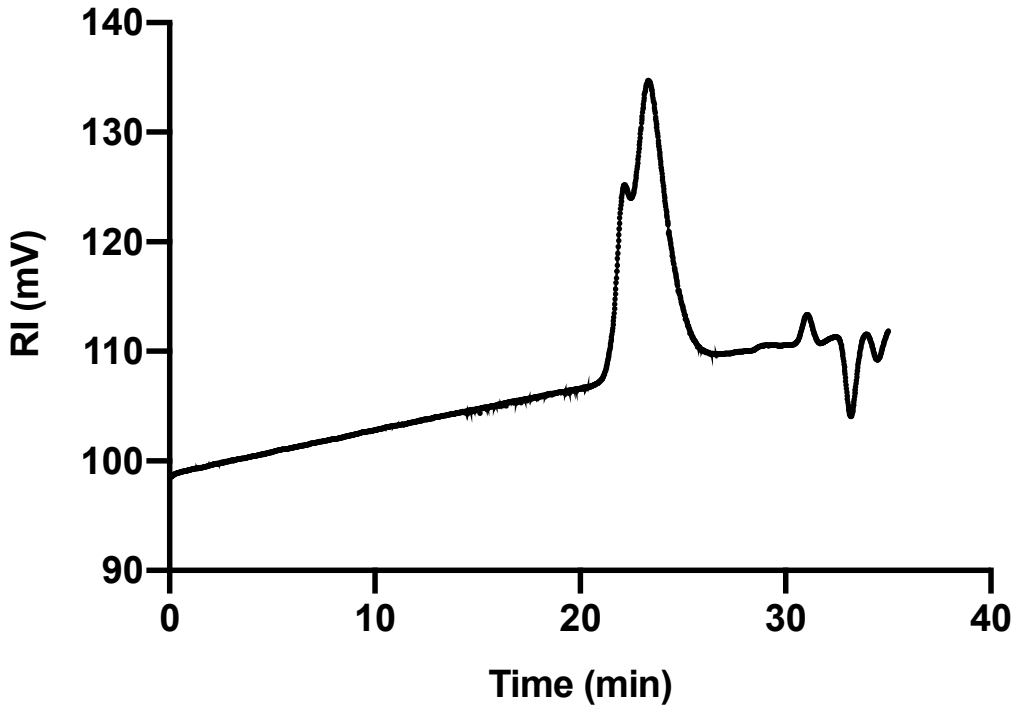

Fig A.14 GPC Trace of PCL70

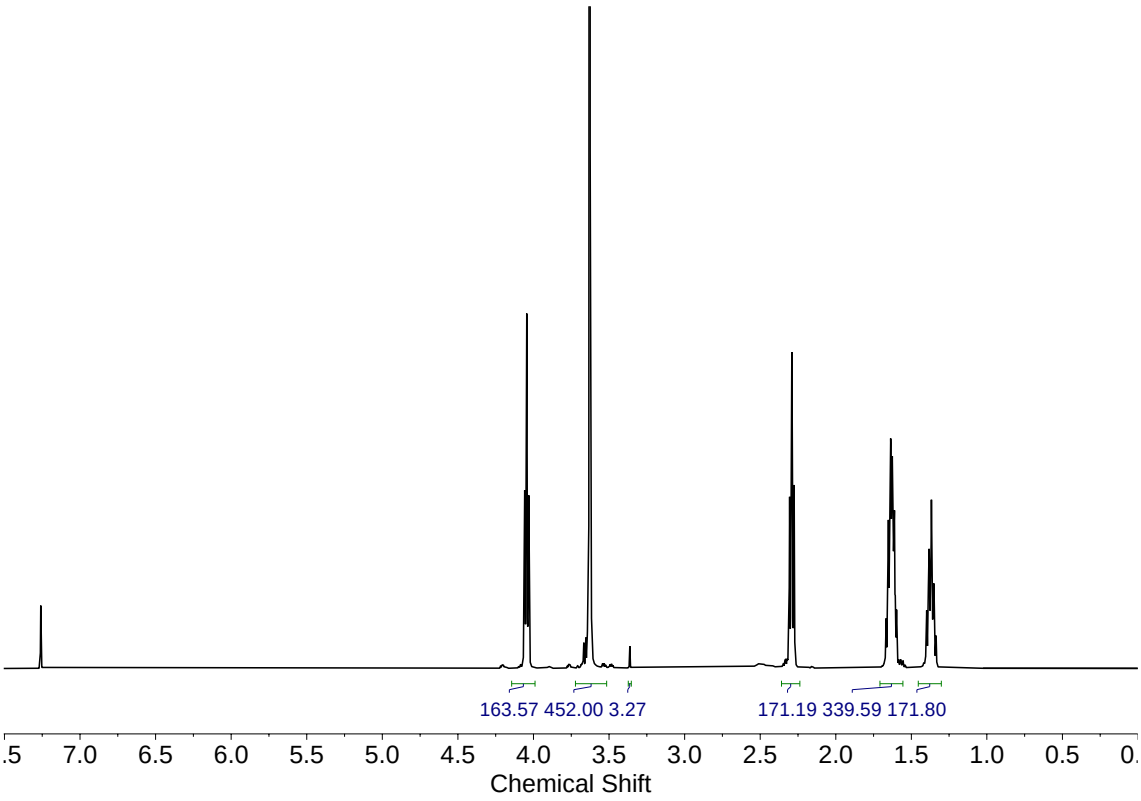

Fig A.15 NMR Spectra of PCL80

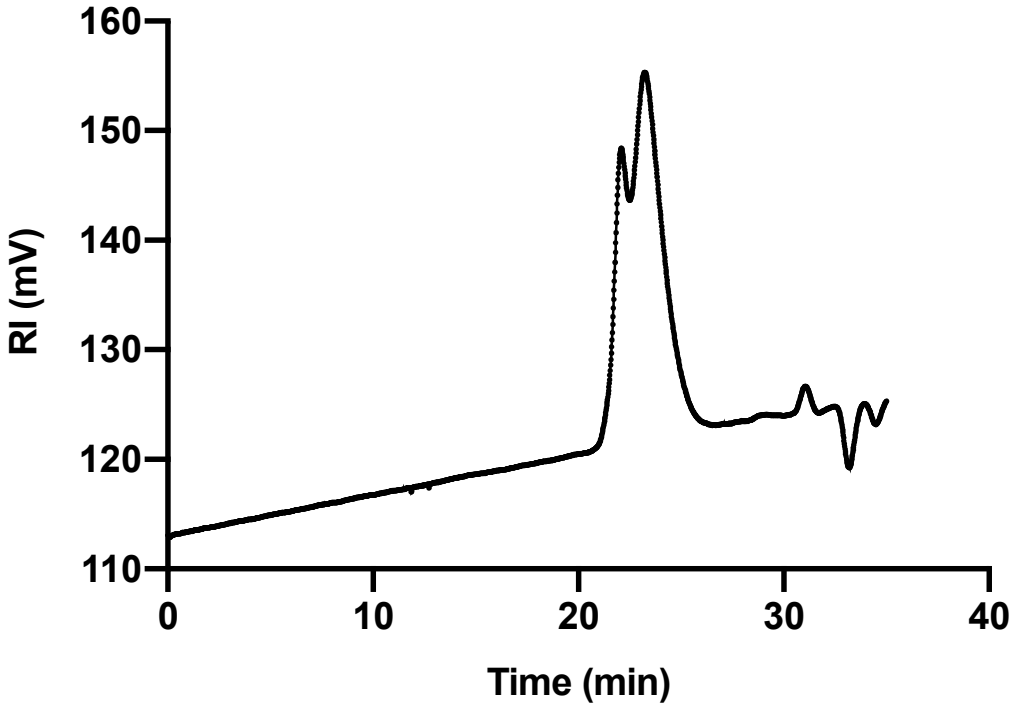

Fig A.16 GPC Trace of PCL80

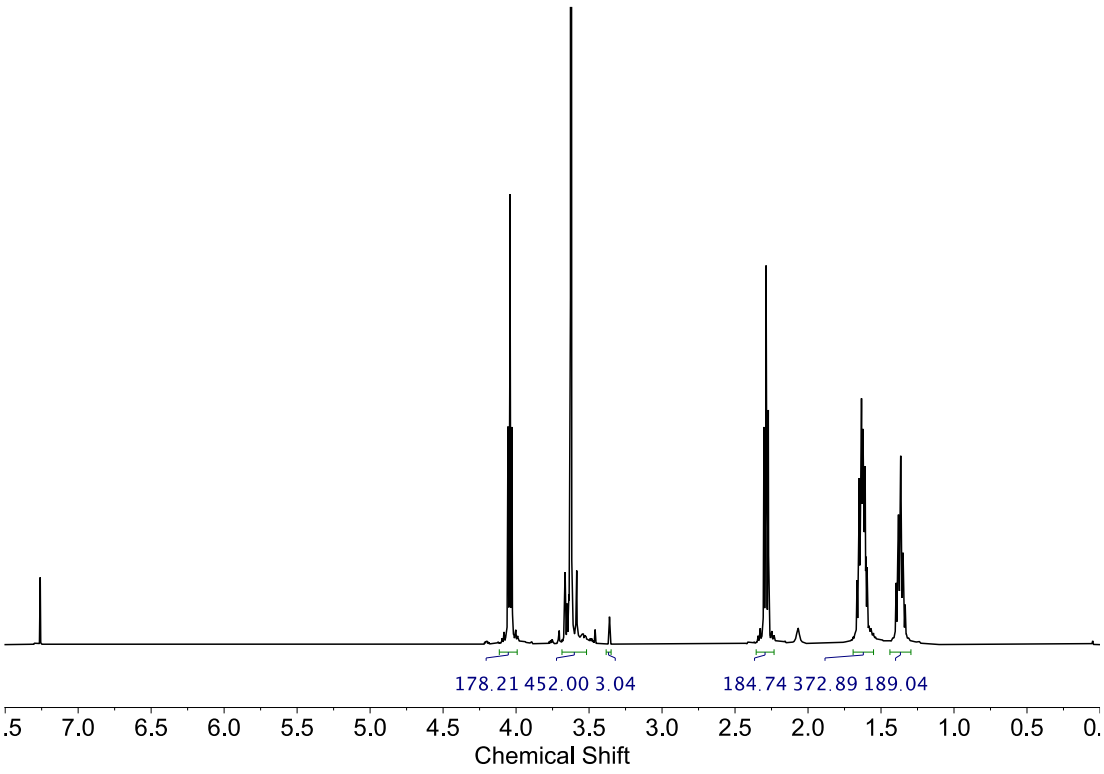

Fig A.17 NMR Spectra of PCL90

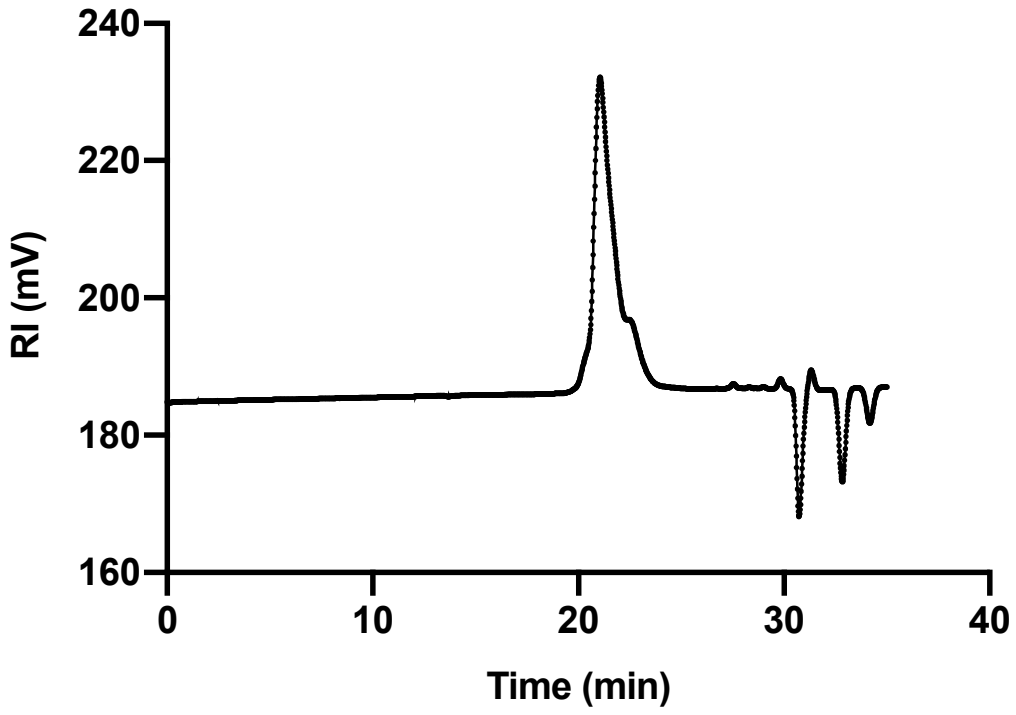

Fig A.18 GPC Trace of PCL90

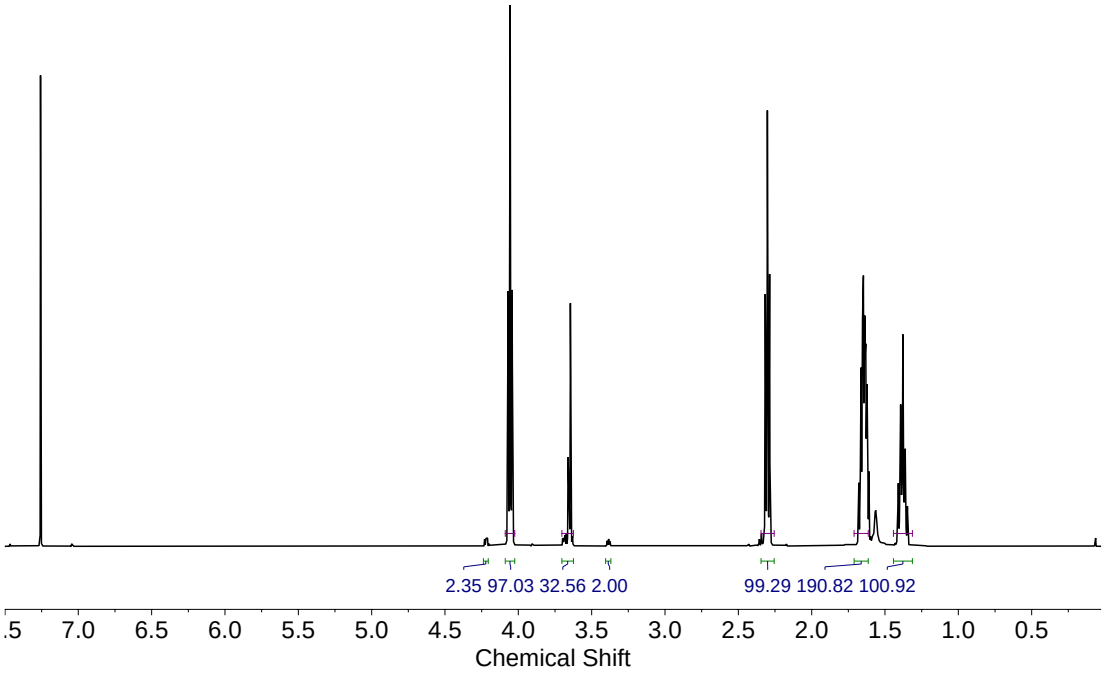

Fig A.19 NMR Spectra of N3PEG8PCL

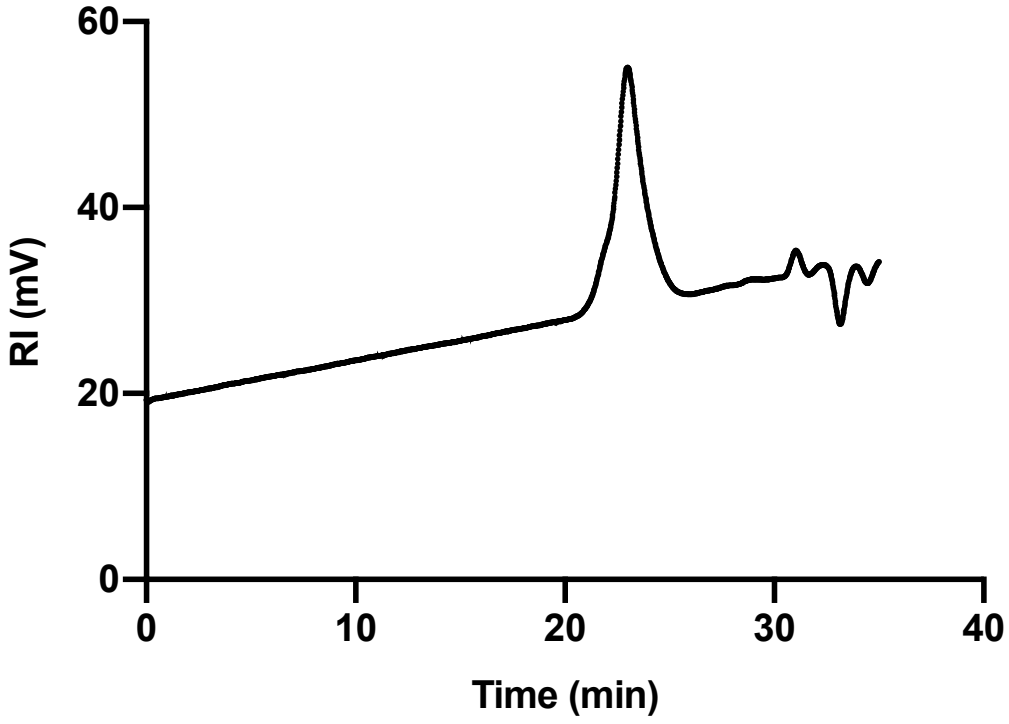

Fig A.20 GPC Trace of N3PEG8PCL

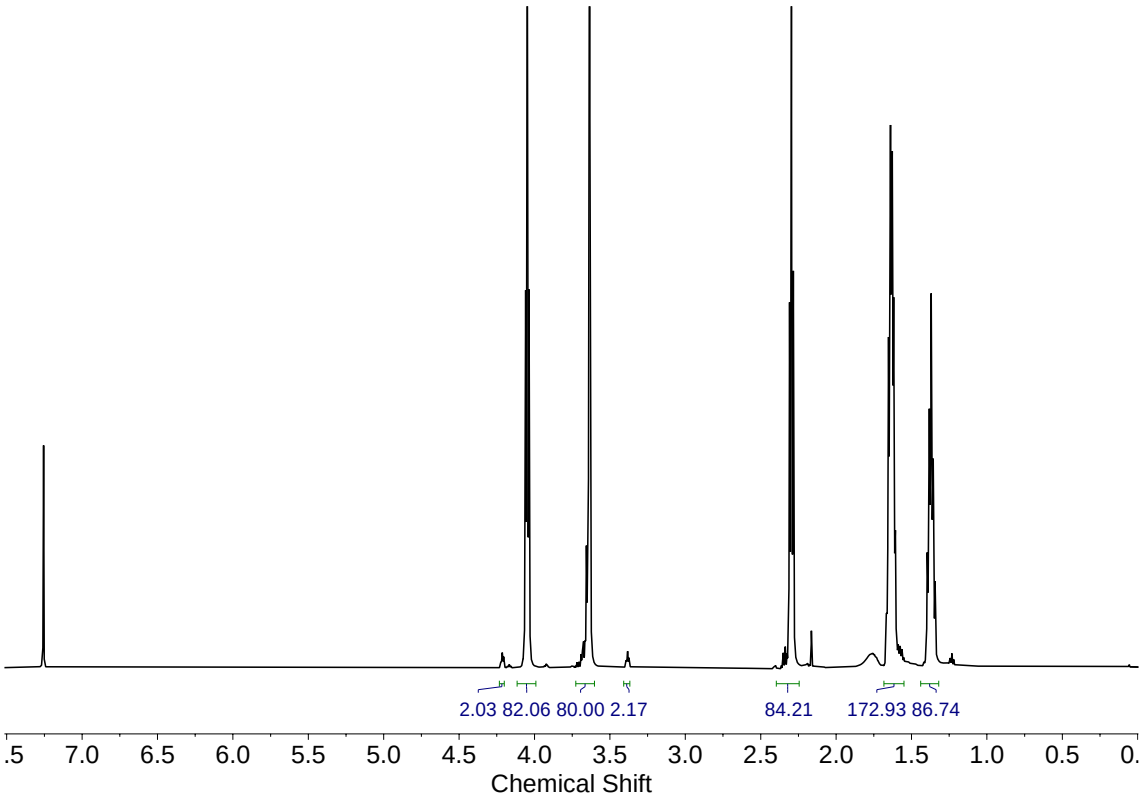

Fig A.21 NMR Spectra of N3PEG20PCL

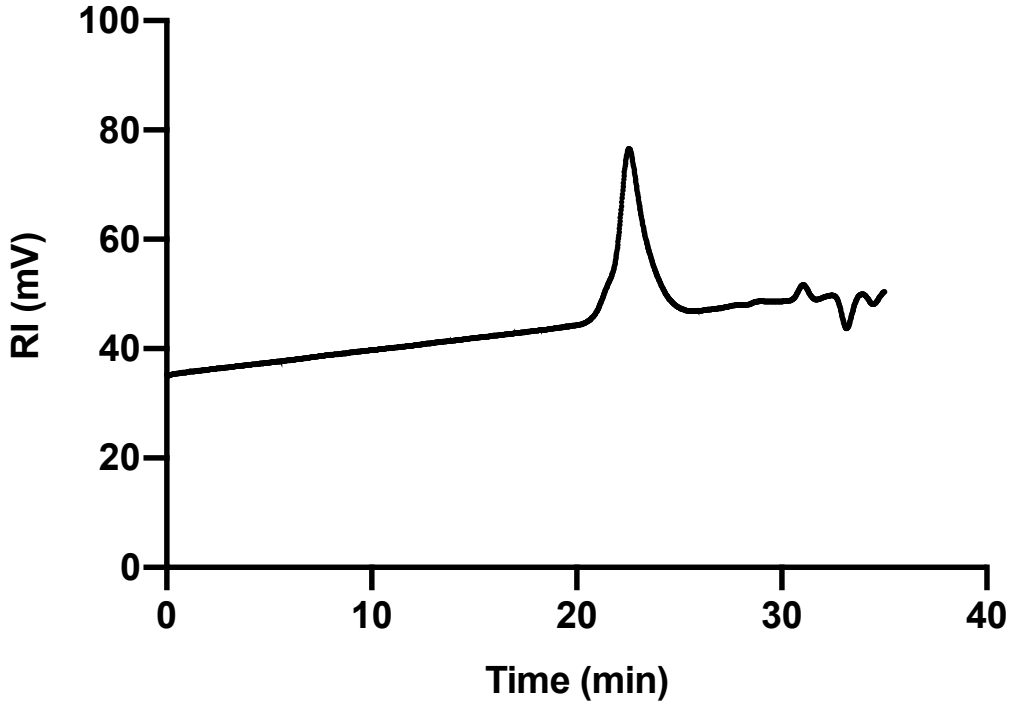

Fig A.22 GPC Trace of N3PEG20PCL

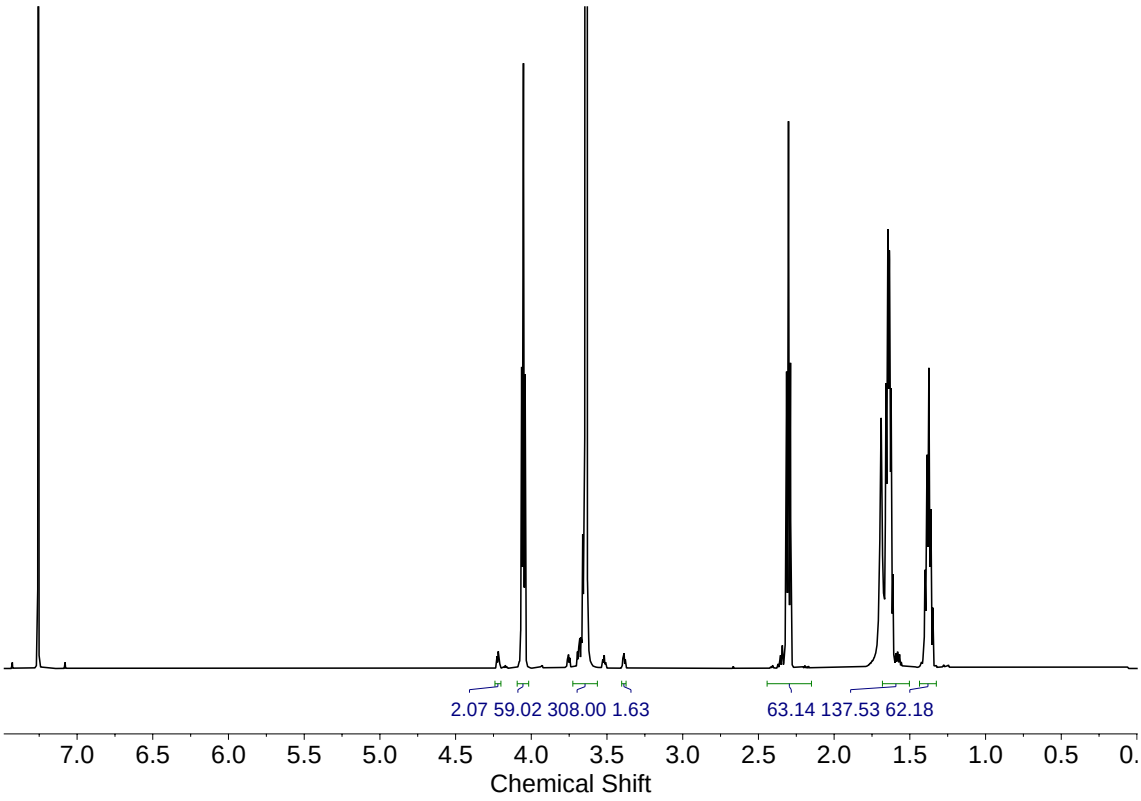

Fig A.23 NMR Spectra of N3PEG68PCL

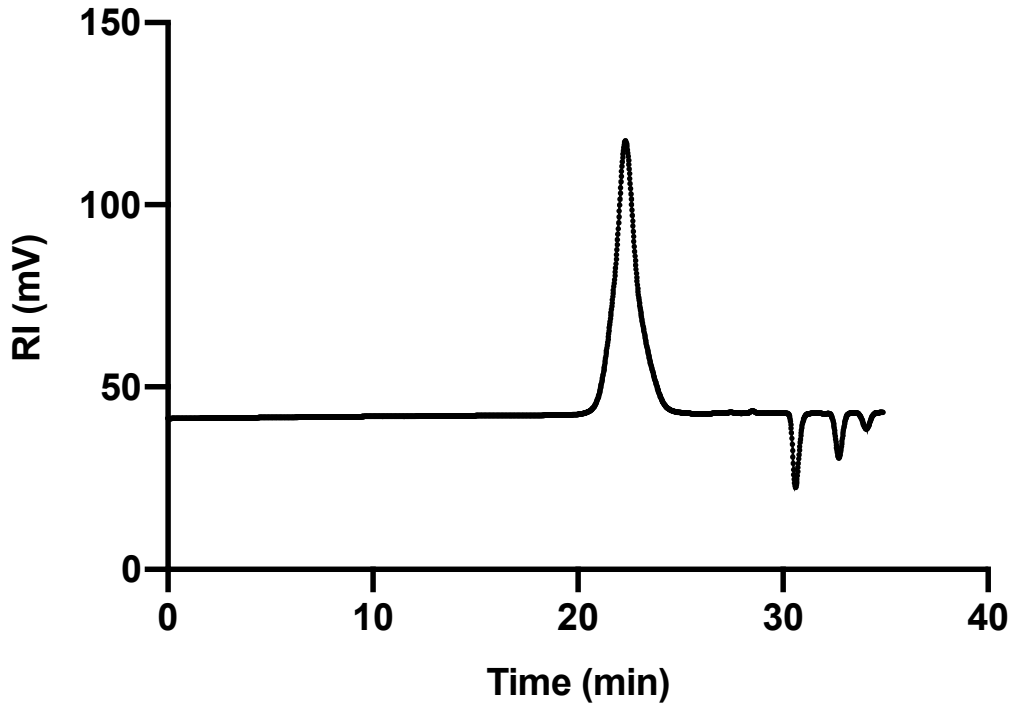

Fig A.24 GPC Trace of N3PEG68PCL

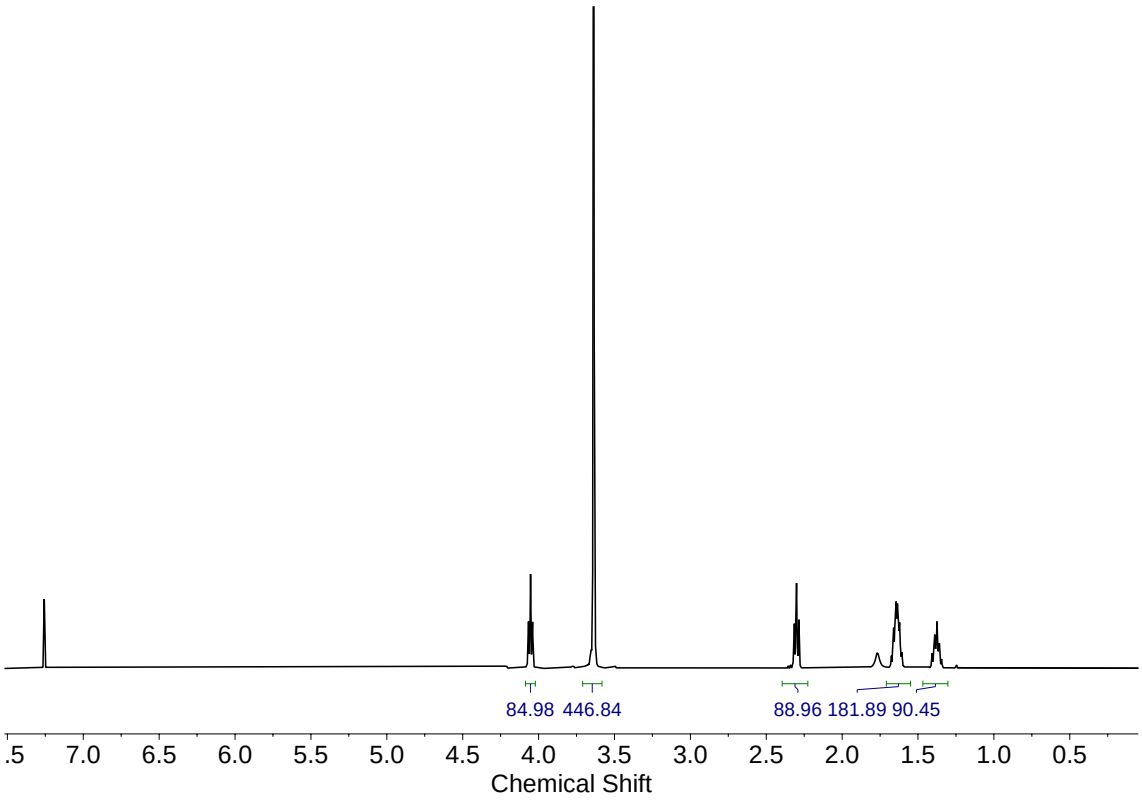

Fig A.25 NMR Spectra of N3PEG113PCL

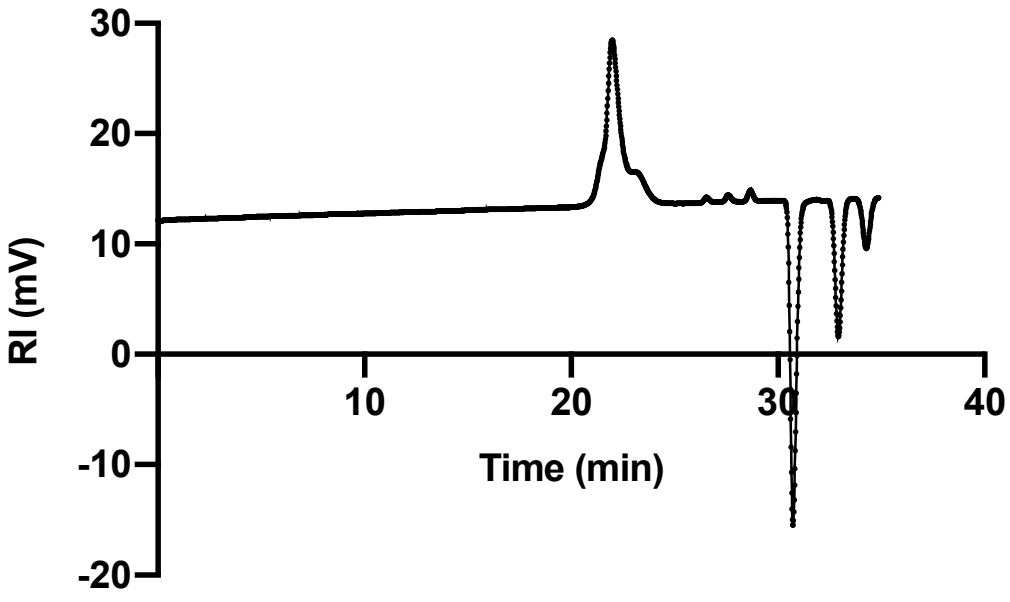

Fig A.26 GPC Trace of N3PEG113PCL

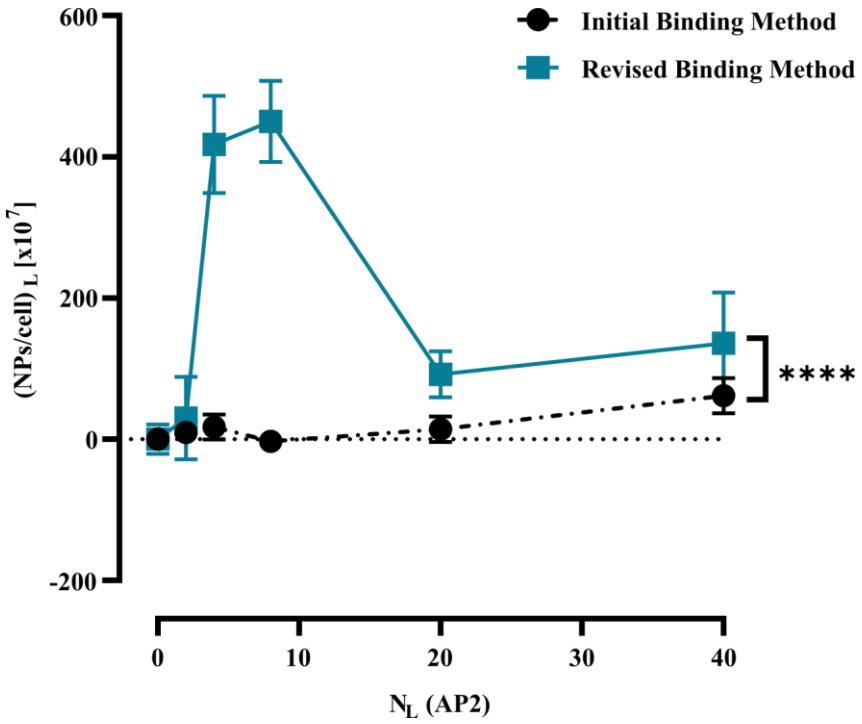

Fig A.27 **Binding method optimisation.** The graph details the $\frac{NPs}{cell_L}$ against N_{Ligand} when using AP2_1 set of nanoparticles to bind onto bEnd3. bEnd3 cells were incubated for 1h with nanoparticles (20 μM) from the AP2_1 set ($\delta_L = 1, N_{Ligand} = 2 - 40$) and the Ctrl set ($N_{Ligand} = 0$) as a control. Each point represents the mean ± SEM (n=3). In the diagram, $N_L = N_{Ligand}$. A one-way ANOVA was used for the statistical analysis alongside a post-hoc Dunnett's multiple comparison test (**** $P \leq 0.0001$).